THE SUPERIOR COLLICULUS/ TECTUM: CELL TYPES, CIRCUITS, COMPUTATIONS, BEHAVIORS

EDITED BY: Karl Farrow, Tadashi Isa, Harald Luksch and Keisuke Yonehara

PUBLISHED IN: Frontiers in Neural Circuits, Frontiers in Cellular Neuroscience, Frontiers in Neuroscience and Frontiers in Neuroanatomy

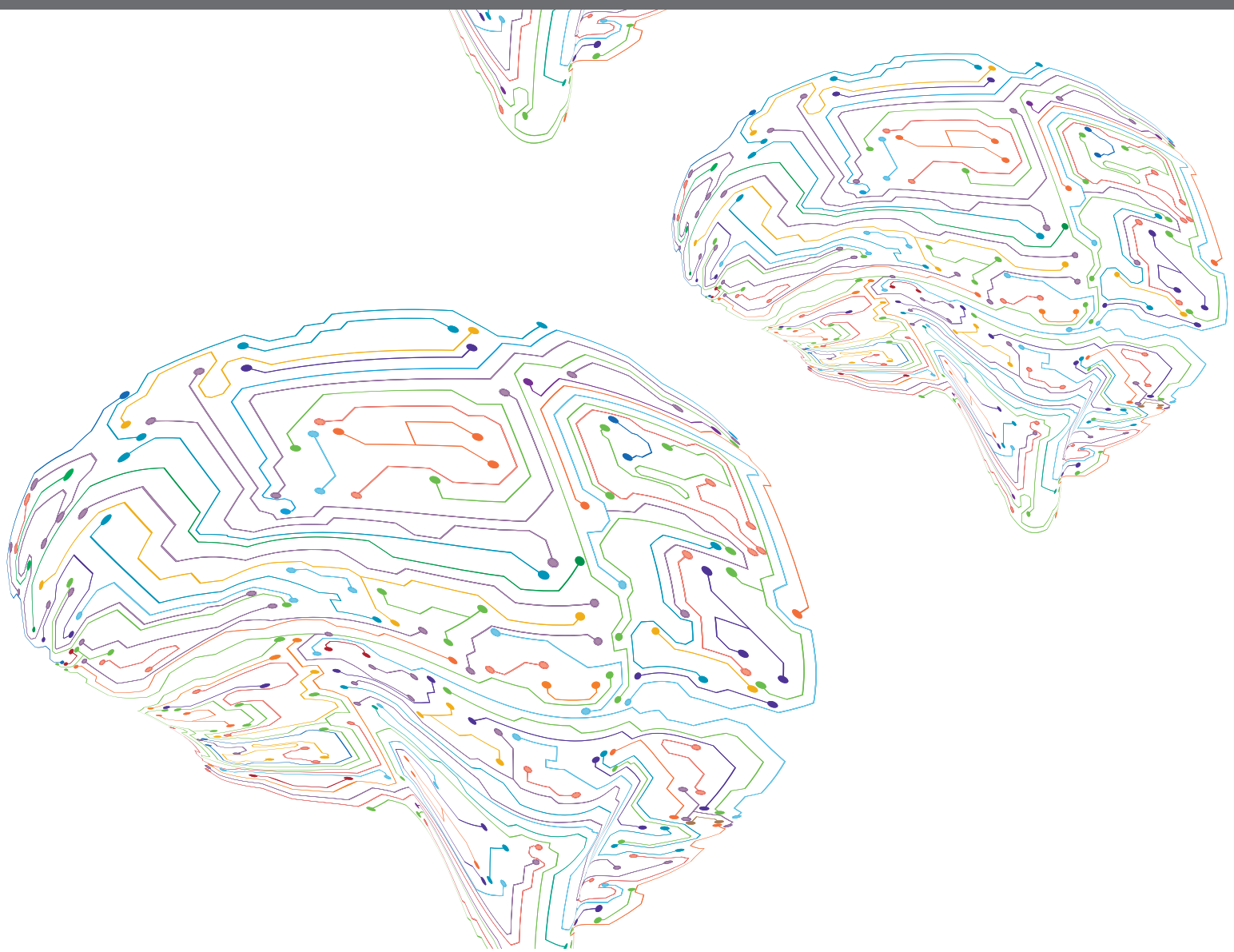

frontiers Research Topics

ISSN 1664-8714
ISBN 978-2-88945-971-1
DOI 10.3389/978-2-88945-971-1

About Frontiers

Frontiers is more than just an open-access publisher of scholarly articles: it is a pioneering approach to the world of academia, radically improving the way scholarly research is managed. The grand vision of Frontiers is a world where all people have an equal opportunity to seek, share and generate knowledge. Frontiers provides immediate and permanent online open access to all its publications, but this alone is not enough to realize our grand goals.

Frontiers Journal Series

The Frontiers Journal Series is a multi-tier and interdisciplinary set of open-access, online journals, promising a paradigm shift from the current review, selection and dissemination processes in academic publishing. All Frontiers journals are driven by researchers for researchers; therefore, they constitute a service to the scholarly community. At the same time, the Frontiers Journal Series operates on a revolutionary invention, the tiered publishing system, initially addressing specific communities of scholars, and gradually climbing up to broader public understanding, thus serving the interests of the lay society, too.

Dedication to Quality

Each Frontiers article is a landmark of the highest quality, thanks to genuinely collaborative interactions between authors and review editors, who include some of the world's best academicians. Research must be certified by peers before entering a stream of knowledge that may eventually reach the public - and shape society; therefore, Frontiers only applies the most rigorous and unbiased reviews.
Frontiers revolutionizes research publishing by freely delivering the most outstanding research, evaluated with no bias from both the academic and social point of view. By applying the most advanced information technologies, Frontiers is catapulting scholarly publishing into a new generation.

What are Frontiers Research Topics?

Frontiers Research Topics are very popular trademarks of the Frontiers Journals Series: they are collections of at least ten articles, all centered on a particular subject. With their unique mix of varied contributions from Original Research to Review Articles, Frontiers Research Topics unify the most influential researchers, the latest key findings and historical advances in a hot research area! Find out more on how to host your own Frontiers Research Topic or contribute to one as an author by contacting the Frontiers Editorial Office: researchtopics@frontiersin.org

THE SUPERIOR COLLICULUS/ TECTUM: CELL TYPES, CIRCUITS, COMPUTATIONS, BEHAVIORS

Topic Editors:
Karl Farrow, Neuro-Electronics Research Flanders, KU Leuven, VIB Leuven, and imec, Belgium
Tadashi Isa, Kyoto University, Japan
Harald Luksch, Technische Universität München, Germany
Keisuke Yonehara, Aarhus University and Danish Research Institute of Translational Neuroscience, Denmark

Citation: Farrow, K., Isa, T., Luksch, H., Yonehara, K., eds. (2019). The Superior Colliculus/Tectum: Cell Types, Circuits, Computations, Behaviors. Lausanne: Frontiers Media. doi: 10.3389/978-2-88945-971-1

Table of Contents

frontiers in Neural Circuits

EDITORIAL
published: 03 June 2019
doi: 10.3389/fncir.2019.00039

Editorial: The Superior Colliculus/Tectum: Cell Types, Circuits, Computations, Behaviors

Karl Farrow[1,2,3,4], *Tadashi Isa*[5], *Harald Luksch*[6] *and Keisuke Yonehara*[7,8]*

[1] Neuro-Electronics Research Flanders, Leuven, Belgium, [2] Department of Biology, Leuven Brain Institute, KU Leuven, Leuven, Belgium, [3] VIB, Leuven, Belgium, [4] imec, Leuven, Belgium, [5] Department Neuroscience, Graduate School of Medicine, Kyoto University, Kyoto, Japan, [6] Lehrstuhl für Zoologie, Technische Universität München, Freising, Germany, [7] Department of Biomedicine, Aarhus University, Aarhus, Denmark, [8] Danish Research Institute of Translational Neuroscience, Aarhus, Denmark

Keywords: superior colliculus, optic tectum, cell types, neuronal circuit, visual processing

Editorial on the Research Topic

The Superior Colliculus/Tectum: Cell Types, Circuits, Computations, Behaviors

The superior colliculus is an important brain structure that transforms sensory inputs into motor outputs for the purpose of directing orienting behaviors and attention. One special feature of the superior colliculus is that sensory and motor maps are aligned topologically across the two-dimensional layers, which facilitates the triggering of behavioral responses in coordination with the sensory environment. However, basic descriptions of physiological and anatomical properties of neurons in the superior colliculus, as well as the input-output relationship with other brain areas is still not satisfactory. Furthermore, the degree to which neuronal and circuitry properties are conserved across species or specialized for specific behaviors remains unclear.

The aim of this research topic is to highlight the breadth of research currently being performed on the superior colliculus across different animal species in the form of original articles, reviews, and perspectives. The research topic successfully collected 11 articles contributed by 48 authors. Among the collected papers in this research topic, two were performed in zebrafish, one in rats, three in mice, and five were about non-human primates.

First, although the superior colliculus (optic tectum in zebrafish) is often studied by testing how to respond to sensory stimuli or generate motor commands, the spontaneous activity of the neurons can provide insights into the spatial organization and functional connectivity within the superior colliculus (Marachlian et al.). Marachlian et al. provide a review of the zebrafish literature focusing on studies using large scale recordings of the spontaneous activity of neurons in the larval zebrafish optic tectum. This review highlights the unique advantages of the larval zebrafish as a model organism to monitor activity in the entire optic tectum simultaneously.

A clear advantage of using the superior colliculus to understand how retinal inputs are further processed is that neurons in the superficial layers of the superior colliculus receive this information directly, and it is localized relatively superficial of the brain, allowing for good experimental access. One key to addressing such research questions is the ability to label cell types for manipulating and dissecting neuronal pathways mediating individual information streams (Oliveira and Yonehara). Along these lines Villalobos et al. present a study investigating whether parvalbumin-positive neurons are a unique cell type within the mouse superior colliculus. They found that the mouse superior colliculus, parvalbumin-positive neurons are heterogeneous, comprising both GABAergic inhibitory and glutamatergic excitatory neurons, which is dissimilar to some other brain areas such as the cortex, hippocampus and striatum, where parvalbumin-positive neurons are almost exclusively inhibitory (Villalobos et al.).

OPEN ACCESS

Edited by:
Edward S. Ruthazer, McGill University, Canada

Reviewed by:
Sarah L. Pallas, University of Massachusetts Amherst, United States

***Correspondence:**
Keisuke Yonehara
keisuke.yonehara@dandrite.au.dk

Received: *27 March 2019*
Accepted: *06 May 2019*
Published: *03 June 2019*

Citation:
Farrow K, Isa T, Luksch H and Yonehara K (2019) Editorial: The Superior Colliculus/Tectum: Cell Types, Circuits, Computations, Behaviors. Front. Neural Circuits 13:39. doi: 10.3389/fncir.2019.00039

Two of the most ubiquitous response features studied in the visual system, from the retina to visual cortex, are orientation and direction selectivity. In mice, recent studies have highlighted the organization and origin of these response features in the superior colliculus. Here Shi et al. demonstrated that the direction and orientation selectivity of collicular neurons increases during the transformation from membrane potential to spiking responses. Intriguingly, the degree of increase depends on the receptive field size of the neuron (Shi et al.). In macaque monkeys, Chen and Hafed detail how neurons in the superficial layers of the superior colliculus are tuned to orientation, contrast, and temporal flicker fusion characteristics. These findings suggest that the primate superior colliculus might mediate coarse, but rapid, object detection and identification that can either facilitate or inhibit orienting responses of the animal (Chen and Hafed).

In addition to the retina, the superior colliculus receives an abundance of inputs from a variety of brain areas likely for the purpose of modulating the triggering of behaviors in ethologically relevant ways. Here Heap et al. demonstrate that in zebrafish hypothalamic neurons provide inhibitory projects to optic tectum, and this pathway appears to gate predatory behavior of the fish. In addition, Matsumoto et al. reviewed the causal role of inputs from frontal eye field to superior colliculus of monkeys during saccade generation.

Reflecting the diverse non-retinal inputs from other brain areas, the activity of superior colliculus neurons can be affected by internal states. Here two studies in monkeys illustrate how learning and expected reward values affect neuronal activity in the superior colliculus. Griggs et al. demonstrate that neurons in the superior colliculus can discriminate objects based on reward values, and such modulation is likely provided by the basal ganglia. In addition, Sadeh et al. show that the spatial coding of visual and motor responses of neurons in the superior colliculus are altered by the introduction of a trained delay during a memory-delay saccade task.

Like its inputs the output pathways of the superior colliculus show remarkable diversity. In rats, Kaneshige et al. show that the superior colliculus provides direct input to the contralateral facial nucleus, and indirectly to central pattern generators that are involved in modulating vibrissal movements. In macaque monkeys, Elorette et al. provide compelling anatomical evidence that the superior colliculus projects via pulvinar nuclei to the lateral amygdala, providing a short route for salient visual information to influence emotions.

As illustrated by the topics and methods of the collected papers, the study of the superior colliculus involves diverse questions, research methods, and animal models, with each providing a unique prospective on its role. Our hope is that this research topic illuminates the current trends and future directions of this field. In particular, we hope this collection will inspire researchers to integrate knowledge gained from different species and approaches to inform the next steps to be taken, and questions to be asked in the coming years.

AUTHOR CONTRIBUTIONS

All authors listed have made a substantial, direct and intellectual contribution to the work, and approved it for publication.

Conflict of Interest Statement: The authors declare that the research was conducted in the absence of any commercial or financial relationships that could be construed as a potential conflict of interest.

frontiers in Neural Circuits

ORIGINAL RESEARCH
published: 22 November 2018
doi: 10.3389/fncir.2018.00100

A Descending Circuit Derived From the Superior Colliculus Modulates Vibrissal Movements

*Miki Kaneshige[1,2], Ken-ichi Shibata[1], Jun Matsubayashi[2], Akira Mitani[2] and Takahiro Furuta[1,3]**

[1] Department of Morphological Brain Science, Graduate School of Medicine, Kyoto University, Kyoto, Japan, [2] Laboratory of Physiology, Department of Human Health Sciences, Graduate School of Medicine, Kyoto University, Kyoto, Japan, [3] Department of Oral Anatomy and Neurobiology, Graduate School of Dentistry, Osaka University, Suita, Japan

The superior colliculus (SC) is an essential structure for the control of eye movements. In rodents, the SC is also considered to play an important role in whisking behavior, in which animals actively move their vibrissae (mechanosensors) to gather tactile information about the space around them during exploration. We investigated how the SC contributes to vibrissal movement control. We found that when the SC was unilaterally lesioned, the resting position of the vibrissae shifted backward on the side contralateral to the lesion. The unilateral SC lesion also induced an increase in the whisking amplitude on the contralateral side. To explore the anatomical basis for SC involvement in vibrissal movement control, we then quantitatively evaluated axonal projections from the SC to the brainstem using neuronal labeling with a virus vector. Neurons of the SC mainly sent axons to the contralateral side in the lower brainstem. We found that the facial nucleus received input directly from the SC, and that the descending projections from the SC also reached the intermediate reticular formation and pre-Bötzinger complex, which are both considered to contain neural oscillators generating rhythmic movements of the vibrissae. Together, these results indicate the existence of a neural circuit in which the SC modulates vibrissal movements mainly on the contralateral side, via direct connections to motoneurons, and via indirect connections including the central pattern generators.

Keywords: whisker, premotor neurons, rat, anterograde tracing, kinematic analysis, CPGs

OPEN ACCESS

Edited by:
Tadashi Isa,
Kyoto University, Japan

Reviewed by:
Konstantinos Hadjidimitrakis,
Monash University, Australia
Kaoru Takakusaki,
Asahikawa Medical University, Japan

***Correspondence:**
Takahiro Furuta
furuta@dent.osaka-u.ac.jp

Received: *23 March 2018*
Accepted: *22 October 2018*
Published: *22 November 2018*

Citation:
Kaneshige M, Shibata K-i, Matsubayashi J, Mitani A and Furuta T (2018) A Descending Circuit Derived From the Superior Colliculus Modulates Vibrissal Movements. Front. Neural Circuits 12:100. doi: 10.3389/fncir.2018.00100

INTRODUCTION

The superior colliculus (SC), in the midbrain, has long been considered an essential structure for eye movement control (for reviews, see Fuchs et al., 1985; Sparks and Mays, 1990; Sommer and Wurtz, 2008). Eye movements are necessary for visual sensation because the majority of ganglion cells are of the transient type, which quickly adapt, and thus static images on the retina quickly

Abbreviations: Amb, ambiguus nucleus; AN, abducens nucleus; Bo, Bötzinger complex; contra, side contralateral to the lesion; CPGs, central pattern generators; FN, facial nucleus; GiRt, gigantocellular reticular nucleus; ipsi, side ipsilateral to the lesion; IRt, intermediate reticular formation; LPG, lateral paragigantocellular nucleus; PAG, periaqueductal gray; PCRt, parvicellular reticular nucleus; PPRF, paramedian pontine reticular formation; preBötC, pre-Bötzinger complex; SC, superior colliculus; Sp5I, spinal trigeminal nucleus, interpolar part; Sp5O, spinal trigeminal nucleus, oral part; vMC, vibrissal motor cortex.

disappear from perception. The small visual field of the fovea is another reason why animals have to move their eyes (for review, see Gegenfurtner, 2016). Many brain regions related to the oculomotor system receive input from the SC, which obtains visual information from the retina and visual cortices (for review, see May, 2006).

Like visual sensation, tactile sensation of the vibrissal system in rodents is generated by actively moving the sensors themselves. Facial vibrissae (whiskers) on rodents are excellent tactile apparatus. Rats and mice sweep their vibrissae backward and forward to touch objects with the vibrissae when exploring. This vibrissal movement pattern is called whisking (Zucker and Welker, 1969). Depending on the situation, animals modulate the amplitude, velocity, and midpoint of their whisking (Mitchinson et al., 2007; Grant et al., 2009; Hill et al., 2011).

The SC is part of the neural circuit that processes vibrissal sensorimotor information. Previous studies have shown that SC neurons are responsive to a passive touch of the vibrissae (McHaffie et al., 1989; Grunwerg and Krauthamer, 1990; Castro-Alamancos and Favero, 2016), and to artificial vibrissal movements produced by facial nerve stimulation in anesthetized rats (Bezdudnaya and Castro-Alamancos, 2011, 2014). It has also been reported that electrical stimulation of the SC evokes vibrissal movements (McHaffie and Stein, 1982; Hemelt and Keller, 2008). Furthermore, the SC sends axons to the facial nucleus (FN), where the vibrissal motoneurons are located (Isokawa-Akesson and Komisaruk, 1987; Miyashita et al., 1994; Miyashita and Mori, 1995; Hattox et al., 2002). These earlier findings suggest that the SC may play an important role in control of vibrissal movements as well as eye movements.

In general, periodic movements of animals' bodies are considered to be generated by the central pattern generators (CPGs), which are composed of small networks of neurons in the brainstem (for review, see Guertin, 2009). Whisking mainly consists of repetitive strokes of vibrissae along the rostrocaudal direction, and is controlled by the CPGs of whisking, which are located in the intermediate reticular formation (IRt) of the medulla oblongata and the pre-Bötzinger complex (preBötC) (Moore et al., 2013; Deschênes et al., 2016; for review, see Moore et al., 2014). The CPGs of whisking receive descending input from the vibrissal motor cortex (vMC), which modulates whisking behavior (Hattox et al., 2002; Grinevich et al., 2005). Hemelt and Keller (2008) previously reported that the vibrissal movements evoked by stimulating the vMC were substantially different from those induced by SC stimulation, suggesting that the role of the SC in whisking behavior differs from that of the vMC. Here, we hypothesized that the mechanism of the SC controlling vibrissal movements is closely correlated with architecture of neural circuits provided from the SC to the vibrissal motor related structures. To examine how the SC contributes to vibrissal movement control, we first analyzed differences in trajectories of vibrissal motion between normal rats and SC-lesioned rats. We also anterogradely traced the axonal projections from the SC to the CPGs and FN by using an axon-labeling technique with a virus vector.

MATERIALS AND METHODS

All animal use was in accordance with the National Institutes of Health Guide for the Care and Use of Laboratory Animals, and the experiments were approved by the Committee for Animal Care and Use (MedKyo 17039) and that for Recombinant DNA Study (141009) in Kyoto University. All efforts were made to minimize the number of animals used and the animal suffering.

Surgical Procedures

Kinematic analyses of vibrissal movements were performed in 32 adult male Long-Evans rats (250–400 g, 16 control rats and 16 SC-lesioned rats). A light-weight, sliding head fixation frame (SR-8N; Narishige, Tokyo, Japan) was surgically attached to the skull with screws and dental resin cement (Miky plus; Nissin Dental Products Inc., Kyoto, Japan) under anesthesia produced by an intraperitoneal injection of chloral hydrate (35 mg/100 g body weight). At the same time, the unilateral side of the SC was lesioned by passing direct electrical current (2 mA, 5–10 s) two to three times through a stainless steel electrode. We lesioned the right side of the SC in eight rats, and the left side of the SC in another eight rats. The stereotaxic coordinates for the lesions were 6.5 mm behind the bregma, 1.5 mm lateral to the midline and 4 mm below the pia (Paxinos and Watson, 2007). All vibrissae on each side, except the C2, were cut off at the base. During the surgical recovery period, the rats had free access to water and food in their home cages.

Apparatus and Experimental Design

Data on vibrissal movement trajectories were obtained by recording the movements of a pair of bilaterally homologous vibrissae. Two high-speed video cameras (CV-H035M; Keyence, Osaka, Japan), set above the awake, head-restrained rat, monitored vibrissal motion with a 100-Hz frame rate (**Figure 1A**). One camera imaged the base of the C2 vibrissa on the right side, and the other imaged the base of the C2 vibrissa on the left. Vibrissal movements of the awake rats were recorded for 15 min (89170 sampling points) daily, for three consecutive days starting 3 days after the surgery. To acclimate the rats to head-fixation in the stereotaxic apparatus, for 2 days, starting on the day after surgery, they were head-fixed in the same manner that they would later be in the recording sessions. All the head fixed rats were not trained for any behavioral task and moved vibrissae freely as spontaneous behavior. The extent of each lesion was assessed on Nissl-stained frontal sections of the SC at the end of the experiment.

Kinematic Analysis

Consecutive angle data were recorded for 15 min/day and imported into custom-written software (MATLAB; Mathworks, Natick, MA, United States). We defined the absolute angles of 0–180°, relative to the head-tail line of the rat, as the vibrissal position (see **Figure 1B**). Protractions on both the right and left sides of the face were represented as increasing vibrissal positions. Vibrissal tracking produced plots, like **Figure 1C**, of vibrissal positions against time (vibrissal motion on one side of the face is shown). We had a few error values (outliers), which were caused

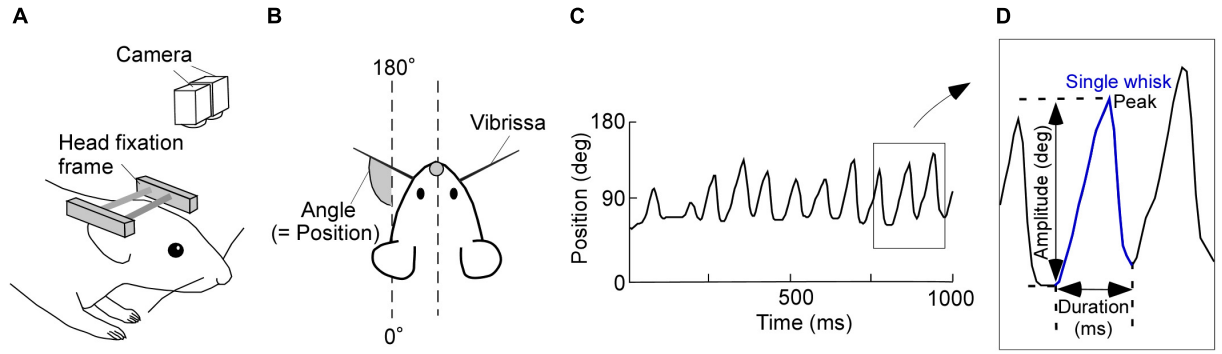

FIGURE 1 | Experimental design and image tracking. **(A)** Schematic of the experimental setup for recording vibrissal movements in a head-restrained rat. Two high-speed cameras above the rat were used to monitor vibrissal movements. **(B)** Top view of the head-restrained rat. **(C)** Representative movement record. Upward and downward shifts in this plot represent forward and backward movements of a vibrissa, respectively. **(D)** Diagram of a typical single whisk, with the kinematic parameters labeled.

by failures in the measurement of the vibrissal angles. After removing the outliers, data were interpolated by spline or linear functions. We then applied a moving average of three sampling points.

Data segments of whisking periods and those of resting periods were extracted from the acquired vibrissal motion recordings. To evaluate the dynamic states of the vibrissae, we defined a single whisk as the combination of a forward vibrissal movement and a backward vibrissal movement (**Figure 1D**). A pair of forward and backward movements was identified as a whisk when the speed of vibrissal movement exceeded an angular velocity of 0.05 degrees/ms for longer than 20 ms. The peak and the duration of a movement, respectively, were defined as the maximum vibrissal position and the time between the beginning of the forward movement and the end of backward movement. The amplitude was defined as the angle between the beginning of the forward movement and the peak in a single whisk. Whisks were required to have a duration between 40 and 340 ms and an amplitude of $\geq 5°$, to avoid the detection of vibrissal twitches (see Chen et al., 2016).

After detecting the whisks, resting periods were extracted from the residual recorded data by separated them into 500 ms epochs. We then found the maximum and minimum vibrissal positions in each epoch. When the difference between the maximum and minimum vibrissal positions was $<5°$, the epoch was defined as a resting period. Recorded data that did not correspond to either "whisking" or "resting" were categorized as "non-classified movement."

Statistical Analysis

The kinematic analyses were based on the 45-min record (15 min/day, for three successive days) from each animal. Data on vibrissal movements on the right and left sides of the face in control rats were merged (control: $n = 32$). Data from the two sides of the face in SC-lesioned rats were separated into vibrissal movements on the side ipsilateral to the lesion (ipsi: $n = 16$) and those contralateral to the lesion (contra: $n = 16$). All statistical analyses were performed in MATLAB. Differences between groups were tested with the Wilcoxon signed-rank test for paired data (ipsi versus contra) and the Mann–Whitney U-test for unpaired data (control rats versus SC-lesioned rats; control versus ipsi; control versus contra). The significance level was set at $p < 0.05$.

The vibrissal positions were evaluated after dividing the individual data into resting and whisking periods. The medians of the resting and whisking positions for each animal were computed and compared among the three (control, ipsi, and contra) groups in each period. We also calculated the distributions of whisk amplitudes for each animal, and compared the amplitude distributions between control rats and SC-lesioned rats (control versus ipsi; control versus contra). The distributions of whisk durations were computed in the same way, and compared between control rats and SC-lesioned rats. The coherence and phase lags between vibrissal movements on the right and left sides of the face were computed using Welch's method [MATLAB magnitude-squared coherence (mscohere) and cross power spectral density (cpsd), respectively; 5.12 s Hamming window, 50% overlap, and 512 fast Fourier transform (fft) points]. Both the coherence and the phase lag per animal were first calculated using the 15 min of data from the separate days, and then the coherence and the phase lag for the 3 days were averaged and compared between SC-lesioned and control rats.

Injection of Sindbis Virus and Fixation

Adult male Long-Evans rats (250–400 g) were used in the tract-tracing experiments. Eleven rats were anesthetized by intraperitoneal injection of chloral hydrate (35 mg/100 g body weight). For labeling of the SC neurons, we used Sindbis virus vector, which expresses palmitoylation site-attached green fluorescent protein (palGFP) (Furuta et al., 2001). PalGFP was targeted to the plasma membranes of the infected neurons (Moriyoshi et al., 1996), and was effective in visualizing the complete structure of neurons. We injected 0.2–0.4 μl of Sindbis virus vector ($1–2 \times 10^2$ infectious units) into the unilateral SC (5.8–7.0 mm posterior to the bregma, 0.7–2.0 mm lateral to the midline, and 3.5–4.3 mm deep from the brain surface) through

a glass micropipette attached to a Picospritzer III (General Valve Corporation, East Hanover, NJ, United States). Sixty to sixty-five hours after virus vector injection, the rats were anesthetized with chloral hydrate (350 mg/kg body weight) and perfused transcardially with 200 ml of sodium phosphate (pH 7.4)-buffered 0.9% saline (PBS), followed by 300 ml of 3.7% (v/v) formaldehyde in 0.1 M sodium phosphate (PB), pH 7.0. The brains were removed, and post-fixed for 4 h at 4°C in the same fixative. After cryoprotection with 30% (w/v) sucrose in PBS, the blocks were cut into 40 μm-thick frontal sections on a freezing microtome, and the sections were collected serially in 0.1 M PB.

Cell Count of palGFP-Expressing SC Neurons

The sections including the virus injection site were examined under an Axiophot epifluorescence microscope (Zeiss, Oberkochen, Germany) with a filter set for GFP (excitation, 450–490 nm; emission, 515–565 nm) to detect palGFP-labeled SC neurons. The number of infected neurons was manually counted in extracted sections, and the total number of infected neurons was properly estimated.

Immunostaining for GFP

The sections including the axons of anterogradely labeled SC neurons were incubated overnight with 0.5 μg/ml affinity-purified rabbit antibody to GFP (Tamamaki et al., 2000; Nakamura et al., 2008) in PBS containing 0.3% (v/v) Triton X-100 (PBS-X). After three rinses with PBS-X, the sections were incubated for 2 h with 10 μg/ml biotinylated anti-[rabbit IgG] goat antibody (BA-1000; Vector Laboratories, Burlingame, CA, United States) and then for 2 h with avidin-biotinylated peroxidase complex (ABC) (1:100; ABC-Elite; Vector Laboratories) in PBS-X. After three rinses in PBS, we applied the biotinylated tyramine (BT)-glucose oxidase (GO) amplification method (Furuta et al., 2009; Kuramoto et al., 2009). The sections were incubated for 30 min in a BT-GO reaction mixture containing 1.25 μM BT, 3 μg/ml of GO (257 U/mg; 16831-14; Nacalai Tesque, Kyoto, Japan), 2 mg/ml of beta-D glucose, and 2% bovine serum albumin in 0.1 M PB, followed by three washes with PBS. This was followed by incubation for 2 h in ABC-Elite in PBS-X, and the bound peroxidase was visualized as a dark blue stain with a nickel-diaminobenzidine reaction. Finally, these sections were stained with neutral red.

Quantitative Analysis of Anatomical Data

The axons of stained SC neurons were examined as described previously (Ohno et al., 2012). Briefly, a coronal section was automatically captured into a large color image, with a spatial resolution of 1.038 μm/pixel, by using a TOCO digital slide scanner (Claro, Aomori, Japan) equipped with a 10× objective lens (EC Plan-Neofluar; NA, 0.30; Zeiss). We traced the axon fibers on the images with CANVAS XII software (ACD Systems International Inc., VIC, Canada). The axon fibers were quantified using an "axon density index," defined as follows. We first divided each section into 72 equal, quadrilateral areas, and calculated the length of traced axons in each of the areas with Adobe Illustrator CS4 software (Adobe Systems, San Jose, CA, United States). The axonal length in each area was divided by the number of infected SC neurons in each animal. We then normalized axon density index to eliminate the differences in the size of individual brains and brain sites in the lower brainstem.

To observe the axon fibers projecting to the IRt, preBötC, and FN, we first found the center of the facial nerve for each animal. Using this as a landmark, we picked out the three sections located 1.2, 2.16, and 2.64 mm posterior to the landmark. These extracted sections were located approximately 11.28 mm, 12.24 mm, and 12.72 mm posterior to the bregma according to the atlas by Paxinos and Watson (2007). These locations included the FN, IRt, and preBötC, respectively.

We also calculated the axon density index even in areas which contains the paramedian pontine reticular formation (PPRF) and abducens nucleus (AN), to compare the axon densities of SC projections to the vibrissal motor related structures with those of SC projections to the oculomotor related structures in the brainstem. Because the brain sections of the midbrain which contained the oculomotor nucleus were subjected to cell counting of infected neurons in the injection sites, axon density index of the oculomotor nucleus was not measured.

RESULTS

Occurrence Rate of Vibrissal Reciprocating Motion (Whisks)

In each of the SC lesion experiments, we confirmed that both the medial and lateral parts of the unilateral SC were mostly (more than 80%) lesioned (**Figure 2A**). Unilateral lesioning of the SC did not clearly affect how often the vibrissal reciprocating movements known as whisks occurred (i.e., did not affect the "occurrence rate" of whisks) (**Figure 2B**). The numbers of whisks in control rats and SC-lesioned rats were not significantly different (control versus ipsi, Mann–Whitney *U*-test, $p = 0.068$;

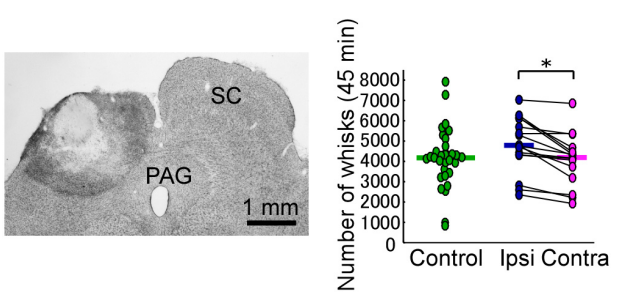

FIGURE 2 | Unilateral lesion of the SC leads to differences in the occurrence rate of bilateral vibrissal reciprocating motions (whisks). **(A)** The extent of the SC lesion for a representative rat. **(B)** Numbers of whisks in each of the rats (45 min/day for 3 days). Horizontal lines indicate the median numbers of whisks. *$p < 0.05$ using Wilcoxon ranked-sum test (ipsi vs. contra). SC, superior colliculus; PAG, periaqueductal gray; ipsi, side ipsilateral to the lesion; contra, side contralateral to the lesion.

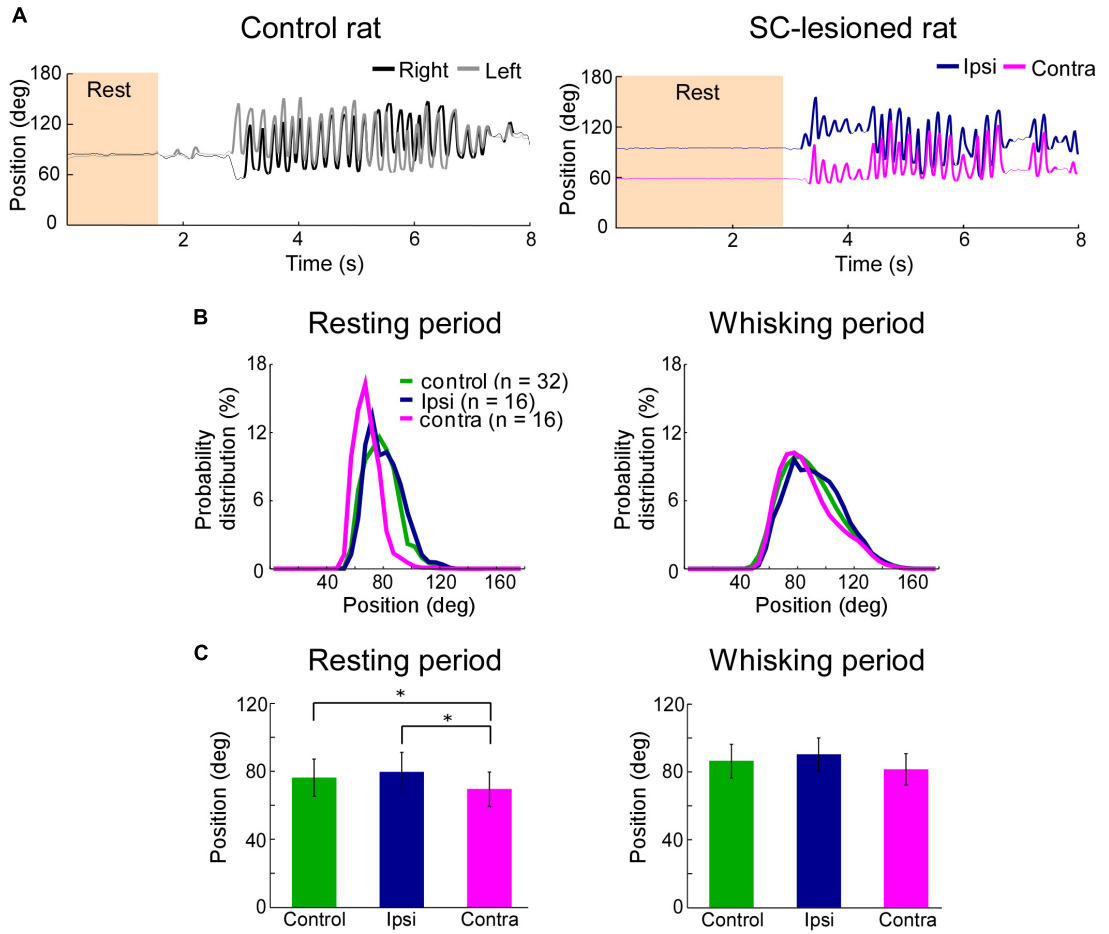

FIGURE 3 | Backward shift of resting vibrissal position on the side contralateral to the lesion. **(A)** Movements of the right and left C2 vibrissae of a control rat (Left) and a SC-lesioned rat (Right). Examples of resting (shaded region) and whisking (bold trajectory) periods are shown. **(B)** The distributions of vibrissal positions in resting (Left) and whisking (Right) periods. The medians of the vibrissal position distributions of individual rats in each group (control, ipsi, or contra) are shown. **(C)** The medians of vibrissal positions of the individual rats were averaged in resting (Left) and whisking (Right) periods. All of the error bars indicate standard deviations. *$p < 0.05$ using Mann–Whitney *U*-test (control vs. ipsi; control vs. contra) and Wilcoxon ranked-sum test (ipsi vs. contra). SC, superior colliculus; ipsi, side ipsilateral to the lesion; contra, side contralateral to the lesion.

control versus contra, Mann–Whitney *U*-test, $p = 0.84$), whereas the number of whisks on the contralateral side in SC-lesioned rats was significantly lower than that on the ipsilateral side (Wilcoxon ranked-sum test, $p = 0.00053$). **Figure 3A** shows representative examples of vibrissal movement data in control and SC-lesioned rats. All of the rats exhibited resting periods and whisking periods.

Vibrissal Position

To clarify the influence of SC lesions on the static parameters of vibrissae, we analyzed the median vibrissal positions in SC-lesioned rats and control rats. During resting periods, SC-lesioned rats exhibited significant differences in positions between the vibrissae ipsilateral to the lesion and those contralateral to the lesion (**Figures 3B,C**, Wilcoxon ranked-sum test, $p = 0.0097$). The contralateral vibrissae were also shifted backward relative to the vibrissal positions of the control rats (Mann–Whitney *U*-test, $p = 0.0388$). Conversely, during whisking periods, there were no significant differences in position between the ipsilateral and contralateral vibrissae or between the SC-lesioned rats and the control rats (control versus ipsi, Mann–Whitney *U*-test, $p = 0.29$; control versus contra, Mann–Whitney *U*-test, $p = 0.10$; ipsi versus contra, Wilcoxon ranked-sum test, $p = 0.070$).

Whisking Amplitude and Whisking Frequency

The amplitude distributions show that the vibrissae contralateral to the lesioned SC exhibited large-amplitude whisks (>70°) more frequently than did the vibrissae of the control rats (**Figure 4A**, Mann–Whitney *U*-test, $p < 0.05$), whereas moderate-amplitude whisks (>30°, <50°) were less frequent on the contralateral side of SC-lesioned rats (Mann–Whitney *U*-test, $p < 0.05$) than in control rats. There were no significant differences between whisks on the ipsilateral side of SC-lesioned rats and those of control rats.

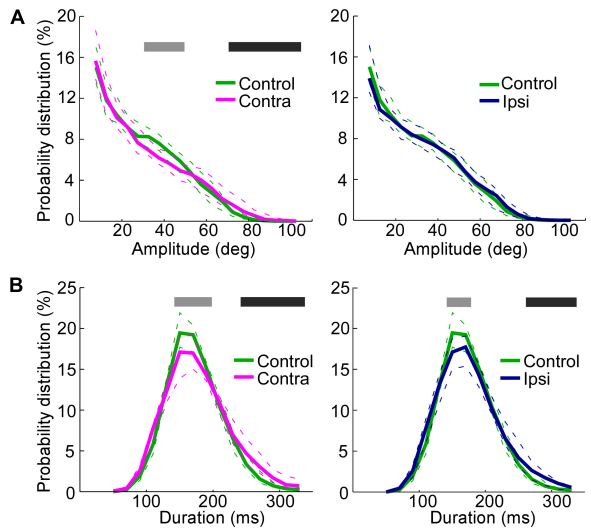

FIGURE 4 | Increase in the whisking amplitude on the side contralateral to the lesion and decrease in the whisking frequencies on both the ipsilateral and contralateral sides. **(A)** Probability distributions of amplitudes, comparing the control rats with the contralateral side in SC-lesioned rats (Left) and the control rats with the ipsilateral side in SC-lesioned rats (Right). **(B)** Probability distributions of durations, comparing the control rats with the contralateral side in SC-lesioned rats (Left) and the control rats with the ipsilateral side in SC-lesioned rats (Right). Solid lines and dashed lines indicate medians and interquartile ranges, respectively. Black bars show $p < 0.05$ (control < ipsi; control < contra) using Mann–Whitney *U*-test. Gray bars show $p < 0.05$ (control > ipsi; control > contra) using Mann–Whitney *U*-test. SC, superior colliculus; ipsi, side ipsilateral to the lesion; contra, side contralateral to the lesion.

The duration of single whisks was also analyzed (**Figure 4B**). The effects of SC lesions on whisk durations were similar on the ipsilateral and contralateral sides. On both sides, whisks of moderate duration (140–180 ms on the ipsilateral side, 140–200 ms on the contralateral side) were less common (Mann–Whitney *U*-test, $p < 0.05$), and whisks of long durations (260–340 ms on the ipsilateral side, 240–340 ms on the contralateral side) were more common (Mann–Whitney *U*-test, $p < 0.05$), than in the control rats. To rephrase these findings, SC-lesioned rats increased their whisking activities at low frequencies (about 3–4 Hz) and decreased those at moderate frequencies (about 6–7 Hz).

Coherence of the Right and Left Vibrissal Movements

SC lesions decreased the coherence of vibrissal movements between the right and left sides across a wide range of frequencies (**Figure 5A**). There were statistically significant reductions in coherence for the middle ranges of frequencies (3.3–5.5 Hz, 5.9–7.6 Hz, 8.4–8.8 Hz, 9.4–9.6 Hz, Mann–Whitney *U*-test, $p < 0.05$). In addition, SC-lesioned rats exhibited differences in kinematic phase between right and left vibrissal movements (**Figure 5B**). When the rats moved their vibrissae at moderate or high frequencies (>3.3 Hz), the vibrissae on the contralateral side lagged behind the movements of the ipsilateral vibrissae. The delay was about 8.6 ms for movements at a frequency of 5 Hz. The reduction of coherence might be explained by the altered whisking kinematics in the SC-lesioned rats; lower occurrence rate of whisking, increased whisking amplitude and phase delay on the contralateral side.

All of the observed effects of SC lesions are summarized in **Table 1**, which shows that such lesions mainly affected vibrissal movements on the contralateral side. To explore the neural circuitry underlying these results, we next morphologically analyzed the projection patterns of descending axons that originate from the SC.

Axonal Projections From the SC to the Brainstem

We injected the recombinant Sindbis virus vector unilaterally into the SC of 11 rats. The locations of all of the injection sites are shown in **Figure 6A**. The injections were located in the range of 5.8–7.0 mm caudal to the bregma, although the centers of the injections were scattered along the dorso-ventral and medio-lateral directions. We estimated that each injection site contained several tens of infected neurons within the SC (**Figures 6B,C**). In the present study, we traced labeled axons only in the brainstem caudal to the injection site, because we were primarily interested in the descending circuit from the SC to the FN and the CPGs of whisking. As shown in **Figures 6D–I**, the SC mostly sent axons to the contralateral side of the brainstem. The descending axons from the SC were mainly distributed in the ventral and medial regions of the lower brainstem, and we confirmed that the labeled axons projected to the FN, IRt, and preBötC. Additionally, many labeled axons reached the parvicellular reticular nucleus, gigantocellular reticular nucleus, and spinal trigeminal interpolaris nucleus on the contralateral side, as well as the lateral paragigantocellular nuclei on both sides. It has been reported that premotor neurons for vibrissal motoneurons are distributed in all of these brain regions (Takatoh et al., 2013).

To compare the SC projection axons to the vibrissal motor related structures in the brainstem with those to oculomotor related structures (**Supplementary Figure 1**), we calculated axon density index of the PPRF and AN. Axon density index of the areas containing the IRt and FN in the contralateral side were 0.094 and 0.145, respectively, while axon density index of SC projections to the PPRF and AN in the contralateral side were 0.219 and 0.004, respectively. This result suggests that the vibrissal movement related circuit in the brainstem receives considerable projections from the SC, although the density of the projection axons in the PPRF is higher than that in vibrissal motor structures. It should be noted that the SC directly sent many axons to the FN while a motor nucleus of ocular movement, the AN, only receives a few axons from the SC.

In earlier studies, the SC has been reported to send descending projections not only to the contralateral side but also to the ipsilateral brainstem (Redgrave et al., 1986, 1987; for review see Dean et al., 1989). The contralateral projection is considered to originate in the lateral part of the SC, whereas the cells

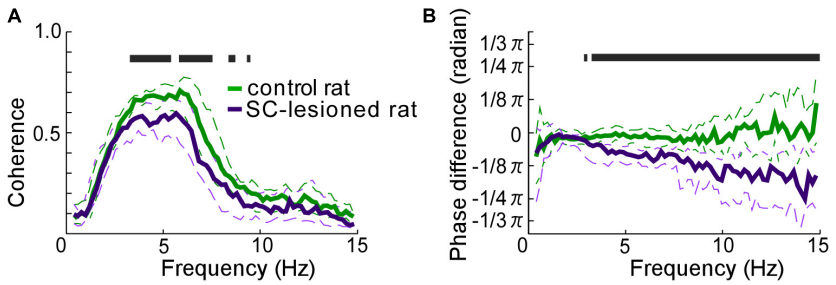

FIGURE 5 | Coordination of vibrissal movements on the right and left sides of the face. **(A)** There was less coherence between the right- and left-side vibrissal movements in SC-lesioned rats (n = 16) than in the control rats (n = 16). **(B)** Phase differences between right and left vibrissal movements in SC-lesioned rats were statistically larger than those in control rats. Solid lines and dashed lines indicate medians and interquartile ranges, respectively. Black bars show $p < 0.05$ using Mann–Whitney U-test. SC, superior colliculus; ipsi, side ipsilateral to the lesion; contra, side contralateral to the lesion.

TABLE 1 | The effects on vibrissal movements of unilateral lesions of the SC are different for the ipsilateral and contralateral sides.

Affected side	Component	Effect
Contralateral	Occurrence rate of whisks	n.s.[a]
	Position	Backward shift of resting vibrissal positions.
	Amplitude	Decrease in moderate-amplitude whisks and increase in large-amplitude whisks.
	Duration	Decrease in whisks of moderate duration and increase in whisks of long durations.
Ipsilateral	Occurrence rate of whisks	n.s.[a]
	Position	n.s.
	Amplitude	n.s.
	Duration	Decrease in whisks of moderate duration and increase in whisks of long durations.
	Coherence	Decrease in coherence between right and left vibrissal movements in SC-lesioned rats.[b]

n.s., not significant. [a]The number of whisks on the contralateral side is less than that on the ipsilateral side. [b]The phase lag between bilateral vibrissal movements in SC-lesioned rats is larger than that in control rats.

in the medial part of the SC send descending axons mainly to the ipsilateral side. Accordingly, we extracted cases with injections into the lateral part of the SC (n = 4) and those with injections into the medial part (n = 3) to compare projection patterns in these two groups. In the former group, labeled axons traversed the midline and descended to the medial regions of the pons and medulla oblongata (**Figures 7A–D**). We also found that many axon collaterals of labeled neurons spread widely in the contralateral brainstem, which contains whisker-movement related structures, such as the FN, IRt, and preBötC. In contrast, infected neurons in the medial part of the SC sent caudally projecting axons to both sides of the brainstem. Axons from the medial SC were localized principally in the medial part of the brainstem, and only a few axons were observed in the FN, IRt, and preBötC on both sides (**Figures 7E–H**).

DISCUSSION

The schematic diagram in **Figure 8** illustrates potential circuits for the generation of vibrissal movements. In the present experiment with awake rats, SC lesions mainly affected vibrissal movements on the contralateral side. Our anatomical analysis of descending axons demonstrated that the SC primarily projects to the contralateral brainstem, which contains structures involved in vibrissal movements. Furthermore, we newly evaluated the SC-originated descending axons to the medulla oblongata structures semi-quantitatively, and revealed dominance of the direct projections from the SC to the FN. This architectonic characteristic is in accordance with the results of the vibrissal movement analysis as discussed below.

Methodological Considerations

We made the lesions in the SC by passing direct electrical current. This method not only lesioned the SC neurons that send descending axons to the lower brainstem, but also damaged other SC neurons. Because the SC projects to the thalamus, anterior pretectal nucleus, zona incerta, and pedunculopontine tegmental nucleus (for review, see Bosman et al., 2011), the present SC lesions may have ablated projection fibers reaching those areas. Given that those structures rarely send direct input to the FN, where the whisking-associated motoneurons are located, we suspect that the destruction of the other projections from the SC made less of an impact than did the destruction of the direct connections to the FN or the descending connections to the whisking CPGs (Moore et al., 2013; Deschênes et al., 2016) from the SC. Therefore, in this report, we discuss the effects of SC lesions on vibrissal movements in relation to the functions of SC-CPGs and SC-FN circuits.

In the present virus-labeling technique, we used a small volume of virus solution for each injection to limit the numbers of infected neurons. Even in these small-volume injections, virus particles spread from the tips of the injection pipettes, and thus the technique resulted in scattered distributions of infected neurons (**Figure 6B**). Therefore, we could not obtain layer-specific labeling for projection fibers in the SC. The layer-dependent projection patterns have been reported in previous

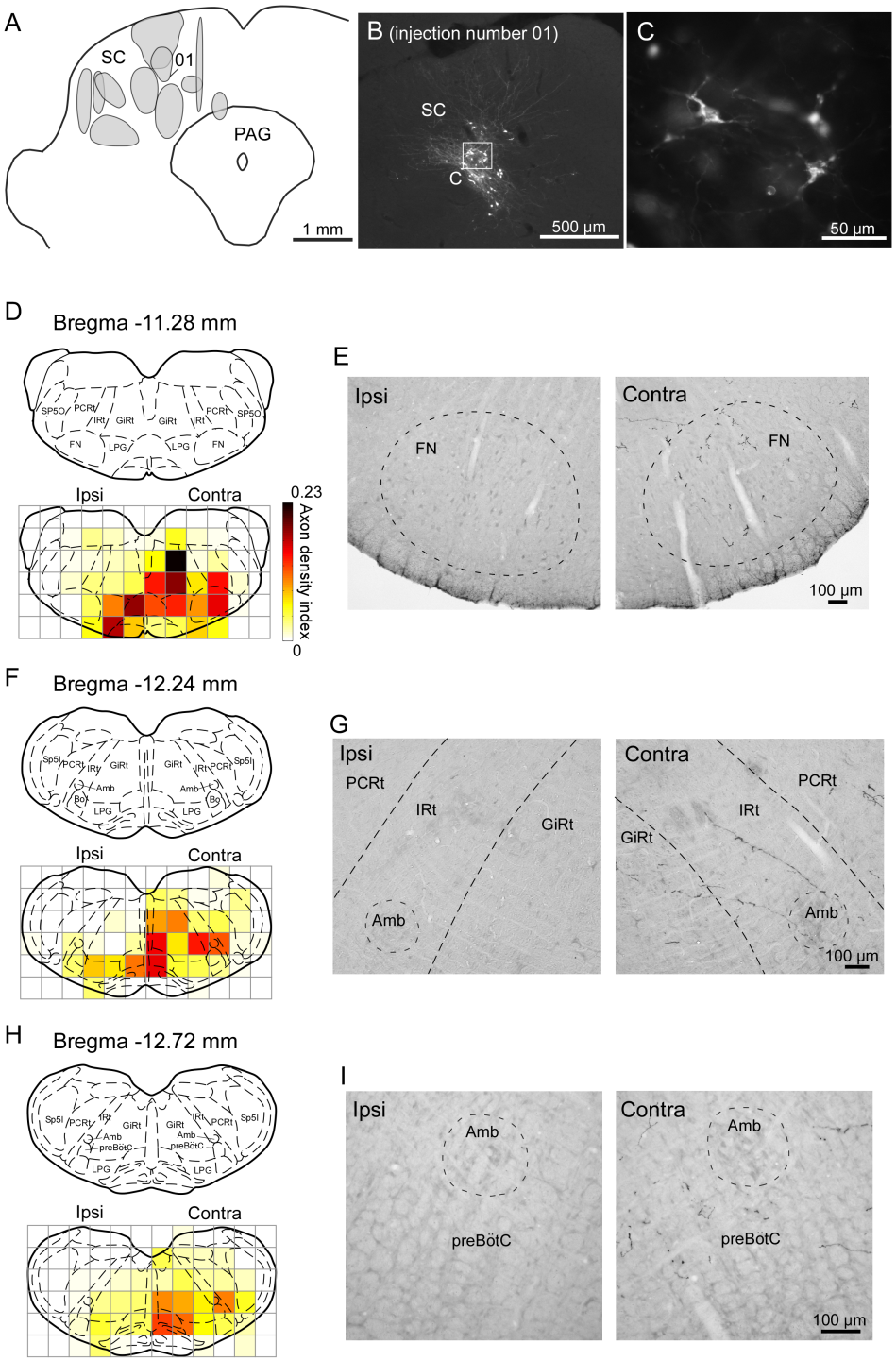

FIGURE 6 | Sindbis virus injections into unilateral SC and the anterogradely labeled axon fibers. **(A)** Light grays on the drawing of the coronal plane indicate the central regions of injection sites. **(B,C)** PalGFP-expressing SC neurons. **(D–I)** Coronal sections at the level of the FN **(D,E)**, IRt **(F,G)**, and preBötC **(H,I)**. Axonal density in each area was expressed as the axon density index (see section "Materials and Methods"). The coronal images at the bottom in panels **D,F,H** were overlaid with the corresponding schematic drawings from the top in those panels (Paxinos and Watson, 2007). Many axonal fibers from the SC were observed in the lower brainstem contralateral to the injection. The two photomicrographs in each row are from the same rat. Amb, ambiguus nucleus; Bo, Bötzinger complex; contra, side contralateral to the lesion; CPGs, central pattern generators; FN, facial nucleus; GiRt, gigantocellular reticular nucleus; ipsi, side ipsilateral to the lesion; IRt, intermediate reticular formation; LPG, lateral paragigantocellular nucleus; PAG, periaqueductal gray; PCRt, parvicellular reticular nucleus; preBötC, pre-Bötzinger complex; SC, superior colliculus; Sp5I, spinal trigeminal nucleus, interpolar part; Sp5O, spinal trigeminal nucleus, oral part.

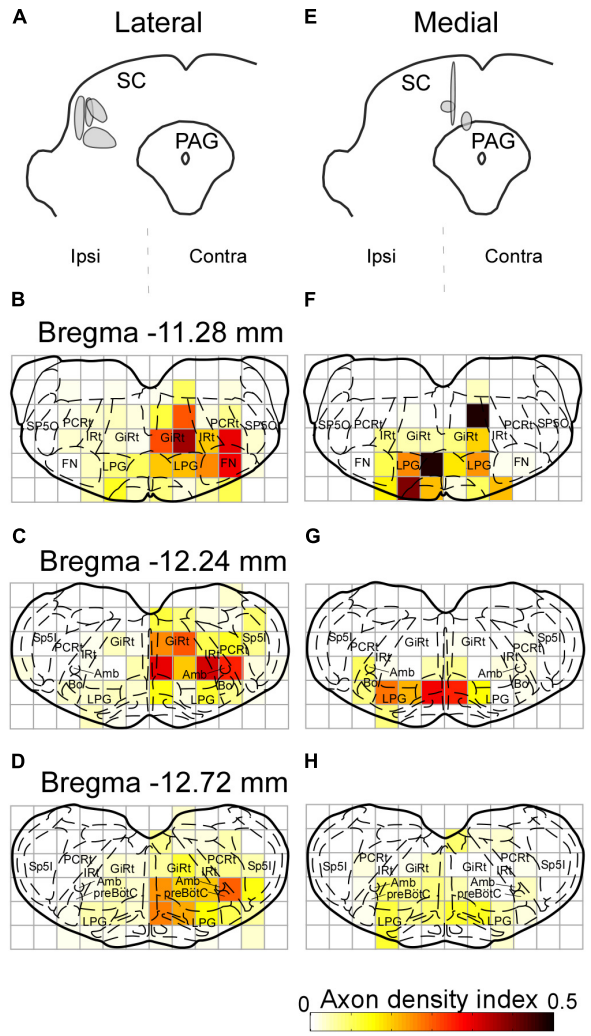

FIGURE 7 | Axonal projections from the lateral and medial parts of the SC. The injection sites of the Sindbis virus into the lateral and medial areas of the SC are shown in panels **A**,**E**, respectively. Light grays indicate the central regions of the injection. **(B–D)** Lateral SC neurons projected to the contralateral FN, IRt, and preBötC. **(F–H)** Few medial SC neurons projected to the FN, IRt, and preBötC contralateral to the injection. Axonal density in each area was expressed as the axon density index (see section "Materials and Methods"). For the abbreviations, see the legend of **Figure 6**.

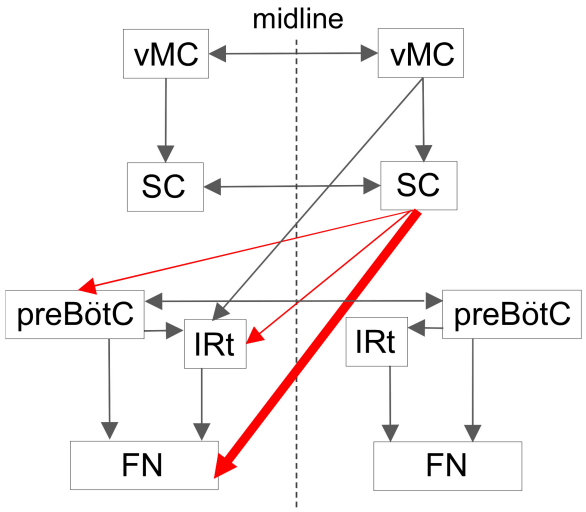

FIGURE 8 | Proposed central projections from the SC for the vibrissal sensorimotor system. The SC receives input from the ipsilateral vMC. The SC and the vMC send their output to the contralateral CPGs and FN, where the vibrissal motoneurons are located. This study indicates that there is a descending circuit from the SC (red lines) that modulates vibrissal movements. Descending pathways from the vMC and the SC are shown on only one side. vMC, vibrissal motor cortex. For the remaining abbreviations, see the legend of **Figure 6**.

studies, where the descending collicular projections to the lower brainstem and spinal cord were found to derive from the intermediate and deep layers of the SC (Harting et al., 1973; Graham, 1977; Huerta and Harting, 1982; Redgrave et al., 1986). It is reasonable to conclude that, in the present experiment, the labeled axons found in the lower brainstem originated from the intermediate and deep layers of the SC. Overall, the results of the present tract-tracing experiment are in good agreement with previous reports of the projection patterns from the SC (Waldron and Gwyn, 1969; Redgrave et al., 1987; Yasui et al., 1994). Furthermore, our study presents a new analysis of the axonal projection patterns. The virus-labeling technique clearly visualized axons even if only a small volume of virus was injected (and, as such, the number of infected neurons was small). This technique facilitated the quantitative analysis of axonal distributions.

Relationship Between the Effects of the Unilateral SC Lesion and the Anatomical Basis

The present tract-tracing experiment showed that the descending pathways from the SC mainly reach the contralateral lower brainstem, which contains the whisking-associated areas (**Figure 6**). This observation may explain the results of the SC lesion study, where most effects of the lesion were exhibited by the contralateral vibrissae. The backward shift of the position of the contralateral vibrissae during resting periods in the SC-lesioned rats (**Figure 3**) suggests that the baseline activity of the motoneurons that innervate the whisking muscles (intrinsic muscles, Hill et al., 2008; Haidarliu et al., 2010) had decreased. This shift of vibrissal position in the lesion study is considered to relate to the direct input from the SC to the contralateral FN, because the motoneurons for whisking are located in the FN. Whisking behavior is generated by periodic input to the FN from the CPGs of whisking (Moore et al., 2013; Deschênes et al., 2016). The direct connections from the SC to the FN might also affect amplitude control by providing subthreshold input to the FN, which has been suggested to modulate the input/output relation of the neurons (Chance et al., 2002; for review, see Salinas and Sejnowski, 2001). We had suspected that the ablation of direct input from the SC to

the FN reduced activity of FN neurons because resting position (angle) of vibrissae, which are protracted by only contraction of intrinsic vibrissal muscle and return to the resting position by elastic nature, was shifted toward the retracted direction in lesioned rats. However, large-amplitude whisks were increased in the contralateral side of the lesioned rats. In oculomotor control, the previous studies in monkeys and cats reported that saccadic amplitudes and neck EMG are affected by the initial eye position (Moschovakis et al., 1998; Corneil et al., 2002; Hadjidimitrakis et al., 2007). Even in vibrissal movement control, it is possible that the resting position affects the size of whisking amplitude. The present increase of whisking amplitude in lesioned rats might be caused by the caudal shift of resting vibrissal position.

The vibrissal movement is also modulated by another higher control center, the vMC, where neurons encode whisking amplitude and/or midpoint (Hill et al., 2011). In the previous study, Hemelt and Keller (2008) showed that microstimulation in the vMC evoked rhythmic vibrissal movements while a sustained vibrissal motion was induced by microstimulation in the SC. Given that the vMC sends descending axons abundantly to the IRt and only slightly to the FN (Hattox et al., 2002; Grinevich et al., 2005), the vMC is considered to take part in vibrissal movement control via the CPGs of whisking in the brainstem. Thus, the mechanism that the SC contributes to motor control of vibrissae is different from that of the vMC.

Whisking CPGs include the preBötC, whose right and left sides are connected by commissural axons, and which control vibrissal movement on both sides with the common basic oscillator (Koizumi et al., 2013; Moore et al., 2013; Deschênes et al., 2016). In the present SC-lesion study, we observed no significant differences in the distributions of whisk durations between the right and left sides, although the whisk durations tended to be longer than those of the normal rats (**Figure 4B**). Analysis of the coherence of vibrissal movements between the right and left sides revealed that unilateral SC lesions caused desynchronization of the bilateral movements (**Figure 5**). The decreased coherence in SC-lesioned rats is likely caused by the phase delay on the contralateral side. Assuming that most SC projections to the contralateral brainstem are excitatory, ablation of the SC-brainstem connections may decrease neuronal activity in relevant networks and delay the start of muscle contraction. Phase difference is considered to become larger when rats whisked at a high frequency (**Figure 5**) because a fixed time difference between right and left side causes a larger phase difference in a high frequency range than a phase difference in a low frequency range.

As for whisk duration, it could become long as whisk amplitude became large in the contralateral side of the lesioned rats. However, it is not clear why elongation of duration was observed also in the ipsilateral side. We speculate that the duration of the ipsilateral side increased following the contralateral side because the commissural connections between the bilateral preBötCs acted to keep the common rhythm in the both side of whisking CPGs.

Given that, in the unilateral SC-lesioned rats, the structures in the medulla oblongata of the contralateral side to the lesion lose input from the SC, one would consider that the lesion causes serious disorders of vibrissal movements in the contralateral side. However, we found no significant differences in number of whisks between the control rats and the contralateral side of lesioned rats, implying a compensation mechanism. Even in the unilateral SC-lesioned rats, the preBötC may keep coordination of the both sides because this structure possesses dense commissural connections, and then contributes to harmonization of activities between the both sides of vibrissal movement circuit in the brainstem (Deschênes et al., 2016). Although undamaged SC mainly sends axons to the ipsilateral side to the lesion, the ablation of input from lesioned SC to the contralateral CPGs might be compensated by the undamaged SC via the commissural connections of the preBötC.

In the ocular movement control, ablation or pharmacological inactivation of the SC induces disorders of eye movements (Albano et al., 1982; Hikosaka and Wurtz, 1985). On the other hand, in the rhythmic vibrissal movements, relatively small changes were caused by the present SC lesion. The most remarkable effect on vibrissal motor control was the caudal shift of resting vibrissal position. This difference might be explained by the differences in SC projection pattern between the oculomotor related structures and vibrissal movement related structures. Motor nucleus for eye movements received only few axons from the SC, while many axons were projected from the SC to the premotor structures (e.g., PPRF). Compared to the oculomotor circuits concerning the SC, vibrissal movement circuits are characterized by direct axonal projections from the SC to the motor nucleus (**Figure 8**). The SC, in the vibrissal movement control, might mainly act to modulate static parameters (e.g., resting vibrissal position) rather than dynamic parameters (e.g., whisking frequency and amplitude). Future experiments in which activities of each pathway in vibrissal movement circuit are specifically controlled (e.g., by optogenetics) may contribute to identifying the detailed roles of these neural connections.

The Role of the SC in Vibrissal Movements

In rodents, the SC mediates two types of behavior through sensory input from visual, somatosensory, and auditory areas: *orienting responses*, which direct the sensory apparatus of eyes, vibrissae, head and body to a point of interest, and *defensive responses*, such as avoidance or flight (for review, see Dean et al., 1989). Orienting responses are thought to be generated mainly through the crossed tectospinal pathway from the lateral SC, whereas defensive responses are thought to be mediated through the ipsilateral tectospinal pathway from the medial SC (Dean et al., 1986; Redgrave et al., 1986, 1987; Sahibzada et al., 1986; for review see Dean et al., 1989). The present experiments have revealed that the CPGs and FN received input from cells in the lateral SC on the contralateral side (**Figure 7**). This suggests that the SC-brainstem circuit for whisking contributes to directing vibrissae toward objects of interest, or to coordinating vibrissal movements with eye, head, and body movements in orienting responses. The SC is a locus where multisensory information are

combined and transformed into adaptive motor responses (for review, see Wolf et al., 2015). Although the vMC is also relevant to vibrissal movement control, the functions of the vMC reportedly differ from those of the SC circuits. The vMC functions include motor learning with vibrissae (Huber et al., 2012), initiating vibrissal movements (Sreenivasan et al., 2016), and changing modes of vibrissal motor control (Haiss and Schwarz, 2005). To direct the vibrissae toward sensory stimuli, it is necessary to change the vibrissal positions or whisking patterns between the right and left sides. The results of our lesion study and anatomical analysis suggest that the SC may be involved in vibrissal orientation by making such differences between the right and left.

AUTHOR CONTRIBUTIONS

MK performed the experiments. MK and K-iS built the experimental setup. MK and JM analyzed the data. MK and TF designed the study and wrote the paper. AM contributed to the manuscript revisions and editing.

FUNDING

This work was supported by Grants-in-Aid for Scientific Research from Ministry of Education, Culture, Sports, Science, and Technology (15H04266 to TF) and JSPS KAKENHI (JP18J11771 to MK).

ACKNOWLEDGMENTS

We thank Daichi Hirai and Yukio Nishimura for helpful comments. We also thank Claire Barnes, Ph.D., from Edanz Group (www.edanzediting.com/ac) for editing a draft of this manuscript.

SUPPLEMENTARY MATERIAL

The Supplementary Material for this article can be found online at: https://www.frontiersin.org/articles/10.3389/fncir.2018.00100/full#supplementary-material

REFERENCES

Albano, J. E., Mishkin, M., Westbrook, L. E., and Wurtz, R. H. (1982). Visuomotor deficits following ablation of monkey superior colliculus. *J. Neurophysiol.* 48, 338–351. doi: 10.1152/jn.1982.48.2.338

Bezdudnaya, T., and Castro-Alamancos, M. A. (2011). Superior colliculus cells sensitive to active touch and texture during whisking. *J. Neurophysiol.* 106, 332–346. doi: 10.1152/jn.00072.2011

Bezdudnaya, T., and Castro-Alamancos, M. A. (2014). Neuromodulation of whisking related neural activity in superior colliculus. *J. Neurosci.* 34, 7683–7695. doi: 10.1523/JNEUROSCI.0444-14.2014

Bosman, L. W. J., Houweling, A. R., Owens, C. B., Tanke, N., Shevchouk, O. T., Rahmati, N., et al. (2011). Anatomical pathways involved in generating and sensing rhythmic whisker movements. *Front. Integr. Neurosci.* 5:53. doi: 10.3389/fnint.2011.00053

Castro-Alamancos, M. A., and Favero, M. (2016). Whisker-related afferents in superior colliculus. *J. Neurophysiol.* 115, 2265–2279. doi: 10.1152/jn.00028.2016

Chance, F. S., Abbott, L. F., and Reyes, A. D. (2002). Gain modulation from background synaptic input. *Neuron* 35, 773–782. doi: 10.1016/S0896-6273(02)00820-6

Chen, S., Augustine, G. J., and Chadderton, P. (2016). The cerebellum linearly encodes whisker position during voluntary movement. *eLife* 5:e10509. doi: 10.7554/eLife.10509

Corneil, B. D., Olivier, E., and Munoz, D. P. (2002). Neck muscle responses to stimulation of monkey superior colliculus. II. Gaze shift initiation and volitional head movements. *J. Neurophysiol.* 88, 2000–2018. doi: 10.1152/jn.2002.88.4.2000

Dean, P., Redgrave, P., Sahibzada, N., and Tsuji, K. (1986). Head and body movements produced by electrical stimulation of superior colliculus in rats: effects of interruption of crossed tectoreticulospinal pathway. *Neuroscience* 19, 367–380. doi: 10.1016/0306-4522(86)90267-8

Dean, P., Redgrave, P., and Westby, G. W. M. (1989). Event or emergency? Two response systems in the mammalian superior colliculus. *Trends Neurosci.* 12, 137–147. doi: 10.1016/0166-2236(89)90052-0

Deschênes, M., Takatoh, J., Kurnikova, A., Moore, J. D., Demers, M., Elbaz, M., et al. (2016). Inhibition, not excitation, drives rhythmic whisking. *Neuron* 90, 374–387. doi: 10.1016/j.neuron.2016.03.007

Fuchs, A. F., Kaneko, C. R. S., and Scudder, C. A. (1985). Brainstem control of saccadic eye movements. *Annu. Rev. Neurosci.* 8, 307–337. doi: 10.1146/annurev.ne.08.030185.001515

Furuta, T., Kaneko, T., and Deschenes, M. (2009). Septal neurons in barrel cortex derive their receptive field input from the lemniscal pathway. *J. Neurosci.* 29, 4089–4095. doi: 10.1523/JNEUROSCI.5393-08.2009

Furuta, T., Tomioka, R., Taki, K., Nakamura, K., Tamamaki, N., and Kaneko, T. (2001). In vivo transduction of central neurons using recombinant sindbis virus. *J. Histochem. Cytochem.* 49, 1497–1507. doi: 10.1177/002215540104901203

Gegenfurtner, K. R. (2016). The interaction between vision and eye movements. *Perception* 45, 1333–1357. doi: 10.1177/0301006616657097

Graham, J. (1977). An autoradiographic study of the efferent connections of the superior colliculus in the cat. *J. Comp. Neurol.* 173, 629–654. doi: 10.1002/cne.901730403

Grant, R. A., Mitchinson, B., Fox, C. W., and Prescott, T. J. (2009). active touch sensing in the rat: anticipatory and regulatory control of whisker movements during surface exploration. *J. Neurophysiol.* 101, 862–874. doi: 10.1152/jn.90783.2008

Grinevich, V., Brecht, M., and Osten, P. (2005). monosynaptic pathway from rat vibrissa motor cortex to facial motor neurons revealed by lentivirus-based axonal tracing. *J. Neurosci.* 25, 8250–8258. doi: 10.1523/JNEUROSCI.2235-05.2005

Grunwerg, B. S., and Krauthamer, G. M. (1990). Vibrissa-responsive neurons of the superior colliculus that project to the intralaminar thalamus of the rat. *Neurosci. Lett.* 111, 23–27. doi: 10.1016/0304-3940(90)90338-A

Guertin, P. A. (2009). The mammalian central pattern generator for locomotion. *Brain Res. Rev.* 62, 45–56. doi: 10.1016/j.brainresrev.2009.08.002

Hadjidimitrakis, K., Moschovakis, A. K., Dalezios, Y., and Grantyn, A. (2007). Eye position modulates the electromyographic responses of neck muscles to electrical stimulation of the superior colliculus in the alert cat. *Exp. Brain Res.* 179, 1–16. doi: 10.1007/s00221-006-0765-3

Haidarliu, S., Simony, E., Golomb, D., and Ahissar, E. (2010). Muscle architecture in the mystacial pad of the rat. *Anat. Rec.* 293, 1192–1206. doi: 10.1002/ar.21156

Haiss, F., and Schwarz, C. (2005). Spatial segregation of different modes of movement control in the whisker representation of rat primary motor cortex. *J. Neurosci.* 25, 1579–1587. doi: 10.1523/JNEUROSCI.3760-04.2005

Harting, J. K., Hall, W. C., Diamond, I. T., and Martin, G. F. (1973). Anterograde degeneration study of the superior colliculus in *Tupaia glis*: evidence for a subdivision between superficial and deep layers. *J. Comp. Neurol.* 148, 361–386. doi: 10.1002/cne.901480305

Hattox, A. M., Priest, C. A., and Keller, A. (2002). Functional circuitry involved in the regulation of whisker movements. *J. Comp. Neurol.* 442, 266–276. doi: 10.1002/cne.10089

Hemelt, M. E., and Keller, A. (2008). Superior colliculus control of vibrissa movements. *J. Neurophysiol.* 100, 1245–1254. doi: 10.1152/jn.90478.2008

Hikosaka, O., and Wurtz, R. H. (1985). Modification of saccadic eye movements by GABA-related substances. I. Effect of muscimol and bicuculline in monkey superior colliculus. *J. Neurophysiol.* 53, 266–291.

Hill, D. N., Bermejo, R., Zeigler, H. P., and Kleinfeld, D. (2008). Biomechanics of the vibrissa motor plant in rat: rhythmic whisking consists of triphasic neuromuscular activity. *J. Neurosci.* 28, 3438–3455. doi: 10.1523/JNEUROSCI.5008-07.2008

Hill, D. N., Curtis, J. C., Moore, J. D., and Kleinfeld, D. (2011). Primary motor cortex reports efferent control of vibrissa motion on multiple timescales. *Neuron* 72, 344–356. doi: 10.1016/j.neuron.2011.09.020

Huber, D., Gutnisky, D. A., Peron, S., O'Connor, D. H., Wiegert, J. S., Tian, L., et al. (2012). Multiple dynamic representations in the motor cortex during sensorimotor learning. *Nature* 484, 473–478. doi: 10.1038/nature11039

Huerta, M. F., and Harting, J. K. (1982). Projections of the superior colliculus to the supraspinal nucleus and the cervical spinal cord gray of the cat. *Brain Res.* 242, 326–331. doi: 10.1016/0006-8993(82)90317-1

Isokawa-Akesson, M., and Komisaruk, B. R. (1987). Difference in projections to the lateral and medial facial nucleus: anatomically separate pathways for rhythmical vibrissa movement in rats. *Exp. Brain Res.* 65, 385–398. doi: 10.1007/BF00236312

Koizumi, H., Koshiya, N., Chia, J. X., Cao, F., Nugent, J., Zhang, R., et al. (2013). Structural-functional properties of identified excitatory and inhibitory interneurons within pre-botzinger complex respiratory microcircuits. *J. Neurosci.* 33, 2994–3009. doi: 10.1523/JNEUROSCI.4427-12.2013

Kuramoto, E., Furuta, T., Nakamura, K. C., Unzai, T., Hioki, H., and Kaneko, T. (2009). Two types of thalamocortical projections from the motor thalamic nuclei of the rat: a single neuron-tracing study using viral vectors. *Cereb. Cortex* 19, 2065–2077. doi: 10.1093/cercor/bhn231

May, P. J. (2006). The mammalian superior colliculus: laminar structure and connections. *Prog. Brain Res.* 151, 321–378. doi: 10.1016/S0079-6123(05)51011-2

McHaffie, J. G., Kao, C. Q., and Stein, B. E. (1989). Nociceptive neurons in rat superior colliculus: response properties, topography, and functional implications. *J. Neurophysiol.* 62, 510–525. doi: 10.1152/jn.1989.62.2.510

McHaffie, J. G., and Stein, B. E. (1982). Eye movements evoked by electrical stimulation in the superior colliculus of rats and hamsters. *Brain Res.* 247, 243–253. doi: 10.1016/0006-8993(82)91249-5

Mitchinson, B., Martin, C. J., Grant, R. A., and Prescott, T. J. (2007). Feedback control in active sensing: rat exploratory whisking is modulated by environmental contact. *Proc. Biol. Sci.* 274, 1035–1041. doi: 10.1098/rspb.2006.0347

Miyashita, E., Keller, A., and Asanuma, H. (1994). Input-output organization of the rat vibrissal motor cortex. *Exp. Brain Res.* 99, 223–232. doi: 10.1007/BF00239589

Miyashita, E., and Mori, S. (1995). The superior colliculus relays signals descending from the vibrissal motor cortex to the facial nerve nucleus in the rat. *Neurosci. Lett.* 195, 69–71. doi: 10.1016/0304-3940(95)11782-R

Moore, J. D., Deschênes, M., Furuta, T., Huber, D., Smear, M. C., Demers, M., et al. (2013). Hierarchy of orofacial rhythms revealed through whisking and breathing. *Nature* 497, 205–210. doi: 10.1038/nature12076

Moore, J. D., Kleinfeld, D., and Wang, F. (2014). How the brainstem controls orofacial behaviors comprised of rhythmic actions. *Trends Neurosci.* 37, 370–380. doi: 10.1016/j.tins.2014.05.001

Moriyoshi, K., Richards, L. J., Akazawa, C., O'Leary, D. D. M., and Nakanishi, S. (1996). Labeling neural cells using adenoviral gene transfer of membrane-targeted GFP. *Neuron* 16, 255–260. doi: 10.1016/S0896-6273(00)80044-6

Moschovakis, A. K., Dalezios, Y., Petit, J., and Grantyn, A. A. (1998). New mechanism that accounts for position sensitivity of saccades evoked in response to stimulation of superior colliculus. *J. Neurophysiol.* 80, 3373–3379. doi: 10.1152/jn.1998.80.6.3373

Nakamura, K. C., Kameda, H., Koshimizu, Y., Yanagawa, Y., and Kaneko, T. (2008). Production and histological application of affinity-purified antibodies to heat-denatured green fluorescent protein. *J. Histochem. Cytochem.* 56, 647–657. doi: 10.1369/jhc.2008.950915

Ohno, S., Kuramoto, E., Furuta, T., Hioki, H., Tanaka, Y. R., Fujiyama, F., et al. (2012). A morphological analysis of thalamocortical axon fibers of rat posterior thalamic nuclei: a single neuron tracing study with viral vectors. *Cereb. Cortex* 22, 2840–2857. doi: 10.1093/cercor/bhr356

Paxinos, G., and Watson, C. (2007). *The Rat Brain in Stereotaxic Coordinates*, 6th Edn. San Diego, CA: Elsevier.

Redgrave, P., Mitchell, I. J., and Dean, P. (1987). Descending projections from the superior colliculus in rat: a study using orthograde transport of wheatgerm-agglutinin conjugated horseradish peroxidase. *Exp. Brain Res.* 68, 147–167. doi: 10.1007/BF00255241

Redgrave, P., Odekunle, A., and Dean, P. (1986). Tectal cells of origin of predorsal bundle in rat: location and segregation from ipsilateral descending pathway. *Exp. Brain Res.* 63, 279–293. doi: 10.1007/BF00236845

Sahibzada, N., Dean, P., and Redgrave, P. (1986). Movements resembling orientation or avoidance elicited by electrical stimulation of the superior colliculus in rats. *J. Neurosci.* 6, 723–733.

Salinias, E., and Sejnowski, T. J. (2001). Gain modulation in the central nervous system: where behavior. Neurophysiol. Comput. Meet. *Neuroscientist* 7, 430–440. doi: 10.1177/107385840100700512

Sommer, M. A., and Wurtz, R. H. (2008). Brain circuits for the internal monitoring of movements. *Annu. Rev. Neurosci.* 31, 317–338. doi: 10.1146/annurev.neuro.31.060407.125627

Sparks, D. L., and Mays, L. E. (1990). Signal transformations required for the generation of saccadic eye movements. *Annu. Rev. Neurosci.* 13, 309–336. doi: 10.1146/annurev.ne.13.030190.001521

Sreenivasan, V., Esmaeili, V., Kiritani, T., Galan, K., Crochet, S., and Petersen, C. C. H. (2016). Movement initiation signals in mouse whisker motor cortex. *Neuron* 92, 1368–1382. doi: 10.1016/j.neuron.2016.12.001

Takatoh, J., Nelson, A., Zhou, X., Bolton, M. M., Ehlers, M. D., Arenkiel, B. R., et al. (2013). New modules are added to vibrissal premotor circuitry with the emergence of exploratory whisking. *Neuron* 77, 346–360. doi: 10.1016/j.neuron.2012.11.010

Tamamaki, N., Nakamura, K., Furuta, T., Asamoto, K., and Kaneko, T. (2000). Neurons in Golgi-stain-like images revealed by GFP-adenovirus infection in vivo. *Neurosci. Res.* 38, 231–236. doi: 10.1016/S0168-0102(00)00176-0

Waldron, H. A., and Gwyn, D. G. (1969). Descending nerve tracts in the spinal cord of the rat. I. Fibers from the midbrain. *J. Comp. Neurol.* 137, 143–153. doi: 10.1002/cne.901370203

Wolf, A. B., Lintz, M. J., Costabile, J. D., Thompson, J. A., Stubblefield, E. A., and Felsen, G. (2015). An integrative role for the superior colliculus in selecting targets for movements. *J. Neurophysiol.* 114, 2118–2131. doi: 10.1152/jn.00262.2015

Yasui, Y., Tsumori, T., Ando, A., Domoto, T., Kayahara, T., and Nakano, K. (1994). Descending projections from the superior colliculus to the reticular formation around the motor trigeminal nucleus and the parvicellular reticular formation of the medulla oblongata in the rat. *Brain Res.* 656, 420–426. doi: 10.1016/0006-8993(94)91489-3

Zucker, E., and Welker, W. I. (1969). Coding of somatic sensory input by vibrissae neurons in the rat's trigeminal ganglion. *Brain Res.* 12, 138–156.

Conflict of Interest Statement: The authors declare that the research was conducted in the absence of any commercial or financial relationships that could be construed as a potential conflict of interest.

The handling Editor declared a shared affiliation, though no other collaboration, with the authors.

frontiers in Neural Circuits

ORIGINAL RESEARCH
published: 24 October 2018
doi: 10.3389/fncir.2018.00091

Colocalization of Tectal Inputs With Amygdala-Projecting Neurons in the Macaque Pulvinar

Catherine Elorette[1,2], *Patrick A. Forcelli*[1,2,3], *Richard C. Saunders*[4] *and Ludise Malkova*[1,2]*

[1]*Interdisciplinary Program in Neuroscience, Georgetown University School of Medicine, Washington, DC, United States,* [2]*Department of Pharmacology and Physiology, Georgetown University School of Medicine, Washington, DC, United States,* [3]*Department of Neuroscience, Georgetown University School of Medicine, Washington, DC, United States,* [4]*Laboratory of Neuropsychology, National Institute of Mental Health (NIMH), Bethesda, ML, United States*

Neuropsychological and neuroimaging studies have suggested the presence of a fast, subcortical route for the processing of emotionally-salient visual information in the primate brain. This putative pathway consists of the superior colliculus (SC), pulvinar and amygdala. While the presence of such a pathway has been confirmed in sub-primate species, it has yet to be documented in the primate brain using conventional anatomical methods. We injected retrograde tracers into the amygdala and anterograde tracers into the colliculus, and examined regions of colocalization of these signals within the pulvinar of the macaque. Anterograde tracers injected into the SC labeled axonal projections within the pulvinar, primarily within the oral, lateral and medial subdivisions. These axonal projections from the colliculus colocalized with cell bodies within the pulvinar that were labeled by retrograde tracer injected into the lateral amygdala. This zone of overlap was most notable in the medial portions of the medial (PM), oral (PO) and inferior pulvinar (PI), and was often densely concentrated in the vicinity of the brachium of the SC. These data provide an anatomical basis for the previously suggested pathway mediating fast processing of emotionally salient information.

Keywords: subcortical, superior colliculus, blindsight, retrograde, anterograde, anatomy

OPEN ACCESS

Edited by:
Tadashi Isa,
Kyoto University, Japan

Reviewed by:
Hisao Nishijo,
University of Toyama, Japan
Paul J. May,
University of Mississippi Medical Center, United States

***Correspondence:**
Ludise Malkova
malkoval@georgetown.edu

Received: *21 June 2018*
Accepted: *03 October 2018*
Published: *24 October 2018*

Citation:
Elorette C, Forcelli PA, Saunders RC and Malkova L (2018) Colocalization of Tectal Inputs With Amygdala-Projecting Neurons in the Macaque Pulvinar. Front. Neural Circuits 12:91. doi: 10.3389/fncir.2018.00091

INTRODUCTION

Threatening stimuli require fast detection and response from an organism. The canonical cortical visual processing stream refines information from coarse, low level representations in early cortical areas to detailed, high level information. The "trade off" for this refinement is that it requires many synaptic connections. Conserved patterns of low-level visual information, e.g., something moving quickly in peripheral vision, may be sufficient to serve as a threat detection pathway (Dean et al., 1989; Soares et al., 2017). On the basis of behavioral and anatomical studies some have suggested that low level or coarse visual information may travel to the forebrain in a rapid, subcortical manner (LeDoux, 1996; Silverstein and Ingvar, 2015).

Despite a lack of conscious recognition, patients with damage to primary visual cortex can retain appropriate responses to visual stimuli (Pöppel et al., 1973; Richards, 1973; Sanders et al., 1974; Weiskrantz et al., 1974). In a non-conscious manner, patients with so-called "blindsight" can detect, localize, and distinguish between stimuli that are presented within the field of vision damaged by a lesion (Cowey and Stoerig, 1991; Sahraie et al., 1998). Similarly, even after total destruction of V1, non-human primates can track moving stimuli and distinguish between different textures, colors,

shape, or frequency of presentation of stimuli (Weiskrantz, 1963; Humphrey and Weiskrantz, 1967; Mohler and Wurtz, 1977; Miller et al., 1980). The preservation of visual processing in blindsight is subserved in part by projections from the retina to the lateral geniculate nucleus (LGN) of the thalamus (Warner et al., 2010). The LGN, which is the primary relay to visual cortex, projects not only to primary visual areas, but also to higher order cortical regions (e.g., V4, MT; Born and Bradley, 2005). These extrastriate projections are likely preserved after damage to V1 (Schmid et al., 2009). In addition, the superior colliculus (SC), which receives direct retinal input, may provide a relay for visual processing in the absence of V1. Accordingly, inactivation of either the LGN or the SC disrupts blindsight in macaques (Schmid et al., 2010; Kato et al., 2011; Takakuwa et al., 2017).

In addition to the preservation of these non-conscious visual abilities, processing of emotional information in patients with blindsight is likewise preserved. For example, patients can continue to discriminate between facial expressions (de Gelder et al., 1999) or fear-evoking images (Morris et al., 2001) after damage to V1. Furthermore, activation of the amygdala in response to emotionally salient visual stimuli has been observed using fMRI in cortically blind individuals (Vuilleumier et al., 2002). Consistent with the notion that rapid detection of threatening stimuli may rely on a fast (subcortical) relay, in intact individuals masked presentation of emotionally salient stimuli likewise activates the amygdala in the absence of conscious awareness (Whalen et al., 1998; Liddell et al., 2005). While the LGN likely mediates many features of blindsight as described above, other subcortical structures have been suggested to mediate the fast processing of emotionally salient information. Notably, both the SC and pulvinar display coincident activation with the amygdala during processing of emotional stimuli (Morris et al., 1999; Koller et al., 2018); together with the amygdala, these structures have been suggested to serve as a coarse, fast, subcortical pathway for the detection and response to emotionally salient visual information (Weiskrantz et al., 1974; LeDoux, 1996).

The SC in primates receives input from ∼10% of retinal ganglion cells, and detects stimuli both in the central and peripheral field of vision (Perry and Cowey, 1984; Hofbauer and Dräger, 1985); in this way the SC may be optimally suited for detection of approaching threats. While the SC does not project directly to the amygdala, there is a well-documented projection from the SC to the pulvinar (Gattass et al., 2018, for review). Both the superficial and deep layers of SC project to pulvinar, including to the inferior (Stepniewska et al., 2000) medial, lateral and oral regions (Benevento and Fallon, 1975; Trojanowski and Jacobson, 1975; Benevento and Standage, 1983). Likewise, a projection from the pulvinar to the amygdala has been described (Locke, 1960; Jones and Burton, 1976; Aggleton et al., 1980; Norita and Kawamura, 1980; Romanski et al., 1997; Stefanacci and Amaral, 2000) with the majority of this projection targeting the lateral nucleus. This finding is consistent with previous findings that the bulk of subcortical and cortical inputs in the amygdala enter through the lateral nucleus (Amaral et al., 1992), considered the main input nucleus of the amygdala. Neuroimaging studies in both human and macaque subjects have shown probabilistic connectivity among SC, pulvinar and amygdala (Tamietto et al., 2012; Rafal et al., 2015) using diffusion tensor imaging (DTI) and tractography methods. However, it remains to be determined if the regions of the pulvinar that project to the amygdala are the same regions that receive input from the SC. In the present study, we aimed to address this gap. To achieve this goal, we injected anterograde tracers in the SC and retrograde tracers in the lateral nucleus of the amygdala and documented an overlap between retrograde and anterograde labeling within the pulvinar.

MATERIALS AND METHODS

Subjects

Two male macaque monkeys (1 *Macaca mulatta* (Y), 1 *Macaca nemestrina* (S)) were used for these experiments. Animal Y was 4 years old and weighed 8.2 kg and Animal S was 6 years old and weighed 17.4 kg at the time of surgery. MRI-guided injections of anatomical tracers were performed stereotaxically under sterile conditions. Injections sites, tracers used and volumes of injection for each case are shown in **Table 1**. The animals received bilateral injections of anterograde tracer (fluoroemerald, FE) in SC and retrograde tracer (choleratoxin B, CTB) in the lateral nucleus of the amygdala; this yielded four cases for anatomical analysis. This study was carried out in accordance with the recommendations of the Guide for the Care and Use of Laboratory Animals. The protocol was approved by the Georgetown University Animal Care and Use Committee.

MRI, Surgery and Injections

To obtain a pre-operative MRI scan, each animal was sedated with ketamine (10 mg/kg), intubated, and maintained at a stable plane of anesthesia using isoflurane (1%–4%). Animals were then transported to the imaging facility (Center for Molecular Imaging at Georgetown University Medical Center) where they were placed into a standard MRI-compatible stereotaxic frame. Each animal received a T1-weighted MRI scan using a custom surface coil in Siemens Trio 3T MRI scanner, as previously described (Wellman et al., 2005). An MPRAGE pulse sequence (TR = 1,600 ms, TE = 4.38 ms, TI = 640 ms, flip angle = 15 degrees, averages = 3, FOV = 256 × 256 mm^2) was used to acquire a 3D volume of the monkey brain with an effective resolution of 1.0 mm^3. The resulting subject-specific

TABLE 1 | Tracer injections across cases.

Case	Tracer	Supplier	Site	Volume (μl)
Y1	Choleratoxin B	List Labs	L Amygdala	2
	Fluoroemerald	Invitrogen	L SC	2.3
Y2	Choleratoxin B	List Labs	R Amygdala	2.5
	Fluoroemerald	Invitrogen	R SC	2.3
S1	Choleratoxin B AlexaFluor-594 conjugate	Invitrogen	L Amygdala	2.6
	Fluoroemerald	Invitrogen	L SC	2
S2	Choleratoxin B	List Labs	R Amygdala	1.8
	Fluoroemerald	Invitrogen	R SC	2

atlas was used to calculate injection coordinates relative to the earbar and the superior sagittal sinus, both of which were visible on the scans (Saunders et al., 1990).

After the MRI scan, each animal was transported to the surgical suite while remaining in the stereotaxic frame. During surgery, vital signs (heart rate, respiratory rate, body temperature, oxygen saturation, electrocardiogram and end-tidal CO_2) were monitored. Body temperature was maintained using a heated table and blankets. Intravenous fluids (lactated Ringer's solution) were delivered during the surgery.

The skin and galea were opened in anatomical layers to expose the cranium. A midline craniotomy (approximately 4 by 6 mm) was placed at the anteroposterior level of the intra-aural plane to expose the superior sagittal sinus, which served as the midline reference point. Craniotomies were placed above the amygdala and SC (three in total), the dura was incised, and a Hamilton syringe (30 gauge) was lowered to the MRI-derived coordinates. Injections were performed at a rate of 0.2 μL/min, and the syringe was left in place for a minimum of 10 min following injection to prevent reflux of the tracer up the needle tract. At the conclusion of the injections, the dura, galea and skin were closed in anatomical layers. Post-operatively, animals received antibiotics, analgesics and dexamethasone (0.5–1 mg/kg) in consultation with the facility veterinarians.

Tissue Preparation

After a survival period of 14 days for Animal Y and 15 days for Animal S, the animals were deeply anesthetized with a sodium pentobarbital-based euthanasia solution and perfused transcardially with phosphate buffered saline followed by 4% paraformaldehyde. Brains were removed from the skull and post-fixed overnight in 4% paraformaldehyde. Following post-fixation, brains were cryoprotected in a solution of 10% glycerol and 2% DMSO in phosphate buffer for 24 h, then transferred to a 20% glycerol, 2% DMSO solution in phosphate buffer for 48 h (Rosene et al., 1986). Cryoprotected brains were blocked in the coronal plane and then flash frozen in −80°C isopentane and stored at −80°C until sectioning. The tissue was cut coronally in sections of 40 μm thickness on a freezing stage sliding microtome (American Optical Model 860 Microtome Physitemp Instruments Inc., BFS-40MP Freezing stage).

Histological Procedures

Every 10th section from each brain was mounted onto gelatin subbed slides and air dried. The mounted sections were processed through a series of ethanol solutions, defatted, stained with thionin and cover slipped using DPX mountant (Sigma-Aldrich, St. Louis, MO, USA). These thionin stained sections were used to visualize the subdivisions of the thalamic nuclei, amygdala and SC.

To visualize CTB and FE labeling a series of sections was processed for each case through the pulvinar; adjacent sections were spaced by ∼400 μm. The antibodies, suppliers and dilutions used for immunohistochemical and immunofluorescent staining procedures are listed in **Table 2**.

Immunofluorescence

The sections were washed in phosphate-buffered saline (PBS) containing 0.3% TX-100 three times for 5 min and placed in blocking solution with agitation for 1 h. Blocking solution consisted of 2% bovine serum albumin, 3.75% normal goat serum, 0.3% TX-100, all in PBS. Primary antibodies (anti-CTB and anti-FE, described in **Table 2**), were added to the blocking solution and the tissue was incubated for an additional 48 h at 4°C. The sections were washed five times for 5 min, then placed in secondary antibody solution (donkey anti-goat Alexa 594 and donkey anti-rabbit Alexa 488, described in **Table 2**), which consisted of 2% BSA, 0.3% TX-100, and 3.75% normal goat serum, all in PBS. The sections were incubated in secondary antibody for 90 min with agitation at room temperature. Following incubation in secondary antibody, sections were washed with PBS five times for 5 min each, mounted on gelatin-coated slides, briefly air dried, and coverslipped with Vectashield hard set with DAPI (Vector Laboratories). This process was used for cases Y1, Y2 and S2. In case S1, two 1-in-10 series through the pulvinar were stained separately. In one series, axons projecting from the SC to the pulvinar were visualized via immunofluorescence as described above, using only the antibodies (anti-FE) corresponding to the tracer injected in SC. The second series was processed for immunohistochemistry (described below).

For all cases, sections through the amygdala and SC were processed as described above to visualize the injection sites. The procedure was the same as that described for immunofluorescence above, but only the antibodies that corresponded to the injection sites were used (anti-CTB in the amygdala and anti-FE in the SC).

Immunohistochemistry

For one case (S1), visualization of the CTB was enhanced using immunohistochemistry. Sections were washed in PBS containing 0.3% Triton X-100 (TX-100) three times for 5 min, quenched in 0.6% peroxide and PBS solution for 10 min, and placed in blocking solution with agitation for 1 h. Blocking solution consisted of 2% bovine serum albumin, 3.75% normal goat serum, 0.3% TX-100, all in PBS. Primary antibody (anti-CTB,

TABLE 2 | Antibodies used for immunofluorescence and immunohistochemistry.

Antibody	Supplier Catalog #	Type	Host	Dilution	Immunogen
Anti-CTB	List Biological #703	Polyclonal	Goat	1:3,200	B subunit (choleragenoid)
Anti-Goat AlexaFluor-594 conjugated secondary	Jackson Immunoresearch #705-586-147	IgG (H + L)	Donkey	1:2,000	Goat IgG
Anti-goat HRP-conjugated secondary	Jackson Immunoresearch #705-005-147	IgG (H + L)	Donkey	1:200	Goat IgG
Anti-FE	ThermoFisher #A-11095	Polyclonal	Rabbit	1:4,000	Fluorescein
Anti-rabbit AlexaFluor-488 conjugated secondary	Jackson Immunoresearch #705-545-003	IgG (H + L)	Donkey	1:2,000	Rabbit IgG

described in **Table 2**) was added to the blocking solution and the tissue was incubated for an additional 48 h at 4°C. The sections were washed five times for 5 min, then placed in secondary antibody solution (Biotin-SP conjugated donkey anti-goat, described in **Table 2**) and incubated with agitation for 90 min at room temperature. These sections were washed five times for 5 min in PBS, placed in ABC solution (Vector Labs) for 90 min with agitation, washed five times for 5 min, and placed in diaminobenzidine tetrachloride (DAB, Sigma Aldrich, St. Louis, MO, USA) solution for 10 min with agitation. Then 0.025% peroxide was added and the sections were allowed to stain for approximately 3.5 min until there was visible contrast in the tissue. The sections were then washed with PBS five times, mounted on gelatin-coated slides, air-dried and dehydrated through ascending concentrations of ethanol before being cleared in xylenes and coverslipped with DPX.

Microscopy and Data Analysis

To outline the boundaries of individual subdivisions of the pulvinar, amygdala, and SC, we used thionin stained sections from a normal macaque brain (**Figure 1**). These sections were photographed using a Nikon NiE-E research microscope. Images were uniformly edited for brightness and noise reduction. The boundaries of amygdala nuclei and layers of the SC follow the divisions of Amaral et al. (1992) and May (2006), respectively. The boundaries of thalamic subnuclei were drawn following the conventions of the macaque thalamus atlas of Olszewski (1952). For further discussion of inferior pulvinar (PI) divisions, see Gutierrez et al. (1995).

To document the sites of tracer injections, immunofluorescent sections through the amygdala and the SC were photographed using a stereo microscope (Omano, China). Resulting micrographs were adjusted for brightness and contrast in Photoshop CC 2017 (Adobe) and are presented in **Figure 2** together with drawings of matching sections from a standard rhesus macaque brain atlas generated in the Laboratory of Neuropsychology (LN), at the National Institute of Mental Health (NIMH).

Using sections processed for immunofluorescence (cases Y1, Y2, S2), labeled cell bodies and fibers (**Figures 3**, **4**, **6**) were

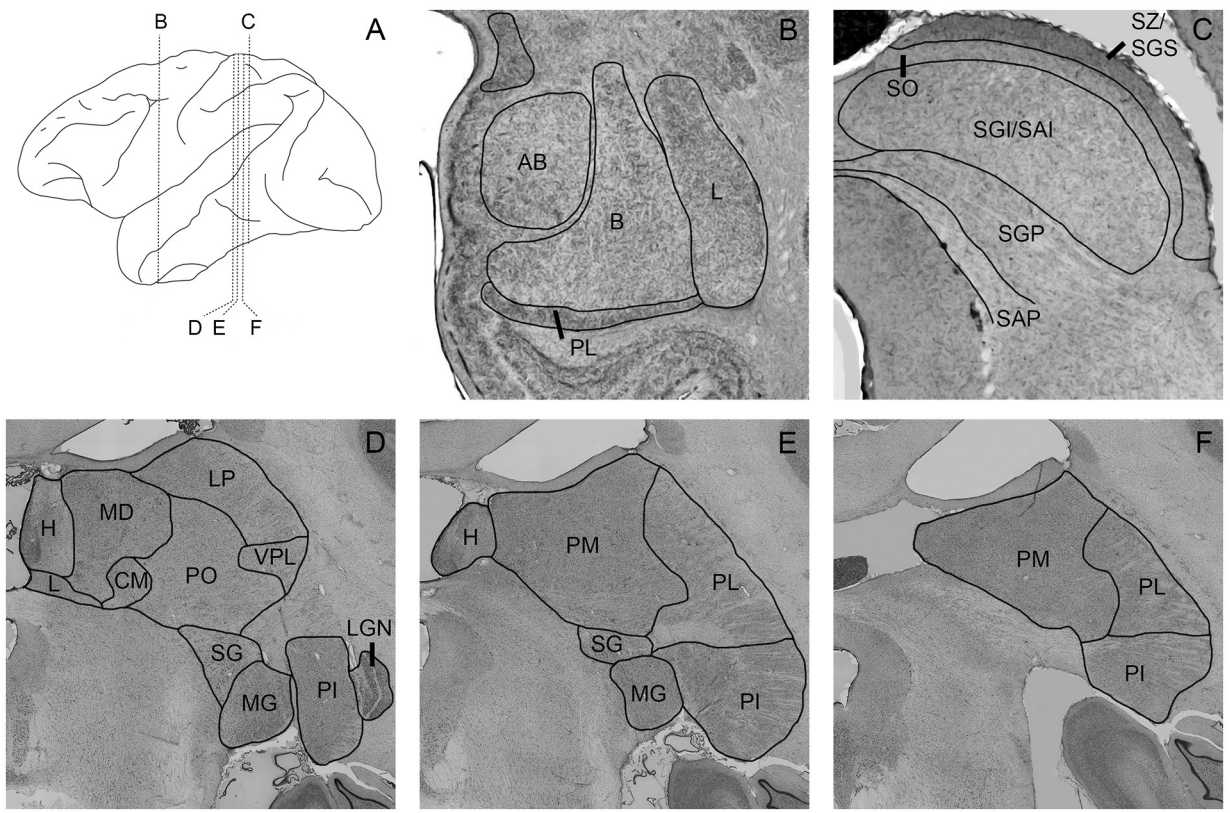

FIGURE 1 | Photomicrographs of nissl-stained sections through the amygdala, superior colliculus (SC), and pulvinar. Panel **(A)** shows the location of panels **(B–F)** within the brain. Amygdala nuclei **(B)** are outlined and labeled according to Amaral et al. (1992). AB, accessory basal; B, basal; L, lateral; M, medial; PL, paralaminar. SC nuclei **(C)** are outlined and labeled according to May (2006). SZ/SGS, stratum zonale/stratum griseum superficiale; SO, stratum opticum; SGI/SAI, stratum griseum intermedium/stratum album intermedium; SGP, stratum griseum profundum; SAP, stratum album profundum. Thalamic nuclei **(D–F)** are outlined and labeled according to the delineations of the Olszewski (1952). CM, centromedial nucleus; H, habenula; L, nucleus limitans; LGN, lateral geniculate nucleus; LP, lateral posterior nucleus; MD, mediodorsal nucleus; MG, medial geniculate nucleus; PI, inferior pulvinar; PL, lateral pulvinar; PM, medial pulvinar; PO, oral pulvinar; SG, suprageniculate nucleus; VPL, ventroposteriolateral nucleus.

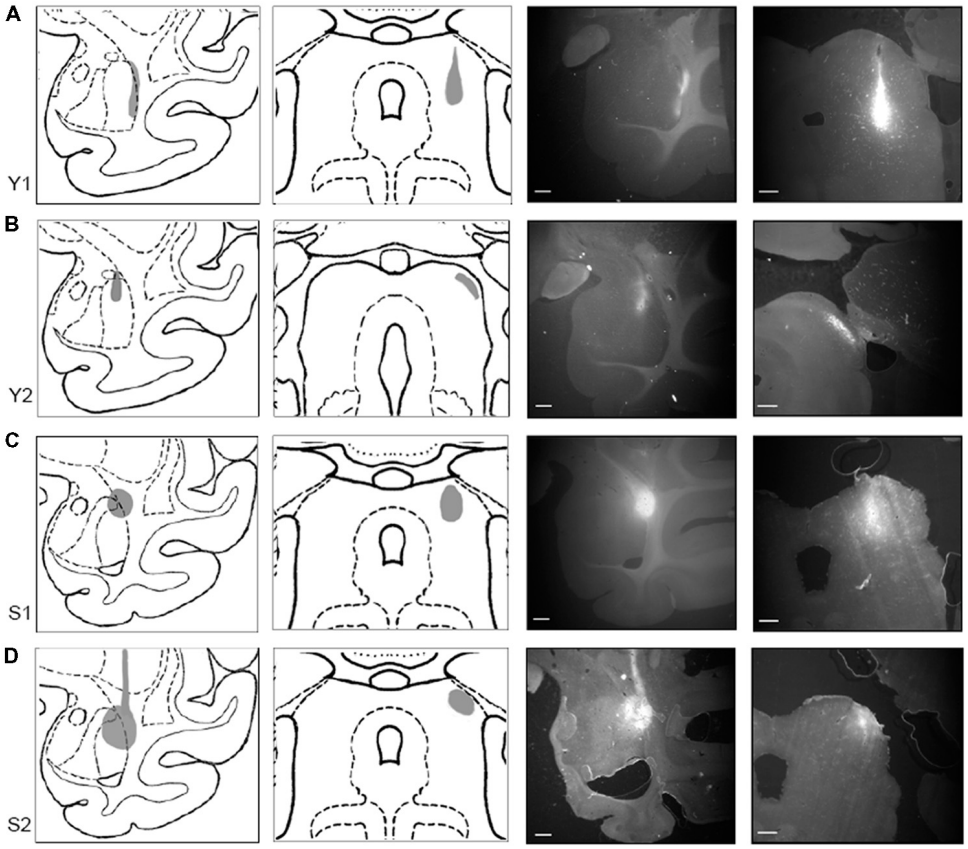

FIGURE 2 | Tracer injections localized in SC and amygdala. Injection sites for cases Y1 **(A)**, Y2 **(B)**, S1 **(C)**, and S2 **(D)**. Each injection site is shown (in gray) on drawings of coronal sections through a standardized rhesus macaque atlas at the level of the amygdala (1st column) and the SC (2nd column). Images on the right show photomicrographs of the fluorescent tracer injections in amygdala (choleratoxin B (CTB); 3rd column; scale bar = 5 mm) and SC (fluoroemerald (FE); 4th column; scale bar = 1 mm).

localized using a Zeiss Axiophot microscope fitted with an MDPlot digitizer and software (Accustage, Shoreview, MN, USA). The outline of each section was traced and the individual axons and cell bodies labeled with the different tracers were plotted. Cell bodies labeled with CTB within the pulvinar were differentiated from non-specific background signal on the basis of distinctive color, luminance and morphology. Labeled cells were brighter than background signal and had a characteristic nuclear exclusion of fluorescence. The plotted sections were exported to Illustrator CS (Adobe) and aligned with images of the adjacent thionin stained section. In case S1, DAB staining of cell bodies in the pulvinar and fluorescent staining of axons from SC were marked as described above, then overlaid onto each other. These merged images were overlaid onto their corresponding thionin sections (**Figure 5**). In all figures, the plotted sections were cropped to show only the relevant regions. Labeling outside of the thalamus is not shown.

Sections through the pulvinar containing both retrogradely labeled cell bodies from tracers in the amygdala and axons labeled by anterograde tracers placed in the SC were acquired using a confocal microscope (Leica SP8) with 20× and 63× lenses (Leica HC PL APO 20 ×/0.75 IMM CORR CS2, Leica HC PL APO 63×/1.40 OIL CS2). Z-stacks were acquired for each region of interest, and maximal Z-projections were then pseudocolored and adjusted for brightness and contrast using ImageJ. Brightness and contrast were separately adjusted for each channel and each image, but all processes were applied to the *entire* image. Representative examples are presented in **Figure 7**.

RESULTS

Injection Sites

In Case Y1 (**Figure 2A**), the CTB injection site in the amygdala extended along the lateral border of the lateral nucleus. Tracer extended into the white matter at the dorsal aspect of the injection. The dorsoventral extent of this injection spanned the majority of the lateral nucleus. The corresponding injection site in SC was localized to the lateral portion of stratum griseum intermedium (SGI), stratum album intermedium (SAI), stratum griseum profundum (SGP) and stratum album profundum (SAP). Together, these layers constitute the intermediate and deep layers of the SC. This injection site was the most ventral of the four cases.

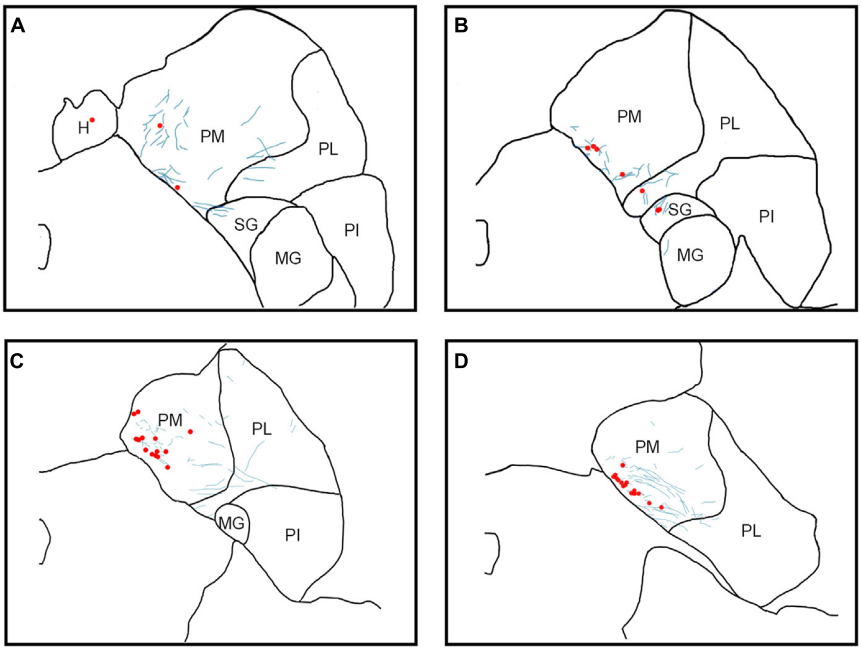

FIGURE 3 | Pattern of overlapping label in Case Y1. Each panel **(A–D)** presents a plot of labeled cell bodies or fibers from different rostro-caudal levels through the pulvinar. Anterograde label (putative axons) after injection of FE in the SC are shown in cyan. Retrograde label (cell bodies) after injection of CTB in the amygdala are shown in red. Abbreviations for thalamic nuclei are as in **Figure 1**.

In Case Y2 (**Figure 2B**), the CTB injection site in the amygdala was localized primarily to the dorsal portion of the lateral nucleus. The corresponding injection site in the SC was localized to the lateral stratum opticum (SO), with some tracer extended in to the stratum griseum superficiale (SGS) and SGI. The medial-lateral spread of the tracer was limited with most the tracer located immediately lateral to the brachium.

In Case S1 (**Figure 2C**), the CTB injection site in the amygdala was localized to the dorsolateral portion of the lateral basal nucleus and the dorsal portion of the lateral nucleus. The injection site extended beyond the boundary of the amygdala into the laterally adjacent white matter. The FE SC injection site was centered on the intermediate layers of SC with tracer extending into the superficial (SO, SGS) and stratum zonale (SZ) and deep layers. The SC injection site in this case was the most medial of the four cases.

In Case S2 (**Figure 2D**), the CTB injection site in amygdala was centered in the dorsal aspect of the lateral nucleus. The injection covered the dorsal half of the lateral nucleus and extended medially into the dorsal part of the lateral basal nucleus, with some coverage of the lateral adjacent white matter. The SC injection site was localized to the lateral SC and extended throughout the superficial and intermediate layers. The injection site, while lateral, did not extend into the brachium.

Localization of Anterograde and Retrograde Label Within the Pulvinar

In Case Y1 (**Figure 3**), labeling of SC axons extended through the SC and spread through the medial pulvinar (PM), lateral pulvinar (PL) and suprageniculate (SG). Several fiber bundles followed along the brachium of the SC, with the lateral extent along the borders of the thalamic nuclei. Retrogradely labeled cell bodies from injections in the amygdala were present along the brachium, in the PM, the PL, and within the SG nucleus, and were concentrated to the ventromedial aspects of these regions. Areas of both anterogradely labeled axons (from SC) and retrogradely labeled cell bodies were observed medially, in medial and (sparsely) in PL (**Figures 3B–D**, **7A**).

In Case Y2 (**Figure 4**), labeled axons from anterograde injections in SC extended through the SC into the oral pulvinar (PO) and mediodorsal thalamus, and further extended to the lateral posterior (LP) and ventroposteriolateral (VPL) nuclei of the thalamus. These fibers were localized to the ventromedial PM and the lateral portion of the mediodorsal thalamus. Retrogradely labeled cell bodies were present in PO, PM, PI and nucleus limitans. These labeled cells were located in close proximity to the brachium, although a few cells were observed in the dorsal PO. Areas of overlapping anterograde and retrograde labeling were observed in oral, medial and PI, concentrated ventromedially in these regions (see **Figure 7B** for an example of labeling within PI).

In Case S1 (**Figure 5**), labeled axons extended through the SC and laterally from the brachium into medial, lateral and PI. The tracts largely appeared to travel mediolaterally and were densest in the ventral aspect of the PM and the lateral aspect of the PI. Retrogradely labeled cell bodies resulting from injection in the amygdala were present in medial and

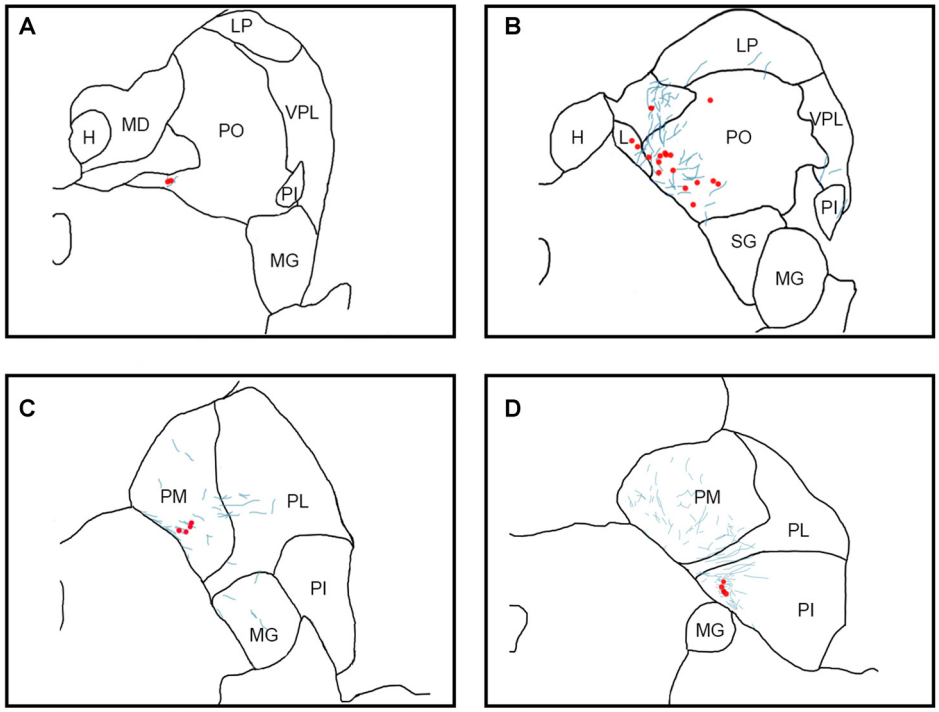

FIGURE 4 | Pattern of overlapping label in Case Y2. Each panel **(A–D)** presents a plot of labeled cell bodies or fibers from different rostro-caudal levels through the pulvinar. Anterograde label (putative axons) after injection of FE in the SC are shown in cyan. Retrograde label (cell bodies) after injection of CTB in the amygdala are shown in red. Abbreviations for thalamic nuclei are as in **Figure 1**.

PL, and to a lesser extent within the SG/medial geniculate (MG) nucleus. Most cell bodies were ventromedially localized, but there were a large number present in PM that extended dorsoventrally to cover approximately half of the area of the nucleus. Areas of overlap between the labeled axons and cell bodies were not directly observed due to the type of staining utilized in this case (see "Materials and Methods" section), but both labeled axons from the SC and labeled neurons projecting to the amygdala were present in the ventromedial aspect of the PM. The more extensive retrograde signal in this case may be due to the better signal-to-noise of the DAB-based immunohistochemistry as compared to immunofluorescence

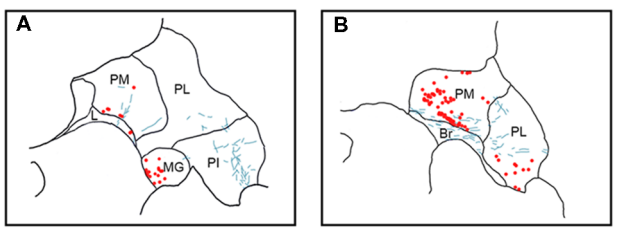

FIGURE 5 | Pattern of overlapping label in Case S1. Each panel **(A,B)** presents a plot of labeled cell bodies or fibers from different rostro-caudal levels through the pulvinar. Anterograde label (putative axons) after injection of FE in the SC are shown in cyan. Retrograde label (cell bodies) after injection of CTB in the amygdala are shown in red. Abbreviations for thalamic nuclei are as in **Figure 1**. Br, brachium of the superior colliculus.

used in other cases. Since in this case, fluorescent CTB was used in one hemisphere and non-fluorescent CTB in the contralateral hemisphere, we were able to evaluate whether labeling was present only ipsilaterally or if it was also present contralaterally. In this case, labeling in the pulvinar appeared to be only ipsilateral.

In Case S2 (**Figure 6**), labeled axons extended from SC along the brachium, through the oral, medial and PL, as well as through central and parafascicular nuclei of the thalamus. Labeled axons were most densely concentrated in oral and PM, in the ventromedial aspect (see **Figure 7D** for high power magnification of an area in ventromedial PO). Retrogradely labeled cell bodies resulting from the amygdala injection were present in oral, medial and PL and the MG nucleus. Likewise, the pattern of labeling was ventromedial across the thalamus, with most cell bodies appearing in small clusters. Areas of overlap between these labeled axons and cell bodies were found within oral, medial and PL and MG. The area of most dense overlap was caudally distributed within the PM.

In summary, within the pulvinar, retrogradely labeled cell bodies were often observed in close proximity to anterogradely labeled axons. In all cases, the labeling of the cell bodies in the pulvinar after amygdala injections was sparse, suggesting it is a small projection. The areas where the retrograde label overlapped with anterograde axonal label from the SC injections were quite limited. While the oral and PM showed the largest degree of overlapping labeling, some overlap was

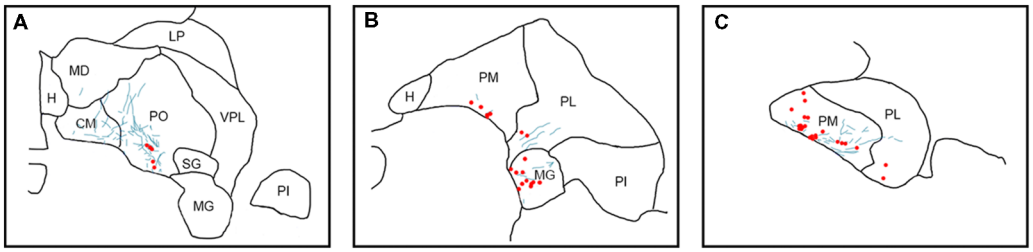

FIGURE 6 | Pattern of overlapping label in Case S2. Each panel **(A–C)** presents a plot of labeled cell bodies or fibers from different rostro-caudal levels through the pulvinar. Anterograde label (putative axons) after injection of FE in the SC are shown in cyan. Retrograde label (cell bodies) after injection of CTB in the amygdala are shown in red. Abbreviations for thalamic nuclei are as in **Figure 1**.

also observed in the lateral and PI, but to a lesser degree. Confocal imaging was used to extend these observations. **Figure 7** shows images within the pulvinar from cases Y1, Y2 and S2. Choleratoxin-positive cell bodies (pseudocolored red) and their processes within the pulvinar were found within a field of FE-labeled axons (pseudocolored cyan) resulting

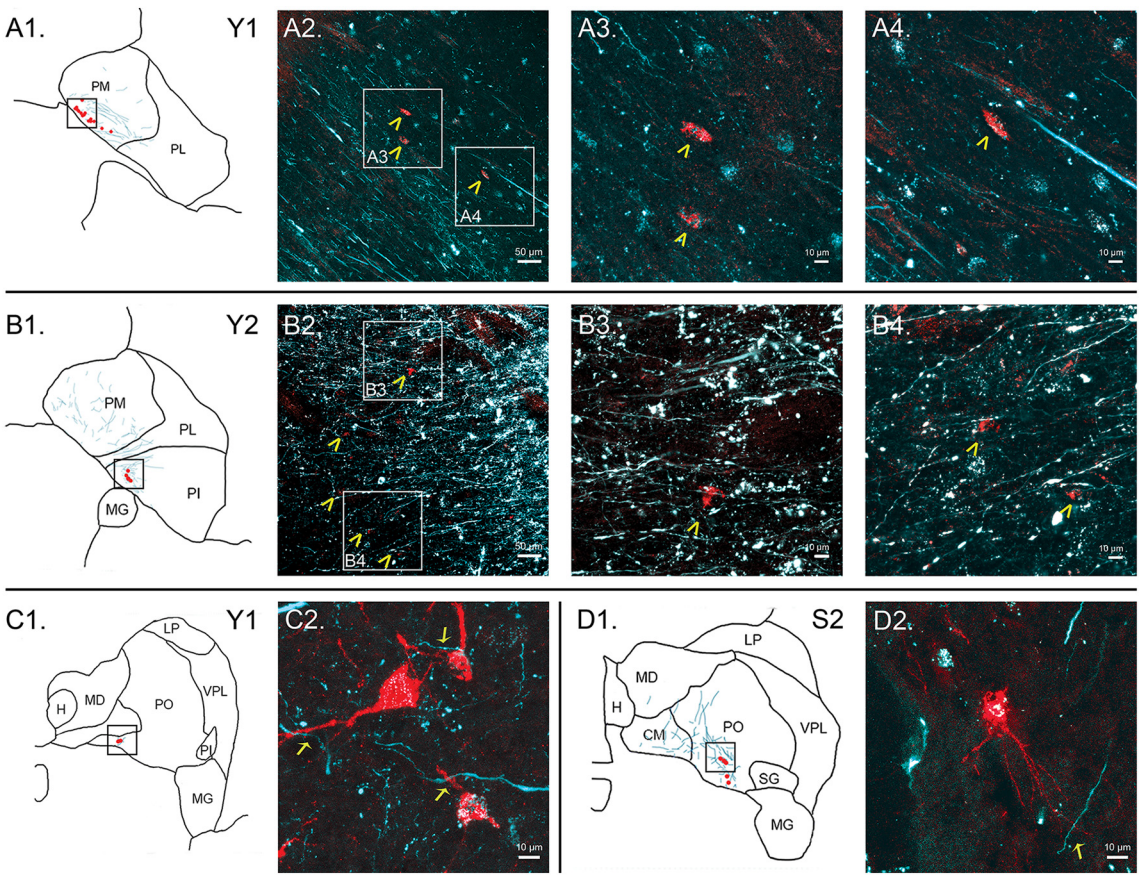

FIGURE 7 | Colocalization of retrograde and anterograde labeling in the pulvinar. FE-labeled fibers resulting from injection into the SC are shown in cyan. CTB-immunoreactive cell bodies resulting from injection into the amygdala are shown in red. Atlas pictures are included to illustrate where each photo was taken. The case from which the images are derived is shown in the upper right corner. **(A)** Images of cells within PM, case Y1. Atlas image is shown in **(A1)**. Low power confocal image (20× magnification, **(A2)**) showing a band of labeled cell bodies (red) within the field of labeled axons running along the medial boundary of the PM, parallel to the brachium of the SC. Atlas image is shown in **(B1)**. Chevrons indicate cell bodies. Panels **(A3,A4)** are higher power (60×) magnifications of the areas indicated by boxes in **(A2)**. **(B)** Images of cells within PI, case Y2. Atlas image is shown in **(B1)**. Low power (20×, **(B2)**) confocal image showing colocalization of labeled cell bodies and axons in PI. Chevrons indicate cell bodies. Panels **(B3, B4)** show high power (60×) magnification. As in **(A)**, chevrons in B3 and B4 indicate areas of overlap in labeled cell bodies and axons. **(C)** Cells within PO, case Y1. Atlas image shown in **(C1)**. High power (63×) confocal image showing individual cell bodies and finer axonal processes in close proximity in **(C2)**. **(D)** Cells within PO, case S2. Atlas image shown in **(D1)**. High power (63×) confocal image in **(D2)**. Arrows indicate close associations between labeled terminal boutons and labeled cells. Scale bars are as indicated in each panel.

from the FE injections in SC. Representative labeling is shown in medial (**Figure 7A**), oral (**Figures 7C,D**) and inferior (**Figure 7B**) pulvinar. Low-power (20×) magnification shows several choleratoxin-positive cell bodies in close proximity to FE-labeled axons, while high-power (60–63×) magnification shows the processes of cell bodies and axons in close proximity to one another. As described above, labeling of cells projecting from the pulvinar to the amygdala was sparse and ventromedially concentrated, while labeling of axons from SC was ubiquitous in all images. FE-labeled axons in PM followed along the brachium, while labeling within oral and PI was more diffuse. CTB-labeled cells frequently appeared within close proximity of one another.

DISCUSSION

Here, we have shown a colocalization of projections from the SC with amygdala-projecting neurons in all nuclei of the macaque pulvinar, with the heaviest label occurring ventromedially in oral and PM. The overlapping distributions of retrograde and anterograde label were present in all four cases analyzed. These data provide an anatomical basis for the previously hypothesized subcortical connection between the SC and the amygdala, via the pulvinar. Since we found the same pattern of labeling in the pulvinar in two species of macaques, it is thus likely that these anatomical projections are preserved throughout this genus. While prior studies have suggested the presence of this pathway in primates through MRI-based approaches, these data provide the first direct anatomical evidence for colocalization of these projections within the primate pulvinar.

The cases we presented were tightly clustered and highly overlapping with respect to their injection sites in the amygdala and SC. Despite this there were some observable differences. For example, following the injection of the tracers in the amygdala, labeling in the PO was present in the two cases with more medial placement (Case Y2 and S2) within the lateral nucleus, and absent in the two cases with more lateral placement (Case Y1 and S1). We did not note other patterns with respect to the location of injections within the amygdala. This projection was examined in more detail by others (e.g., Stefanacci and Amaral, 2000). With respect to the injections in the SC, we noted that the two cases with more superficial injections (Y2 and S2) were associated with stronger labeling in the PO; we did not note any other patterns. As with the amygdala, the topography of projections from SC to pulvinar were examined in detail by others (Benevento and Standage, 1983; Huerta and Harting, 1983). More detailed assessment of this pathway, with injection sites aimed at the different layers of the SC and different subregions of the amygdala, should be addressed in future studies.

Superior Colliculus Projections to the Pulvinar

In the rat and mouse, SC projects to several thalamic nuclei, including the LP nucleus (the rodent pulvinar homolog, see Harting et al., 1972) and the SG nucleus (Taylor et al., 1986; Linke et al., 1999; Zhou et al., 2017). Similarly, the SC projects to the pulvinar of the treeshrew, a proto-primate (Chomsung et al., 2008). This projection is also conserved in primates (May, 2006). In macaques, retrograde tracer injections into PM result in dense labeling of cells within the deep and intermediate layers of SC (Benevento and Standage, 1983). Moreover, lesions made in the superficial, intermediate, and deep layers of the SC result in degenerating fibers in medial and PL (Benevento and Fallon, 1975). Fibers projecting from the SC to pulvinar course laterally from the brachium and terminate throughout all of the subdivisions of the pulvinar of the squirrel monkey, owl monkey and macaque (Benevento and Fallon, 1975; Huerta and Harting, 1983; Stepniewska et al., 2000), a pattern similar to that reported here. Thus, our present findings are in line with those previously reported in the literature.

Pulvinar Projections to the Amygdala

As with projections from the SC to the pulvinar, projections from the pulvinar to the amygdala have also been described across species. In rodents, for example, the LP nucleus projects to the lateral amygdala (Doron and LeDoux, 1999; Zhou et al., 2018). In macaques, large retrograde (horseradish peroxidase) tracer injections into the amygdala (Aggleton et al., 1980), as well as tracer injections restricted to the lateral nucleus (Norita and Kawamura, 1980; Stefanacci and Amaral, 2000), produce light labeling in the PM, primarily in a region adjacent to the brachium. In the latter study, three cases were presented in which retrograde tracers were placed in either the dorsal division or ventral intermediate division of the lateral nucleus of the amygdala. These cases displayed labeling across the rostrocaudal extend of the medial boundary of the pulvinar, a profile similar to that we observed in our cases S2 and Y2 (**Figures 2**, **4**, **6**). These projections have also been confirmed after injections of anterograde tracer into the lateral and PM in both squirrel and macaque monkeys resulted in dense terminal labeling in the dorsal division of the lateral nucleus of the amygdala (Jones and Burton, 1976; Romanski et al., 1997). More restricted injections into the medial division of the PM (i.e., along the brachium of the SC) preferentially label a narrow band at the lateral edge of the lateral nucleus of the amygdala (Burton and Jones, 1976). This pattern of labeling is consistent with what we observed in Case Y1 (**Figures 2**, **3**).

Convergent Labeling Within Pulvinar

In the mouse, a monosynaptic relay between the lateral SC and the lateral amygdala has been described (Wei et al., 2015). This projection is mediated by a synapse in the LP nucleus of the thalamus, the mouse homolog of the primate pulvinar (Harting et al., 1972). Interestingly, this projection is necessary for species typical responses to looming threatening stimuli (Wei et al., 2015). A similar relationship has been suggested in the rat and the treeshrew (Linke et al., 1999; Day-Brown et al., 2010). Evidence from imaging studies is consistent with these findings. In both macaque and human subjects, reports using DTI suggest that axons run from the SC to the pulvinar, and from the pulvinar

to the amygdala (Rafal et al., 2015). Tamietto et al. (2012) used DTI to compare human control subjects to a patient with lesions to striate cortex. They found that probabilistic fiber bundles connecting the SC, pulvinar and amygdala exist in both lesioned and control patients, but that the projection is more robust ipsilateral to the damage in striate cortex in the lesioned subject. DTI is a probabilistic technique and cannot conclusively show either functional or anatomical coupling among the areas. Our data fill the gap between the human and primate imaging studies and the rodent data, by confirming that there is an area of overlapping projection in the pulvinar that likely connects the SC with the amygdala.

Relevance to Behavior

Studies of blindsight have long suggested that SC is necessary for rapid visual processing, by providing an additional subcortical route for information transfer (Schneider, 1969; Weiskrantz et al., 1974). Accordingly, while lesions to striate cortex partially spare performance on visually-mediated tasks (Schmid et al., 2010), lesions or inactivation of both striate cortex and SC produce more profound deficits (Mohler and Wurtz, 1977; Solomon et al., 1981; Kato et al., 2011).

This pathway likely also serves to support rapid, non-conscious perception of threat via projections from the SC to the pulvinar, and from the pulvinar in turn, to the amygdala. Consistent with this, an increase in correlated activation among the amygdala, pulvinar, and SC is observed via fMRI when angry faces are presented in a manner that precludes conscious perception of the stimuli (Morris et al., 1999). The importance of pulvinar in this pathway is further underscored by a finding in a patient with pulvinar damage, who displays impaired fear responses to subliminally presented threatening visual stimuli (Ward et al., 2005).

Studies have also suggested that processing within the pulvinar *per se* may contribute to the rapid detection of and response to visual threats. Both humans (as measured via MRI) and macaques (as measured by single unit activity) display increased activity in the pulvinar when presented with images of snakes (Van Le et al., 2013; Le et al., 2014, 2016; Almeida et al., 2015; Soares et al., 2017). Of particular relevance to our present findings, there are two apparent clusters of snake-responsive neurons in the macaque pulvinar: one cluster in the dorsal portion of the PL, and the other in the ventromedial portion of the PM. This latter area is where we observed consistent colocalization across all four cases. In their article, Van Le et al. (2013) suggested that at least one route that could mediate rapid responses to threating stimuli such as snakes was a pathway from the SC to the pulvinar to the amygdala; our data are consistent with their interpretation.

Although it is possible that the pulvinar is relaying purely visual information to the amygdala, the intermediate and deep layers of the SC, which we have targeted in this study, receive multimodal input from different sensory systems (Stein et al., 2009). Given that other studies (Benevento and Standage, 1983) have reported preferential labeling in the intermediate and deep SC following injections into the PM, it seems likely that the labeling we observed was also due to projections from the deep and intermediate layers. This would be consistent with a multimodal relay, rather than a purely visual relay. The multimodal integration properties of the intermediate and deep layers of SC may enable its critical role for fast, reflexive defense responses (Dean et al., 1989; Brandão et al., 1994). We have recently reported that these defense responses, which are evoked by pharmacological activation of the primate SC (DesJardin et al., 2013), can be partially attenuated by concurrent inactivation of the basolateral amygdala (Forcelli et al., 2016). However, as no direct projection from SC to amygdala has been reported, it is tempting to speculate that the pulvinar is a component of the network underlying these defense responses.

In summary, here we have described a zone within the pulvinar that receives projections from the SC and contains neurons that project to the amygdala. While such a projection has been hypothesized in humans and macaques, these data provide the first direct anatomical evidence for its existence.

AUTHOR CONTRIBUTIONS

CE, PF, RS and LM performed experiments, edited the figures and wrote and edited the manuscript. CE analyzed the data and created the figures.

FUNDING

This work was supported by National Institute of Mental Health R01 MH099505 (LM), National Center for Advancing Translational Sciences KL2 TR001432 (PF) National Institute of Neurological Disorders and Stroke. PF was supported by National Institute of Neurological Disorders and Stroke R01 NS097762. CE was supported by T32 NS041231.

ACKNOWLEDGEMENTS

We thank Brittany Aguilar, Elyssa LaFlamme, Evan Wicker and Hannah Waguespack for technical support.

REFERENCES

Aggleton, J. P., Burton, M. J., and Passingham, R. E. (1980). Cortical and subcortical afferents to the amygdala of the rhesus monkey *(Macaca mulatta)*. *Brain Res.* 190, 347–368. doi: 10.1016/0006-8993(80)90279-6

Almeida, I., Soares, S. C., and Castelo-Branco, M. (2015). The distinct role of the amygdala, superior colliculus and pulvinar in processing of central and peripheral snakes. *PLoS One* 10:e0141175. doi: 10.1371/journal.pone.0141175

Amaral, D. G., Price, J. L., Pitkanen, A., and Carmichael, T. (1992). "Anatomical organization of the primate amygdaloid complex," in *The Amygdala: Neurobiological Aspects of Emotion, Memory and Mental Dysfunction*, ed. J. Aggleton (New York, NY: Wiley-Liss), 1–66.

Benevento, L. A., and Fallon, J. H. (1975). The ascending projections of the superior colliculus in the rhesus monkey *(Macaca mulatta)*. *J. Comp. Neurol.* 160, 339–361. doi: 10.1002/cne.901600306

Benevento, L. A., and Standage, G. P. (1983). The organization of projections of the retinorecipient and nonretinorecipient nuclei of the pretectal complex and

layers of the superior colliculus to the lateral pulvinar and medial pulvinar in the macaque monkey. *J. Comp. Neurol.* 217, 307–336. doi: 10.1002/cne.902170307

Born, R. T., and Bradley, D. C. (2005). Structure and function of visual area MT. *Annu. Rev. Neurosci.* 28, 157–189. doi: 10.1146/annurev.neuro.26.041002.131052

Brandão, M. L., Cardoso, S. H., Melo, L. L., Motta, V., and Coimbra, N. C. (1994). Neural substrate of defensive behavior in the midbrain tectum. *Neurosci. Biobehav. Rev.* 18, 339–346. doi: 10.1016/0149-7634(94)90047-7

Burton, H., and Jones, E. G. (1976). The posterior thalamic region and its cortical projection in new world and old world monkeys. *J. Comp. Neurol.* 168, 249–301. doi: 10.1002/cne.901680204

Chomsung, R. D., Petry, H. M., and Bickford, M. E. (2008). Ultrastructural examination of diffuse and specific tectopulvinar projections in the tree shrew. *J. Comp. Neurol.* 510, 24–46. doi: 10.1002/cne.21763

Cowey, A., and Stoerig, P. (1991). The neurobiology of blindsight. *Trends Neurosci.* 14, 140–145. doi: 10.1016/0166-2236(91)90085-9

Day-Brown, J. D., Wei, H., Chomsung, R. D., Petry, H. M., and Bickford, M. E. (2010). Pulvinar projections to the striatum and amygdala in the tree shrew. *Front. Neuroanat.* 4:143. doi: 10.3389/fnana.2010.00143

de Gelder, B., Vroomen, J., Pourtois, G., and Weiskrantz, L. (1999). Non-conscious recognition of affect in the absence of striate cortex. *Neuroreport* 10, 3759–3763. doi: 10.1097/00001756-199912160-00007

Dean, P., Redgrave, P., and Westby, G. W. M. (1989). Event or emergency? Two response systems in the mammalian superior colliculus. *Trends Neurosci.* 12, 137–147. doi: 10.1016/0166-2236(89)90052-0

DesJardin, J. T., Holmes, A. L., Forcelli, P. A., Cole, C. E., Gale, J. T., Wellman, L. L., et al. (2013). Defense-like behaviors evoked by pharmacological disinhibition of the superior colliculus in the primate. *J. Neurosci.* 33, 150–155. doi: 10.1523/jneurosci.2924-12.2013

Doron, N. N., and LeDoux, J. E. (1999). Organization of projections to the lateral amygdala from auditory and visual areas of thalamus in the rat. *J. Comp. Neurol.* 409, 383–409. doi: 10.1002/(sici)1096-9861(19990927)412:3<383::aid-cne2>3.0.co;2-5

Forcelli, P. A., DesJardin, J. T., West, E. A., Holmes, A. L., Elorette, C., Wellman, L. L., et al. (2016). Amygdala selectively modulates defensive responses evoked from the superior colliculus in non-human primates. *Soc. Cogn. Affect. Neurosci.* 11, 2009–2019. doi: 10.1093/scan/nsw111

Gattass, R., Soares, J. G., and Lima, B. (2018). "Connectivity of the pulvinar," in *The Pulvinar Thalamic Nucleus of Non-Human Primates: Architectonic and Functional Subdivisions*, ed. H. W. Korf (Frankfurt: Springer), 19–29.

Gutierrez, C., Yaun, A., and Cusick, C. G. (1995). Neurochemical subdivisions of the inferior pulvinar in macaque monkeys. *J. Comp. Neurol.* 363, 545–562. doi: 10.1002/cne.903630404

Harting, J. K., Hall, W. C., and Diamond, I. T. (1972). Evolution of the pulvinar. *Brain Behav. Evol.* 6, 424–452. doi: 10.1159/000123767

Hofbauer, A., and Dräger, U. C. (1985). Depth segregation of retinal ganglion cells projecting to mouse superior colliculus. *J. Comp. Neurol.* 234, 465–474. doi: 10.1002/cne.902340405

Huerta, M. F., and Harting, J. K. (1983). Sublamination within the superficial gray layer of the squirrel monkey: an analysis of the tectopulvinar projection using anterograde and retrograde transport methods. *Brain Res.* 261, 119–126. doi: 10.1016/0006-8993(83)91290-8

Humphrey, N. K., and Weiskrantz, L. (1967). Vision in monkeys after removal of the striate cortex. *Nature* 215, 595–597. doi: 10.1038/215595a0

Jones, E. G., and Burton, H. (1976). A projection from the medial pulvinar to the amygdala in primates. *Brain Res.* 104, 142–147. doi: 10.1016/0006-8993(76)90654-5

Kato, R., Takaura, K., Ikeda, T., Yoshida, M., and Isa, T. (2011). Contribution of the retino-tectal pathway to visually guided saccades after lesion of the primary visual cortex in monkeys. *Eur. J.Neurosci.* 33, 1952–1960. doi: 10.1111/j.1460-9568.2011.07729.x

Koller, K., Rafal, R. D., Platt, A., and Mitchell, N. D. (2018). Orienting toward threat: contributions of a subcortical pathway transmitting retinal afferents to the amygdala via the superior colliculus and pulvinar. *Neuropsychologia* doi: 10.1016/j.neuropsychologia.2018.01.027 [Epub ahead of print].

Le, Q. V., Isbell, L. A., Matsumoto, J., Le, V. Q., Nishimaru, H., Hori, E., et al. (2016). Snakes elicit earlier and monkey faces, later, gamma oscillations in macaque pulvinar neurons. *Sci. Rep.* 6:20595. doi: 10.1038/srep20595

Le, Q. V., Isbell, L. A., Matsumoto, J., Le, V. Q., Hori, E., Maior, R. S., et al. (2014). Monkey pulvinar neurons fire differentially to snake postures. *PLoS One* 9:e114258. doi: 10.1371/journal.pone.0114258

LeDoux, J. E. (1996). *The Emotional Brain: the Mysterious Underpinnings of Emotional Life.* (New York, NY: Simon and Schuster).

Liddell, B. J., Brown, K. J., Kemp, A. H., Barton, M. J., Das, P., Peduto, A., et al. (2005). A direct brainstem-amygdala-cortical "alarm" system for subliminal signals of fear. *Neuroimage* 24, 235–243. doi: 10.1016/j.neuroimage.2004.08.016

Linke, R., De Lima, A. D., Schwegler, H., and Pape, H.-C. (1999). Direct synaptic connections of axons from superior colliculus with identified thalamo-amygdaloid projection neurons in the rat: possible substrates of a subcortical visual pathway to the amygdala. *J. Comp. Neurol.* 403, 158–170. doi: 10.1002/(sici)1096-9861(19990111)403:2<158::aid-cne2>3.0.co;2-6

Locke, S. (1960). The projection of the medial pulvinar of the macaque. *J. Comp. Neurol.* 115, 155–169. doi: 10.1002/cne.901150205

May, P. J. (2006). The mammalian superior colliculus: laminar structure and connections. *Prog. Brain Res.* 151, 321–378. doi: 10.1016/s0079-6123(05)51011-2

Miller, M., Pasik, P., and Pasik, T. (1980). Extrageniculostriate vision in the monkey: VII. Contrast sensitivity functions. *J. Neurophysiol.* 43, 1510–1526. doi: 10.1152/jn.1980.43.6.1510

Mohler, C. W., and Wurtz, R. H. (1977). Role of striate cortex and superior colliculus in visual guidance of saccadic eye movements in monkeys. *J. Neurophysiol.* 40, 74–94. doi: 10.1152/jn.1977.40.1.74

Morris, J. S., De Gelder, B., Weiskrantz, L., and Dolan, R. J. (2001). Differential extrageniculostriate and amygdala responses to presentation of emotional faces in a cortically blind field. *Brain* 124, 1241–1252. doi: 10.1093/brain/124.6.1241

Morris, J. S., Ohman, A., and Dolan, R. J. (1999). A subcortical pathway to the right amygdala mediating "unseen" fear. *Proc. Natl. Acad. Sci. U S A* 96, 1680–1685. doi: 10.1073/pnas.96.4.1680

Norita, M., and Kawamura, K. (1980). Subcortical afferents to the monkey amygdala: an HRP study. *Brain Res.* 190, 225–230. doi: 10.1016/0006-8993(80)91171-3

Olszewski, J. (1952). *The Thalamus of the Macaca Mulatta: An Atlas for Use With the Stereotaxic Instrument.* Basel and New York: Karger.

Perry, V. H., and Cowey, A. (1984). Retinal ganglion cells that project to the superior colliculus and pretectum in the macaque monkey. *Neuroscience* 12, 1125–1137. doi: 10.1016/0306-4522(84)90007-1

Pöppel, E., Held, R., and Frost, D. (1973). Residual visual function after brain wounds involving the central visual pathways in man. *Nature* 243, 295–296. doi: 10.1038/243295a0

Rafal, R. D., Koller, K., Bultitude, J. H., Mullins, P., Ward, R., Mitchell, A. S., et al. (2015). Connectivity between the superior colliculus and the amygdala in humans and macaque monkeys: virtual dissection with probabilistic DTI tractography. *J. Neurophysiol.* 114, 1947–1962. doi: 10.1152/jn.01016.2014

Richards, W. (1973). Visual processing in scotomata. *Exp. Brain Res.* 17, 333–347. doi: 10.1007/bf00234098

Romanski, L. M., Giguere, M., Bates, J. F., and Goldman-Rakic, P. S. (1997). Topographic organization of medial pulvinar connections with the prefrontal cortex in the rhesus monkey. *J. Comp. Neurol.* 379, 313–332. doi: 10.1002/(sici)1096-9861(19970317)379:3<313::aid-cne1>3.0.co;2-6

Rosene, D. L., Roy, N. J., and Davis, B. J. (1986). A cryoprotection method that facilitates cutting frozen sections of whole monkey brains for histological and histochemical processing without freezing artifact. *J. Histochem. Cytochem.* 34, 1301–1315. doi: 10.1177/34.10.3745909

Sahraie, A., Weiskrantz, L., and Barbur, J. L. (1998). Awareness and confidence ratings in motion perception without geniculo-striate projection. *Behav. Brain Res.* 96, 71–77. doi: 10.1016/s0166-4328(97)00194-0

Sanders, M. D., Warrington, E., Marshall, J., and Wieskrantz, L. (1974). "Blindsight" vision in a field defect. *Lancet* 303, 707–708. doi: 10.1016/s0140-6736(74)92907-9

Saunders, R. C., Aigner, T. G., and Frank, J. A. (1990). Magnetic resonance imaging of the rhesus monkey brain: use for stereotactic neurosurgery. *Exp. Brain Res.* 81, 443–446. doi: 10.1007/bf00228139

Schmid, M. C., Mrowka, S. W., Turchi, J., Saunders, R. C., Peters, A. J., Ye, F. Q., et al. (2010). Blindsight depends on the lateral geniculate nucleus. *Nature* 466, 373–377. doi: 10.1038/nature09179

Schmid, M. C., Panagiotaropoulos, T., Augath, M. A., Logothetis, N. K., and Smirnakis, S. M. (2009). Visually driven activation in macaque areas V2 and V3 without input from the primary visual cortex. *PLoS One* 4:e5527. doi: 10.1371/journal.pone.0005527

Schneider, G. E. (1969). Two visual systems. *Science* 163, 895–902. doi: 10.1126/science.163.3870.895

Silverstein, D. N., and Ingvar, M. (2015). A multi-pathway hypothesis for human visual fear signaling. *Front. Syst. Neurosci.* 9:101. doi: 10.3389/fnsys.2015.00101

Soares, S. C., Maior, R. S., Isbell, L. A., Tomaz, C., and Nishijo, H. (2017). Fast detector/first responder: interactions between the superior colliculus-pulvinar pathway and stimuli relevant to primates. *Front. Neurosci.* 11:67. doi: 10.3389/fnins.2017.00067

Solomon, S. J., Pasik, T., and Pasik, P. (1981). Extrageniculostriate vision in the monkey. VIII. Critical structures for spatial localization. *Exp. Brain Res.* 44, 259–270. doi: 10.1007/bf00236563

Stefanacci, L., and Amaral, D. G. (2000). Topographic organization of cortical inputs to the lateral nucleus of the macaque monkey amygdala: a retrograde tracing study. *J. Comp. Neurol.* 421, 52–79. doi: 10.1002/(sici)1096-9861(20000522)421:1<52::aid-cne4>3.0.co;2-o

Stein, B. E., Stanford, T. R., and Rowland, B. A. (2009). The neural basis of multisensory integration in the midbrain: its organization and maturation. *Hear. Res.* 258, 4–15. doi: 10.1016/j.heares.2009.03.012

Stepniewska, I., Qi, H.-X., and Kaas, J. H. (2000). Projections of the superior colliculus to subdivisions of the inferior pulvinar in new world and old world monkeys. *Vis. Neurosci.* 17, 529–549. doi: 10.1017/s0952523800174048

Takakuwa, N., Kato, R., Redgrave, P., and Isa, T. (2017). Emergence of visually-evoked reward expectation signals in dopamine neurons via the superior colliculus in V1 lesioned monkeys. *Elife* 6:e24459. doi: 10.7554/elife.24459

Tamietto, M., Pullens, P., De Gelder, B., Weiskrantz, L., and Goebel, R. (2012). Subcortical connections to human amygdala and changes following destruction of the visual cortex. *Curr. Biol.* 22, 1449–1455. doi: 10.1016/j.cub.2012.06.006

Taylor, A. M., Jeffery, G., and Lieberman, A. R. (1986). Subcortical afferent and efferent connections of the superior colliculus in the rat and comparisons between albino and pigmented strains. *Exp. Brain Res.* 62, 131–142. doi: 10.1007/bf00237409

Trojanowski, J. Q., and Jacobson, S. (1975). Peroxidase labeled subcortical afferents to pulvinar in rhesus monkey. *Brain Res.* 97, 144–150. doi: 10.1016/0006-8993(75)90922-1

Van Le, Q., Isbell, L. A., Matsumoto, J., Nguyen, M., Hori, E., Maior, R. S., et al. (2013). Pulvinar neurons reveal neurobiological evidence of past selection for rapid detection of snakes. *Proc. Natl. Acad. Sci. U S A* 110, 19000–19005. doi: 10.1073/pnas.1312648110

Vuilleumier, P., Armony, J. L., Clarke, K., Husain, M., Driver, J., and Dolan, R. J. (2002). Neural response to emotional faces with and without awareness: event-related fMRI in a parietal patient with visual extinction and spatial neglect. *Neuropsychologia* 40, 2156–2166. doi: 10.1016/s0028-3932(02)00045-3

Ward, R., Danziger, S., and Bamford, S. (2005). Response to visual threat following damage to the pulvinar. *Curr. Biol.* 15, 571–573. doi: 10.1016/j.cub.2005.01.056

Warner, C. E., Goldschmidt, Y., and Bourne, J. A. (2010). Retinal afferents synapse with relay cells targeting the middle temporal area in the pulvinar and lateral geniculate nuclei. *Front. Neuroanat.* 4:8. doi: 10.3389/neuro.05.008.2010

Wei, P., Liu, N., Zhang, Z., Liu, X., Tang, Y., He, X., et al. (2015). Processing of visually evoked innate fear by a non-canonical thalamic pathway. *Nat. Commun.* 6:6756. doi: 10.1038/ncomms7756

Weiskrantz, L. (1963). Contour discrimination in a young monkey with striate cortex ablation. *Neuropsychologia* 1, 145–164. doi: 10.1016/0028-3932(63)90004-6

Weiskrantz, L., Warrington, E. K., Sanders, M. D., and Marshall, J. (1974). Visual capacity in the hemianopic field following a restricted occipital ablation. *Brain* 97, 709–728. doi: 10.1093/brain/97.4.709

Wellman, L. L., Gale, K., and Malkova, L. (2005). GABAA-mediated inhibition of basolateral amygdala blocks reward devaluation in macaques. *J. Neurosci.* 25, 4577–4586. doi: 10.1523/jneurosci.2257-04.2005

Whalen, P. J., Rauch, S. L., Etcoff, N. L., Mcinerney, S. C., Lee, M. B., and Jenike, M. A. (1998). Masked presentations of emotional facial expressions modulate amygdala activity without explicit knowledge. *J. Neurosci.* 18, 411–418. doi: 10.1523/jneurosci.18-01-00411.1998

Zhou, N. A., Maire, P. S., Masterson, S. P., and Bickford, M. E. (2017). The mouse pulvinar nucleus: organization of the tectorecipient zones. *Vis. Neurosci.* 34:E011. doi: 10.1017/s0952523817000050

Zhou, N., Masterson, S. P., Damron, J. K., Guido, W., and Bickford, M. E. (2018). The mouse pulvinar nucleus links the lateral extrastriate cortex, striatum and amygdala. *J. Neurosci.* 38, 347–362. doi: 10.1523/jneurosci.1279-17.2017

Conflict of Interest Statement: The authors declare that the research was conducted in the absence of any commercial or financial relationships that could be construed as a potential conflict of interest.

frontiers in Neural Circuits

ORIGINAL RESEARCH
published: 22 October 2018
doi: 10.3389/fncir.2018.00074

The Influence of a Memory Delay on Spatial Coding in the Superior Colliculus: Is Visual Always Visual and Motor Always Motor?

Morteza Sadeh[1,2,3,4,5], *Amirsaman Sajad*[1,3,4,5], *Hongying Wang*[1,2], *Xiaogang Yan*[1,2] *and John Douglas Crawford*[1,2,3,4,5]*

[1]York Centre for Vision Research, York University, Toronto, ON, Canada, [2]Vision: Science to Applications (VISTA) Program, York University, Toronto, ON, Canada, [3]York Neuroscience Graduate Diploma Program, York University, Toronto, ON, Canada, [4]Canadian Action and Perception Network (CAPnet), York University, Toronto, ON, Canada, [5]Departments of Psychology, Biology and Kinesiology and Health Science, York University, Toronto, ON, Canada

The memory-delay saccade task is often used to separate visual and motor responses in oculomotor structures such as the superior colliculus (SC), with the assumption that these same responses would sum with a short delay during immediate "reactive" saccades to visual stimuli. However, it is also possible that additional signals (suppression, delay) alter visual and/or motor response in the memory delay task. Here, we compared the spatiotemporal properties of visual and motor responses of the *same* SC neurons recorded during both the reactive and memory-delay tasks in two head-unrestrained monkeys. Comparing tasks, visual (aligned with target onset) and motor (aligned on saccade onset) responses were highly correlated across neurons, but the peak response of visual neurons and peak motor responses (of both visuomotor (VM) and motor neurons) were significantly higher in the reactive task. Receptive field organization was generally similar in both tasks. Spatial coding (along a Target-Gaze (TG) continuum) was also similar, with the exception that pure motor cells showed a stronger tendency to code future gaze location in the memory delay task, suggesting a more complete transformation. These results suggest that the introduction of a trained memory delay alters both the vigor and spatial coding of SC visual and motor responses, likely due to a combination of saccade suppression signals and greater signal noise accumulation during the delay in the memory delay task.

Keywords: superior colliculi, saccades, primates, memory, gaze shift

OPEN ACCESS

Edited by:
Tadashi Isa,
Kyoto University, Japan

Reviewed by:
Rossella Breveglieri,
Università degli Studi di Bologna, Italy
Mingsha Zhang,
Beijing Normal University, China

***Correspondence:**
John Douglas Crawford
jdc@yorku.ca

Received: *06 May 2018*
Accepted: *29 August 2018*
Published: *22 October 2018*

Citation:
Sadeh M, Sajad A, Wang H, Yan X and Crawford JD (2018) The Influence of a Memory Delay on Spatial Coding in the Superior Colliculus: Is Visual Always Visual and Motor Always Motor? Front. Neural Circuits 12:74. doi: 10.3389/fncir.2018.00074

INTRODUCTION

The primate superior colliculus (SC) has been studied extensively both for its specific role in generating saccades and head-unrestrained gaze shifts, and as a general model for sensory-motor transformations (Mays and Sparks, 1980; Wurtz and Albano, 1980; Optican, 1995; Marino et al., 2008; Sadeh et al., 2015). One defining characteristic of the SC is that its neurons can be categorized into populations with only "visual" responses (briefly delayed burst responses to a visual stimulus), only "motor" responses (burst activity just before and after a saccade) or visuomotor (VM) responses, i.e., both visual and motor (Wurtz and Goldberg, 1972a,b;

Sparks, 1978; Harris, 1980; Wurtz and Albano, 1980; Bruce and Goldberg, 1985; Bruce et al., 1985; Munoz and Wurtz, 1995a,b; Stricanne et al., 1996; Freedman and Sparks, 1997a; Gandhi and Katnani, 2011; Bremmer et al., 2016). Implicit in this categorization is the assumption that these responses are task-independent, but this is not necessarily the case. Here, we specifically examined whether the task typically used to separate these cell types might itself influence their neural code, and conversely, whether these responses code something different in simpler gaze saccades.

The typical way to separate visual and motor responses is to introduce a memory delay between a transient visual stimulus and the gaze saccade (Wurtz and Goldberg, 1972a; Sparks, 1978; Wurtz and Albano, 1980; Sparks and Hartwich-Young, 1989; Stanford and Sparks, 1994; Munoz and Wurtz, 1995a,b; Sajad et al., 2015). Delays of 500–1500 ms provide a clean temporal segregation between the visual response and/or motor response. The addition of a spatial separation between the visual stimulus and the saccade vector across the memory delay (e.g., using a double step saccade task or the anti-saccades task) likewise separate the spatial tuning of visual and motor responses (Everling and Munoz, 2000; Munoz and Everling, 2004) More recently, we have shown that even in the absence of these spatial manipulations, the SC visual response encodes target location relative to initial eye orientation whereas after a memory delay the motor response encodes future gaze direction relative to current eye orientation (Sadeh et al., 2015).

Saccades made immediately and directly to a transient visual stimulus, without a memory delay, are called "reactive saccades" (Sparks, 1978; Pierrot-Deseilligny et al., 1991a; Deubel, 1995; Munoz and Wurtz, 1995a,b). During such saccades there is typically a 25–50 ms peak-to-peak delay between visual and motor responses, although this is prolonged during head unrestrained gaze shifts (Freedman, 2008; DeSouza et al., 2011; Sadeh et al., 2018). In either case, there is significant temporal overlap between these responses. As a result, VM cells often show a continuous burst, but often with a slight inflection between peaks that correspond in time to the visual and motor burst (Sparks, 1978; Munoz and Wurtz, 1995a,b; Dorris et al., 1997; DeSouza et al., 2011). Often, investigators use such inflections to arbitrarily draw a "line" between visual and motor responses, knowing very well that they might actually blend into each other (Mays and Sparks, 1980; Everling et al., 1999; Marino et al., 2008, 2015; DeSouza et al., 2011; Sadeh et al., 2015). It is generally assumed that these responses summate linearly in reactive saccades. This assumption seems to be supported by our recent finding that during reactive saccades, SC cells show a transition from target coding in their visual response to gaze coding in their motor responses (Sadeh et al., 2018) similar to that observed previously after a memory delay (Sadeh et al., 2015). However, in the absence of a direct comparison, it cannot be assumed that the spatial codes of SC visual and motor responses are quantitatively identical both with and without a memory delay.

First, the temporal overlap between visual and motor signals in VM cells might influence their respective codes. For example, VM cells showed a progressive transition between intermediate target-gaze codes during both reactive and memory delay saccades, but with very different time courses (Sadeh et al., 2015, 2018). This could lead to greater overlap in VM cell codes in the reactive task. Conversely, the addition of a memory delay likely introduces additional signals that could influence spatial codes. These include saccade suppression signals that could influence the vigor of both visual and motor responses (Thiele et al., 2002; Munoz and Everling, 2004), and memory delay/motor build up activity that might specifically influence the final motor response (Munoz and Wurtz, 1995a,b; Miller et al., 1996; Pesaran et al., 2002; Sajad et al., 2016a,b). In the past it was not possible to test all of these predictions, because the technology was lacking to probe specific VM codes in the absence of additional spatial manipulations.

In the current study, we investigated if the visual and motor responses observed in reactive saccades altered, either in amplitude or spatial content, by the insertion of a memory delay. To do this, we recorded from the same SC neurons using both the reactive and memory delay tasks, and analyzed and directly compared their firing rates and spatial content. We did this using an analytic approach based on variable gaze errors that allowed us to fit activity from specific visual and motor response epochs against models along a visual-motor continuum (Keith and Crawford, 2008; DeSouza et al., 2011; Sadeh et al., 2015; Sajad et al., 2015). This was done in head unrestrained animals because this reflects a more natural behavioral condition, allowed us to eliminate some other models in our initial analysis (Sadeh et al., 2015), and in this specific case provided more prolonged and temporally rich response profiles for our analysis. We found that, although certain fundamental aspects are retained in visual and motor responses (such as the preference for target vs. gaze coding) the addition of a memory delay does introduce subtle alterations to the amplitudes and spatial codes of SC signals, particularly in the motor responses, which may influence behavior.

MATERIALS AND METHODS

Animals and Surgical Procedures

The data were collected from two female monkeys (Macaca Mulatta, M1 and M2; age, 10 years; weights, 6.5 and 7 kg) with a protocol approved by the York University Animal Care Committee in accordance with guidelines published by the Canadian Council for Animal Care. With similar surgical procedures as described previously (Crawford et al., 1999; Klier et al., 2001), the monkeys were prepared for long-term electrophysiology and 3D gaze movement recordings. Each monkey was subjected to general anesthesia with 1%–2% isoflurane after intramuscular injection of ketamine hydrochloride (10 mg/kg), atropine sulfate (0.05 mg/kg) and acepromazine (0.5 mg/kg). To minimize the collisions between experimental setup and Microdrive/electrode we implanted a vertically aligned unit recording chamber (i.e., with no tilt) placed 5 mm anterior and 0 mm lateral in stereotaxic coordinates, which allowed access to the left and right SC. This chamber angle

and position were chosen to minimize collisions between the electrode/microdrive and the experimental setup during head movements, and to simplify the use of stereotaxic coordinates during recordings. The chamber was then surrounded by a dental acrylic cap, which was anchored to the skull with 13 stainless steel cortex screws. Two scleral search coils (diameter, 5 mm) were implanted in one eye of the monkeys to record 3D eye movements. Two orthogonal coils, which were secured with a screw on a plastic base on the cap, recorded the 3D head movements during the experiments. 3D recordings and analysis were performed as described previously (Crawford et al., 1999; DeSouza et al., 2011).

Experimental Equipment

We used a Pentium IV PC and custom-designed software to present stimuli, control behavior paradigms, send digital codes to a Plexon data acquisition system, and deliver juice rewards to the monkeys. Stimuli were presented on a screen 60 cm in front of the monkey, by use of a projector (WT600 DLP projector; NEC). Monkeys were seated on a custom-designed primate chair in order to have their heads move freely at the center of a 1-m^3 magnetic field generator (Crawford et al., 1999) and a juice spout (Crist Instruments) was placed on the skull cap for computer-controlled delivery of the juice reward to the monkey's mouth.

Behavioral Recordings ad Paradigms

All experiments were performed using 3D recordings in head-unrestrained conditions (Crawford et al., 1999; Sadeh et al., 2015). Head motion was not analyzed in the current experiment, but provided some advantages: for comfort, natural system behavior, adequate range of gaze motion for testing large neural response fields (RF; see below). Conversely, 3D recordings and analysis were required, to account for the significant torsional eye rotation and prominent non-linearities that occur in the head unrestrained gaze range (Tweed and Vilis, 1990; Crawford et al., 1999; Klier et al., 2001; Keith et al., 2009; DeSouza et al., 2011). The target-relative-to-eye (Te) and gaze-relative-to-eye (Ge) models tested in this study were computed by rotating (not subtracting) a vector pointing from the eye toward the target or future gaze position by the inverse of initial 3D eye orientation (Klier et al., 2002).

All neurons described in the current study were tested in both of the following two paradigms.

Reactive Task (Figures 1A,C)

Animals were trained to fixate a central range of positions for 900–1000 ms (randomly varied interval). A tolerance window of 2–4° (radius) with respect to the fixation position was required during this period. Simultaneous with initial fixation point disappearance-serving as GO signal—a target (red circle with a size of 0.5°) was presented in the periphery for 125 ms, at locations selected for RF mapping (**Figure 1C**; see below for details). Note that the reason is that we aimed to control initial gaze to separate gaze-centered vs. space-centered responses, therefore we allowed the animal to produce variable final gaze errors in order to separate the T and G models as described in the current analysis. The initial fixation range is not a tolerance window; it is basically a range of an area which possible initial fixation positions (i.e., green circles) may appear in a random fashion. Animals were then required to make a gaze shift toward the briefly flashing stimulus and fixate on it for 200 ms in order to receive juice reward. In order to spatially separate targets vs. gaze coding, we designated a relatively wide tolerance window of 6–12° (diameter) for gaze errors around the locations of the targets, and thus allowed monkeys to produce a self-selected distribution of gaze end point errors around the targets. Also, every trial was inspected, and any trial in which the gaze shift was anticipated (reaction time of <100 ms after the go signal) was excluded from the analysis (see **Figures 1A,C,D**).

A total of 13,068 trials were completed in each of the tasks, of these 1,555 trials (11.9%) were excluded -based on the exclusion criteria explained above-in the reactive task and 1,921 (14.7) were excluded in the MD task.

Memory Delay Task (Figure 1B)

The conditions, fixation point and stimulus characteristics in this task were identical to the reactive task except that after 300 ms of fixation, a target stimulus appeared in the periphery for 125 ms. The fixation light remained on for another 400–700 ms in order to introduce a variable memory delay and discourage anticipation of the go signal. In addition, every trial was inspected, and any trial in which the gaze shift was anticipated (reaction time of <100 ms after the go signal) was excluded from the analysis. When the GO signal was presented, the monkeys made a gaze shift towards the remembered location of the target, and were required to maintain fixation for at least 200 ms at that final position to obtain the juice reward.

Data from these two tasks were described previously (Sadeh et al., 2015, Sadeh et al., submitted), but this is the first time that we provide a direct quantitative comparison.

Off-Line Trial Definition and Inclusion Criteria

During our off-line analysis the beginning of a trial was defined by the appearance of the initial fixation point. The beginning of the gaze saccade was defined as the instant when its velocity exceeded 50°/s, and its end when its velocity decreased to 30°/s. All trials were considered for analysis irrespective of whether the monkey received a reward after the trial. We excluded trials based on spatial and temporal criteria. First, trials in which the directions of the gaze shifts were completely unrelated to the direction of the target (e.g., opposite direction) were removed. Then, we obtained the regression between errors in gaze vs. retinal error (the retinal angle between the fovea and the target at the initial position before the gaze shift), and removed trials with gaze error two standard deviations greater than this regression line. Furthermore, every trial was visually inspected, and any trial in which the gaze shift was anticipated (reaction time of <100 ms after the go signal) and when the gaze shift consisted of multistep saccades was excluded from the analyses described below.

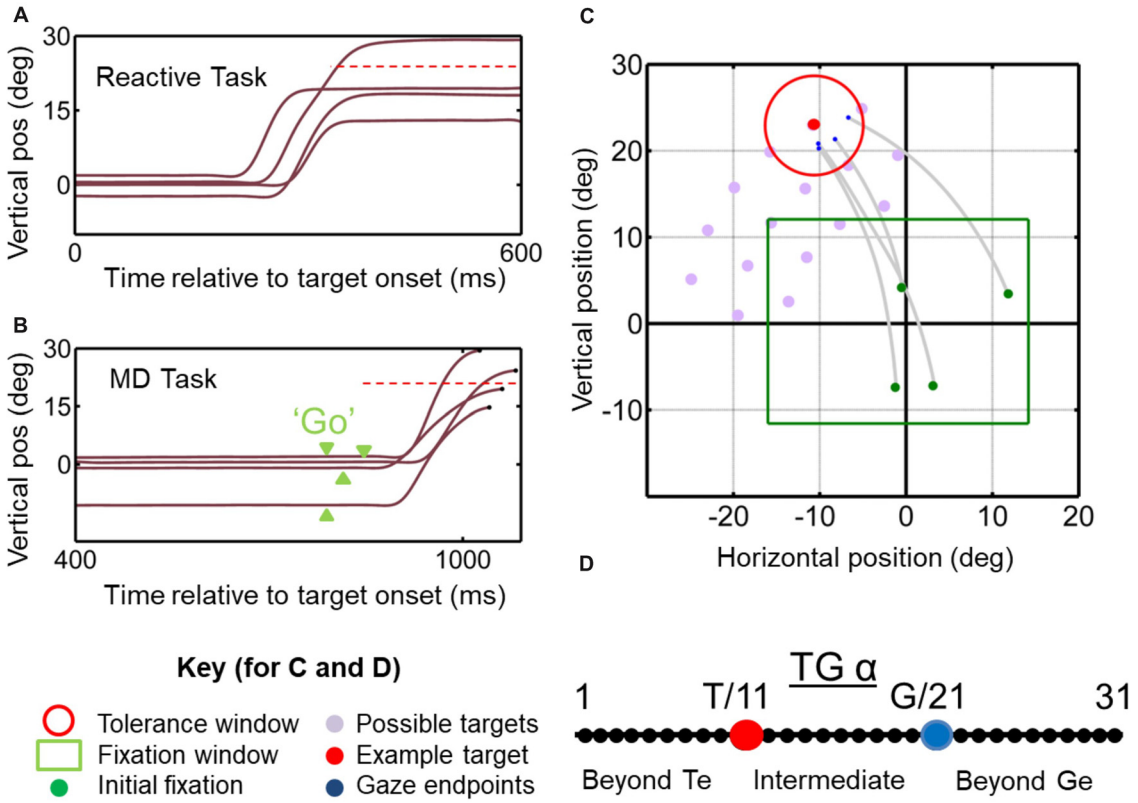

FIGURE 1 | Temporal **(A,B)** and spatial **(C,D)** aspects of the behavioral tasks. **(A)** Vertical gaze position toward an upward target (dashed red horizontal line) plotted as a function of time for example trials in the *reactive task*. Results from this task are reported in Sadeh et al. (2018). **(B)** Similar gaze traces for the same target, but obtained from the *memory delay task*. Note that the memory delay is variable, so the "go" signal (extinction of the fixation point) occurred at different time points (green arrow heads). Results from this task were reported in detail previously (Sadeh et al., 2015). **(C)** Two-dimensional gaze trajectories (gray lines) from the *reactive task* for an example target in monkey M2. Also shown are the range of initial fixation positions (green square), the tolerance window (red circle) and the other possible targets used in this experimental session (gray circles) to map a neuron's receptive field. The identical spatial layouts were used for both tasks to test each neuron. **(D)** Target-Gaze (TG) continuum constructed between and beyond target position (red dot) and gaze end point (blue dot) for each trial, and used to determine best fits for neural receptive fields.

Neural Recordings and Receptive Field Mapping

We recorded extracellular activity from the left and right SC with tungsten microelectrodes (FHC). The electrode was inserted through a guide tube, which was controlled by a hydraulic microdrive (MO-90S; Narishige International, East Meadow, NY, USA). Isolated signals were amplified, filtered and stored for off-line sorting with the Plexon MAP system. The SC was identified according to criteria published previously (DeSouza et al., 2011; Sadeh et al., 2015). The steps of SC identification and confirmation are identical to those explained previously (Sadeh et al., 2015). Once an SC neuron was isolated, the target stimuli were presented in the visual field contralateral to the hemi field of the recording site to begin RF mapping. RFs were estimated through initial mapping, which involved monkeys performing visually guided saccades to a wide range of stimuli presented on the screen while cell activity was monitored on-line. Test stimuli were then selected within a grid (12–32 targets, depending on the RF size) that extended just beyond the cell's receptive field. **Figure 1C** illustrates spatial the array of target used for one particular cell in the reactive task. During testing, stimuli were presented in a randomized order, and each target was presented for at least seven gaze shifts. The *MD* task was done first in all experiment sessions in order to separate the visual and motor bursts and characterize the neuron type, the behavioral task that ran afterwards were randomized for each given experiment session.

Neuron Classification

The memory delay saccade task was used to dissociate between visual and movement related activities and categorize cells into visual, visuomotor (VM) and motor neurons. Visual neurons were defined as cells that showed a robust burst of activity (>50 spikes/s above the baseline) 40–60 ms after the stimulus presentation that lasted for ∼180 ms afterwards (Goldberg and Wurtz, 1972). Motor neurons were those with robust activity or a buildup of activity peaking around the time of gaze onset, with activity starting prior to the gaze onset (100–40 ms before

saccade), and that continued to ∼100 ms after gaze onset. Neurons that met both of these criteria were classified as VM. When we refer to "number of spikes" below, this refers to number of action potentials in these defined temporal windows, also we use neural activity and burst interchangeably to refer to the same concept of action potentials.

Temporal Windows for Neural Analysis

The temporal windows that we used for analysis of bursting activity are illustrated in the results section (**Figure 2**). Although we observed a variable range of burst onset for visual activities which reflects different subtypes of visual and VM neuron with inputs from different brain areas, we used a fixed window of +60 to +160 ms relative to visual target presentation for visual activity based on both the visual inspection of spike density plots as well as an objective approach explained here. A time window of ±50 ms relative to saccade onset was considered for the motor activity. The fixed time windows are marked by black dashed vertical lines on **Figures 3**, **5**, **6**.

To use an objective method of determining and comparing the onset of visual bursts in each task, we used a method developed and reported by Legéndy and Salcman (1985) and applied to neural recording data for identifying burst onset by Hanes et al. (1995) as well as Thompson et al. (1996). Briefly this approach assumes that spike activity behaves in a Poisson manner (which is now generally accepted) and for every trial calculates the periods of spiking activity in which the spikes are too close in time, surpassing that described by chance levels (referred to as "surprise"). We calculated all bursts in the entire

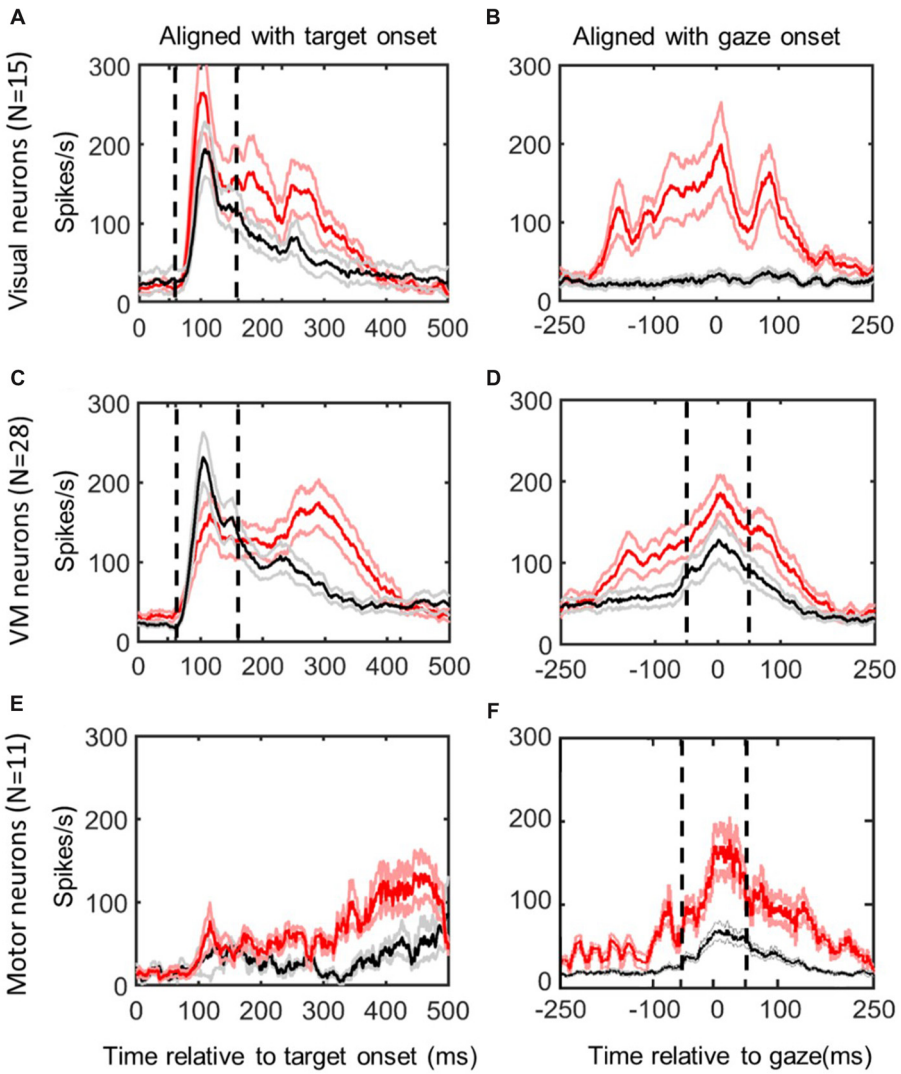

FIGURE 2 | Mean spike density plots/10% confidence intervals from the same neurons in *reactive task* (red/pink) vs. the memory delay task (black/gray). Data aligned with stimulus onset (left column) and gaze movement (right column). *Top row* **(A,B)**: visual neurons, *N* = 15; *middle row* **(C,D)**: visuomotor (VM) neurons (*N* = 28); bottom row **(E,F)**: motor neurons (*N* = 11), identified using the memory delay task (Sadeh et al., 2015). Dashed vertical lines indicate the time intervals used for the "fixed window" visual (60–160 ms relative to target presentation) and motor (−50 to +50 ms relative to gaze onset) analyses.

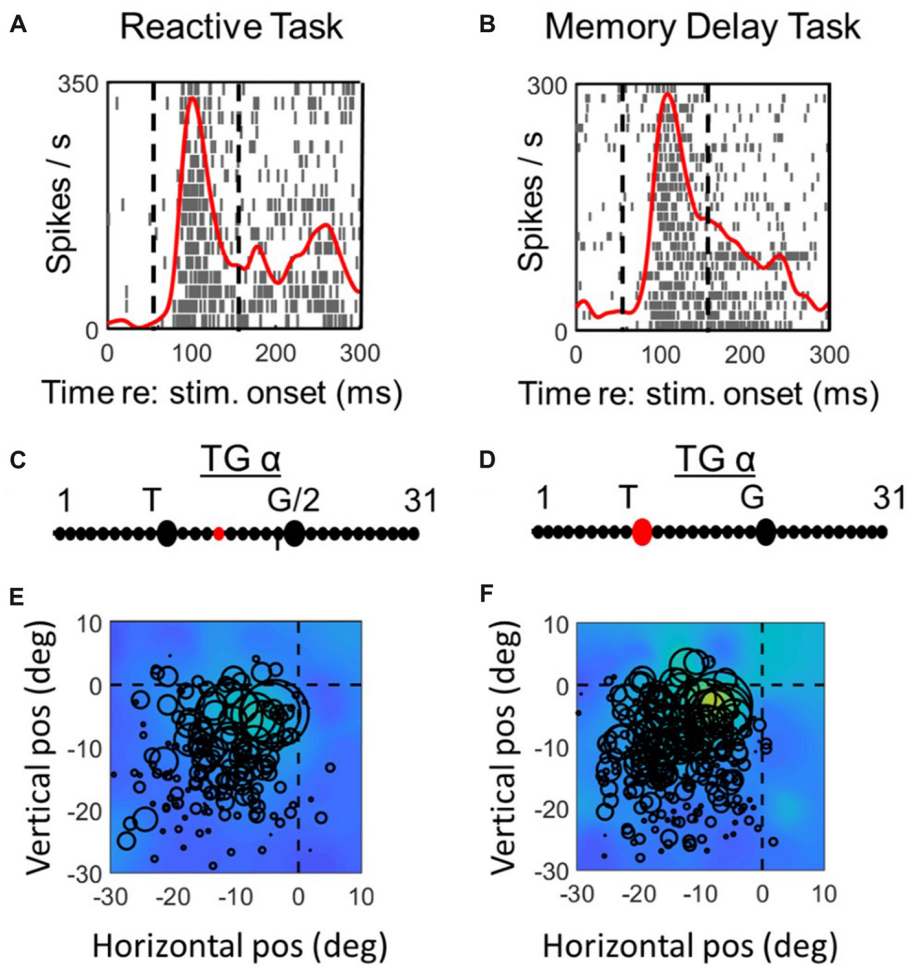

FIGURE 3 | Spatial analysis of *visual* activity during *reactive task* (left column) vs. *memory delay task* for one example *visual* neuron. *Top row* **(A,C)**: spike density and raster plot aligned with target onset. Vertical dashed lines represent the fixed window of activity which was considered in our visual analysis (60–160 ms relative to target presentation). *Second row* **(B,D)**: point of best fit (red dot) on the TG continuum for the response. *Bottom row* **(E,F)**: response fields (RFs) plotted according to the best TG fit from middle row, note that the circles represent the total number of spikes in the time window for each trial (with larger circles indicating more spikes) and the overall similarity of the circle sizes for a given point in space indicate the coherency and the quality of fit (See "Materials and Methods" section). The heat maps in the background represent the non-parametric RF fits made to these data. Thus, lighter colors/larger circles indicate the "hot spots" of the receptive field.

spike train and then applied this method to determine the onset of the burst, we then calculated the mean discharge rate determined by number of spikes from the period which fixation on the initial position started (20–150 ms) which is a period which the start of visual burst definitely falls within. Once we determined the burst onset time for every trial, we then obtained the average it to obtain the burst onset time estimate and the standard deviation.

We previously used a sliding window analysis to look at the transition of spatial codes in individual time epochs in reactive saccades (Sadeh et al., 2018) and in another paper on SC memory delay currently in preparation, and in both cases there was a transition from visual to motor codes. We do not do this here to compare the tasks because the timing of the tasks is so different it would be difficult to normalize them to the same time scale. So instead we focused here on fixed visual and motor windows.

Spatial Analysis of Neuronal Response Fields: The TG Continuum

Visual and motor RFs were obtained for each neuron (using the temporal windows described above) and analyzed using a method that has previously been described several times (Keith et al., 2009; DeSouza et al., 2011; Sadeh et al., 2015; Sajad et al., 2015). Briefly, the RF of the neuron was plotted by overlapping firing rate data over two-dimensional position data corresponding to the spatial parameter related to the given model, such as final gaze position relative to the eye. The quality of the model for the data was quantified by calculating the Predicted Sum of Squares (PRESS) residuals for all trials, which is a type of cross validation in regression analysis (Keith et al., 2009). Specifically, the PRESS residual for a single trial was obtained by: (1) eliminating that trial from RF data; (2) fitting the remaining data points non-parametrically

using Gaussian kernels at various bandwidths (2–15°); and (3) obtaining the residual between the fit and the missing data point. The overall predictability power of the model for the recorded data set was quantified by the average of PRESS residuals across all trials for that neuron. Once PRESS residuals of all the spatial models were obtained the spatial code of a neuron was then defined as the model (at the kernel bandwidth) that yielded the overall best fit (i.e., smallest residual) to the data. In order to characterize the spatial coding of the population of neurons the final step of our analysis involves combining the results of individual neurons in order to obtain the best fit model of that population (Keith et al., 2009).

Our previous studies have tested various spatial models of SC activity but have found the spatial continuum spanning the location of the target and the eventual gaze endpoint (i.e., *target-gaze (TG) continuum*) defined in eye-centered coordinates to be most useful in distinguishing visual from motor coding (Sadeh et al., submitted). The physical basis of the TG continuum is illustrated in **Figure 1C**, which shows the TG continuum for an example trial in space coordinates, which would look similar when rotated into eye coordinates (Klier et al., 2001). This continuum extends between, and beyond T and G position for every such trial, based on our behavioral measures. As described previously (Sadeh et al., 2015; Sajad et al., 2015), in our analysis the TG continuum was constructed by extending the possibility of the best fit for neural activity between and beyond target and gaze models within the same reference frames (eye coordinates). The intermediate spatial models were constructed by dividing the distance between target position and final gaze position for each trial into 10 equal intervals and 10 additional intervals extended on either end. Depending on the location of a neuron on the continuum a value (here referred to as TG alpha value), between 1 and 31 (the Target and Gaze locations are arbitrarily numbered 11 and 21, respectively) which indicates their relative preference for coding target vs. gaze related spatial information. For example, if the fit and TG continuum analysis for the activity of a given neuron yields the value of 11, this indicates that the spatial information encoded by this neuron's activity is regarding the target location information rather than gaze endpoint information. Once the optimal TG value is determined, it can then be used to plot each neural RF in its intrinsic coordinate system, by plotting activity for each trial according to its location along the TG continuum (in eye-centered coordinates).

This TG continuum analysis is insensitive to systematic gaze errors and will automatically adjust to any magnitude of variable error, so long as the range of these errors sufficiently exceeds the noise range of the gaze recording system. In our previous papers we reported a variable error range of 0.7–10.8° for the Reactive Task and 1.3–12° for the Memory Delay task, both of whichreported a variable error range of exceed the level of noise in our recording system by more than an order of magnitude. The recording noise would thus show up as small constant residuals in the model fitting algorithm, and thus have little influence on the T-G comparison to comparison between tasks.

RESULTS

General Observations

Of 86 neurons sampled on-line, we recorded complete datasets (in both the *reactive* and *memory delay task*) from 74 SC neurons from the left and right SC of two head unrestrained monkeys. Of these 54 neurons met all our inclusion criteria (Sajad et al., 2015), including 15 visual, 28 VM and 11 motor neurons (as identified using the memory delay task; Sadeh et al., 2015).

Figure 2 shows the activity profiles of each category of neurons in our study (Visual, VM, Motor) during gaze saccades to the top 10% data (corresponding to the RF "hot spot") derived from the *reactive task (red) and memory delay task (black)*. Each panel provides mean spike density plots (averaged across neurons ± SEM). Data are aligned both with target onset (Left column; **Figures 2A,C,E**) and when aligned with gaze onset (Right Column, **Figures 3B,D,F**). By definition, visual neurons only showed a target-aligned response in the memory delay task (Black data in **Figures 2A,B**), whereas VM cells showed both visual and motor responses in both tasks (**Figures 3C,D**), and motor neurons only showed peak saccade-aligned responses (**Figures 3E,F**). Henceforth we will refer to the data from our fixed target and saccade-related windows as "visual activity" and "motor activity," based on their temporal profiles, but later we will use our analysis methods to quantify what spatial parameters these activities encode in different neurons and at different times.

Temporal Analysis of Reactive vs. Memory-Delay Population Activity Profiles

Although our main aim was to compare spatial tuning in neurons between the reactive and memory tasks, we also took the opportunity to compare their temporal firing profiles (**Figure 2**; selected individual examples are provided below in **Figures 3**, **4**, **6**, **7**). In general, visual neuron responses (**Figure 2A**) and motor neuron responses (**Figure 2F**) showed similar response profiles in the *reactive* (red) and *memory delay* (black) tasks. However, there were some notable differences such as generally stronger peak activation in the reactive task, followed by a more robust, complex, and prolonged "tail." To quantify the degree of response similarity across tasks, we performed a Pearson bivariate two tailed correlations through time on the population activity, and a paired two tailed *t*-test test to compare the peak top 10% of neural firing rate within the defined windows, in the visual and/or motor alignments as appropriate. Visual neurons (in the visual alignment) showed correlation of 0.934 between the two tasks for the fixed window analysis ($p < 0.0001$). But the peak activities were significantly higher in the reactive tasks (237 + 23 SD vs. 175 + 15 SD in *MD* task, $p < 0.0001$). Motor neurons (in the motor alignment) showed correlation of 0.90 ($p < 0.0001$; fixed window), but again had significantly higher firing rate in the reactive task (116 + 19 SD vs. 100 + 12 SD in *MD*, $p < 0.0001$). Thus, visual and motor profiles were highly correlated between the two tasks, but the peak responses were higher in the reactive task.

In contrast, VM cells (**Figures 2C,D**) showed very different profiles in our two tasks, presumably because the reactive burst

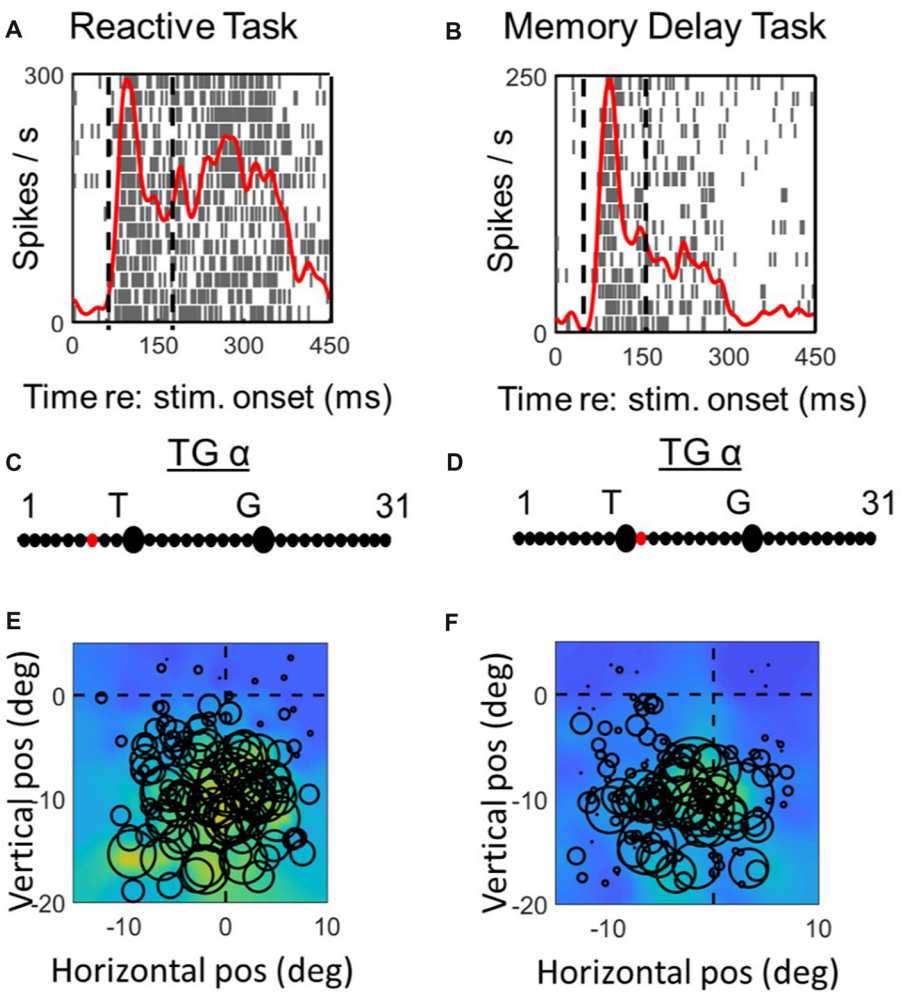

FIGURE 4 | Spatial analysis of *visual* activity during *reactive task* (left column) vs. *memory delay task* for one example *VM* neuron. The plotting conventions are the same as in **Figure 3**.

contains both visual and motor activity. This is most evident in the visual alignment, where the *memory delay task* yields a burst that aligns well with the initial burst of activity from the *reactive task* data, but the latter shows an additional delayed peak that is presumably the motor response. Further, the visual response in the memory paradigm now seems higher, if anything. In the saccade alignment (D), the reactive task produced heightened earlier activation that could correspond to visual activation, but also a higher and more persistent motor peak that is harder to account for. When we repeated our statistical tests on these data (restricted within the fixed visual and motor temporal windows), we found lower, but still significant correlations in both the visual and motor windows ($r = 0.7634$ and 0.8164 respectively, with $p < 0.0001$ for both). There was no significant difference in the peaks of activity in the visual window of VM neurons (155 ± 10 in reactive, 150 ± 39 in *MD*, $p = 0.1195$), but a significant difference in peak activity in motor window (153 ± 15 in reactive vs. 103 ± 14 in the *MD* task, $p < 0.0001$). Thus, if we only look within the fixed visual or motor response windows of VM neurons, they again look somewhat similar and are highly correlated, but with differences in the gain of the motor (not visual) response.

Using the Poisson analysis approach, we found that the average onset of the visual burst in visual neurons in the reactive task is 65.24 ms (SD: 20.5 ms) relative to target onset and 64.6 ms in the MD task (SD: 21.9) with a range of 48.11–78.46 ms in reactive and 53.21–85.11 ms in MD task. The difference of burst onset was found to be non-significant ($p = 0.8099$, two tailed paired *t*-test). For the VM neurons the onset of visual burst was found to be 68.18 ms (SD: 20.5) relative to target onset in the reactive task and 67.78 ms (SD: 19.1) in the MD task, with a range of 54.71–84.79 in reactive and 57.12–88.36 ms in the MD task. The burst onset differences were also found to be non-significant ($p = 0.6414$, two tailed paired *t*-test). Furthermore, the onset of visual burst was not significantly different between the visual neurons and the VM neurons in reactive ($p = 0.154$, two tailed unpaired *t*-test) and MD ($p = 0.2259$, two tailed unpaired *t*-test) tasks.

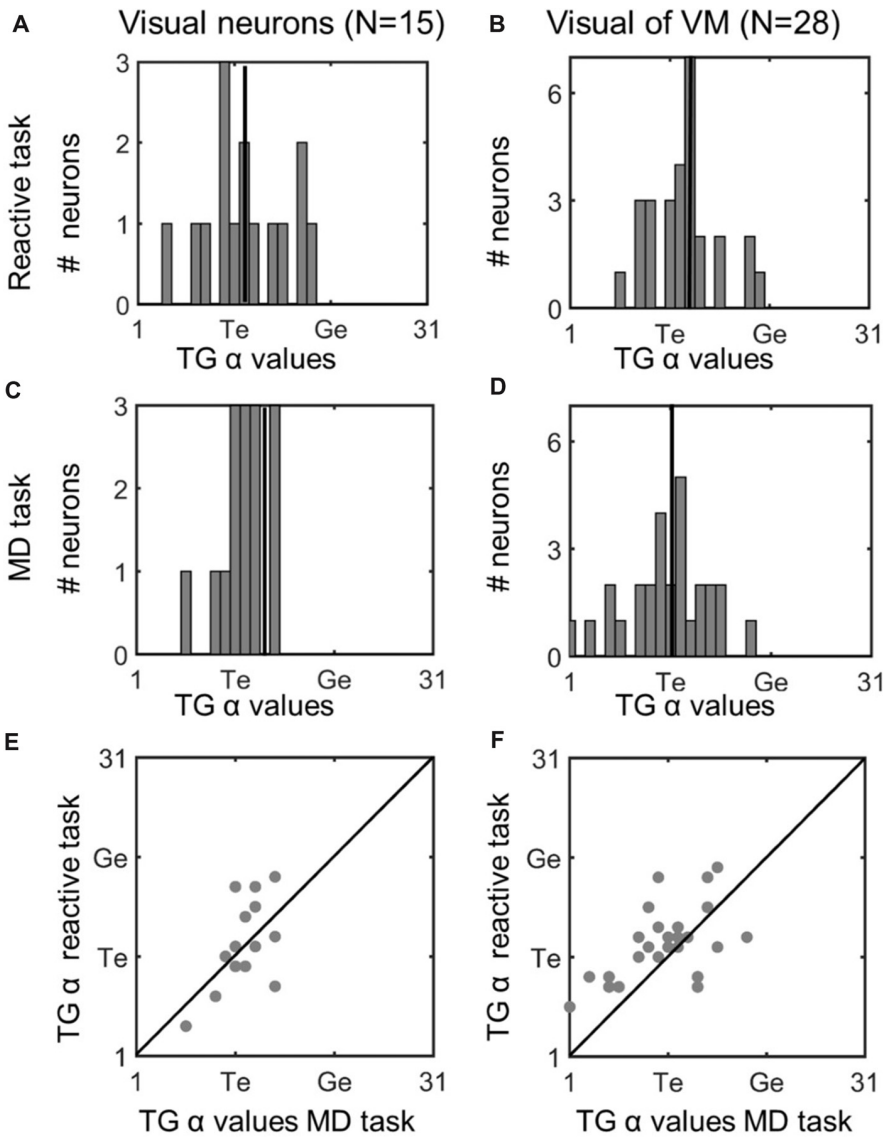

FIGURE 5 | Comparison of TG continuum coding of reactive vs. memory delay task in visual responses. *Left column* **(A,C,E)**: visual neurons; *right column* **(B,D,F)**: visual response of VM neurons. Top row **(A,B)**: TG value distributions in the *reactive task.* Vertical line indicates the median. Second row **(C,D)**: distributions for same neurons in the memory delay (MD) task. Visual neurons showed a more restricted distribution, but there was no significant difference between the TG values between the two tasks. Bottom row **(E,F)**: illustrates neuron-by-neuron comparison between the two tasks in the visual activity of Visual and VM neurons, respectively, plotting the TG continuum values from the reactive task as a function of the MD task.

Overall comparing the reactive task to the *MD* task, visual responses showed the same sharp rise but peaked higher in (in visual, not VM neurons), whereas motor responses were higher and more prolonged in both VM and motor neurons. In general, these results were consistent with similar temporal analyses of activity profiles that have been performed previously in head-restrained studies (Goldberg and Wurtz, 1972; Wurtz and Goldberg, 1972a; Sparks, 1978; Mays and Sparks, 1980; Munoz and Wurtz, 1995a,b; Dorris et al., 1997; Everling et al., 1999; Gandhi and Katnani, 2011), except that, as expected from past studies (Freedman and Sparks, 1997a; Crawford et al., 2003; Stuphorn, 2007; Walton et al., 2007; Freedman, 2008; Sadeh et al., 2012), our head-unrestrained responses were more prolonged and complex.

It is possible that head movements modulate the neural responses and possibly the spatial codes (Cowie and Robinson, 1994; Klier et al., 2002; Klier and Crawford, 2003; Corneil et al., 2007; Stuphorn, 2007; Walton et al., 2007). To ensure that the head movements are comparable for our spatial code comparison, we compared the head contribution to gaze (Head amplitude/Gaze amplitude) in MD (mean: 0.1011, SD: 0.1291) and reactive (0.1103 SD: 0.1301) and found no significant difference between the two (p = 0.61). We also compared the onset of head movements relative to onset of eye movements

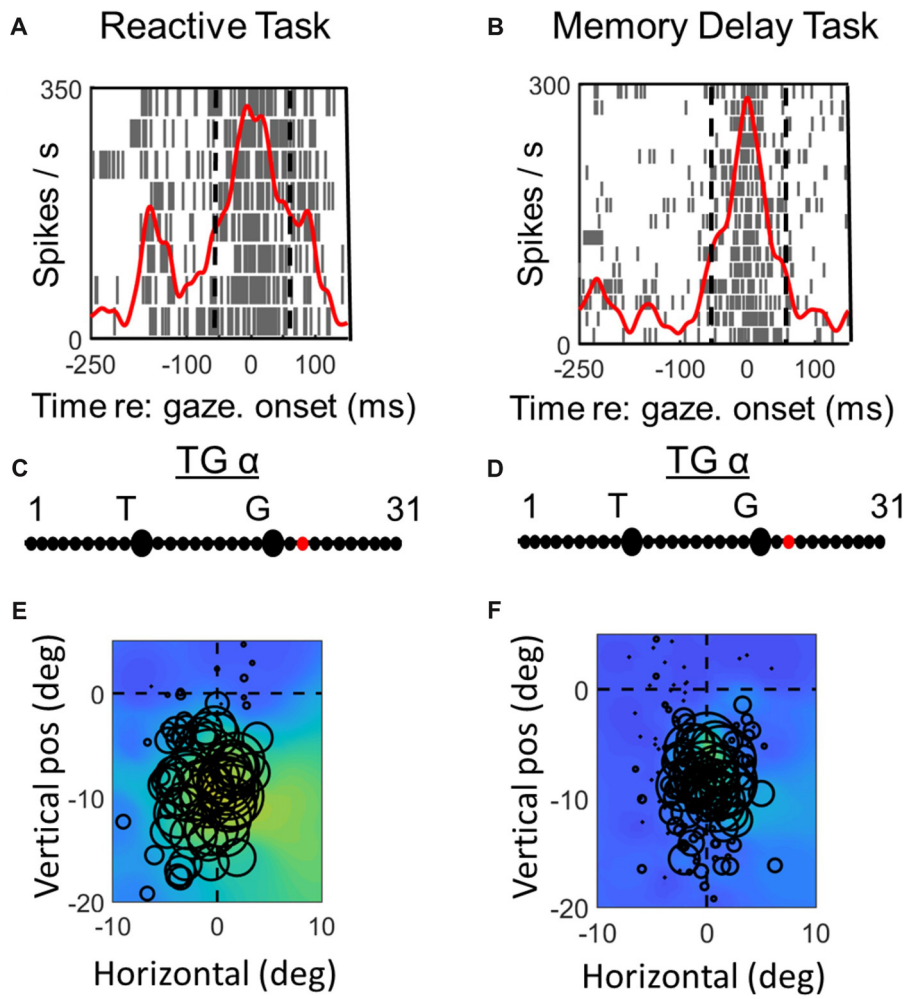

FIGURE 6 | Spatial analysis of *motor* activity during reactive task (left column) vs. memory delay task for one example *VM* neuron. Vertical dashed lines in **(A,B)** represent the fixed motor analysis windows (−50 to + 50 ms relative to gaze onset). Otherwise the plotting conventions are the same as in **Figure 3**.

in reactive and MD tasks, where positive (+) indicates head onsets after the saccade onset. Head movements occurred after eye movements in both tasks, but movement onsets were not significantly later (+64 ms ± 33.3 ms SD) in the reactive task compared to the MD task (+52.5 ms ± 36.8 ms SD) (p = 0.09, unpaired t-test). This difference might influence the late temporal profiles described above (see "Discussion" section). However, our previous analysis did not find any neurons that showed a preferential code for head position or displacement during our visual or saccade-related analysis windows (Sadeh et al., 2015). The following *spatial* analysis exclusively focuses on those windows and only differentiated target vs. gaze coding.

Comparison Between Spatial Coding in Reactive vs. Memory Delay Tasks: Visual Responses

The preceding temporal analysis suggests both similarities and differences in the Visual and Motor responses to our two tasks, but this itself does not indicate whether the same or different spatial information is being encoded. As noted in the introduction, it is likely that visual and motor responses interact in the *reactive task*, and that suppression and memory signals are present in the *MD* task (White et al., 1994; Brown et al., 2004). These factors could affect not only the vigor of the responses (described above) but also their spatial code. To test these various assumptions an independent criterion is required. Here, we did this by using the TG alpha continuum as an independent test of spatial coding in various points of these tasks. Note that for the TG-alpha analysis, all trials were used (not just those to the "hot spot," so this analysis is based on a much larger, richer dataset.

Figures 3, **4** compares spike density and raster plots (A vs. B), best fits along the TG continuum (C vs. D) and visual receptive fields plotted in these ideal coordinate frames (E vs. F) tested on the same stimulus locations with the reactive task (left column) vs. the *MD* task (right column), for an example visual neuron (**Figure 3**) and the visual response of an example VM

neuron (**Figure 4**). These representative visual neuron raster plot (**Figure 3**) resembles the population raster seen in **Figure 2**, with a more prolonged burst and a more prominent second burst in the reactive task. However, the best TG fit for the visual response is shifted leftward toward T in the memory delay task. The overall location and shape of RF remains similar in the two tasks, despite some slight distortions in stimulus location caused by the change in coordinate frame used for the plot. The Visual response of the example VM neuron (**Figure 4**) showed similar patterns, except that the relative TG shift was in the opposite direction.

To assess whether these TG shifts followed a pattern (or were randomly distributed across neurons) we compared fits for the two tasks across our entire neuron populations. **Figure 5** does this for the visual neurons population (left column), and visual response of the VM population (right column), providing frequency histograms for TG-alpha fits from the *reactive task* (top row; **Figure 5A,B**) and *MD task* (middle row; **Figure 5C,D**), recorded from the same neurons (recall that TG = 11 denotes a pure target code, whereas 21 denotes a pure gaze code). For this analysis, we used the fixed target-aligned window to compare the two tasks. The mean TG alpha value for visual neurons in the reactive task was 12.2 (SD = 4.35) which was not significantly different from 11.87 (SD = 2.42) in the memory delay task ($p = 0.91$, paired t-test). This indicates a slight, but not statistically significant, shift toward coding target location in the *MD* task. In the visual activity of VM neurons the same trend (mean reactive: 12.4 SD = 3.4, *MD*: 10.9 SD = 4.6) is observed with a borderline non-significant ($p = 0.058$, paired t-test) shift toward target coding in the *MD* task.

To directly visualize these comparisons we plotted the TG alpha values of each neuron in the *MD* task (x axis) and the reactive task (y axis), For the visual neurons (**Figure 5E**) there is an almost equal number of neurons which do ($n = 7$) and do not ($n = 8$) have different spatial coding between the tasks, in visual activity of VM neurons (**Figure 6F**) more neurons ($n = 21$) do not have a change of what spatial info is being encoded in MG vs. the reactive task. When we combined the TG values all the visual activity (i.e., visual neurons and the visual activity of VM neurons) and compared them between the two tasks there is a slight, but not significant ($p = 0.34$, paired t-test), preference for target coding in *MD* (mean TG = 11.53 $\pm$ 4.45) compare to reactive task (mean 12.33 $\pm$ 3.73). Finally, there was no significant difference between the goodness of fit (i.e., the mean PRESS residual) of these models to the visual data across all visual and VM neurons in the reactive vs. *MD* tasks ($p = 0.89$, paired t-test). In summary, there was no significant task-dependent difference in spatial coding for the visual responses of the visual and VM neuron populations.

Comparison of Spatial Coding in Reactive vs. Memory Delay Tasks: Motor Responses

Figures 6, **7** (similar to 3 and 4) provide comparisons between the spike density plots, rasters, and non-parametric best fits of motor response fields tested on the same stimulus locations, for the motor response of an example VM neuron (**Figure 6**) and motor neuron (**Figure 7**), respectively. The motor burst of the VM neuron (**Figure 6**, top row) illustrates trends seen in the population (**Figure 2**), being completely separated temporally from the visual burst in the *MD* task (**Figure 6B**) but not the reactive task (**Figure 6A**). For this neuron, the TG fits for the motor response are quite close to G in both tasks (**Figures 6C,D**). As a result, the motor RFs for this neuron (which shows a fairly poor spatial organization) looks nearly identical in both tasks (**Figures 6E,F**).

In the case of the motor neuron example, the TG fit is shifted more toward G in the *MD* task (**Figures 7C,D**). As a result, the saccade end locations for the RF plot are slightly compressed in the horizontal dimension for the *MD* data, i.e., because of gaze undershoots in this task. But otherwise, the RFs are similar, showing a downward-leftward preference.

Figure 8 (similar to **Figure 5**) compares the TG alpha values for the fixed window motor responses of VM and Motor Neurons. The motor activity of the VM neurons showed more gaze preference in the *MD* task (mean: 18.3; SD = 4.8) than reactive task (mean = 17.6; SD = 4.9), but this was not significantly different ($p = 0.58$). Interestingly in our pure motor neurons the TG alpha values showed a significantly ($p = 0.021$, paired t-test) more preference (mean: 20; SD = 2.29) for coding the gaze end points in the MG task compare to the reactive task (Mean: 17.2; SD = 2.9). This can be visualized in **Figure 8F** as a shift in the data from the line of unity, whereas the VM data (**Figure 5E**) are evenly distributed across this line. The TG values for the combined motor activity, however, were not significantly different between the two tasks (*MD* task mean = 19 $\pm$ 4.2, reactive task mean = 17.5 $\pm$ 4, $p = 0.08$). In the case of these motor fits, there was a significant increase in the mean PRESS residual across cells ($p = 0.03$), for the *MD* vs. reactive task, possibly because the delay introduced more non-spatial noise in the system. Thus, overall our data tend to confirm the assumption that what is spatial encoded in motor responses of VM neurons is the same regardless of the interposition of a memory delay, but suggests that motor cells show a purer gaze code following a memory delay.

DISCUSSION

Gaze shifts occur in a variety of circumstances (e.g., exploring the environment, selecting the stimulus of interest, looking at a suddenly appearing stimulus, etc.) and in each case the number of brain VM areas and the extent of their involvement in generating gaze shifts are different (Fischer, 1986; Dean et al., 1989; Gnadt et al., 1991; Pierrot-Deseilligny et al., 1991a,b; Andersen, 1995; Deubel, 1995; Horwitz and Newsome, 1999; Hikosaka et al., 2000; Schall, 2001; Brown et al., 2004; Fecteau and Munoz, 2006; Sajad et al., 2016a). It is, however, unclear if these differences in the task demands and behavior has any influence in the spatial information encoded by the neurons.

Here, we compared the visual and gaze movement related neural activity during head-unrestrained reactive and memory delay gaze tasks in the SC, a key oculomotor area where many signals from cortex and subcortical areas converge and which directly influences the brainstem premotor neurons that control eye and head rotation (Guitton et al., 1980; Harris, 1980; Sparks and Hartwich-Young, 1989; Klier et al., 2002; Sparks, 2002; Klier

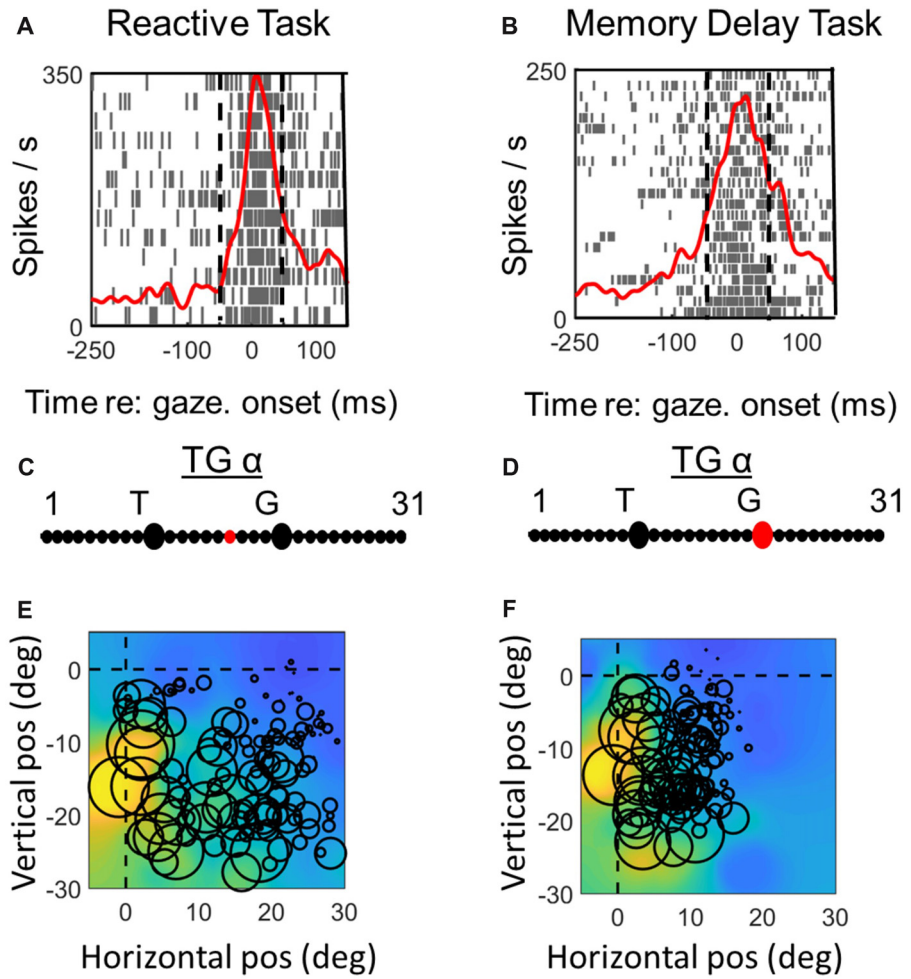

FIGURE 7 | Spatial analysis of *motor* activity during reactive task (left column) vs. memory delay task for one example *motor* neuron. Vertical dashed lines in **(A,B)** represent the fixed motor analysis windows (−50 to + 50 ms relative to gaze onset). Otherwise the plotting conventions are the same as in **Figure 3**.

and Crawford, 2003; Walton et al., 2007; Gandhi and Katnani, 2011). We found both similarities and differences between the overall activity profiles and spatial information encoded by SC neurons between the memory guided and the reactive gaze shifts.

Differences in the Timing and Vigor of Visual and Movement Related Neural Responses

By comparing spike density profiles recorded from the same neurons in two different tasks (**Figure 2**), we were able to make several noteworthy observations. As expected, the onset and peaks of the visual responses occurred at roughly the same time after target presentation, and the peak of the motor response was similar in both tasks. There was also a strong correlation between the peaks in each task. However, visual neurons showed a higher peak firing rate and all motor responses were higher, as reported in several previous studies (Goldberg and Wurtz, 1972; Mays and Sparks, 1980; Krauzlis et al., 2013). This might be accounted for by the presence of saccade suppression signals during the early portion of the *MD* task, and conversely, the presence of visual target and increased bottom-up attention in the reactive task (Desimone and Duncan, 1995; Itti, 2005; Buschman and Miller, 2007).

Effects of offset timing were pronounced in the head-unrestrained condition, where the visual and motor bursts are already prolonged to accompany the longer duration of the eye + head motion (Freedman and Sparks, 1997a; Roy and Cullen, 1998; Freedman, 2008). For example, the motor burst, already prolonged in head-unrestrained gaze shifts, was even more prolonged in the reactive task than the *MD* task. This and the prolonged, multi-peaked burst activity of visual neurons in reactive task could be attributed to modulations such as attention (Goldberg and Wurtz, 1972; Desimone and Duncan, 1995; Robinson and Kertzman, 1995; Krauzlis et al., 2013), motivation (Redgrave et al., 2010; Otmakhova et al., 2013). The reactive task trials were shorter so monkeys were rewarded at a higher rate compared to the *MD* task, suggesting that

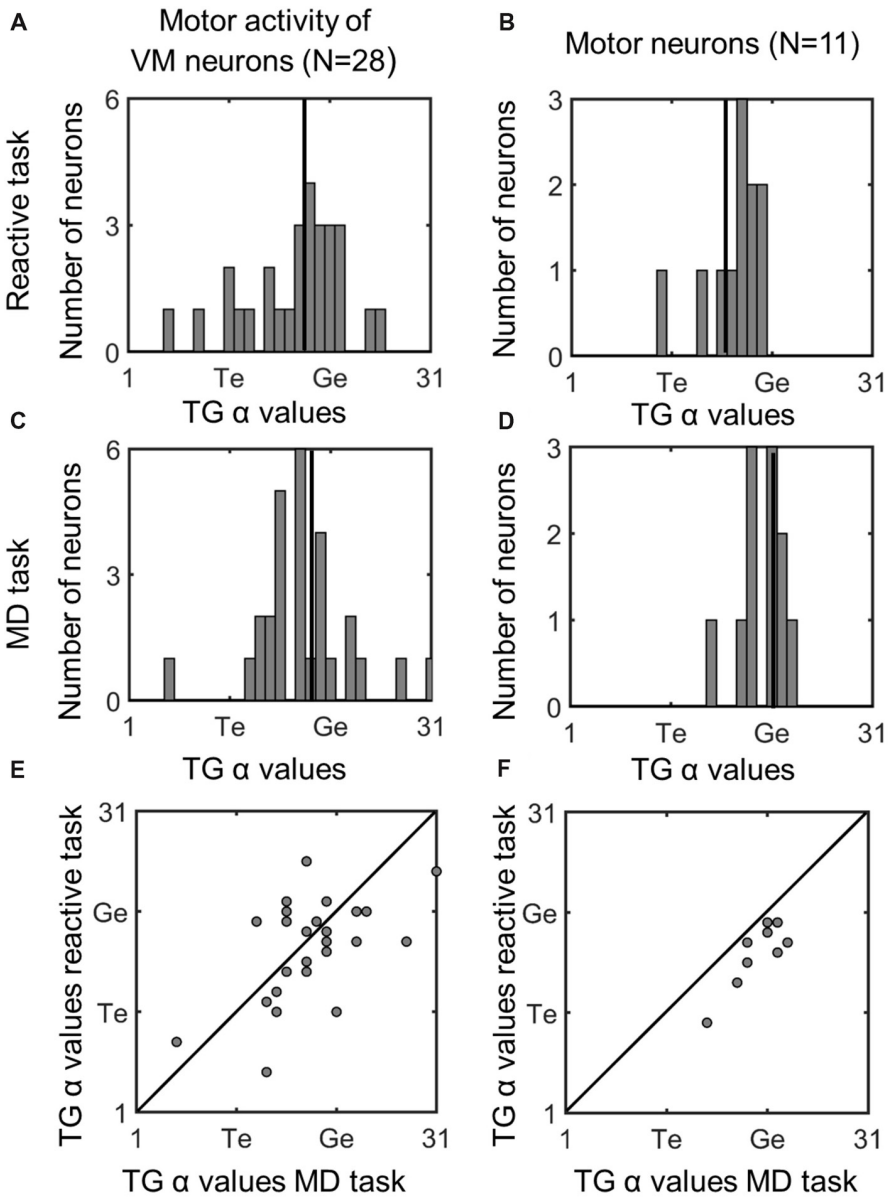

FIGURE 8 | Comparison of TG continuum coding of reactive vs. memory delay task in *motor* responses. *Left column* **(A,C,E)**: motor response of VM neurons; *right column* **(B,D,F)**: motor response of motor neurons. Otherwise, the conventions are the same as **Figure 5**. There was a significant difference between the TG values in the two tasks in Motor Neurons, i.e., the fits were below the diagonal line in part (F) meaning motor neurons were more gaze-related in the MD task.

reward signals may have also had an influence (Glimcher and Sparks, 1992; Schall, 2001; Ikeda and Hikosaka, 2003). These differences in firing could account for differences in speed (Tweed and Vilis, 1990; Lefèvre et al., 1998; Groh, 2001; Sparks, 2002), accuracy (Lee et al., 1988; Goldberg and Bruce, 1990; Gottlieb and Goldberg, 1999) and amplitude (Sparks et al., 1990; Dorris et al., 1997; Freedman and Sparks, 1997a,b) reported here and previously in these tasks. The differences in gaze precision reported here (see "Materials and Methods" section) might also be due to lower signal-to-noise ratio in the *MD* firing rates, related differences in spatial coding, which we will describe more directly in the following sections.

Finally, task-related head movement strategies could modulate SC responses (Guitton et al., 1990; Cowie and Robinson, 1994; Crawford and Guitton, 1997; Crawford et al., 1999, 2003; Sparks et al., 2001; Corneil et al., 2002; Klier et al., 2002; Corneil et al., 2007; Walton et al., 2007; Freedman, 2008). There was no significant difference in head contribution to the gaze shift between our tasks, but head onset occurred earlier in the MD task. This is in agreement with prior observations of eye head coordination timing during various tasks and conditions

(Berthoz and Grantyn, 1986; Guitton, 1992; Freedman and Sparks, 1997b; Crawford et al., 1999; Pélisson et al., 2001; Corneil et al., 2002; Snyder et al., 2002). It is possible that head related activities influence the neural response differently in each activity (Cowie and Robinson, 1994; Sparks et al., 2001; Klier et al., 2002; Klier and Crawford, 2003; Knight and Fuchs, 2007; Stuphorn, 2007; Walton et al., 2007; Freedman, 2008; Monteon et al., 2012). Specifically, this timing difference might explain the more prolonged motor burst we observed in the reactive task. However, it is unlikely to explain the higher peak in the saccade-related response. Further, it is unlikely to have influenced the spatial analysis described in the next sections because; (1) this analysis focused on target vs. gaze coding during the earlier visual and saccade epochs; (2) head movements started from a central range and tended to be quite small (Sadeh et al., 2015); and (3) we found no neurons that preferentially encoded head movement or position during these epochs (Sadeh et al., 2015). It remains possible that some of these neurons might predict or code head movement in tasks that involve larger head movements and/or offsets (Walton et al., 2005, 2007; Monteon et al., 2012).

Spatial Code Differences in Visual Activity

In both the reactive and *MD* tasks the visual activity preferentially coded for Te, and there was no significant difference between these codes. However, there were subtler differences in the distribution of the TG alpha values of the visual responses between the two tasks (**Figures 5A,C**). In visual neurons, the distribution of the TG values was clearly more narrow and clustered around the Te model in the *MD* task compared to the reactive task (**Figures 5A,C**). In VM neurons, the peak of the TG distribution was shifted slightly (although not significantly) toward Te. Overall, this suggests a more faithful coding of the target in visual responses in the *MD* task.

This could be due to an almost simultaneous need for encoding target location as well as preparing for the movement in the reactive task, thus some of the visual responses may have been influenced by movement preparation (Munoz and Wurtz, 1993; Dorris et al., 1997; Horwitz and Newsome, 1999; Bell et al., 2005) which may shift the spatial information away from the Te model. In the *MD* paradigm when a delay is expected, the visual burst encodes the target location and the signals regarding the movement preparation and from the working memory circuit contribute to the later movement related burst and therefore less intermixing of the activities occurs. This could occur between suprathreshold excitatory motor signals in VM neurons, or through subthreshold or inhibitory motor signals in visual neurons.

Spatial Code Differences in Motor Activity

In both tasks, the motor related response of the VM neurons tend to encode spatial information related to gaze endpoint locations rather than target, but this shift toward G coding was more complete in pure motor cells, with closer clustering around the G model in both tasks (**Figures 5B,D**). This is consistent with our previous results from the frontal eye fields, where moto-only cells showed a pure G code (Sadeh et al., 2015). Since our method of fitting G is based on fitting variable errors in gaze end points, this suggests that SC motor responses, particularly in pure motor cells, are casually involved in generating these errors in both tasks, perhaps in communication with other areas like the FEF (Sajad et al., 2015). Alternatively, pure motor cells may receive feedback from downstream premotor cells that provide a better estimate of actual behavioral output (Waitzman et al., 1991; Matsuo et al., 2004; Walton et al., 2005).

In addition, there was a significantly further shift toward G coding (in pure motor cells) in the *MD* task (**Figures 5B,D,F**). Our model normalizes fits relative to the magnitude of errors (Keith et al., 2009; Sajad et al., 2015; Sadeh et al., 2015), but the quality of the fits could have been influenced by signal-to-noise ratio. However, this does not account for why this task-dependance occurred only in motor neurons and not VM neurons. One possible explanation is that by the time motor neurons became active after the memory delay, there was less influence from other neurons with mixed coding on behavior (perhaps through selective gating), and thus an even better relationship between their firing rate and gaze errors. Alternatively, if we consider feedback, it may be that more delay allows a more accurate estimate of output. Other more general explanations will be considered in the "Spatial Transformation in Reactive and Memory Delay Tasks" section.

Spatial Transformation in Reactive and Memory Delay Tasks

In both the reactive and *MD* tasks the general observation is that based on the significantly different TG values, there is a transformation away from coding the location of target to coding the location of gaze end points. In our previous articles, we have suggested that this is due to the accumulation of noise in the system (Sadeh et al., 2015, 2018) and as confirmed here, this appears to happen with or without the interposition of a memory delay.

However, despite this similar trend there are some interesting findings which suggest different VM transformation mechanism in each task (Gnadt et al., 1991; Munoz and Everling, 2004; Sajad et al., 2016a,b). As noted above, the visual code represents the target more faithfully in the *MD* task (in terms of overall distribution), whereas the motor response (at least in pure motor cells) more faithfully represents the gaze end point. This would seem to suggest a more perfect transformation, and yet gaze saccades are less accurate and precise after a memory delay in our data and in previous studies (Gnadt et al., 1991; Pierrot-Deseilligny et al., 1991a; Stanford and Sparks, 1994; White et al., 1994).

The answer to this apparent contradiction may be that, despite the rapid mixing of visual and motor signals in the reactive task, at the overall population level the transformation is relatively effective. Second, although the final motor output in the *MD* task faithfully encodes gaze, this includes gaze errors, and the SC (and FEF) is likely one source of these errors, or as suggested above, in the monitoring of those errors as movement progresses.

Finally, the transformation is not necessarily complete at the SC. For example, the TG values of motor activities are significantly different from that for the gaze model, shifted

towards the target model, and in the *MD* task they are not. Therefore, it is reasonable to conclude that the SC encodes a gaze goal, which is then subject to further transformations. Errors in those additional transformations could be proportionately larger in the reactive task than the *MD* task, hence the difference in motor code between these tasks. Alternatively, this difference could be attributed to the increase in distribution of errors with time across the entire gaze control system, hence any one area like SC could reflect the gaze errors more closely.

Finally, the current study demonstrates that the model-fitting approach used here is sufficiently robust to identify not only differences in neural codes and transformations (Sajad et al., 2015, 2016a; Sadeh et al., 2015, 2018), but also how these depend on brain states. The memory delay interval is known to induce inaccuracies in motor response in a variety of the settings (Postle et al., 2000; Bays et al., 2011; Barber et al., 2013; Chatham and Badre, 2015; Hollingworth, 2015), but so do other behaviors like express saccades (Pierrot-Deseilligny et al., 1991b; Postle et al., 2000; Corneil et al., 2004). More importantly, one would expect such errors to be even larger in clinical disorders (Munoz et al., 2003; Anderson and MacAskill, 2013), so this technology might have practical application for detecting quantitative biomarkers in disease states.

CONCLUSION

In this article, we aimed to provide a comprehensive comparison between the spatial information encoded by visual and motor activities of SC in two different tasks: reactive and memory delay gaze shifts. We found that despite overall similarities in visual to motor transformation, there are several important differences. Most importantly the visual to motor transformation is more extensive in the *MD* task since the TG values in the motor population are closer to gaze models in the *MD* task. This suggests that the brain areas involved in each task contribute to changes in spatial code and ultimately to saccadic errors.

AUTHOR CONTRIBUTIONS

MS performed experiments, assisted in surgeries, analyzed data and wrote the article. AS assisted in data analysis and edited the article. HW performed surgeries, assisted in experiments and edited the article. XY set-up the equipment, assisted in experiments and edited the article. JC designed and funded the experiment, provided advice on experiments and analysis and co-wrote the article.

FUNDING

This project was supported by a grant from the Canadian Institute of Health Research. JC is supported by a Canada Research Chair award. MS and AS were supported by Ontario Graduate Scholarships.

ACKNOWLEDGMENTS

We thank S. Sun for the computer programming support.

REFERENCES

Andersen, R. A. (1995). Encoding of intention and spatial location in the posterior parietal cortex. *Cereb. Cortex* 5, 457–469. doi: 10.1093/cercor/5.5.457

Anderson, T. J., and MacAskill, M. R. (2013). Eye movements in patients with neurodegenerative disorders. *Nat. Rev. Neurol.* 9, 74–85. doi: 10.1038/nrneurol.2012.273

Barber, A. D., Caffo, B. S., Pekar, J. J., and Mostofsky, S. H. (2013). Effects of working memory demand on neural mechanisms of motor response selection and control. *J. Cogn. Neurosci.* 25, 1235–1248. doi: 10.1162/jocn_a_00394

Bays, P. M., Gorgoraptis, N., Wee, N., Marshall, L., and Husain, M. (2011). Temporal dynamics of encoding, storage and reallocation of visual working memory. *J. Vis.* 11:6. doi: 10.1167/11.10.6

Bell, A. H., Meredith, M. A., Van Opstal, A. J., and Munoz, D. P. (2005). Crossmodal integration in the primate superior colliculus underlying the preparation and initiation of saccadic eye movements. *J. Neurophysiol.* 93, 3659–3673. doi: 10.1152/jn.01214.2004

Berthoz, A., and Grantyn, A. (1986). Neuronal mechanisms underlying eye-head coordination. *Prog. Brain Res.* 64, 325–343. doi: 10.1016/s0079-6123(08)63427-5

Bremmer, F., Kaminiarz, A., Klingenhoefer, S., and Churan, J. (2016). Decoding target distance and saccade amplitude from population activity in the macaque lateral intraparietal area (LIP). *Front. Integr. Neurosci.* 10:30. doi: 10.3389/fnint.2016.00030

Brown, M. R., DeSouza, J. F., Goltz, H. C., Ford, K., Menon, R. S., Goodale, M. A., et al. (2004). Comparison of memory- and visually guided saccades using event-related fMRI. *J. Neurophysiol.* 91, 873–889. doi: 10.1152/jn.00382.2003

Bruce, C. J., and Goldberg, M. E. (1985). Primate frontal eye fields: I. Single neurons discharging before saccades. *J. Neurophysiol.* 53, 603–635. doi: 10.1152/jn.1985.53.3.603

Bruce, C. J., Goldberg, M. E., Bushnell, M. C., and Stanton, G. B. (1985). Primate frontal eye fields: II. Physiological and anatomical correlates of electrically evoked eye movements. *J. Neurophysiol.* 54, 714–734. doi: 10.1152/jn.1985.54.3.714

Buschman, T. J., and Miller, E. K. (2007). Top-down versus bottom-up control of attention in the prefrontal and posterior parietal cortices. *Science* 315, 1860–1862. doi: 10.1126/science.1138071

Chatham, C. H., and Badre, D. (2015). Multiple gates on working memory. *Curr. Opin. Behav. Sci.* 1, 23–31. doi: 10.1016/j.cobeha.2014.08.001

Corneil, B. D., Munoz, D. P., and Olivier, E. (2007). Priming of head premotor circuits during oculomotor preparation. *J. Neurophysiol.* 97, 701–714. doi: 10.1152/jn.00670.2006

Corneil, B. D., Olivier, E., and Munoz, D. P. (2002). Neck muscle responses to stimulation of monkey superior colliculus: II. Gaze shift initiation and volitional head movements. *J. Neurophysiol.* 88, 2000–2018. doi: 10.1152/jn.2002.88.4.2000

Corneil, B. D., Olivier, E., and Munoz, D. P. (2004). Visual responses on neck muscles reveal selective gating that prevents express saccades. *Neuron* 42, 831–841. doi: 10.1016/s0896-6273(04)00267-3

Cowie, R. J., and Robinson, D. L. (1994). Subcortical contributions to head movements in macaques. I. Contrasting effects of electrical stimulation of a medial pontomedullary region and the superior colliculus. *J. Neurophysiol.* 72, 2648–2664. doi: 10.1152/jn.1994.72.6.2648

Crawford, J. D., Ceylan, M. Z., Klier, E. M., and Guitton, D. (1999). Three-dimensional eye-head coordination during gaze saccades in the primate. *J. Neurophysiol.* 81, 1760–1782. doi: 10.1152/jn.1999.81.4.1760

Crawford, J. D., and Guitton, D. (1997). Primate head-free saccade generator implements a desired (post-VOR) eye position command by anticipating intended head motion. *J. Neurophysiol.* 78, 2811–2816. doi: 10.1152/jn.1997.78.5.2811

Crawford, J. D., Martinez-Trujillo, J. C., and Klier, E. M. (2003). Neural control of three-dimensional eye and head movements. *Curr. Opin. Neurobiol.* 13, 655–662. doi: 10.1016/j.conb.2003.10.009

Dean, P., Redgrave, P., and Westby, G. (1989). Event or emergency? Two response systems in the mammalian superior colliculus. *Trends Neurosci.* 12, 137–147. doi: 10.1016/0166-2236(89)90052-0

Desimone, R., and Duncan, J. (1995). Neural mechanisms of selective visual attention. *Annu. Rev. Neurosci.* 18, 193–222. doi: 10.1146/annurev.ne.18.030195.001205

DeSouza, J. F., Keith, G. P., Yan, X., Blohm, G., Wang, H., and Crawford, J. D. (2011). Intrinsic reference frames of superior colliculus visuomotor receptive fields during head-unrestrained gaze shifts. *J. Neurosci.* 31, 18313–18326. doi: 10.1523/jneurosci.0990-11.2011

Deubel, H. (1995). Separate adaptive mechanisms for the control of reactive and volitional saccadic eye movements. *Vision Res.* 35, 3529–3540. doi: 10.1016/0042-6989(95)00058-m

Dorris, M. C., Paré, M., and Munoz, D. P. (1997). Neuronal activity in monkey superior colliculus related to the initiation of saccadic eye movements. *J. Neurosci.* 17, 8566–8579. doi: 10.1523/jneurosci.17-21-08566.1997

Everling, S., Dorris, M. C., Klein, R. M., and Munoz, D. P. (1999). Role of primate superior colliculus in preparation and execution of anti-saccades and pro-saccades. *J. Neurosci.* 19, 2740–2754. doi: 10.1523/jneurosci.19-07-02740.1999

Everling, S., and Munoz, D. P. (2000). Neuronal correlates for preparatory set associated with pro-saccades and anti-saccades in the primate frontal eye field. *J. Neurosci.* 20, 387–400. doi: 10.1523/jneurosci.20-01-00387.2000

Fecteau, J. H., and Munoz, D. P. (2006). Salience, relevance, and firing: a priority map for target selection. *Trends Cogn. Sci.* 10, 382–390. doi: 10.1016/j.tics.2006.06.011

Fischer, B. (1986). Express saccades in man and monkey. *Prog. Brain Res.* 64, 155–160. doi: 10.1016/s0079-6123(08)63410-x

Freedman, E. G. (2008). Coordination of the eyes and head during visual orienting. *Exp. Brain Res.* 190, 369–387. doi: 10.1007/s00221-008-1504-8

Freedman, E. G., and Sparks, D. L. (1997a). Activity of cells in the deeper layers of the superior colliculus of the rhesus monkey: evidence for a gaze displacement command. *J. Neurophysiol.* 78, 1669–1690. doi: 10.1152/jn.1997.78.3.1669

Freedman, E. G., and Sparks, D. L. (1997b). Eye-head coordination during head-unrestrained gaze shifts in rhesus monkeys. *J. Neurophysiol.* 77, 2328–2348. doi: 10.1152/jn.1997.77.5.2328

Gandhi, N. J., and Katnani, H. A. (2011). Motor functions of the superior colliculus. *Annu. Rev. Neurosci.* 34, 205–231. doi: 10.1146/annurev-neuro-061010-113728

Glimcher, P. W., and Sparks, D. L. (1992). Movement selection in advance of action in the superior colliculus. *Nature* 355, 542–545. doi: 10.1038/355542a0

Gnadt, J. W., Bracewell, R. M., and Andersen, R. A. (1991). Sensorimotor transformation during eye movements to remembered visual targets. *Vision Res.* 31, 693–715. doi: 10.1016/0042-6989(91)90010-3

Goldberg, M. E., and Bruce, C. J. (1990). Primate frontal eye fields: III. Maintenance of a spatially accurate saccade signal. *J. Neurophysiol.* 64, 489–508. doi: 10.1152/jn.1990.64.2.489

Goldberg, M. E., and Wurtz, R. H. (1972). Activity of superior colliculus in behaving monkey: II. Effect of attention on neuronal responses. *J. Neurophysiol.* 35, 560–574. doi: 10.1152/jn.1972.35.4.560

Gottlieb, J., and Goldberg, M. E. (1999). Activity of neurons in the lateral intraparietal area of the monkey during an antisaccade task. *Nat. Neurosci.* 2, 906–912. doi: 10.1038/13209

Groh, J. M. (2001). Converting neural signals from place codes to rate codes. *Biol. Cybern.* 85, 159–165. doi: 10.1007/s004220100249

Guitton, D. (1992). Control of eye-head coordination during orienting gaze shifts. *Trends Neurosci.* 15, 174–179. doi: 10.1016/0166-2236(92)90169-9

Guitton, D., Crommelinck, M., and Roucoux, A. (1980). Stimulation of the superior colliculus in the alert cat: I. Eye movements and neck EMG activity evoked when the head is restrained. *Exp. Brain Res.* 39, 63–73. doi: 10.1007/bf00237070

Guitton, D., Munoz, D. P., and Galiana, H. L. (1990). Gaze control in the cat: studies and modeling of the coupling between orienting eye and head movements in different behavioral tasks. *J. Neurophysiol.* 64, 509–531. doi: 10.1152/jn.1990.64.2.509

Hanes, D. P., Thompson, K. G., and Schall, J. D. (1995). Relationship of presaccadic activity in frontal eye field and supplementary eye field to saccade initiation in macaque: poisson spike train analysis. *Exp. Brain Res.* 103, 85–96. doi: 10.1007/bf00241967

Harris, L. R. (1980). The superior colliculus and movements of the head and eyes in cats. *J. Physiol.* 300, 367–391. doi: 10.1113/jphysiol.1980.sp013167

Hikosaka, O., Takikawa, Y., and Kawagoe, R. (2000). Role of the basal ganglia in the control of purposive saccadic eye movements. *Physiol. Rev.* 80, 953–978. doi: 10.1152/physrev.2000.80.3.953

Hollingworth, A. (2015). Visual working memory modulates within-object metrics of saccade landing position. *Ann. N Y Acad. Sci.* 1339, 11–19. doi: 10.1111/nyas.12664

Horwitz, G. D., and Newsome, W. T. (1999). Separate signals for target selection and movement specification in the superior colliculus. *Science* 284, 1158–1161. doi: 10.1126/science.284.5417.1158

Ikeda, T., and Hikosaka, O. (2003). Reward-dependent gain and bias of visual responses in primate superior colliculus. *Neuron* 39, 693–700. doi: 10.1016/s0896-6273(03)00464-1

Itti, L. (2005). "Models of bottom-up attention and saliency," in *Neurobiology of Attention*, eds L. Itti, G. Rees and J. K. Tsotsos (San Diego, CA: Elsevier), 576–582. doi: 10.1016/B978-012375731-9/50098-7

Keith, G. P., and Crawford, J. D. (2008). Saccade-related remapping of target representations between topographic maps: a neural network study. *J. Comput. Neurosci.* 24, 157–178. doi: 10.1007/s10827-007-0046-6

Keith, G. P., DeSouza, J. F., Yan, X., Wang, H., and Crawford, J. D. (2009). A method for mapping response fields and determining intrinsic reference frames of single-unit activity: applied to 3D head-unrestrained gaze shifts. *J. Neurosci. Methods* 180, 171–184. doi: 10.1016/j.jneumeth.2009.03.004

Klier, E. M., and Crawford, J. D. (2003). Neural control of three-dimensional eye and head posture. *Ann. N Y Acad. Sci.* 1004, 122–131. doi: 10.1196/annals.1303.011

Klier, E. M., Wang, H., Constantin, A. G., and Crawford, J. D. (2002). Midbrain control of three-dimensional head orientation. *Science* 295, 1314–1316. doi: 10.1126/science.1067300

Klier, E. M., Wang, H., and Crawford, J. D. (2001). The superior colliculus encodes gaze commands in retinal coordinates. *Nat. Neurosci.* 4, 627–632. doi: 10.1038/88450

Knight, T. A., and Fuchs, A. F. (2007). Contribution of the frontal eye field to gaze shifts in the head-unrestrained monkey: effects of microstimulation. *J. Neurophysiol.* 97, 618–634. doi: 10.1152/jn.00256.2006

Krauzlis, R. J., Lovejoy, L. P., and Zenon, A. (2013). Superior colliculus and visual spatial attention. *Annu. Rev. Neurosci.* 36, 165–182. doi: 10.1146/annurev-neuro-062012-170249

Lee, C., Rohrer, W. H., and Sparks, D. L. (1988). Population coding of saccadic eye movements by neurons in the superior colliculus. *Nature* 332, 357–360. doi: 10.1038/332357a0

Lefèvre, P., Quaia, C., and Optican, L. M. (1998). Distributed model of control of saccades by superior colliculus and cerebellum. *Neural Netw.* 11, 1175–1190. doi: 10.1016/s0893-6080(98)00071-9

Legéndy, C. R., and Salcman, M. (1985). Bursts and recurrences of bursts in the spike trains of spontaneously active striate cortex neurons. *J. Neurophysiol.* 53, 926–939. doi: 10.1152/jn.1985.53.4.926

Marino, R. A., Levy, R., and Munoz, D. P. (2015). Linking express saccade occurance to stimulus properties and sensorimotor integration in the superior colliculus. *J. Neurophysiol.* 114, 879–892. doi: 10.1152/jn.00047.2015

Marino, R. A., Rodgers, C. K., Levy, R., and Munoz, D. P. (2008). Spatial relationships of visuomotor transformations in the superior colliculus map. *J. Neurophysiol.* 100, 2564–2576. doi: 10.1152/jn.90688.2008

Matsuo, S., Bergeron, A., and Guitton, D. (2004). Evidence for gaze feedback to the cat superior colliculus: discharges reflect gaze trajectory

perturbations. *J. Neurosci.* 24, 2760–2773. doi: 10.1523/jneurosci.5120-03.2004

Mays, L. E., and Sparks, D. L. (1980). Dissociation of visual and saccade-related responses in superior colliculus neurons. *J. Neurophysiol.* 43, 207–232. doi: 10.1152/jn.1980.43.1.207

Miller, E. K., Erickson, C. A., and Desimone, R. (1996). Neural mechanisms of visual working memory in prefrontal cortex of the macaque. *J. Neurosci.* 16, 5154–5167. doi: 10.1523/jneurosci.16-16-05154.1996

Monteon, J. A., Avillac, M., Yan, X., Wang, H., and Crawford, J. D. (2012). Neural mechanisms for predictive head movement strategies during sequential gaze shifts. *J. Neurophysiol.* 108, 2689–2707. doi: 10.1152/jn.00222.2012

Munoz, D. P., Armstrong, I. T., Hampton, K. A., and Moore, K. D. (2003). Altered control of visual fixation and saccadic eye movements in attention-deficit hyperactivity disorder. *J. Neurophysiol.* 90, 503–514. doi: 10.1152/jn.00192.2003

Munoz, D. P., and Everling, S. (2004). Look away: the anti-saccade task and the voluntary control of eye movement. *Nat. Rev. Neurosci.* 5, 218–228. doi: 10.1038/nrn1345

Munoz, D. P., and Wurtz, R. H. (1993). Fixation cells in monkey superior colliculus: I. Characteristics of cell discharge. *J. Neurophysiol.* 70, 559–575. doi: 10.1152/jn.1993.70.2.559

Munoz, D. P., and Wurtz, R. H. (1995a). Saccade-related activity in monkey superior colliculus: I. Characteristics of burst and buildup cells. *J. Neurophysiol.* 73, 2313–2333. doi: 10.1152/jn.1995.73.6.2313

Munoz, D. P., and Wurtz, R. H. (1995b). Saccade-related activity in monkey superior colliculus: II. Spread of activity during saccades. *J. Neurophysiol.* 73, 2334–2348. doi: 10.1152/jn.1995.73.6.2334

Optican, L. M. (1995). A field theory of saccade generation: temporal-to-spatial transform in the superior colliculus. *Vision Res.* 35, 3313–3320. doi: 10.1016/0042-6989(95)00129-3

Otmakhova, N., Duzel, E., Deutch, A. Y., and Lisman, J. (2013). "The hippocampal-VTA loop: the role of novelty and motivation in controlling the entry of information into long-term memory," in *Intrinsically Motivated Learning in Natural and Artificial Systems*, eds G. Baldassarre and M. Mirolli (Berlin: Springer), 235–254.

Pélisson, D., Goffart, L., Guillaume, A., Catz, N., and Raboyeau, G. (2001). Early head movements elicited by visual stimuli or collicular electrical stimulation in the cat. *Vision Res.* 41, 3283–3294. doi: 10.1016/s0042-6989(01)00224-3

Pesaran, B., Pezaris, J. S., Sahani, M., Mitra, P. P., and Andersen, R. A. (2002). Temporal structure in neuronal activity during working memory in macaque parietal cortex. *Nat. Neurosci.* 5, 805–811. doi: 10.1038/nn890

Pierrot-Deseilligny, C., Rivaud, S., Gaymard, B., and Agid, Y. (1991a). Cortical control of memory-guided saccades in man. *Exp. Brain Res.* 83, 607–617. doi: 10.1007/bf00229839

Pierrot-Deseilligny, C., Rivaud, S., Gaymard, B., and Agid, Y. (1991b). Cortical control of reflexive visually-guided saccades. *Brain* 114, 1473–1485. doi: 10.1093/brain/114.3.1473

Postle, B. R., Berger, J. S., Taich, A. M., and D'Esposito, M. (2000). Activity in human frontal cortex associated with spatial working memory and saccadic behavior. *J. Cogn. Neurosci.* 12, 2–14. doi: 10.1162/089892900564028

Redgrave, P., Coizet, V., Comoli, E., McHaffie, J. G., Leriche, M., Vautrelle, N., et al. (2010). Interactions between the midbrain superior colliculus and the basal ganglia. *Front. Neuroanat.* 4:132. doi: 10.3389/fnana.2010.00132

Robinson, D. L., and Kertzman, C. (1995). Covert orienting of attention in macaques. III. Contributions of the superior colliculus. *J. Neurophysiol.* 74, 713–721. doi: 10.1152/jn.1995.74.2.713

Roy, J. E., and Cullen, K. E. (1998). A neural correlate for vestibulo-ocular reflex suppression during voluntary eye-head gaze shifts. *Nat. Neurosci.* 1, 404–410. doi: 10.1038/1619

Sadeh, M., Sajad, A., Wang, H., Yan, X., and Crawford, J. D. (2015). Spatial transformations between superior colliculus visual and motor response fields during head-unrestrained gaze shifts. *Eur. J. Neurosci.* 42, 2934–2951. doi: 10.1111/ejn.13093

Sadeh, M., Sajad, A., Wang, H., Yan, X., and Crawford, J. D. (2018). Timing determines tuning: a rapid spatiotemporal transformation in superior colliculus neurons during reactive gaze shifts. *BioRxiv:302125 [Preprint]*. doi: 10.1101/302125

Sadeh, M., Wang, H. Y., Keith, G. P., and Crawford, J. D. (2012). Visual and motor frames of reference in primates' superior colliculus during head-unrestrained gaze shifts. *Can. J. Exp. Psychol. Rev.* 66, 319–319.

Sajad, A., Sadeh, M., Keith, G. P., Yan, X., Wang, H., and Crawford, J. D. (2015). Visual-motor transformations within frontal eye fields during head-unrestrained gaze shifts in the monkey. *Cereb. Cortex* 25, 3932–3952. doi: 10.1093/cercor/bhu279

Sajad, A., Sadeh, M., Yan, X., Wang, H., and Crawford, J. D. (2016a). *Time Course for the Accumulation of Errors in the Superior Colliculus During Memory-Guided Gaze Shift.* San Diego, CA: Society for Neuroscience.

Sajad, A., Sadeh, M., Yan, X., Wang, H., and Crawford, J. D. (2016b). Transition from target to gaze coding in primate frontal eye field during memory delay and memory-motor transformation. *eNeuro* 3:ENEURO.0040-16.2016. doi: 10.1523/ENEURO.0040-16.2016

Schall, J. D. (2001). Neural basis of deciding, choosing and acting. *Nat. Rev. Neurosci.* 2, 33–42. doi: 10.1038/35049054

Snyder, L. H., Calton, J. L., Dickinson, A. R., and Lawrence, B. M. (2002). Eye-hand coordination: saccades are faster when accompanied by a coordinated arm movement. *J. Neurophysiol.* 87, 2279–2286. doi: 10.1152/jn.00854.2001

Sparks, D. L. (1978). Functional properties of neurons in the monkey superior colliculus: coupling of neuronal activity and saccade onset. *Brain Res.* 156, 1–16. doi: 10.1016/0006-8993(78)90075-6

Sparks, D. L. (2002). The brainstem control of saccadic eye movements. *Nat. Rev. Neurosci.* 3, 952–964. doi: 10.1038/nrn986

Sparks, D. L., Freedman, E. G., Chen, L. L., and Gandhi, N. J. (2001). Cortical and subcortical contributions to coordinated eye and head movements. *Vision Res.* 41, 3295–3305. doi: 10.1016/s0042-6989(01)00063-3

Sparks, D. L., and Hartwich-Young, R. (1989). The deep layers of the superior colliculus. *Rev. Oculomot. Res.* 3, 213–255.

Sparks, D., Lee, C., and Rohrer, W. (1990). Population coding of the direction, amplitude and velocity of saccadic eye movements by neurons in the superior colliculus. *Cold Spring Harb. Symp. Quant. Biol.* 55, 805–811. doi: 10.1101/SQB.1990.055.01.075

Stanford, T. R., and Sparks, D. L. (1994). Systematic errors for saccades to remembered targets: evidence for a dissociation between saccade metrics and activity in the superior colliculus. *Vision Res.* 34, 93–106. doi: 10.1016/0042-6989(94)90260-7

Stricanne, B., Andersen, R. A., and Mazzoni, P. (1996). Eye-centered, head-centered and intermediate coding of remembered sound locations in area LIP. *J. Neurophysiol.* 76, 2071–2076. doi: 10.1152/jn.1996.76.3.2071

Stuphorn, V. (2007). New functions for an old structure: superior colliculus and head-only movements. Focus on "The role of primate superior colliculus in the control of head movements". *J. Neurophysiol.* 98, 1847–1848. doi: 10.1152/jn.00665.2007

Thiele, A., Henning, P., Kubischik, M., and Hoffmann, K.-P. (2002). Neural mechanisms of saccadic suppression. *Science* 295, 2460–2462. doi: 10.1126/science.1068788

Thompson, K. G., Hanes, D. P., Bichot, N. P., and Schall, J. D. (1996). Perceptual and motor processing stages identified in the activity of macaque frontal eye field neurons during visual search. *J. Neurophysiol.* 76, 4040–4055. doi: 10.1152/jn.1996.76.6.4040

Tweed, D. B., and Vilis, T. (1990). The superior colliculus and spatiotemporal translation in the saccadic system. *Neural Netw.* 3, 75–86. doi: 10.1016/0893-6080(90)90046-n

Waitzman, D. M., Ma, T. P., Optican, L. M., and Wurtz, R. H. (1991). Superior colliculus neurons mediate the dynamic characteristics of saccades. *J. Neurophysiol.* 66, 1716–1737. doi: 10.1152/jn.1991.66.5.1716

Walton, M. M., Bechara, B., and Gandhi, N. J. (2007). Role of the primate superior colliculus in the control of head movements. *J. Neurophysiol.* 98, 2022–2037. doi: 10.1152/jn.00258.2007

Walton, M. M., Sparks, D. L., and Gandhi, N. J. (2005). Simulations of saccade curvature by models that place superior colliculus upstream from the local feedback loop. *J. Neurophysiol.* 93, 2354–2358. doi: 10.1152/jn.01199.2004

White, J. M., Sparks, D. L., and Stanford, T. R. (1994). Saccades to remembered target locations: an analysis of systematic and

variable errors. *Vision Res.* 34, 79–92. doi: 10.1016/0042-6989(94)90259-3

Wurtz, R. H., and Albano, J. E. (1980). Visual-motor function of the primate superior colliculus. *Annu. Rev. Neurosci.* 3, 189–226. doi: 10.1146/annurev.ne.03.030180.001201

Wurtz, R. H., and Goldberg, M. E. (1972a). Activity of superior colliculus in behaving monkey: 3. Cells discharging before eye movements. *J. Neurophysiol.* 35, 575–586. doi: 10.1152/jn.1972.35.4.575

Wurtz, R. H., and Goldberg, M. E. (1972b). Activity of superior colliculus in behaving monkey: IV. Effects of lesions on eye movements. *J. Neurophysiol.* 35, 587–596. doi: 10.1152/jn.1972.35.4.587

Conflict of Interest Statement: The authors declare that the research was conducted in the absence of any commercial or financial relationships that could be construed as a potential conflict of interest.

frontiers in Neural Circuits

MINI REVIEW
published: 28 August 2018
doi: 10.3389/fncir.2018.00069

Causal Role of Neural Signals Transmitted From the Frontal Eye Field to the Superior Colliculus in Saccade Generation

Masayuki Matsumoto[1,2,3]*, *Ken-ichi Inoue*[4,5] *and Masahiko Takada*[4]

[1]*Division of Biomedical Science, Faculty of Medicine, University of Tsukuba, Tsukuba, Japan,* [2]*Graduate School of Comprehensive Human Sciences, University of Tsukuba, Tsukuba, Japan,* [3]*Transborder Medical Research Center, University of Tsukuba, Tsukuba, Japan,* [4]*Systems Neuroscience Section, Primate Research Institute, Kyoto University, Inuyama, Japan,* [5]*Precursory Research for Embryonic Science and Technology (PRESTO), Japan Science and Technology Agency (JST), Kawaguchi, Japan*

The frontal eye field (FEF) and superior colliculus (SC) are major and well-studied components of the oculomotor system. The FEF sends strong projections to the SC directly, and neurons in these brain regions transmit a variety of signals related to saccadic eye movements. Electrical microstimulation and pharmacological manipulation targeting the FEF or SC affect saccadic eye movements. These data suggest the causal contribution of each region to saccade generation. To understand how the brain generates behavior, however, it is critical not only to identify the structures and functions of individual regions, but also to elucidate how they interact with each other. In this review article, we first survey previous works that aimed at investigating whether and how the FEF and SC interact to regulate saccadic eye movements using electrophysiological and pharmacological techniques. These works have reported what signals FEF neurons transmit to the SC and what roles such signals play in regulating oculomotor behavior. We then highlight a recent attempt of our own that has applied an optogenetic approach to stimulate the neural pathway from the FEF to the SC in nonhuman primates. This study has shown that optogenetic stimulation of the FEF-SC pathway is sufficiently effective not only to modulate SC neuron activity, but also to evoke saccadic eye movements. Although the oculomotor system is a complex neural network composed of numbers of cortical and subcortical regions, the optogenetic approach will provide a powerful strategy for elucidating the role of each neural pathway constituting this network.

Keywords: frontal eye field, superior colliculus, saccade, optogenetics, macaque monkey

OPEN ACCESS

Edited by:
Tadashi Isa,
Kyoto University, Japan

Reviewed by:
Marc A. Sommer,
Duke University, United States
Laurent Petit,
Centre National de la Recherche Scientifique (CNRS), France
Ziad M. Hafed,
Universität Tübingen, Germany

***Correspondence:**
Masayuki Matsumoto
mmatsumoto@md.tsukuba.ac.jp

Received: *26 February 2018*
Accepted: *07 August 2018*
Published: *28 August 2018*

Citation:
Matsumoto M, Inoue K and Takada M (2018) Causal Role of Neural Signals Transmitted From the Frontal Eye Field to the Superior Colliculus in Saccade Generation. Front. Neural Circuits 12:69. doi: 10.3389/fncir.2018.00069

INTRODUCTION

The oculomotor system is composed of numbers of cortical and subcortical regions that form a complex neural network. The frontal eye field (FEF) and the superior colliculus (SC) are major components of this system. The roles of the FEF and SC in regulating oculomotor behavior have long been investigated in macaque monkeys in which the oculomotor system is substantially developed. Electrophysiological recording studies have reported that

neurons in both the FEF and the SC transmit a variety of signals related to saccadic eye movements, ranging from visual responses evoked by saccadic targets to burst firing before and after the execution of the eye movements (Bizzi, 1968; Schiller and Koerner, 1971; Wurtz and Goldberg, 1971; Mohler et al., 1973; Bruce and Goldberg, 1985). Electrical microstimulation of the FEF or SC elicits saccadic eye movements (Robinson and Fuchs, 1969; Robinson, 1972; Schiller and Stryker, 1972; Bruce et al., 1985), while pharmacological inactivation of either region severely disrupts the eye movements (Hikosaka and Wurtz, 1985; Dias et al., 1995; Sommer and Tehovnik, 1997; Dias and Segraves, 1999). Notably, inactivation of the FEF more severely disrupts saccadic eye movements than that of other cortical oculomotor areas (Sommer and Tehovnik, 1999; Chafee and Goldman-Rakic, 2000). These works suggest the strong causal contribution of the FEF and SC to saccade generation.

Understanding how the brain generates behavior, however, requires more than just analyzing the roles of individual regions. It is critical to determine how particular regions interact with each other and how their interaction contributes to behavior. Since the FEF and SC are mutually connected in a manner that the former projects directly to the latter (Fries, 1984; Komatsu and Suzuki, 1985; Stanton et al., 1988b), while the latter sends signals indirectly to the former via the mediodorsal nucleus of the thalamus (MD; Sommer and Wurtz, 2002, 2004a,b), these regions could interact to regulate saccadic eye movements. Here we first review prior electrophysiological and pharmacological studies that aimed at investigating what signals FEF neurons transmit to the SC and what roles these signals play in regulating oculomotor behavior. Evidence accumulated by these studies indicates that the FEF is largely involved in saccade generation by conveying oculomotor signals to the SC.

The optogenetic methodology that has been used to stimulate signal transmission connecting two given brain regions (Bernstein and Boyden, 2011; Tye and Deisseroth, 2012) allows us to directly address what roles the neural signals transmitted from the FEF to the SC play in regulating saccadic eye movements. Such optogenetic methodology has brought substantial success in modulating behaviors in rodents (Stuber et al., 2011; Tye et al., 2011; Stamatakis and Stuber, 2012; Warden et al., 2012; Ahmari et al., 2013; Miyamoto et al., 2016), and has advanced our understanding of the roles of particular neural circuits in behaviors. After reviewing the electrophysiological and pharmacological studies, we highlight a recent attempt of our own that has applied an optogenetic approach to stimulate the neural pathway from the FEF to the SC in macaque monkeys. This study has shown that optogenetic stimulation of the FEF-SC pathway is sufficiently effective not only to modulate SC neuron activity, but also to evoke saccadic eye movements. The same procedure will be relevant to elucidating other neural network functions as well and will provide significant advances in understanding of brain mechanisms underlying behavioral control in nonhuman primates.

ROLES OF THE FEF-SC PATHWAY IN SACCADE GENERATION: ELECTROPHYSIOLOGICAL AND PHARMACOLOGICAL STUDIES

In order to consider how the FEF and SC interact to regulate saccadic eye movements, it is crucial to determine what signals FEF neurons transmit to the SC. To address this issue, previous studies identified FEF neurons projecting to the SC and recorded the activity of these neurons in macaque monkeys performing a visually- or memory-guided saccade task (Segraves and Goldberg, 1987; Sommer and Wurtz, 2000, 2001). To identify the SC-projecting FEF neurons, they were antidromically activated by electrical microstimulation of the SC. Sommer and Wurtz (2000) found that the corticotectal neurons transmitted a variety of signals related to saccadic eye movements. These neurons exhibited visual responses to saccadic targets, tonic discharges during the delay period of the memory-guided saccade task, and/or burst firing before and after the execution of the eye movements. In addition, some corticotectal neurons showed discharges during fixation. Thus, the FEF relays visual-, memory-, motor- and even fixation-related signals to the SC (**Figure 1**). Since all these signals are observed in a broad population of FEF neurons as well, the FEF is likely to provide the SC with non-biased, general signals rather than any specific signals.

In contrast with the above observations, however, Segraves and Goldberg (1987) reported that SC-projecting FEF neurons preferentially transmitted motor-related signals. They found that the corticotectal neurons had little or no response to visual stimuli, but exhibited very strong activity before both visually- and memory-guided saccadic eye movements. Sommer and Wurtz (2000) discussed why these two studies reached the contradictory results. The most critical reason may be related to the topographic distribution of responsive neurons. Although Sommer and Wurtz (2000) found that the corticotectal neurons conveyed a variety of signals, neuronal populations with distinct

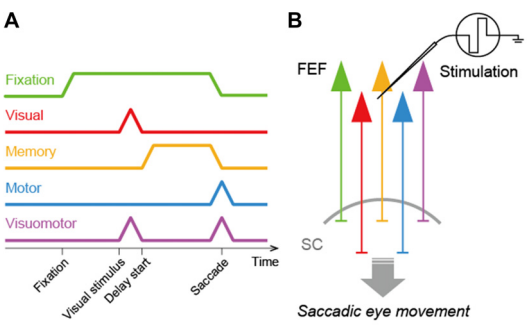

FIGURE 1 | Signal transmission in the frontal eye field-superior colliculus (FEF-SC) pathway. **(A)** Diagram of signals transmitted from the FEF to the SC. The FEF transmits fixation- (green), visual- (red), memory- (orange), motor- (blue) and visuomotor- (purple) related signals to the SC. **(B)** Schema of the FEF-SC pathway. The effect of FEF stimulation on saccadic eye movements is predominantly mediated by this pathway.

signals were distributed differently in the FEF. In fact, the neurons with motor-related signals tended to be located in the medial part of the FEF, and tended to project to the caudal level of the SC. If Segraves and Goldberg (1987) focused their recordings on the medial FEF or their stimulations on the caudal SC, this could account for why they observed a larger proportion of motor-related neurons than other neuron types. Consistent with the observations in the study of Sommer and Wurtz (2000); Everling and Munoz (2000) found that the antidromically-identified corticotectal neurons in the FEF transmitted not only motor-, but also visual-related signals during the performance of a pro- or an anti-saccade task.

The FEF sends projections not only to the SC, but also to other oculomotor structures in the brainstem (Stanton et al., 1988b). Therefore, the FEF might contribute to saccade generation via its output pathway to the brainstem that bypasses the SC. To test whether FEF signals transmitted to the SC participate in saccade generation, Hanes and Wurtz (2001) pharmacologically inactivated the SC in macaque monkeys and examined the effect of electrical microstimulation of the FEF on saccadic eye movements in the animals. In their experimental condition, the FEF-SC pathway was disrupted but the FEF-brainstem pathway was kept intact. If the FEF-brainstem pathway is more responsible for saccade generation than the FEF-SC pathway, then the FEF microstimulation is supposed to evoke saccadic eye movements even in SC-inactivated animals. Contrary to this supposition, they found that the SC inactivation eliminated saccadic eye movements evoked by the FEF microstimulation. Notably, this effect was observed when the stimulation site in the FEF and the inactivation site in the SC topographically overlapped. These findings suggest that the FEF-brainstem pathway is not sufficiently operative to generate saccadic eye movements on their own, and that FEF signals transmitted to the SC contribute to saccade generation. It should be noted, however, that bilateral lesions of the SC do not completely disrupt saccade generation. Schiller et al. (1980) reported that monkeys can produce voluntary saccadic eye movements even only 4 days after bilateral SC lesions, whereas paired lesions of the FEF and SC cause drastic deficits in the eye movements. These findings suggest that the FEF may possess functional routes that bypass the SC to generate saccadic eye movements. Such routes might not work in normal animals, but become active in the absence of the SC.

ROLES OF THE FEF-SC PATHWAY IN SACCADE GENERATION: OPTOGENETIC APPROACH

As mentioned above, Hanes and Wurtz (2001) showed the causal contribution of the FEF signals transmitted to the SC to saccade generation. However, the FEF not only directly projects to the SC, but also indirectly sends signals to the SC via other brain structures, such as the basal ganglia (for details, see the "Future Directions" section). It remains unclear whether the causal contribution is mediated by the direct or indirect pathway from the FEF to the SC. Optogenetics has provided a powerful tool to address these issues. For instance, neurons in a particular brain region are genetically modified to express channelrhodopsin-2 (ChR2), a blue-light-sensitive cation channel, by injecting a viral vector thereinto. Then, an optical fiber is placed into another region that receives projections from the infected region. Photo-stimulation of the ChR2 expressed on axon terminals induces a synaptic response to evoke signal transmission connecting the two regions. This methodology has brought substantial success in modulating behaviors in rodents (Stuber et al., 2011; Tye et al., 2011; Stamatakis and Stuber, 2012; Warden et al., 2012; Ahmari et al., 2013; Miyamoto et al., 2016), and has advanced our understanding of the roles of particular neural pathways in behaviors. However, the use of this methodology has greatly been restricted to small animals, and its application to primates which have much larger brains than rodents has so far been limited.

In our recent study (Inoue et al., 2015), we made an attempt to apply the optogenetic methodology to the primate oculomotor system that is substantially developed, as compared to the rodent system. Using this methodology, we stimulated the pathway from the FEF to the SC in macaque monkeys and analyzed the causal role of FEF signals transmitted to the SC in saccade generation (**Figure 2A**). An adeno-associated virus type 2 vector (AAV2-CMV-ChR2-EYFP) was injected unilaterally into the FEF, and, consequently, ChR2-positive axon terminals were observed in the ipsilateral SC, but not in the contralateral SC (**Figure 2B**). The axon terminals were stimulated by illuminating laser light into the SC. Through the optical stimulation of FEF axon terminals in the ipsilateral SC, many of recorded SC neurons exhibited an excitation that was sustained during laser light emission (left in **Figure 2C**), while only a few of them displayed an inhibition (right in **Figure 2C**). Thus, the direct stimulation of FEF signals transmitted to the SC can modulate SC neuron activity.

A pivotal issue of this research is whether the optogenetic methodology could induce behavioral modulations in primates. The optical stimulation of FEF axon terminals often evoked saccadic eye movements toward the response fields (RFs) corresponding to the stimulation sites in the SC (for a representative stimulation site, see **Figure 2D**). However, as a population, the magnitude of evoked saccadic eye movements was smaller than the eccentricity of the RF center (**Figure 2E**), suggesting that the intensity of optical stimulation was not enough to evoke full saccades that reach the eccentricity. The stimulation also modulated the latency of saccadic eye movements in a visually-guided saccade task in which the optical stimulation started simultaneously with the onset of a saccadic target that was presented inside or outside the RF. The stimulation decreased the latency of saccades toward the RF (for a representative stimulation site, see left in **Figure 2F**) and increased it away from the RF (see right in **Figure 2F**). These data indicate that stimulating the FEF-SC pathway, among the complex oculomotor network, is effective not only to modulate SC neuron activity, but also to initiate saccadic eye movements in macaque monkeys. The same optogenetic approach will be relevant to elucidating the roles of other neural pathways constituting the oculomotor network such as the pathway from the FEF to the lateral intraparietal area (LIP) and that from the LIP to the SC.

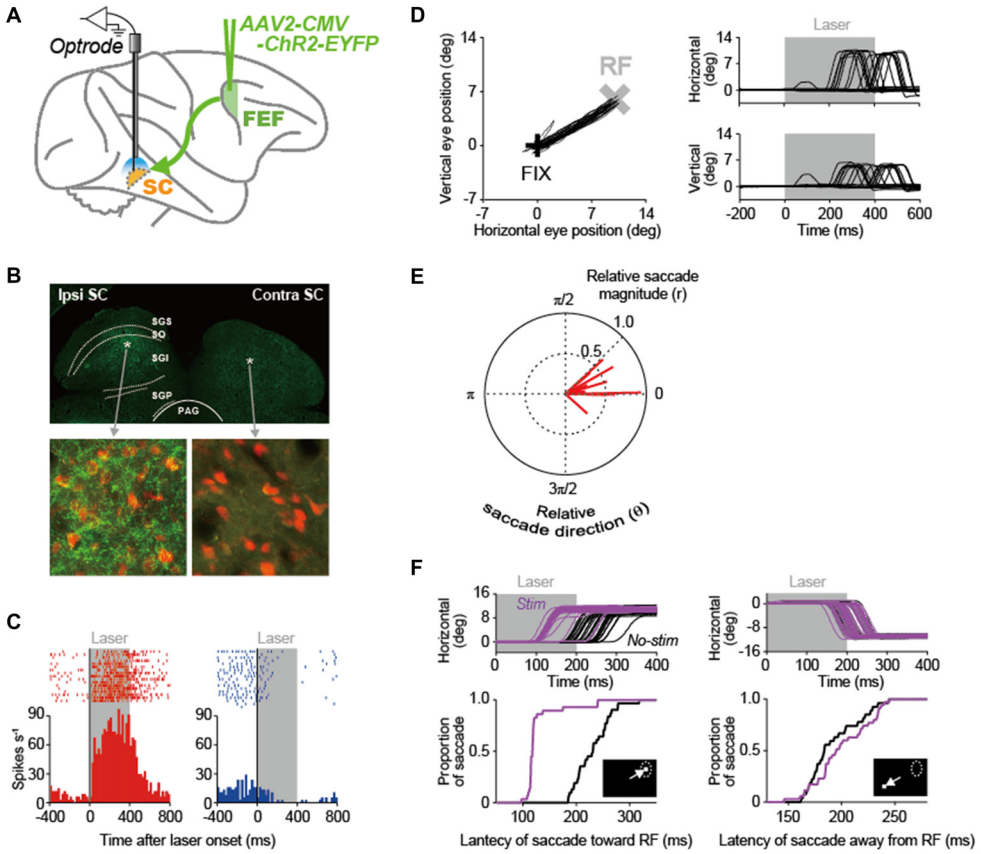

FIGURE 2 | Optogenetic approach to elucidating the role of the FEF-SC pathway in oculomotor behavior. **(A)** Experimental design. In order to deliver the channelrhodopsin-2 (ChR2) gene into FEF neurons, adeno-associated virus type 2 vector (AAV2-CMV-ChR2-EYFP) was injected unilaterally into the FEF. Using optrodes (an optic fiber attached to a recording electrode), 473-nm blue laser light was emitted into the SC and single-unit activity was simultaneously recorded. **(B)** ChR2-EYFP expression in the SC. Top, wide-field immunofluorescent image of a coronal section through the SC. Bottom, immunofluorescence of YFP-expressing axons in the ipsilateral and contralateral SC. NeuN-expressing SC neurons are shown in red. Asterisks in the above panel indicate the locations of the ipsilateral and contralateral images in the SC. PAG, periaqueductal gray; SGI, stratum griseum intermediale; SGP, stratum griseum profundum; SGS, stratum griseum superficiale; SO, stratum opticum. **(C)** Activity of two neuron examples that were excited (left) and inhibited (right) during laser light emission in the ipsilateral SC. Gray areas indicate the period of laser light emission. **(D)** Saccadic eye movements evoked by optical stimulation at a representative site in the ipsilateral SC. Left, trajectories of eye positions. Black and gray crosses indicate the fixation point (FIX) and the center of the response field (RF) at the stimulation site in the SC. The FIX was kept on during laser light emission. Right, horizontal and vertical eye traces. **(E)** Polar plot of the magnitude (r) and direction (θ) of evoked saccades relative to the RF center of the stimulation sites. Red lines indicate the averaged vector of evoked saccades at each stimulation site (n = 15). Saccade toward the RF center is denoted with (r, θ) = (1.0, 0). **(F)** Effect of optical stimulation at a representative site in the ipsilateral SC on saccade latency. Top, horizontal eye traces. Bottom, cumulative distribution of the latency of saccades toward the RF (left) and those away from the RF (right). Purple and black curves indicate stimulated and non-stimulated saccades, respectively. Reproduced with permission from Inoue et al. (2015).

FUTURE DIRECTIONS

Here, we have introduced the previous studies reporting what signals FEF neurons transmit to the SC and the causal contribution of these signals to saccade generation. However, it is not yet completely clear how the FEF and SC interact to generate saccadic eye movements. For instance, although FEF neurons seem to transmit visual-, memory- and motor-related signals to the SC, it remains to be determined which of these signals are involved in saccade generation. A recent study applied an optogenetic approach to the FEF in macaque monkeys and suppressed the activity of FEF neurons at any given timing in a memory-guided saccade task (Acker et al., 2016). This study found that suppression of FEF neurons during the visual, delay (i.e., memory), or movement periods altered the pattern of saccadic eye movements, suggesting that all of the FEF signals contribute to memory-guided saccades. By applying the circuit-level manipulation to their study, the role of each FEF signal transmitted to the SC in saccade generation will be determined.

The FEF is known to transmit signals related not only to simple saccade generation, but also to several executive functions, such as visual attention (Kodaka et al., 1997; Schall, 2004; Thompson et al., 2005), saccadic response inhibition (Hanes et al., 1998), and working memory (Sommer and Wurtz, 2001; Umeno and Goldberg, 2001). Some of these signals have been shown to be transmitted to the SC (Everling and Munoz, 2000;

Sommer and Wurtz, 2001). For instance, Everling and Munoz (2000) identified FEF neurons projecting to the SC using antidromic stimulation in monkeys, and recorded their activity while the monkey was performing a pro- or an anti-saccade task. They found that saccade-related corticotectal neurons were inhibited in the context in which the monkey was required to inhibit a reflexive saccadic eye movement toward a visual stimulus (i.e., anti-saccade task) compared with the context in which the animal was simply required to make the reflexive eye movement (i.e., pro-saccade task). Their findings suggest that the FEF transmits signals involved in the executive control of oculomotor behavior to the SC. It remains to be determined, however, what roles such corticotectal signals play in regulating executive functions. The electrophysiological, pharmacological and optogenetic approaches that we have introduced above will be applicable to address this issue.

Neurons in the FEF exert their effects on the SC not only through the direct projection to the SC, especially to its deeper layers, but also by way of the basal ganglia. The caudate nucleus and the rostral part of the putamen, input stations of the basal ganglia, receive projections from the FEF (Stanton et al., 1988a; Parthasarathy et al., 1992; Neggers et al., 2015) and, in turn, send projections to the substantia nigra pars reticulata (SNr; Parent et al., 1984;François et al., 1987), an output station of the basal ganglia. Then, the SNr sends projections to the deeper layers of the SC (Beckstead et al., 1981; Francois et al., 1984). Thus, the basal ganglia appear to mediate signal transmission from the FEF to the SC. Notably, since the SNr sends GABAergic projections to the SC (Vincent et al., 1978; Di Chiara et al., 1979), the SNr is most likely to exert a strong inhibitory effect on the activity of SC neurons (Hikosaka and Wurtz, 1983). In particular, it has been proposed that the SNr contributes to saccade generation by disinhibiting SC neuron activity (Hikosaka et al., 2000), although the exact role of the FEF-basal ganglia-SC pathway is still unclear. It remains to be determined how the two parallel pathways, i.e., the FEF-SC and FEF-basal ganglia-SC pathways, cooperate in regulating saccadic eye movements.

There are other brain structures than the basal ganglia that connect the FEF and SC. Among them, the cerebellum has attracted attention for its crucial roles in voluntary eye movements (Robinson and Fuchs, 2001). The anatomical organization of cerebro-cerebellar circuits has been established especially by Strick and colleagues (Lynch et al., 1994; Kelly and Strick, 2003; Strick et al., 2009). At least part of the cerebellum projects directly to the SC (May et al., 1990). The cerebellum also communicates with the basal ganglia multisynaptically (Hoshi et al., 2005; Bostan et al., 2010).

We have so far introduced prior attempts that investigated the role of signals transmitted from the FEF to the SC. On the other hand, the SC sends back signals to the FEF via the MD (Sommer and Wurtz, 2002, 2004a,b). It has previously been shown that the SC-MD-FEF pathway transmit signals related to the corollary discharge (or internal copy) of oculomotor command, and that pharmacological inactivation of the MD impairs sequential eye movements consistent with the loss of the corollary discharge (Sommer and Wurtz, 2002, 2004b). Understanding how the entire oculomotor network including the FEF, SC, basal ganglia, cerebellum and MD generates oculomotor behavior is a challenging issue. Optogenetic techniques applicable to primates could have advantages to address this issue.

AUTHOR CONTRIBUTIONS

MM conceived of the review topic and all authors wrote the review article.

FUNDING

This work was supported by Grants-in-Aid for Scientific Research (15H05879 and 17H05565 to KI, 16H02454 to MT and 26120707, 26710001 and 16H06567 to MM) from the Ministry of Education, Science, Sports, Culture and Technology of Japan; PREST (JPMJPR1683) from the Japan Science and Technology Agency (JST) to KI; Funding Program for Next Generation World-Leading Researchers (LS074) to MM from Cabinet Office, Government of Japan; the Takeda Science Foundation to MM; the Inamori Foundation to MM; and the Uehara Memorial Foundation to MM.

REFERENCES

Acker, L., Pino, E. N., Boyden, E. S., and Desimone, R. (2016). FEF inactivation with improved optogenetic methods. *Proc. Natl. Acad. Sci. U S A* 113, E7297–E7306. doi: 10.1073/pnas.1610784113

Ahmari, S. E., Spellman, T., Douglass, N. L., Kheirbek, M. A., Simpson, H. B., Deisseroth, K., et al. (2013). Repeated cortico-striatal stimulation generates persistent OCD-like behavior. *Science* 340, 1234–1239. doi: 10.1126/science.1234733

Beckstead, R. M., Edwards, S. B., and Frankfurter, A. (1981). A comparison of the intranigral distribution of nigrotectal neurons labeled with horseradish peroxidase in the monkey, cat and rat. *J. Neurosci.* 1, 121–125. doi: 10.1523/JNEUROSCI.01-02-00121.1981

Bernstein, J. G., and Boyden, E. S. (2011). Optogenetic tools for analyzing the neural circuits of behavior. *Trends Cogn. Sci.* 15, 592–600. doi: 10.1016/j.tics.2011.10.003

Bizzi, E. (1968). Discharge of frontal eye field neurons during saccadic and following eye movements in unanesthetized monkeys. *Exp. Brain Res.* 6, 69–80. doi: 10.1007/bf00235447

Bostan, A. C., Dum, R. P., and Strick, P. L. (2010). The basal ganglia communicate with the cerebellum. *Proc. Natl. Acad. Sci. U S A* 107, 8452–8456. doi: 10.1073/pnas.1000496107

Bruce, C. J., and Goldberg, M. E. (1985). Primate frontal eye fields. I. Single neurons discharging before saccades. *J. Neurophysiol.* 53, 603–635. doi: 10.1152/jn.1985.53.3.603

Bruce, C. J., Goldberg, M. E., Bushnell, M. C., and Stanton, G. B. (1985). Primate frontal eye fields. II. Physiological and anatomical correlates of electrically evoked eye movements. *J. Neurophysiol.* 54, 714–734. doi: 10.1152/jn.1985.54.3.714

Chafee, M. V., and Goldman-Rakic, P. S. (2000). Inactivation of parietal and prefrontal cortex reveals interdependence of neural activity during memory-guided saccades. *J. Neurophysiol.* 83, 1550–1566. doi: 10.1152/jn.2000.83.3.1550

Di Chiara, G., Porceddu, M. L., Morelli, M., Mulas, M. L., and Gessa, G. L. (1979). Evidence for a GABAergic projection from the substantia nigra to the ventromedial thalamus and to the superior colliculus of the rat. *Brain Res.* 176, 273–284. doi: 10.1016/0006-8993(79)90983-1

Dias, E. C., Kiesau, M., and Segraves, M. A. (1995). Acute activation and inactivation of macaque frontal eye field with GABA-related

drugs. *J. Neurophysiol.* 74, 2744–2748. doi: 10.1152/jn.1995.74.6.2744

Dias, E. C., and Segraves, M. A. (1999). Muscimol-induced inactivation of monkey frontal eye field: effects on visually and memory-guided saccades. *J. Neurophysiol.* 81, 2191–2214. doi: 10.1152/jn.1999.81.5.2191

Everling, S., and Munoz, D. P. (2000). Neuronal correlates for preparatory set associated with pro-saccades and anti-saccades in the primate frontal eye field. *J. Neurosci.* 20, 387–400. doi: 10.1523/JNEUROSCI.20-01-00387.2000

Francois, C., Percheron, G., and Yelnik, J. (1984). Localization of nigrostriatal, nigrothalamic and nigrotectal neurons in ventricular coordinates in macaques. *Neuroscience* 13, 61–76. doi: 10.1016/0306-4522(84)90259-8

François, C., Yelnik, J., and Percheron, G. (1987). Golgi study of the primate substantia nigra. II. Spatial organization of dendritic arborizations in relation to the cytoarchitectonic boundaries and to the striatonigral bundle. *J. Comp. Neurol.* 265, 473–493. doi: 10.1002/cne.902650403

Fries, W. (1984). Cortical projections to the superior colliculus in the macaque monkey: a retrograde study using horseradish peroxidase. *J. Comp. Neurol.* 230, 55–76. doi: 10.1002/cne.902300106

Hanes, D. P., Patterson, W. F. II., and Schall, J. D. (1998). Role of frontal eye fields in countermanding saccades: visual, movement and fixation activity. *J. Neurophysiol.* 79, 817–834. doi: 10.1152/jn.1998.79.2.817

Hanes, D. P., and Wurtz, R. H. (2001). Interaction of the frontal eye field and superior colliculus for saccade generation. *J. Neurophysiol.* 85, 804–815. doi: 10.1152/jn.2001.85.2.804

Hikosaka, O., and Wurtz, R. H. (1983). Visual and oculomotor functions of monkey substantia nigra pars reticulata. IV. Relation of substantia nigra to superior colliculus. *J. Neurophysiol.* 49, 1285–1301. doi: 10.1152/jn.1983.49.5.1285

Hikosaka, O., and Wurtz, R. H. (1985). Modification of saccadic eye movements by GABA-related substances. I. Effect of muscimol and bicuculline in monkey superior colliculus. *J. Neurophysiol.* 53, 266–291. doi: 10.1152/jn.1985.53.1.266

Hikosaka, O., Takikawa, Y., and Kawagoe, R. (2000). Role of the basal ganglia in the control of purposive saccadic eye movements. *Physiol. Rev.* 80, 953–978. doi: 10.1152/physrev.2000.80.3.953

Hoshi, E., Tremblay, L., Féger, J., Carras, P. L., and Strick, P. L. (2005). The cerebellum communicates with the basal ganglia. *Nat. Neurosci.* 8, 1491–1493. doi: 10.1038/nn1544

Inoue, K., Takada, M., and Matsumoto, M. (2015). Neuronal and behavioural modulations by pathway-selective optogenetic stimulation of the primate oculomotor system. *Nat. Commun.* 6:8378. doi: 10.1038/ncomms9378

Kelly, R. M., and Strick, P. L. (2003). Cerebellar loops with motor cortex and prefrontal cortex of a nonhuman primate. *J. Neurosci.* 23, 8432–8444. doi: 10.1523/JNEUROSCI.23-23-08432.2003

Kodaka, Y., Mikami, A., and Kubota, K. (1997). Neuronal activity in the frontal eye field of the monkey is modulated while attention is focused on to a stimulus in the peripheral visual field, irrespective of eye movement. *Neurosci. Res.* 28, 291–298. doi: 10.1016/s0168-0102(97)00055-2

Komatsu, H., and Suzuki, H. (1985). Projections from the functional subdivisions of the frontal eye field to the superior colliculus in the monkey. *Brain Res.* 327, 324–327. doi: 10.1016/0006-8993(85)91528-8

Lynch, J. C., Hoover, J. E., and Strick, P. L. (1994). Input to the primate frontal eye field from the substantia nigra, superior colliculus and dentate nucleus demonstrated by transneuronal transport. *Exp. Brain Res.* 100, 181–186. doi: 10.1007/bf00227293

May, P. J., Hartwich-Young, R., Nelson, J., Sparks, D. L., and Porter, J. D. (1990). Cerebellotectal pathways in the macaque: implications for collicular generation of saccades. *Neuroscience* 36, 305–324. doi: 10.1016/0306-4522(90)90428-7

Miyamoto, D., Hirai, D., Fung, C. C., Inutsuka, A., Odagawa, M., Suzuki, T., et al. (2016). Top-down cortical input during NREM sleep consolidates perceptual memory. *Science* 352, 1315–1318. doi: 10.1126/science.aaf0902

Mohler, C. W., Goldberg, M. E., and Wurtz, R. H. (1973). Visual receptive fields of frontal eye field neurons. *Brain Res.* 61, 385–389. doi: 10.1016/0006-8993(73)90543-x

Neggers, S. F., Zandbelt, B. B., Schall, M. S., and Schall, J. D. (2015). Comparative diffusion tractography of corticostriatal motor pathways reveals differences between humans and macaques. *J. Neurophysiol.* 113, 2164–2172. doi: 10.1152/jn.00569.2014

Parent, A., Bouchard, C., and Smith, Y. (1984). The striatopallidal and striatonigral projections: two distinct fiber systems in primate. *Brain Res.* 303, 385–390. doi: 10.1016/0006-8993(84)91224-1

Parthasarathy, H. B., Schall, J. D., and Graybiel, A. M. (1992). Distributed but convergent ordering of corticostriatal projections: analysis of the frontal eye field and the supplementary eye field in the macaque monkey. *J. Neurosci.* 12, 4468–4488. doi: 10.1523/JNEUROSCI.12-11-04468.1992

Robinson, D. A. (1972). Eye movements evoked by collicular stimulation in the alert monkey. *Vision Res.* 12, 1795–1808. doi: 10.1016/0042-6989(72)90070-3

Robinson, D. A., and Fuchs, A. F. (1969). Eye movements evoked by stimulation of frontal eye fields. *J. Neurophysiol.* 32, 637–648. doi: 10.1152/jn.1969.32.5.637

Robinson, F. R., and Fuchs, A. F. (2001). The role of the cerebellum in voluntary eye movements. *Annu. Rev. Neurosci.* 24, 981–1004. doi: 10.1146/annurev.neuro.24.1.981

Schall, J. D. (2004). On the role of frontal eye field in guiding attention and saccades. *Vision Res.* 44, 1453–1467. doi: 10.1016/j.visres.2003.10.025

Schiller, P. H., and Koerner, F. (1971). Discharge characteristics of single units in superior colliculus of the alert rhesus monkey. *J. Neurophysiol.* 34, 920–936. doi: 10.1152/jn.1971.34.5.920

Schiller, P. H., and Stryker, M. (1972). Single-unit recording and stimulation in superior colliculus of the alert rhesus monkey. *J. Neurophysiol.* 35, 915–924. doi: 10.1152/jn.1972.35.6.915

Schiller, P. H., True, S. D., and Conway, J. L. (1980). Deficits in eye movements following frontal eye-field and superior colliculus ablations. *J. Neurophysiol.* 44, 1175–1189. doi: 10.1152/jn.1980.44.6.1175

Segraves, M. A., and Goldberg, M. E. (1987). Functional properties of corticotectal neurons in the monkey's frontal eye field. *J. Neurophysiol.* 58, 1387–1419. doi: 10.1152/jn.1987.58.6.1387

Sommer, M. A., and Tehovnik, E. J. (1997). Reversible inactivation of macaque frontal eye field. *Exp. Brain Res.* 116, 229–249. doi: 10.1007/pl00005752

Sommer, M. A., and Tehovnik, E. J. (1999). Reversible inactivation of macaque dorsomedial frontal cortex: effects on saccades and fixations. *Exp. Brain Res.* 124, 429–446. doi: 10.1007/s002210050639

Sommer, M. A., and Wurtz, R. H. (2000). Composition and topographic organization of signals sent from the frontal eye field to the superior colliculus. *J. Neurophysiol.* 83, 1979–2001. doi: 10.1152/jn.2000.83.4.1979

Sommer, M. A., and Wurtz, R. H. (2001). Frontal eye field sends delay activity related to movement, memory and vision to the superior colliculus. *J. Neurophysiol.* 85, 1673–1685. doi: 10.1152/jn.2001.85.4.1673

Sommer, M. A., and Wurtz, R. H. (2002). A pathway in primate brain for internal monitoring of movements. *Science* 296, 1480–1482. doi: 10.1126/science.1069590

Sommer, M. A., and Wurtz, R. H. (2004a). What the brain stem tells the frontal cortex. I. Oculomotor signals sent from superior colliculus to frontal eye field via mediodorsal thalamus. *J. Neurophysiol.* 91, 1381–1402. doi: 10.1152/jn.00738.2003

Sommer, M. A., and Wurtz, R. H. (2004b). What the brain stem tells the frontal cortex. II. Role of the SC-MD-FEF pathway in corollary discharge. *J. Neurophysiol.* 91, 1403–1423. doi: 10.1152/jn.00740.2003

Stamatakis, A. M., and Stuber, G. D. (2012). Activation of lateral habenula inputs to the ventral midbrain promotes behavioral avoidance. *Nat. Neurosci.* 15, 1105–1107. doi: 10.1038/nn.3145

Stanton, G. B., Goldberg, M. E., and Bruce, C. J. (1988a). Frontal eye field efferents in the macaque monkey: I. Subcortical pathways and topography of striatal and thalamic terminal fields. *J. Comp. Neurol.* 271, 473–492. doi: 10.1002/cne.902710402

Stanton, G. B., Goldberg, M. E., and Bruce, C. J. (1988b). Frontal eye field efferents in the macaque monkey: II. Topography of terminal fields in midbrain and pons. *J. Comp. Neurol.* 271, 493–506. doi: 10.1002/cne.902710403

Strick, P. L., Dum, R. P., and Fiez, J. A. (2009). Cerebellum and nonmotor function. *Annu. Rev. Neurosci.* 32, 413–434. doi: 10.1146/annurev.neuro.31.060407.125606

Stuber, G. D., Sparta, D. R., Stamatakis, A. M., van Leeuwen, W. A., Hardjoprajitno, J. E., Cho, S., et al. (2011). Excitatory transmission from the amygdala to nucleus accumbens facilitates reward seeking. *Nature* 475, 377–380. doi: 10.1038/nature10194

Thompson, K. G., Biscoe, K. L., and Sato, T. R. (2005). Neuronal basis of covert spatial attention in the frontal eye field. *J. Neurosci.* 25, 9479–9487. doi: 10.1523/JNEUROSCI.0741-05.2005

Tye, K. M., and Deisseroth, K. (2012). Optogenetic investigation of neural circuits underlying brain disease in animal models. *Nat. Rev. Neurosci.* 13, 251–266. doi: 10.1038/nrn3171

Tye, K. M., Prakash, R., Kim, S. Y., Fenno, L. E., Grosenick, L., Zarabi, H., et al. (2011). Amygdala circuitry mediating reversible and bidirectional control of anxiety. *Nature* 471, 358–362. doi: 10.1038/nature09820

Umeno, M. M., and Goldberg, M. E. (2001). Spatial processing in the monkey frontal eye field. II. Memory responses. *J. Neurophysiol.* 86, 2344–2352. doi: 10.1152/jn.2001.86.5.2344

Vincent, S. R., Hattori, T., and McGeer, E. G. (1978). The nigrotectal projection: a biochemical and ultrastructural characterization. *Brain Res.* 151, 159–164. doi: 10.1016/0006-8993(78)90959-9

Warden, M. R., Selimbeyoglu, A., Mirzabekov, J. J., Lo, M., Thompson, K. R., Kim, S. Y., et al. (2012). A prefrontal cortex-brainstem neuronal projection that controls response to behavioural challenge. *Nature* 492, 428–432. doi: 10.1038/nature11617

Wurtz, R. H., and Goldberg, M. E. (1971). Superior colliculus cell responses related to eye movements in awake monkeys. *Science* 171, 82–84. doi: 10.1126/science.171.3966.82

Conflict of Interest Statement: The authors declare that the research was conducted in the absence of any commercial or financial relationships that could be construed as a potential conflict of interest.

frontiers in Neural Circuits

PERSPECTIVE
published: 24 July 2018
doi: 10.3389/fncir.2018.00059

The Mouse Superior Colliculus as a Model System for Investigating Cell Type-Based Mechanisms of Visual Motor Transformation

Ana F. Oliveira[1,2] *and Keisuke Yonehara*[1,2]*

[1] *DANDRITE – Danish Research Institute of Translational Neuroscience, Nordic EMBL Partnership for Molecular Medicine, Aarhus, Denmark,* [2] *Department of Biomedicine, Aarhus University, Aarhus, Denmark*

The mouse superior colliculus (SC) is a laminar midbrain structure involved in processing and transforming multimodal sensory stimuli into ethologically relevant behaviors such as escape, defense, and orienting movements. The SC is unique in that the sensory (visual, auditory, and somatosensory) and motor maps are overlaid. In the mouse, the SC receives inputs from more retinal ganglion cells than any other visual area. This makes the mouse SC an ideal model system for understanding how visual signals processed by retinal circuits are used to mediate visually guided behaviors. This Perspective provides an overview of the current understanding of visual motor transformations operated by the mouse SC and discusses the challenges to be overcome when investigating the input–output relationships in single collicular cell types.

Keywords: superior colliculus, visual processing, sensorimotor transformation, retinal ganglion cell, functional connectivity

OPEN ACCESS

Edited by:
Jason W. Triplett,
Children's National Health System,
United States

Reviewed by:
Martha E. Bickford,
University of Louisville, United States
Jianhua Cang,
University of Virginia, United States

***Correspondence:**
Keisuke Yonehara
keisuke.yonehara@dandrite.au.dk

Received: *30 March 2018*
Accepted: *03 July 2018*
Published: *24 July 2018*

Citation:
Oliveira AF and Yonehara K (2018) The Mouse Superior Colliculus as a Model System for Investigating Cell Type-Based Mechanisms of Visual Motor Transformation. Front. Neural Circuits 12:59. doi: 10.3389/fncir.2018.00059

INTRODUCTION

The superior colliculus (SC) is an evolutionarily conserved brain region found in mammals, homologous to the tectum in non-mammalian vertebrate species. It receives retinotopically organized synaptic inputs from retinal ganglion cells and reconstructs the spatial structure of the visual image (Cang and Feldheim, 2013; Cang et al., 2018). Historically, the SC has been studied in order to understand two different biological problems. The first is the mechanisms governing how topographic axonal projections from the chick and mouse retinas become established. These rely on axon guidance molecules (Frisén et al., 1998; Feldheim et al., 2000; Sweeney et al., 2015; Ito and Feldheim, 2018) and on spontaneous retinal waves (Chandrasekaran, 2005; Liu et al., 2014; Ito and Feldheim, 2018). However, until recently, the diversity of presynaptic retinal ganglion cell types (Kong et al., 2005; Völgyi et al., 2009; Sümbül et al., 2014; Baden et al., 2016) and postsynaptic collicular cell types (Mooney et al., 1988b; Gale and Murphy, 2014; Shang et al., 2015) has seldom been related to the organization of the retino-collicular projection (McIlwain, 1978; Hong et al., 2011; Joesch et al., 2016; Reinhard et al., 2018). The second problem concerns the neural mechanisms underlying saccadic eye movements in non-human primates (Schiller et al., 1980, 1979; Campos et al., 2006; Basso and May, 2017).

In rodents, the SC has also been used for studying innate behaviors related to avoidance or orientation (Sahibzada et al., 1986; Dean et al., 1988, 1989). These output behaviors are of great ecological value: the detection of (and consequent escape from) a predator, or effective localization

and orientation adjustments to catch prey, can determine survival. Although these SC functions were uncovered several decades ago, it was not until recently that the physiological and behavioral roles of each collicular cell type began to be investigated (Gale and Murphy, 2014; Shang et al., 2015, 2018; Wei et al., 2015).

In the coming years, we expect we will determine a unified understanding of the function of the mouse SC at many levels: from gene function, cell types, and circuits to behavior. This Perspective aims to discuss the advantages of using the mouse SC as a model system for investigating the contribution of individual visual channels to visually guided behaviors, and proposes future research directions.

FUNCTIONAL ORGANIZATION OF THE SUPERFICIAL LAYERS OF THE MOUSE SUPERIOR COLLICULUS

The SC can be subdivided in the visuosensory and the motor layers. The latter consists of the intermediate and deeper layers. The superficial layers are visuosensory and include (from the surface): the *stratum zonale* (SZ), the *stratum griseum superficiale* (SGS), and the *stratum opticum* (SO; May, 2006; Ito and Feldheim, 2018).

In the mouse, the superficial layers of the SC (sSC) are the major retino-recipient structure in the brain, receiving input from ca. 90% of retinal ganglion cells (Ellis et al., 2016), and from the striate and extrastriate visual cortex (Wang and Burkhalter, 2013).

Visual responses to the appearance, disappearance, or movement of a stimulus were first detected in the mouse sSC several decades ago (Dräger and Hubel, 1975a,b). Later, single-unit extracellular recordings from the sSC in anesthetized mice during visual stimulation revealed several types of visual responses, including ON/OFF responses to flashing spot stimuli and orientation-selective (OS) responses. Interestingly, there were no changes in OS responses following a V1 lesion or dark-rearing-mediated visual deprivation (Wang et al., 2010), suggesting that collicular OS responses might either emerge *de novo* in the SC or be inherited from the retina. In addition, *in vivo* two-photon calcium imaging recordings identified direction-selective (DS) neurons in the most superficial lamina of the SC, the density of which declines with increasing distance from the surface of the SC (Inayat et al., 2015). Recently, it has been reported that DS responses in the sSC are inherited from the retina (Shi et al., 2017).

THE SC AS A MODEL SYSTEM FOR VISUAL PROCESSING

Visual processing begins in the retina, where ca. 40 types of ganglion cells have been identified (Baden et al., 2016). Evidence from zebrafish (Robles et al., 2014) and mice (Ellis et al., 2016) indicates that there is massive divergence and convergence of axonal projections from retinal ganglion cell types to the brain. In other words, many ganglion cells project to multiple brain targets using collaterals (Ellis et al., 2016; Huang et al., 2017), and single brain centers receive inputs from multiple retinal ganglion cell types (Ellis et al., 2016; Reinhard et al., 2018). However, it is not yet understood how different ganglion cell types contribute to animal behavior, except for a few specialized cell types such as melanopsin-positive ganglion cells (Chen et al., 2011; Schmidt et al., 2011) or ON DS cells (Yonehara et al., 2009; Dhande et al., 2013).

The retina can be viewed as a parallel assemblage of small circuit modules represented by approximately 40 mosaics of retinal ganglion cells. Is the SC also functionally organized in parallel modules, operating the same computation throughout the SC? Recently, a column-like organization of OS cells was identified in the mouse SC where all angles and positions are not covered uniformly in the sSC. Feinberg and Meister (2015) revealed large patches containing OS cells with similar tuning. Ahmadlou and Heimel (2015) reported that neurons in the same column tend to prefer the same orientation, which is parallel to the concentric circle around the center of the visual field; this spatial organization could allow SC neurons to best respond to an expanding and receding optic flow. Another example of non-uniform coverage is the clustered distribution of the axon terminals of a transient OFF alpha ganglion cell type (Huberman et al., 2008) and an ON–OFF DS ganglion cell type (Rivlin-Etzion et al., 2011) along the surface of the SC, failing to cover all retinotopic locations on the SC. Investigating the synaptic and circuit mechanisms underlying the tuning to the expanding and receding optic flow in the sSC could reveal the key principles governing retino-collicular visual processing.

THE SC MEDIATES TRACTABLE BEHAVIORS

The rodent SC has commonly been associated with three types of output: escape/freezing defense-like behaviors, orienting movements, and autonomic responses. Defense-like behaviors consist of movements directed away from aversive stimuli, whereas orienting movements are generally directed toward attractive stimuli (Dean et al., 1989). Autonomic responses include marked changes in heart rate and blood pressure, and cortical arousal in response to visual emergencies (Redgrave and Dean, 1985; Keay et al., 1988).

Investigations into avoidance behaviors after visual stimulation have demonstrated that mice freeze and/or escape in response to a looming stimulus in the upper visual field, but not in the lower visual field, thereby suggesting that behavioral decisions are made based on the location of the stimulus within the visual field (Yilmaz and Meister, 2013; DeFranceschi et al., 2016). Follow-up studies have revealed that the sSC play a role in this behavior (Shang et al., 2015, 2018; Wei et al., 2015; Huang et al., 2017).

Orienting movements performed by the mouse are also being investigated. Mice exposed to crickets exhibit robust prey capture behavior and this behavior relies on vision (Hoy et al., 2016). While it has not yet been confirmed that the SC has a role in prey capture behavior in the mouse, undercutting the SC in the hamster impaired the pursuit of crickets (Finlay et al., 1980). Similarly, the SC has been shown to be involved in prey capture in other vertebrates (Ewert, 1974; Semmelhack et al., 2014).

THE SC AS A MODEL SYSTEM FOR SENSORIMOTOR TRANSFORMATION

The SC processes both aversive and appetitive visual stimuli, generating motor output responses related to avoidance and orientation, but the exact contributions of different retinal ganglion cell types to these visual motor transformations are not yet understood.

It has been suggested that one type of OFF ganglion cell in the retina is approach sensitive, as it responds to expanding, but not receding, black spots (Münch et al., 2009). Another population of ganglion cells, characterized as having the smallest and densest receptive fields, is thought to serve as an alarm neuron for overhead predators (Zhang Y. et al., 2012). How these approach or alarm retinal signals are processed by the sSC circuitry and transmitted to downstream premotor areas remains unknown.

Interestingly, stimulating the medial SC evokes avoidance or defense reactions in rodents, whereas stimulating the lateral SC elicits orienting or approach responses (Sahibzada et al., 1986; Dean et al., 1988). Because the medial and lateral SCs analyze the upper and lower visual field, respectively, these findings echo the behavioral observations that looming stimuli evoke escape/freeze behaviors only when presented from above.

Neurons in the sSC project to the intermediate (iSC) and deep layers (dSC) of the SC (Mooney et al., 1988a). Projections from deeper layers to the nuclei of the brainstem can be either contralateral (from the lateral regions of the SC) or ipsilateral (from medial regions; Bickford and Hall, 1989). Consequently, contralateral projections tend to mediate orienting behaviors, while ipsilateral projections tend to mediate avoidance behaviors (Redgrave et al., 1996a,b; Comoli et al., 2012). In line with these findings, stimulating the cuneiform nucleus (Cn) and the parabigeminal nucleus (PbG), two of the main targets of ipsilateral descending projections (Redgrave et al., 1987), evokes escape/freezing behaviors in rodents (Parker and Sinnamon, 1983; Mitchell et al., 1988; Shang et al., 2015; Caggiano et al., 2018). Furthermore, the Cn receives projections from the medial part of the SC, a region representing the upper visual field (Westby et al., 1990). Future research should examine how distinct dSC output cells collect information from retinal ganglion cell types *via* sSC neurons to extract salient features from the visual scene (**Figure 1**).

Together, these reports suggest that visual pathways dedicated to survival-related behaviors are hard-wired by segregated neuronal projections, possibly by intrinsic genetic mechanisms.

GENETIC LABELING OF SC CELL TYPES IN MICE

To understand the circuit mechanisms underlying visual processing and sensorimotor transformation, cell type-based studies are crucial, as they make it possible to link light responses, connectivity, behavior, and gene expression (**Figure 1**). As with zebrafish (Robles et al., 2011), gaining genetic access to cell types in the mouse SC will be critical for untangling the functional connectivity of neuronal circuits in the SC.

To date, four distinct cell types have been identified in the mouse sSC: narrow-field, wide-field, horizontal, and stellate cells. It has been suggested that a group of small cells at the border of the SZ, with dendrites extending toward the upper SGS, make up a fifth cell type, the marginal cells (May, 2006). However, attempts to characterize the electrophysiological properties of this cell type have failed to distinguish it from stellate cells (Gale and Murphy, 2014). Nonetheless, a population of DS cells with compact receptive fields, containing both excitatory and inhibitory neurons, has been found in the superficial SGS: these could be marginal cells (Inayat et al., 2015).

Narrow-field cells are labeled with Cre recombinase in the transgenic mouse Grp-KH288-Cre (Gerfen et al., 2013; Gale and Murphy, 2014). They are small, with thick dendrites extending dorsally toward the SC surface and ventrally toward the SC deeper layers. They have small receptive fields, respond to slowly moving stimuli and are DS (Gale and Murphy, 2014). Narrow-field cells project to the deeper layers of the SC and to the PbG (**Figure 1**). Given their projection pattern and their physiological responses, it is tempting to speculate that these cells could be involved in signaling the location of salient visual inputs to the iSC and therefore shifting the gaze toward a target, and/or in avoidance responses mediated by the SC–PbG–amygdala pathway (Shang et al., 2015).

Wide-field cells are labeled with Cre recombinase in the transgenic mouse Ntsr1-GN209-Cre (Gerfen et al., 2013; Gale and Murphy, 2014). These cells display dendrites extending diagonally to the surface of the SC and forming a large field. They respond best to slowly moving stimuli and can be DS and/or OS. These cells project to the lateral posterior nucleus of the thalamus (LP; **Figure 1**; Gale and Murphy, 2014), which makes them a good candidate to mediate avoidance behaviors *via* the pathway connecting the SC–LP–amygdala (Wei et al., 2015).

Horizontal cells are labeled with Cre recombinase in the transgenic mouse line GAD2-Cre (Gerfen et al., 2013; Gale and Murphy, 2014). These cells have large receptive fields, respond best to either large stationary or fast-moving visual stimuli, and are rarely DS. They provide inhibitory input to both the dorsal and ventral lateral geniculate nucleus of the thalamus (LGN) and to the PbG (**Figure 1**; Gale and Murphy, 2014).

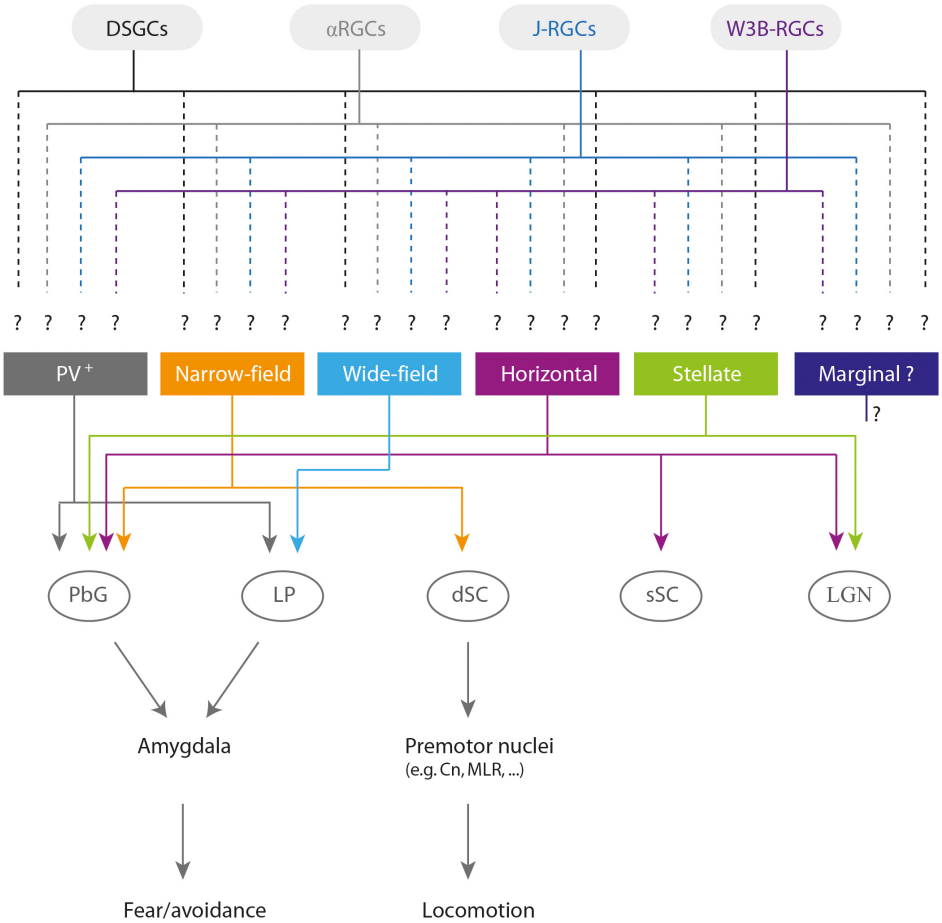

FIGURE 1 | Overview of the sSC cell types (Gale and Murphy, 2014; Inayat et al., 2015; Shang et al., 2015, 2018), potential inputs from retinal ganglion cell types (Sanes and Masland, 2015), relevant output brain targets, and behavioral roles. Note that the identity of the retinal ganglion cells projecting to each collicular cell type remains unknown. Abbreviations: DSGCs, direction-selective ganglion cells; αRGCs, alpha retinal ganglion cells; J-RGCs, JAM-B-expressing OFF retinal ganglion cells; PV^+, parvalbumin-positive neurons; dSC, deep layers of the superior colliculus; PbG, parabigeminal nucleus; LP, lateral posterior nucleus of the thalamus; sSC, superficial layers of the superior colliculus; LGN, lateral geniculate nucleus of the thalamus; Cn, cuneiform nucleus; MLR, mesencephalic locomotor region.

Stellate cells have multiple dendrites with no clear orientation and have small receptive fields. They respond best to small visual stimuli and project to both the PbG and LGN (**Figure 1**; Gale and Murphy, 2014, 2018). These cells are labelled in the transgenic mouse line Rorb-Cre, but horizontal and narrow-field cells are also labelled in this mouse line (Gale and Murphy, 2018), thereby hindering the investigation of the specific role of stellate cells in innate visual motor behavior.

The transgenic mouse line PV-ires-Cre labels cells in the SGS and SO known to project to the amygdala *via* the PbG and to mediate escape and freezing behavior (**Figure 1**; Shang et al., 2015, 2018). Recently, it has been shown that a subpopulation of parvalbumin-positive (PV^+) cells located in the SO projects to the LP and specifically mediates freezing behavior (**Figure 1**; Shang et al., 2018). Even though it was demonstrated that the PV^+ neurons in these studies were glutamatergic (Shang et al., 2015, 2018), PV^+ cells in the SC form a distinct mixed population of glutamatergic and GABAergic neurons with heterogeneous morphological and electrophysiological properties (Villalobos et al., 2018). While the morphological analysis described by Shang et al. (2015) suggests that these neurons might be narrow-field cells, a new report demonstrated that PV^+ neurons in the sSC also include stellate and horizontal cells (Villalobos et al., 2018). The diversity encountered among PV^+ neurons could indicate that these neurons serve multiple circuit and behavioral functions.

FUTURE DIRECTIONS AND CHALLENGES: VISUAL MOTOR TRANSFORMATION AT THE LEVEL OF A SINGLE CELL TYPE

A plethora of new molecular, genetic, and imaging tools that has become available in recent years now means that visual motor

transformations can be dissected at the single-cell type level. These tools make it possible to identify the locus of synapses within specific neuronal circuits mediating visual motor integration; this information will enable molecular and activity-dependent mechanisms underlying the circuit assembly to be studied.

Advances in mouse genetics have provided most of the essential tools for exploring the role of single cell types in visual motor behavior. Multiple mouse lines are now available, expressing Cre recombinase in specific cell types of particular brain regions (Taniguchi et al., 2011; Gerfen et al., 2013). However, a systematic approach for identifying and labeling SC cell types has rarely been applied (Byun et al., 2016). An unbiased method for characterizing cell types based on gene expression pattern, such as dropSeq (Klein et al., 2015; Macosko et al., 2015), could be used to identify cell types based on specific molecular markers. These could, then, be exploited to create transgenic mice in which a single cell type is labeled with Cre recombinase. Other approaches for targeting individual cell types could be selecting AAVs with tropism and/or a promoter for selective neuronal populations (Dimidschstein et al., 2016), or nanobodies that are reconstituted only when presented with a specific antigen (Tang et al., 2013).

Having a valuable collection of mouse lines with labeled SC cell types will provide excellent opportunities for linking their activity and connectivity. It will then be possible to examine how the convergence of ganglion cell types is organized at the level of brain targets' single cell types (**Figure 1**; Rompani et al., 2017) by combining trans-synaptic tracing with modified viral tracers expressing activity sensors and two-photon imaging (Yonehara et al., 2013; Wertz et al., 2015; Zingg et al., 2017).

Another unanswered question is how retinal signals processed by the sSC circuitry are transmitted to downstream premotor areas (**Figure 1**). Recent work has examined a similar problem using retrograde rabies virus-based trans-synaptic circuit tracing, and determined the combinations of neuronal pathways originating from retinal ganglion cell types projecting to two brain centers that mediate avoidance responses *via* the sSC (Reinhard et al., 2018). Follow-up experiments using specific inactivation and activation of the involved retinal ganglion cell types will be fundamental to understanding the contribution of each ganglion cell type to visual motor transformations.

Next, it will be imperative to examine how the retino-collicular connectivity that underlies visual processing operated by individual genetically labeled SC cell types is established by genetic- and activity-dependent mechanisms. The genetic mechanisms can be analyzed by testing the effect of gene knockdown in genetically labelled presynaptic ganglion cell types or postsynaptic sSC cell types, using conditional knockout mice or adeno-associated virus- or electroporation-mediated cell type-specific delivery of RNAi or CRISPR/Cas9 constructs. The contribution of activity-dependent mechanisms can be addressed by transiently activating or suppressing presynaptic or postsynaptic activity in a cell type- and developmental-specific manner, using optogenetic and chemogenetic tools (Zhang J. et al., 2012).

Finally, understanding to what extent the mechanistic insights obtained from the mouse SC are conserved across different animal species will be fundamental. Such work will deepen our understanding of how the species-specific functional organization of the SC is built to meet ethological requirements.

CONCLUSION

Here, we propose the mouse SC as an outstanding model for investigating sensorimotor transformation at the single-cell level. First, the laminar organization of the mouse (May, 2006) facilitates the identification of individual cell types. Second, the mouse is a genetically tractable animal and individual cell types can be labelled with DNA recombinase (Gerfen et al., 2013; Gale and Murphy, 2014), enabling manipulation and monitoring of specific collicular cell types. Third, the sSC receives monosynaptic inputs from retinal ganglion cells (Ellis et al., 2016) and is located relatively superficially, being accessible for imaging with two-photon microscopy (Ahmadlou and Heimel, 2015; Feinberg and Meister, 2015). Fourth, in the mouse, ca. 90% of the retinal ganglion cells project to the SC. Fifth, several behavioral paradigms are available for probing visual motor transformations processed by the SC (Shang et al., 2015; Wei et al., 2015). Last, breeding mice is faster, cheaper, and easier than breeding non-human primates, making the mouse a readily available tool to the wider scientific community. For these reasons, we expect the mouse SC to become heavily studied in the next years as a valuable system for examining cell type-based mechanisms underlying visual motor processing.

AUTHOR CONTRIBUTIONS

AO and KY wrote, edited, and revised the manuscript.

FUNDING

KY acknowledges grants from Lundbeckfonden, European Research Council Starting Grant (638730) and Novo Nordisk Foundation. AO was funded by a Marie Skłodowska-Curie individual fellowship "RETICULUS" and a MOBILEX grant from the Danish Research Council.

ACKNOWLEDGMENTS

We thank DANDRITE co-financed by Lundbeckfonden and Aarhus University. We also thank Sara Oakeley for commenting on the manuscript.

REFERENCES

Ahmadlou, M., and Heimel, J. A. (2015). Preference for concentric orientations in the mouse superior colliculus. *Nat. Commun.* 6:6773. doi: 10.1038/ncomms7773

Baden, T., Berens, P., Franke, K., Bethge, M., and Euler, T. (2016). The functional diversity of retinal ganglion cells in the mouse. *Nature* 529, 345–350. doi: 10.1038/nature16468

Basso, M. A., and May, P. J. (2017). Circuits for action and cognition: a view from the superior colliculus. *Annu. Rev. Vis. Sci.* 3, 197–226. doi: 10.1146/annurev-vision-102016-061234

Bickford, M. E., and Hall, W. C. (1989). Collateral projections of predorsal bundle cells of the superior colliculus in the rat. *J. Comp. Neurol.* 283, 86–106. doi: 10.1002/cne.902830108

Byun, H., Kwon, S., Ahn, H. J., Liu, H., Forrest, D., Demb, J. B., et al. (2016). Molecular features distinguish ten neuronal types in the mouse superficial superior colliculus. *J. Comp. Neurol.* 524, 2300–2321. doi: 10.1002/cne.23952

Caggiano, V., Leiras, R., Goñi-Erro, H., Masini, D., Bellardita, C., Bouvier, J., et al. (2018). Midbrain circuits that set locomotor speed and gait selection. *Nature* 553, 455–460. doi: 10.1038/nature25448

Campos, M., Cherian, A., and Segraves, M. A. (2006). Effects of eye position upon activity of neurons in macaque superior colliculus. *J. Neurophysiol.* 95, 505–526. doi: 10.1152/jn.00639.2005

Cang, J., and Feldheim, D. A. (2013). Developmental mechanisms of topographic map formation and alignment. *Annu. Rev. Neurosci.* 36, 51–77. doi: 10.1146/annurev-neuro-062012-170341

Cang, J., Savier, E., Barchini, J., and Liu, X. (2018). Visual function, organization, and development of the mouse superior colliculus. *Annu. Rev. Vis. Sci.* doi: 10.1146/annurev-vision-091517-034142 [Epub ahead of print].

Chandrasekaran, A. R. (2005). Evidence for an instructive role of retinal activity in retinotopic map refinement in the superior colliculus of the mouse. *J. Neurosci.* 25, 6929–6938. doi: 10.1523/JNEUROSCI.1470-05.2005

Chen, S. K., Badea, T. C., and Hattar, S. (2011). Photoentrainment and pupillary light reflex are mediated by distinct populations of ipRGCs. *Nature* 476, 92–96. doi: 10.1038/nature10206

Comoli, E., Das Neves Favaro, P., Vautrelle, N., Leriche, M., Overton, P. G., and Redgrave, P. (2012). Segregated anatomical input to sub-regions of the rodent superior colliculus associated with approach and defense. *Front. Neuroanat.* 6:9. doi: 10.3389/fnana.2012.00009

Dean, P., Mitchell, I. J., and Redgrave, P. (1988). Responses resembling defensive behaviour produced by microinjection of glutamate into superior colliculus of rats. *Neuroscience* 24, 501–510. doi: 10.1016/0306-4522(88)90345-4

Dean, P., Redgrave, P., and Westby, G. W. (1989). Event or emergency? Two response systems in the mammalian superior colliculus. *Trends Neurosci.* 12, 137–147. doi: 10.1016/0166-2236(89)90052-0

DeFranceschi, G., Vivattanasarn, T., Saleem, A., and Solomon, S. (2016). Vision guides selection of freeze or flight defense strategies in mice. *Curr. Biol.* 26, 2150–2154. doi: 10.1016/j.cub.2016.06.006

Dhande, O. S., Estevez, M. E., Quattrochi, L. E., El-Danaf, R. N., Nguyen, P. L., Berson, D. M., et al. (2013). Genetic dissection of retinal inputs to brainstem nuclei controlling image stabilization. *J. Neurosci.* 33, 17797–17813. doi: 10.1523/JNEUROSCI.2778-13.2013

Dimidschstein, J., Chen, Q., Tremblay, R., Rogers, S. L., Saldi, G.-A., Guo, L., et al. (2016). A viral strategy for targeting and manipulating interneurons across vertebrate species. *Nat. Neurosci.* 19, 1743–1749. doi: 10.1038/nn.4430

Dräger, U. C., and Hubel, D. H. (1975a). Physiology of visual cells in mouse superior colliculus and correlation with somatosensory and auditory input. *Nature* 253, 203–204. doi: 10.1038/253203a0

Dräger, U. C., and Hubel, D. H. (1975b). Responses to visual stimulation and relationship between visual, auditory, and somatosensory inputs in mouse superior colliculus. *J. Neurophysiol.* 38, 690–713.

Ellis, E. M., Gauvain, G., Sivyer, B., and Murphy, G. J. (2016). Shared and distinct retinal input to the mouse superior colliculus and dorsal lateral geniculate nucleus. *J. Neurophysiol.* 116, 602–610. doi: 10.1152/jn.00227.2016

Ewert, J. P. (1974). The neural basis of visually guided behavior. *Sci. Am.* 230, 34–42. doi: 10.1038/scientificamerican0374-34

Feinberg, E. H., and Meister, M. (2015). Orientation columns in the mouse superior colliculus. *Nature* 519, 232–299. doi: 10.1038/nature14103

Feldheim, D. A., Kim, Y.-I., Bergemann, A. D., Frisén, J., Barbacid, M., and Flanagan, J. G. (2000). Genetic analysis of Ephrin-A2 and Ephrin-A5 shows their requirement in multiple aspects of retinocollicular mapping. *Neuron* 25, 563–574. doi: 10.1016/S0896-6273(00)81060-0

Finlay, B. L., Sengelaub, D. R., Berg, A. T., and Cairns, S. J. (1980). A neuroethological approach to hamster vision. *Behav. Brain Res.* 1, 479–496. doi: 10.1016/0166-4328(80)90003-0

Frisén, J., Yates, P. A., McLaughlin, T., Friedman, G. C., O'Leary, D. D. M., and Barbacid, M. (1998). Ephrin-A5 (AL-1/RAGS) is essential for proper retinal axon guidance and topographic mapping in the mammalian visual system. *Neuron* 20, 235–243. doi: 10.1016/S0896-6273(00)80452-3

Gale, S. D., and Murphy, G. J. (2014). Distinct representation and distribution of visual information by specific cell types in mouse superficial superior colliculus. *J. Neurosci.* 34, 13458–13471. doi: 10.1523/JNEUROSCI.2768-14.2014

Gale, S. D., and Murphy, G. J. (2018). Distinct cell types in the superficial superior colliculus project to the dorsal lateral geniculate and lateral posterior thalamic nuclei. *J. Neurophysiol.* doi: 10.1152/jn.00248.2018 [Epub ahead of print].

Gerfen, C. R., Paletzki, R., and Heintz, N. (2013). GENSAT BAC cre-recombinase driver lines to study the functional organization of cerebral cortical and basal ganglia circuits. *Neuron* 80, 1368–1383. doi: 10.1016/j.neuron.2013.10.016

Hong, Y. K., Kim, I. J., and Sanes, J. R. (2011). Stereotyped axonal arbors of retinal ganglion cell subsets in the mouse superior colliculus. *J. Comp. Neurol.* 519, 1691–1711. doi: 10.1002/cne.22595

Hoy, J. L., Yavorska, I., Wehr, M., and Niell, C. M. (2016). Vision drives accurate approach behavior during prey capture in laboratory mice. *Curr. Biol.* 26, 3046–3052. doi: 10.1016/j.cub.2016.09.009

Huang, L., Yuan, T., Tan, M., Xi, Y., Hu, Y., Tao, Q., et al. (2017). A retinoraphe projection regulates serotonergic activity and looming-evoked defensive behaviour. *Nat. Commun.* 8:14908. doi: 10.1038/ncomms14908

Huberman, A. D., Manu, M., Koch, S. M., Susman, M. W., Lutz, A. B., Ullian, E. M., et al. (2008). Architecture and activity-mediated refinement of axonal projections from a mosaic of genetically identified retinal ganglion cells. *Neuron* 59, 425–438. doi: 10.1016/j.neuron.2008.07.018

Inayat, S., Barchini, J., Chen, H., Feng, L., Liu, X., and Cang, J. (2015). Neurons in the most superficial lamina of the mouse superior colliculus are highly selective for stimulus direction. *J. Neurosci.* 35, 7992–8003. doi: 10.1523/JNEUROSCI.0173-15.2015

Ito, S., and Feldheim, D. A. (2018). The mouse superior colliculus: an emerging model for studying circuit formation and function. *Front. Neural Circuits* 12:10. doi: 10.3389/fncir.2018.00010

Joesch, M., Mankus, D., Yamagata, M., Shahbazi, A., Schalek, R., Suissa-Peleg, A., et al. (2016). Reconstruction of genetically identified neurons imaged by serial-section electron microscopy. *eLife* 5:e15015. doi: 10.7554/eLife.15015

Keay, K. A., Redgrave, P., and Dean, P. (1988). Cardiovascular and respiratory changes elicited by stimulation of rat superior colliculus. *Brain Res. Bull.* 20, 13–26. doi: 10.1016/0361-9230(88)90004-4

Klein, A. M., Mazutis, L., Akartuna, I., Tallapragada, N., Veres, A., Li, V., et al. (2015). Droplet barcoding for single-cell transcriptomics applied to embryonic stem cells. *Cell* 161, 1187–1201. doi: 10.1016/j.cell.2015.04.044

Kong, J. H., Fish, D. R., Rockhill, R. L., and Masland, R. H. (2005). Diversity of ganglion cells in the mouse retina: unsupervised morphological classification and its limits. *J. Comp. Neurol.* 489, 293–310. doi: 10.1002/cne.20631

Liu, M., Wang, L., and Cang, J. (2014). Different roles of axon guidance cues and patterned spontaneous activity in establishing receptive fields in the mouse superior colliculus. *Front. Neural Circuits* 8:23. doi: 10.3389/fncir.2014.00023

Macosko, E. Z., Basu, A., Satija, R., Nemesh, J., Shekhar, K., Goldman, M., et al. (2015). Highly parallel genome-wide expression profiling of individual cells using nanoliter droplets. *Cell* 161, 1202–1214. doi: 10.1016/j.cell.2015.05.002

May, P. J. (2006). The mammalian superior colliculus: laminar structure and connections. *Prog. Brain Res.* 151, 321–378. doi: 10.1016/S0079-6123(05)51011-2

McIlwain, J. T. (1978). Cat superior colliculus: extracellular potentials related to W-cell synaptic actions. *J. Neurophysiol.* 41, 1343–1358. doi: 10.1152/jn.1978.41.5.1343

Mitchell, I. J., Dean, P., and Redgrave, P. (1988). The projection from superior colliculus to cuneiform area in the rat. II. Defence-like responses to stimulation with glutamate in cuneiform nucleus and surrounding structures. *Exp. Brain Res.* 72, 626–639. doi: 10.1007/BF00250607

Mooney, R. D., Nikoletseas, M., Hess, P. R., Allen, Z., Lewin, A. C., and Rhoades, R. W. (1988a). The projection from the superficial to the deep layers of the superior colliculus: an intracellular horseradish peroxidase injection study in the hamster. *J. Neurosci.* 8, 1384–1399.

Mooney, R. D., Nikoletseas, M., Ruiz, S., and Rhoades, R. (1988b). Receptive-field properties and morphological characteristics of the superior collicular neurons that project to the lateral posterior and dorsal lateral geniculate nuclei in the hamster. *J. Neurophysiol.* 59, 1333–1351.

Münch, T. A., Da Silveira, R. A., Siegert, S., Viney, T. J., Awatramani, G. B., and Roska, B. (2009). Approach sensitivity in the retina processed by a multifunctional neural circuit. *Nat. Neurosci.* 12, 1308–1316. doi: 10.1038/nn.2389

Parker, S., and Sinnamon, H. (1983). Forward locomotion elicited by electrical stimulation in the diencephalon and mesencephalon of the awake rat. *Physiol. Behav.* 31, 581–587.

Redgrave, P., and Dean, P. (1985). Tonic desynchronization of cortical electroencephalogram by electrical and chemical-stimulation of superior colliculus and surrounding structures in urethane-anaesthetized rats. *Neuroscience* 16, 659–671. doi: 10.1016/0306-4522(85)90199-X

Redgrave, P., McHaffie, J. G., and Stein, B. E. (1996a). Nociceptive neurones in rat superior colliculus. I. Antidromic activation from the contralateral predorsal bundle. *Exp. Brain Res.* 109, 185–196.

Redgrave, P., Simkins, M., McHaffie, J. G., and Stein, B. E. (1996b). Nociceptive neurones in rat superior colliculus. II. Effects of lesions to the contralateral descending output pathway on nocifensive behaviours. *Exp. Brain Res.* 109, 197–208. doi: 10.1007/BF00231781

Redgrave, P., Mitchell, I. J., and Dean, P. (1987). Descending projections from the superior colliculus in rat: a study using orthograde transport of wheatgerm-agglutinin conjugated horseradish peroxidase. *Exp. Brain Res.* 68, 147–167. doi: 10.1007/BF00255241

Reinhard, K., Li, C., Do, Q., Burke, E., Heynderickx, S., and Farrow, K. (2018). Target specific routing of visual information by the superior colliculus. *bioRxiv* [Preprint]. doi: 10.1101/272914

Rivlin-Etzion, M., Zhou, K., Wei, W., Elstrott, J., Nguyen, P. L., Barres, B. A., et al. (2011). Transgenic mice reveal unexpected diversity of on-off direction-selective retinal ganglion cell subtypes and brain structures involved in motion processing. *J. Neurosci.* 31, 8760–8769. doi: 10.1523/JNEUROSCI.0564-11.2011

Robles, E., Laurell, E., and Baier, H. (2014). The retinal projectome reveals brain-area-specific visual representations generated by ganglion cell diversity. *Curr. Biol.* 24, 2085–2096. doi: 10.1016/j.cub.2014.07.080

Robles, E., Smith, S. J., and Baier, H. (2011). Characterization of genetically targeted neuron types in the zebrafish optic tectum. *Front. Neural Circuits* 5:1. doi: 10.3389/fncir.2011.00001

Rompani, S. B., Müllner, F. E., Wanner, A., Zhang, C., Roth, C. N., Yonehara, K., et al. (2017). Different modes of visual integration in the lateral geniculate nucleus revealed by single-cell-initiated transsynaptic tracing. *Neuron* 93, 767–776. doi: 10.1016/j.neuron.2017.01.028

Sahibzada, N., Dean, P., and Redgrave, P. (1986). Movements resembling orientation or avoidance elicited by electrical stimulation of the superior colliculus in rats. *J. Neurosci.* 6, 723–733. doi: 10.1523/JNEUROSCI.06-03-00723.1986

Sanes, J. R., and Masland, R. H. (2015). The types of retinal ganglion cells: current status and implications for neuronal classification. *Annu. Rev. Neurosci.* 38, 221–246. doi: 10.1146/annurev-neuro-071714-034120

Schiller, P. H., True, S. D., and Conway, J. L. (1979). Effects of frontal eye field and superior colliculus ablations on eye movements. *Science* 206, 590–592. doi: 10.1126/science.115091

Schiller, P. H., True, S. D., and Conway, J. L. (1980). Deficits in eye movements following frontal eye-field and superior colliculus ablations. *J. Neurophysiol.* 44, 1175–1189. doi: 10.1152/jn.1980.44.6.1175

Schmidt, T. M., Chen, S. K., and Hattar, S. (2011). Intrinsically photosensitive retinal ganglion cells: many subtypes, diverse functions. *Trends Neurosci.* 34, 572–580. doi: 10.1016/j.tins.2011.07.001

Semmelhack, J. L., Donovan, J. C., Thiele, T. R., Kuehn, E., Laurell, E., and Baier, H. (2014). A dedicated visual pathway for prey detection in larval zebrafish. *eLife* 9:e04878. doi: 10.7554/eLife.04878

Shang, C., Chen, Z., Liu, A., Li, Y., Zhang, J., Qu, B., et al. (2018). Divergent midbrain circuits orchestrate escape and freezing responses to looming stimuli in mice. *Nat. Commun.* 9:1232. doi: 10.1038/s41467-018-03580-7

Shang, C., Liu, Z., Chen, Z., Shi, Y., Wang, Q., Liu, S., et al. (2015). A parvalbumin-positive excitatory visual pathway to trigger fear responses in mice. *Science* 348, 1472–1477. doi: 10.1126/science.aaa8694

Shi, X., Barchini, J., Ledesma, H. A., Koren, D., Jin, Y., Liu, X., et al. (2017). Retinal origin of direction selectivity in the superior colliculus. *Nat. Neurosci.* 20, 550–558. doi: 10.1038/nn.4498

Sümbül, U., Song, S., McCulloch, K., Becker, M., Lin, B., Sanes, J. R., et al. (2014). A genetic and computational approach to structurally classify neuronal types. *Nat. Commun.* 5:3512. doi: 10.1038/ncomms4512

Sweeney, N. T., James, K. N., Sales, E. C., and Feldheim, D. A. (2015). Ephrin-As are required for the topographic mapping but not laminar choice of physiologically distinct RGC types. *Dev. Neurobiol.* 75, 584–593. doi: 10.1002/dneu.22265

Tang, J. C. Y., Szikra, T., Kozorovitskiy, Y., Teixiera, M., Sabatini, B. L., Roska, B., et al. (2013). A nanobody-based system using fluorescent proteins as scaffolds for cell-specific gene manipulation. *Cell* 154, 928–939. doi: 10.1016/j.cell.2013.07.021

Taniguchi, H., He, M., Wu, P., Kim, S., Paik, R., Sugino, K., et al. (2011). A resource of Cre driver lines for genetic targeting of GABAergic neurons in cerebral cortex. *Neuron* 71, 995–1013. doi: 10.1016/j.neuron.2011.07.026

Villalobos, C. A., Wu, Q., Lee, P. H., May, P. J., and Basso, M. A. (2018). Parvalbumin and GABA microcircuits in the mouse superior colliculus. *Front. Neural Circuits* 12:35. doi: 10.3389/fncir.2018.00035

Völgyi, B., Chheda, S., and Bloomfield, S. A. (2009). Tracer coupling patterns of the ganglion cell subtypes in the mouse retina. *J. Comp. Neurol.* 512, 664–687. doi: 10.1002/cne.21912

Wang, L., Sarnaik, R., Rangarajan, K., Liu, X., and Cang, J. (2010). Visual receptive field properties of neurons in the superficial superior colliculus of the mouse. *J. Neurosci.* 30, 16573–16584. doi: 10.1523/JNEUROSCI.3305-10.2010

Wang, Q., and Burkhalter, A. (2013). Stream-related preferences of inputs to the superior colliculus from areas of dorsal and ventral streams of mouse visual cortex. *J. Neurosci.* 33, 1696–1705. doi: 10.1523/JNEUROSCI.3067-12.2013

Wei, P., Liu, N., Zhang, Z., Liu, X., Tang, Y., He, X., et al. (2015). Processing of visually evoked innate fear by a non-canonical thalamic pathway. *Nat. Commun.* 6:6756. doi: 10.1038/ncomms7756

Wertz, A., Trenholm, S., Yonehara, K., Hillier, D., Raics, Z., Leinweber, M., et al. (2015). Single-cell-initiated monosynaptic tracing reveals layer-specific cortical network modules. *Science* 349, 70–74. doi: 10.1126/science.aab1687

Westby, G. W., Keay, K. A., Redgrave, P., Dean, P., and Bannister, M. (1990). Output pathways from the rat superior colliculus mediating approach and avoidance have different sensory properties. *Exp. Brain Res.* 81, 626–638. doi: 10.1007/BF02423513

Yilmaz, M., and Meister, M. (2013). Rapid innate defensive responses of mice to looming visual stimuli. *Curr. Biol.* 23, 2011–2015. doi: 10.1016/j.cub.2013.08.015

Yonehara, K., Farrow, K., Ghanem, A., Hillier, D., Balint, K., Teixeira, M., et al. (2013). The first stage of cardinal direction selectivity is localized to the

dendrites of retinal ganglion cells. *Neuron* 79, 1078–1085. doi: 10.1016/j.neuron.2013.08.005

Yonehara, K., Ishikane, H., Sakuta, H., Shintani, T., Nakamura-Yonehara, K., Kamiji, N. L., et al. (2009). Identification of retinal ganglion cells and their projections involved in central transmission of information about upward and downward image motion. *PLoS One* 4:e4320. doi: 10.1371/journal.pone.0004320

Zhang, Y., Kim, I.-J., Sanes, J. R., and Meister, M. (2012). The most numerous ganglion cell type of the mouse retina is a selective feature detector. *Proc. Natl. Acad. Sci. U.S.A.* 109, E2391–E2398. doi: 10.1073/pnas.1211547109

Zhang, J., Ackman, J. B., Xu, H. P., and Crair, M. C. (2012). Visual map development depends on the temporal pattern of binocular activity in mice. *Nat. Neurosci.* 15, 298–307. doi: 10.1038/nn.3007

Zingg, B., Chou, X. L., Zhang, Z. G., Mesik, L., Liang, F., Tao, H. W., et al. (2017). AAV-mediated anterograde transsynaptic tagging: mapping corticocollicular input-defined neural pathways for defense behaviors. *Neuron* 93, 33–47. doi: 10.1016/j.neuron.2016.11.045

Conflict of Interest Statement: The authors declare that the research was conducted in the absence of any commercial or financial relationships that could be construed as a potential conflict of interest.

frontiers in Neural Circuits

ORIGINAL RESEARCH
published: 24 July 2018
doi: 10.3389/fncir.2018.00058

Orientation and Contrast Tuning Properties and Temporal Flicker Fusion Characteristics of Primate Superior Colliculus Neurons

Chih-Yang Chen [1,2,3] *and Ziad M. Hafed* [1,3]*

[1] *Physiology of Active Vision Laboratory, Werner Reichardt Centre for Integrative Neuroscience, Tübingen University, Tübingen, Germany,* [2] *Graduate School of Neural and Behavioural Sciences, International Max Planck Research School, Tübingen University, Tübingen, Germany,* [3] *Department of Cognitive Neurology, Hertie Institute for Clinical Brain Research, Tübingen University, Tübingen, Germany*

The primate superior colliculus is traditionally studied from the perspectives of gaze control, target selection, and selective attention. However, this structure is also visually responsive, and it is the primary visual structure in several species. Thus, understanding the visual tuning properties of the primate superior colliculus is important, especially given that the superior colliculus is part of an alternative visual pathway running in parallel to the predominant geniculo-cortical pathway. In recent previous studies, we have characterized receptive field organization and spatial frequency tuning properties in the primate (rhesus macaque) superior colliculus. Here, we explored additional aspects like orientation tuning, putative center-surround interactions, and temporal frequency tuning characteristics of visually-responsive superior colliculus neurons. We found that orientation tuning exists in the primate superior colliculus, but that such tuning is relatively moderate in strength. We also used stimuli of different sizes to explore contrast sensitivity and center-surround interactions. We found that stimulus size within a visual receptive field primarily affects the slope of contrast sensitivity curves without altering maximal firing rate. Additionally, sustained firing rates, long after stimulus onset, strongly depend on stimulus size, and this is also reflected in local field potentials. This suggests the presence of inhibitory interactions within and around classical receptive fields. Finally, primate superior colliculus neurons exhibit temporal frequency tuning for frequencies lower than 30 Hz, with critical flicker fusion frequencies of <20 Hz. These results support the hypothesis that the primate superior colliculus might contribute to visual performance, likely by mediating coarse, but rapid, object detection and identification capabilities for the purpose of facilitating or inhibiting orienting responses. Such mediation may be particularly amplified in blindsight subjects who lose portions of their primary visual cortex and therefore rely on alternative visual pathways including the pathway through the superior colliculus.

Keywords: superior colliculus, orientation tuning, contrast sensitivity, center-surround interactions, temporal frequency tuning, flicker fusion

OPEN ACCESS

Edited by:
Karl Farrow, Neuroelectronics Research Flanders, Belgium

Reviewed by:
J. Alexander Heimel, Netherlands Institute for Neuroscience (KNAW), Netherlands
Sarah L. Pallas, Georgia State University, United States

***Correspondence:**
Ziad M. Hafed
ziad.m.hafed@cin.uni-tuebingen.de

Received: *29 March 2018*
Accepted: *03 July 2018*
Published: *24 July 2018*

Citation:
Chen C-Y and Hafed ZM (2018) Orientation and Contrast Tuning Properties and Temporal Flicker Fusion Characteristics of Primate Superior Colliculus Neurons. Front. Neural Circuits 12:58. doi: 10.3389/fncir.2018.00058

INTRODUCTION

It has been shown since more than 70 years ago that superior colliculus (SC) neurons have visual responses. Almost in parallel with these findings, researchers have recognized that the SC is also a crucial midbrain structure for orienting behavior, especially for saccadic eye movements in primates (Wurtz and Optican, 1994). As a result, there was a relative abundance of studies in the primate model aimed at understanding subcortical connections for movement control, as well as cortical neural substrates for eye movements (Gandhi and Katnani, 2011). More recently, studies on the role of the primate SC in active vision have focused more heavily on cognitive tasks like target selection and visual attention (Krauzlis et al., 2013; Basso and May, 2017; Crapse et al., 2018; Odegaard et al., 2018). The visual properties of primate SC neurons, on the other hand, have been largely left out after some simple characterizations using light dots and bars.

In separate lines of research, it became recognized that saccadic viewing patterns, orienting efficiency, and target selection can drastically differ under a variety of visual conditions and in natural scene scenarios, and depending on factors like stimulus salience (White et al., 2008, 2017a,b; Veale et al., 2017). This means that low level image statistics can strongly influence eye movements (Ludwig et al., 2004; White et al., 2008; Chen and Hafed, 2017). Motivated by this, we have recently begun to characterize primate SC visual properties from an ecological perspective (Hafed and Chen, 2016). Our starting point was that the primate SC can be an important neural substrate for implementing visual salience maps that can guide behavior (Veale et al., 2017; White et al., 2017a,b) and this is consistent with how visual topography in the SC seems to be already co-registered with the deeper saccade map topography in the same structure (Cynader and Berman, 1972; Robinson, 1972). We have shown that visual (and saccade-related) topography is asymmetric between upper and lower visual fields (Hafed and Chen, 2016) and also that spatial frequency tuning properties of SC neurons allow this structure to facilitate gaze behavior under natural scene scenarios in which low spatial frequencies are predominant (Hafed and Chen, 2016; Chen and Hafed, 2017; Chen et al., in press). Here, we continued our investigation of the primate SC's visual properties. We focused on orientation tuning, especially given that recent rodent work has yielded some controversy (Ahmadlou and Heimel, 2015; Feinberg and Meister, 2015; Inayat et al., 2015). We also explored potential center-surround RF interactions as well as temporal frequency tuning properties.

Our efforts in the present paper, along with those in our recently published manuscripts, are specifically aimed at complementing early seminal work on the visual functions of the primate SC, primarily performed in the 1970's. For example, Schiller and Koerner conducted experiments on awake primates, like in our case, and reported no direction or orientation selectivity, although this was not explicitly quantified (Schiller and Koerner, 1971). Goldberg and Wurtz also studied awake animals and reported 10% of neurons having directional selectivity, but these authors did not examine orientation selectivity (Goldberg and Wurtz, 1972). We aimed to quantify such selectivity in the present study. Both groups of authors also described atypical center-surround RF interactions (Schiller and Koerner, 1971; Goldberg and Wurtz, 1972) but there were no investigations of how factors like stimulus contrast, sustained visual responses, and local population activity were related to these interactions; a primary objective of our current study was exactly to examine such factors. Finally, Schiller and Koerner also described the SC as a jerk detector (Schiller and Koerner, 1971) but response sensitivity to specific temporal frequencies of stimuli was not mapped, as we have done here. More broadly, the great majority of remaining early work on the visual functions of the primate SC has been performed on anesthetized animals as opposed to awake ones. For example, similar descriptions to those in Schiller and Koerner (1971) were made for anesthetized monkeys in Cynader and Berman (1972), Marrocco and Li (1977) and Moors and Vendrik (1979). Anesthetized monkeys were also used to study interactions of relative motion within SC RF's (Davidson and Bender, 1991). We believe that revisiting such early work (from both anesthetized and awake monkeys) with a more modern context is critical looking forward from now, especially for fully understanding how the SC can support perception, cognition, and action under a variety of naturalistic conditions, including social interactions (Chen et al., in press).

In all, we believe that our experiments, coupled with our recent findings on visual field topography, contrast sensitivity, and spatial frequency tuning (Chen et al., 2015, in press; Hafed and Chen, 2016; Chen and Hafed, 2017) support hypotheses that the SC can play an important role in determining visual capabilities during rapid orienting behavior, and also during clinical conditions of blindsight, in which loss of conscious visual perception through loss of primary visual cortex (V1) results in residual visual capabilities that can reflect involvement of alternative visual pathways (Yoshida et al., 2008, 2017; Cowey, 2010; Kato et al., 2011; Takaura et al., 2011; Leopold, 2012).

MATERIALS AND METHODS

Our monkey experiments were approved by the regional governmental offices in the city of Tuebingen (Regierungspräsidium Tübingen). The study was conducted in strict compliance of the European Union guidelines on animal research, as well as the associated German laws enforcing these guidelines.

Animal Preparation

Rhesus macaque monkeys P and N (male, *Macaca mulatta*, aged 7 years) were prepared for behavior and superior colliculus (SC) recordings earlier (Chen and Hafed, 2013; Chen et al., 2015). Briefly, we placed a recording chamber centered on the midline and aimed at a stereotaxically defined point 1 mm posterior of and 15 mm above the inter-aural line. The chamber was tilted posterior of vertical (by 38 and 35° for monkeys P and N, respectively). We implanted one eye of each monkey with scleral search coils for tracking eye movements, using high spatial and temporal precision, with the magnetic induction technique (Fuchs and Robinson, 1966; Judge et al., 1980). All implant surgeries (head holders, chambers, and eye coils) were performed

under full isoflurane anesthesia, and the animals received a combination of analgesics for several days after each procedure. No experiments were conducted except after full recovery from the surgeries. The animals also benefitted from regular visits from our university's veterinary service, occurring at least once per week.

Orientation Tuning Task

We asked the monkeys to perform a pure fixation task while we recorded the activity of visually-responsive SC neurons. In each trial, a white fixation spot (8.5 × 8.5 min arc) appeared over a gray background. Fixation spot and background luminance were described earlier (Chen and Hafed, 2013). After an initial fixation interval (400–550 ms), the fixation spot transiently dimmed for ∼50 ms. This was useful for resetting microsaccadic rhythms (Hafed and Ignashchenkova, 2013; Tian et al., 2016, 2018; Bellet et al., 2017). After an additional 110–320 ms, a stationary Gabor patch with 80% relative contrast (defined as Lmax – Lmin/Lmax + Lmin) appeared for ∼200 ms within the neuron's response field (RF). The Gabor patch was similar to that described in (Hafed and Chen, 2016; Chen and Hafed, 2017). The RF was estimated earlier in the session using standard saccade tasks (Chen et al., 2015; Hafed and Chen, 2016). In particular, delayed visually-guided and memory-guided saccades were used to allow us to isolate epochs of visual responsiveness (after target onset) or saccade-related discharge (near saccade onset), and we estimate visual and movement RF's by varying the location to which the saccades were made. The Gabor patch size that we presented during a given session (i.e., for a given neuron) was chosen to fill as much of the visual RF (characterized from the saccade tasks) as possible. The spatial frequency of the grating that we used was 2.22 cycles/° (cpd) because this spatial frequency drove our neurons well (Chen et al., 2015). Moreover, the orientation of the grating was varied randomly across trials. In monkey N, the orientations were 0, 30, 60, 90, 120, or 150° clockwise from vertical; in monkey P, the orientations were 0, 45, 90, or 135° clockwise from vertical. Grating phase was randomized from trial to trial, and the monkeys were rewarded only for maintaining fixation; no saccadic orienting to the grating or any other behavioral response was required.

We recorded from 43 well-isolated neurons (isolated and characterized online within each experimental session). The range of preferred eccentricities that we sampled (also for our other tasks below) was similar to our earlier studies (Chen et al., 2015; Hafed and Chen, 2016); also see **Figure 5E**. We excluded trials with microsaccades occurring within ±100 ms from stimulus onset because such occurrence can alter neural activity (Hafed, 2011; Hafed et al., 2015). Because of this, we further excluded 12 neurons that we had recorded, since they did not have >20 repetitions for all of the tested orientations. For the neurons that we included here, we had sufficient trials for analysis (we collected >255 trials per neuron; average: 389 ± 175 s.d.).

Contrast Sensitivity Task With Different Stimulus Sizes

We used the same contrast sensitivity task of Chen et al. (2015). However, in some trials, the stimulus was filling as much of the RF as possible (referred to here as the "big" stimulus condition), as in Chen et al. (2015) and in other trials, the stimulus was small (0.5–1° in size). This size was chosen to still allow at least 1 cycle of the 2.22 cpd grating to appear within the stimulus. We compared contrast sensitivity curves for the big and small stimuli.

We recorded from 27 neurons, each being exposed to the big (Chen et al., 2015) or small stimuli in the same session. The neurons responses to the big stimuli were included in Chen et al. (2015) but for analyses that were distinct from those that we are focusing on in the present study. In the present study, we compared responses to those with small stimuli (not described in our earlier study). We also excluded trials with microsaccades occurring within ±100 ms from stimulus onset as discussed above. We further excluded 3 recorded neurons since they did not have >25 repetitions for all the tested stimuli. Across neurons, we collected >181 trials per neuron (average: 253 ± 50 s.d.).

Temporal Flicker Task

In this task, a vertical Gabor grating of 2.22 cpd spatial frequency (similar to the gratings used in the orientation tuning task above) was flickered within the RF of a neuron for 2,000 ms. Flicker frequency could be 3, 5, 10, 20, or 60 Hz from trial to trial, and the flicker itself was achieved by turning the grating off (i.e., zero contrast grating) at regular temporal intervals dictated by the frequency chosen for any given trial (we used a 50% duty cycle for the flicker). Our display's refresh rate was 120 Hz. To avoid onset and offset transients, we gradually increased stimulus contrast at trial onset in the first 1,000 ms of a trial (to reach 80% contrast), and we similarly gradually decreased stimulus contrast at trial end for the final 1,000 ms of a trial. This was similar to the approach used to study flicker perception capabilities in blindsight human patients (Trevethan and Sahraie, 2003). The monkey was required to maintain fixation throughout the entire stimulus presentation sequence.

We recorded from 55 neurons. Ten neurons were excluded because they did not have >25 repetitions for all the tested stimuli. Across neurons, we collected >137 trials per neuron (average: 166 ± 29 s.d.).

Neuron Classification

We used similar neuron classification criteria to those used in our recent studies (Chen et al., 2015; Hafed and Chen, 2016; Chen and Hafed, 2017). Briefly, a neuron was labeled as visual if its activity 0–200 ms after target onset in a delayed saccade task (Hafed and Krauzlis, 2008; Hafed and Chen, 2016) was higher than activity 0–200 ms before target onset ($p < 0.05$, paired t-test). The neuron was labeled as visual-motor if its pre-saccadic activity (−50 to 0 ms from saccade onset) was also elevated in the delayed saccade task relative to an earlier fixation interval (100–175 ms before saccade onset) (Li and Basso, 2008). Our results were similar for either visual or visual-motor neurons, so we combined neuron types in all of our analyses.

Firing Rate Analyses

We analyzed SC visual bursts by measuring peak firing rate 20–150 ms after stimulus onset (Chen and Hafed, 2017). We then obtained contrast sensitivity curves as in Chen et al. (2015).

Specifically, we estimated semi-saturation contrast, baseline activity, and maximal firing rate (for the highest possible contrast), and we did so for either small or large stimuli. We did so by fitting the measured firing rate data to the following equation:

$$f(c) = R * \frac{c^n}{{C_{50}}^n + c^n} + B \quad (1)$$

where c is the tested contrast (5, 10, 20, 40, 80%) R is the maximal firing rate, C_{50} is the semi-saturation contrast, n is an exponent determining the steepness of the contrast sensitivity curve, and B is the baseline firing rate (obtained from all trials in the interval 0–50 ms before grating onset). The goodness of fit for the above equation was validated according to the approach in Carandini et al. (1997). All of our neurons had >80% explained variance by the fit. To combine different neurons in summary analyses, we first normalized the visual burst activity in each neuron to that observed for the highest contrast, and we then fit the normalized firing rate of all the neurons as one single population (**Figure 2D**). The sustained visual response of neurons was measured by obtaining the mean firing rate 150–250 ms after stimulus onset (**Figure 3D**).

For orientation tuning, we computed an orientation selectivity index (OSI) similar to that used in cortical visual areas, for example (Hansel and van Vreeswijk, 2012). This allowed us to directly compare orientation tuning properties in the SC to other cortical visual areas. Briefly, the OSI was calculated as follows:

$$OSI = \frac{R_{pref} - R_{ortho}}{R_{pref} + R_{ortho}} \quad (2)$$

where R_{pref} is the visual burst strength of the neuron for the preferred orientation (i.e., the orientation eliciting the most spikes) and R_{ortho} is the visual burst strength of the neuron for the orthogonal orientation relative to the preferred one.

To estimate how fast a given visual response was evoked for a given visual condition, we estimated first-spike latency of a visual burst (i.e., the average time from stimulus onset to the first stimulus-evoked action potential by a putative neuron). We did this by using Poisson spike train analysis (Legendy and Salcman, 1985).

For temporal flicker, in addition to raw plots of firing rates, we measured mean firing rate throughout a trial. We then measured all means across trials and plotted the average of these measurements as a function of the temporal frequency of the stimulus. Adopting a similar technique to (Derrington and Lennie, 1984), we fitted these measurements to a function that gave us a "tuning curve" for temporal frequency. The specific function that we used for our data was a difference-of-Gaussians function as follows:

$$f(x) = a_1 * e^{-\left(\frac{x-b_1}{c_1}\right)^2} - a_2 * e^{-\left(\frac{x-b_2}{c_2}\right)^2} + B \quad (3)$$

where x is the tested temporal frequency, a_1 and a_2 represent the amplitudes of each Gaussian function, b_1 and b_2 represent the means of each Gaussian function, c_1 and c_2 are the bandwidths of each Gaussian function, and B is the baseline firing rate (obtained from all trials in the interval 0–50 ms before grating onset). The goodness of fit was again validated using the approach in Carandini et al. (1997). All of our neurons had >80% explained variance by the fit.

We also performed Fourier transforms on the average firing rates obtained from a given flicker frequency. This allowed us to identify the firing rate amplitude at the primary oscillation frequency of neural fluctuations (F1), which should match the flicker frequency of the stimulus. We then computed the ratio of the amplitude of the oscillation at F1 to the amplitude at 0 Hz (i.e., the mean DC value of the firing rate; called F0) to obtain a sensitivity to the flicker at F1. We computed this sensitivity ratio (called F1/F0) for each tested temporal frequency, and we then fitted the data with a simple exponential decay function where the x-axis is temporal frequency and the y-axis is F1/F0. The stimulus flicker frequency for which the ratio of F1 amplitude to mean firing rate (F1/F0) was below 20% of the peak ratio was taken as the critical flicker fusion frequency of a given neuron (Wells et al., 2001); similarly, the stimulus flicker frequency for which the ratio of F1 firing rate to mean firing rate (F1/F0) was maximal was called the "peak" flicker frequency. For our estimates of preferred frequency, peak F1/F0, and critical flicker frequency, we had a lower and upper bound of 3 and 60 Hz, respectively, because these were the bounds of our sampling range for estimating temporal frequency tuning (e.g., see **Figure 5**).

Local Field Potential Analyses

For the stimulus size manipulation, we also analyzed local field potentials (LFP's). We obtained LFP's from wide-band neural signals using methods that we described recently (Hafed and Chen, 2016; Chen and Hafed, 2017). We then aligned LFP traces on stimulus onset, and we measured evoked and sustained responses. First, we measured the strongest deflection occurring in the interval 20–150 ms after stimulus onset, to obtain a measure that we called the transient LFP response. Second, we measured the mean deflection in the period 150–250 ms after stimulus onset, to obtain what we referred to as the sustained LFP response. Since the LFP evoked response is negative going, when we refer to a "peak" LFP response, we mean the most negative value of the measured signal.

RESULTS

Orientation Selective Neurons in the Primate SC

We recorded visual responses in macaque monkeys that were fixating a small spot, while we presented an oriented grating of 2.22 cycles/° (cpd) within a neuron's visual response field (RF). The grating was stationary and was presented for ∼200 ms. **Figure 1A** shows the responses of an example neuron exhibiting some orientation selectivity. Each colored curve shows raw firing rates from the neuron when a specific orientation was presented, and the orientations are arranged graphically according to the graphic placement of a firing rate plot (e.g., the magenta trace reflects responses to a grating that was tilted slightly rightward of purely vertical). The central part of the figure shows a plot

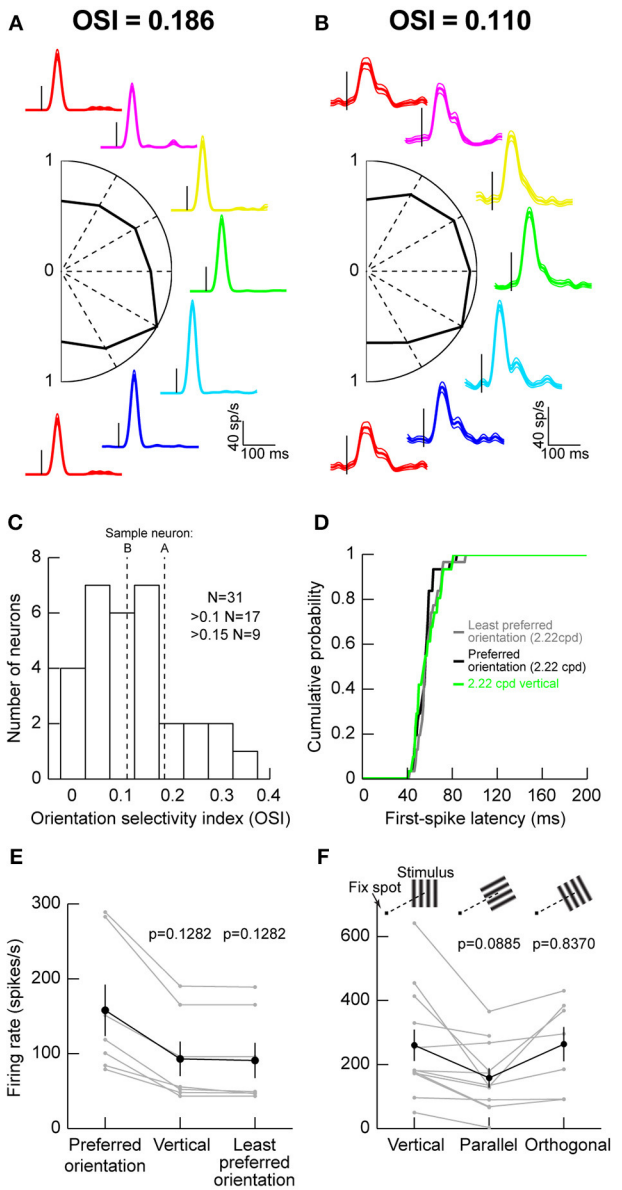

FIGURE 1 | Orientation tuning in the macaque superior colliculus (SC). **(A)** Visual responses of an example SC neuron to gratings of different orientations (color-coded) presented within the neuron's visual response field (RF). The firing rate curves are graphically arranged according to the grating orientation. For example, the red curves are for vertical gratings, and the green curve is for horizontal gratings. Each curve is aligned on stimulus onset (small vertical black line in each firing rate curve), and the data for each orientation show the mean firing rate across trials, accompanied by s.e.m. curves as thin lines. The scale bars in the bottom right apply to all shown firing rate curves. In the center of the panel, we plotted the peak visual response (normalized to the maximum at one of the orientations) as a function of grating orientation. This neuron preferred an orientation of 30° below horizontal (cyan firing rate curve). The orientation selectivity index (OSI; Materials and Methods) of this neuron is indicated above the data. **(B)** A second neuron with weaker orientation selectivity. The neuron responded almost equally well to all orientations. **(C)** Distribution of OSI values across our population. The majority of neurons had mild orientation selectivity. **(D)** Consistent with this, first-spike latency did not depend strongly on stimulus orientation. The figure shows the distribution

(Continued)

FIGURE 1 | of first-spike latencies for the least preferred orientation, the most preferred orientation, or a vertical grating like that we used in Chen et al. (2015). In all cases, first-spike latency was similar ($p = 0.5884$, Kruskal-Wallis test). **(E)** Also, for neurons not preferring vertical orientations, the differences in visual responses between the most preferred, the least preferred, and the vertical orientations were mild. The black curve shows the summary across neurons, and the gray curves show responses for individual neurons. The *p*-values indicate the results of a Wilcoxon rank sum test comparing a given orientation (e.g., vertical or least preferred) to the preferred orientation of a given neuron. **(F)** Testing parallel vs. orthogonal orientations relative to the line connecting the fovea to the RF stimulus location (see schematics above the data points showing a fixation spot and a grating of a given orientation). Parallel gratings (oriented parallel to the line connecting the fovea to the neuron's RF hotspot) had weaker responses than orthogonal ones (oriented orthogonal to the line connecting the fovea to the neuron's RF hotspot). Error bars in all panels denote s.e.m.

of peak firing rate after stimulus onset as a function of grating orientation. As can be seen, this neuron responded the most for a grating oriented to the bottom right (the cyan trace). We computed an OSI according to the literature from early cortical visual areas (Hansel and van Vreeswijk, 2012) (Materials and Methods), and we found that this neuron had an OSI of 0.186. However, this neuron did not represent the majority of SC neurons that we recorded. Instead, we were more likely to encounter neurons like that shown in **Figure 1B**. In this case, orientation tuning was lower, as also reflected by the lower OSI value than in **Figure 1A**. Across the population, only approximately one third of our neurons had strong OSI values >0.15 and only approximately one half had mild OSI values >0.1 (**Figure 1C**).

We also checked the efficiency with which neurons responded to different orientations, by measuring first-spike latency as we had done earlier (Hafed and Chen, 2016). Regardless of whether a grating was vertical (Chen et al., 2015) the least preferred orientation of a given neuron, or the most preferred orientation of a given neuron, first-spike latency was similar (**Figure 1D**). This means that first-spike latency was similar across orientations.

Since in our previous studies, we used vertical gratings to study SC modulations around the time of microsaccades (Chen et al., 2015; Chen and Hafed, 2017), we also confirmed that this was a reasonable strategy for the study of SC neurons. For neurons not preferring vertical orientations, we plotted visual responses to either the most preferred, the least preferred, or a vertical orientation and compared them (**Figure 1E**). We found modest changes in responses across all of these conditions, suggesting that vertical gratings were still able to evoke responses in SC neurons. This is consistent with the results of **Figures 1A–D**, and consistent with our use of vertical gratings in recent studies (Chen et al., 2015; Chen and Hafed, 2017).

We also checked whether placing a grating orthogonal or parallel to the line connecting the fovea to the grating location (or, equivalently, RF location) matters. We collected data from 11 extra neurons, and we found that parallel gratings (**Figure 1F**) were least effective in driving SC neurons. Orthogonal gratings, on the other hand, resulted in stronger

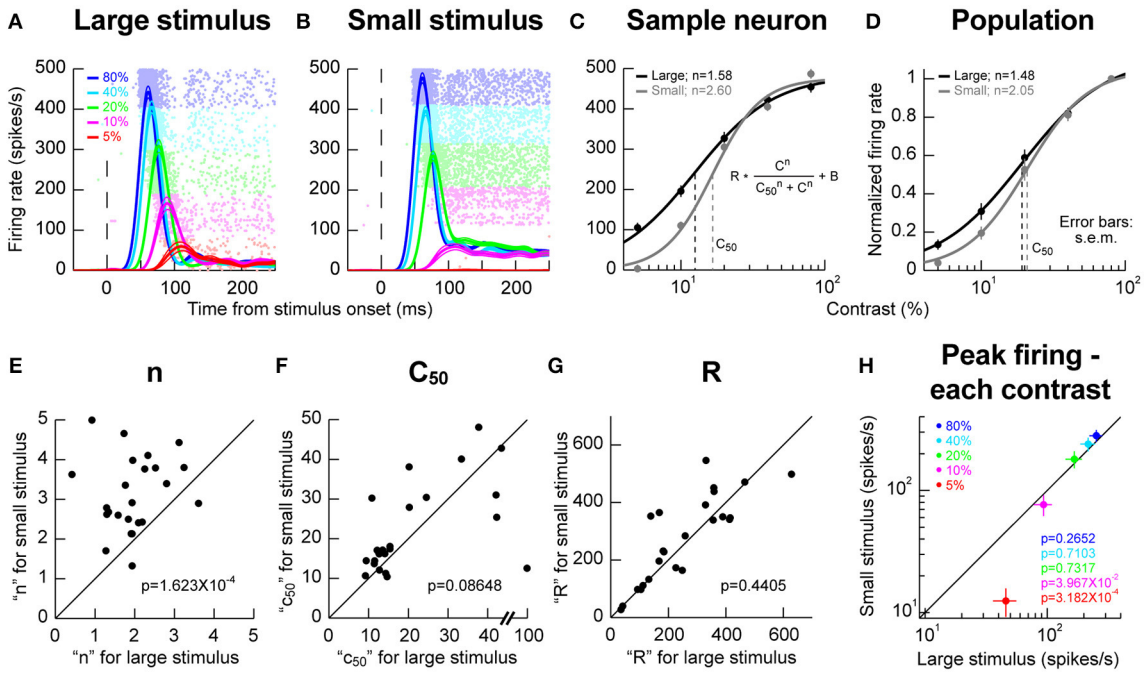

FIGURE 2 | Stimulus size effects on contrast sensitivity. **(A,B)** Responses of a sample neuron to different stimulus contrasts (color-coded according to the legend). The RF hotspot eccentricity of the neuron was 5.6° from the center of gaze and in the upper visual field. On the left **(A)**, the stimulus filled the RF (2° in size); on the right **(B)**, the stimulus was much smaller (0.5° in size). The responses to each individual contrast are shown as an average firing rate curve surrounded by s.e.m. traces across trial repetitions. The faint dots behind the firing rate curves show the individual action potential rasters from each contrast, with each row indicating a trial repetition of a given contrast. The contrasts were interleaved in the experiments, but the rasters are grouped here to facilitate inspection of the results. The responses of the neuron to stimulus contrast were similar except that the evoked response at low contrasts (5 and 10%) was much weaker for the small stimulus than for the big stimulus. **(C)** We plotted the evoked responses (peak visual response 20–150 ms after stimulus onset) as a function of contrast, and we fitted the data with the shown equation. In this neuron, the slope parameter (*n*) was different for large and small stimuli. The semi-saturation contrast (c50) was also apparently altered. **(D)** However, across the population, the only significant effect was on n, meaning that contrast sensitivity curves were sharper for small stimuli. **(E–G)** The parameters of the contrast sensitivity curve equation (shown in C) across neurons for small vs. large stimuli. Across the population, only the parameter n showed a significant effect of stimulus size. The shown *p*-values indicate the result of a Wilcoxon signed rank test comparing small and big stimuli. **(H)** Consistent with this, when we plotted peak firing rate as a function of contrast, we found that the rate was significantly lower for small vs. big stimuli (*p*-values in the colored-text; Wilcoxon signed rank test comparing small and big stimuli) only for low contrasts. For high contrasts, neural sensitivity was similar for different stimulus sizes. Error bars in all panels denote s.e.m.

responses ($p = 0.016$, Wilcoxon signed rank test comparing orthogonal and parallel responses in the neurons with both conditions tested simultaneously). This suggests that, even though orientation selectivity in the primate SC is low in general, there is still substantial dependence of orientation sensitivity on the location of a given neuron within the SC topographic map. This is reminiscent of rodent observations of potential orientation columns in the SC independent of the basic spatial topography (Feinberg and Meister, 2015).

Sharper Contrast Sensitivity Curves for Small Stimuli in Response Fields

We next explored potential local RF interactions by changing stimulus size at a given location. We ran conditions using a vertical grating as in Chen et al. (2015), but this time, we compared responses when the grating was either filling as much of the RF as possible or when the stimulus was significantly smaller (Materials and Methods). We varied the contrast of the grating from trial to trial in order to obtain contrast sensitivity curves. In the sample neuron of **Figures 2A,B**, we obtained an expected dependence of visual response strength on stimulus contrast; the higher the contrast, the higher and earlier the visual response was, and this happened for both a large and a small grating in the RF. However, closer inspection of the contrast sensitivity curves revealed an additional property: there was a sharpening of these curves for the smaller stimulus (**Figure 2C**), primarily because of a change in response strength for low contrast stimuli. In this sample neuron, semi-saturation contrast (c50) appeared to be also affected, but this effect was not significant across the population (**Figure 2D**). Instead, across the population, the only significant effect was on the slope (*n*) of the contrast sensitivity curve. We confirmed this by plotting in **Figures 2E–G** the different parameters of the contrast sensitivity curve equation (displayed in the inset of **Figure 2C**) for each neuron. Across the population, only the slope parameter of contrast sensitivity curves was significantly different between small and large stimuli ($p = 1.623 \times 10^{-4}$, Wilcoxon signed rank test). This effect is also evident in **Figure 2H**, in which we plotted the peak firing rate for each stimulus contrast for either small or large stimuli. Firing rates between small and large

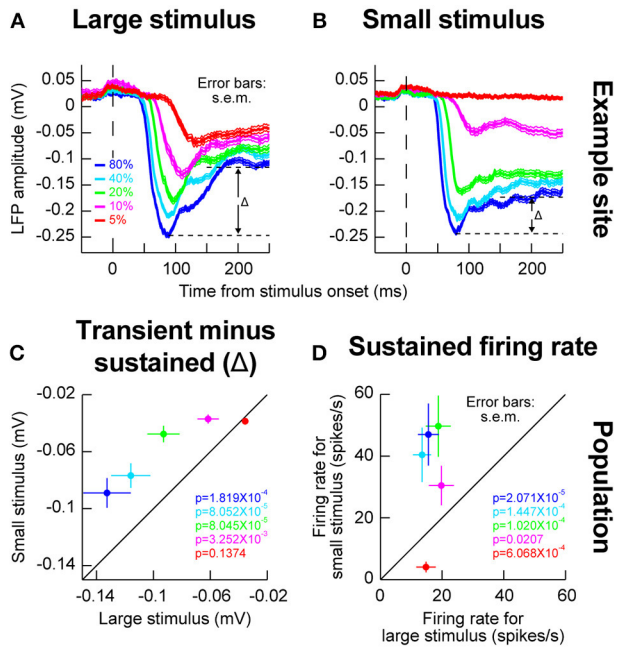

FIGURE 3 | Local population activity for different stimulus sizes within a given RF. **(A)** Local field potential (LFP) responses for the same electrode track as the one for which the example neuron of **Figure 2** was isolated. For the large stimulus, evoked LFP response (a negative-going deflection) resembled the expectations based on firing rate analyses in **Figure 2**. **(B)** When the stimulus was small, the evoked response at 10 and 5% contrast was much smaller (compare magenta and red curves between this panel and **A)**. However, note that the sustained response component remained elevated (i.e., remained more negative long after the evoked response had subsided); the difference between the peak evoked response and the transient response (Δ) was smaller for the small stimulus than for the big stimulus (compare Δ in this panel to **A)**. This means that in the big stimulus, after the evoked excitatory response, a potential inhibitory signal started to kick in to suppress neural activity, explaining the higher sustained firing rates for small stimuli in **Figures 2A,B** even at low stimulus contrasts (10%). **(C)** Across electrode sites, the value of Δ was bigger for the big stimulus than for the small stimulus across contrasts (except for the lowest contrast which already evoked very weak responses). **(D)** Consistent with this, across neurons, sustained firing rates for small stimuli were consistently higher than sustained firing rates for big stimuli, even for low 10% contrasts for which the initial evoked response was much weaker (**Figure 2**). Again, for the lowest contrast, the effect is not present but this contrast evoked very weak or non-existent responses from most neurons to begin with. Thus, stimulus onset in the SC is dominated by an early excitatory drive followed by subsequent inhibition even within a classical RF boundary. Error bars in all panels denote s.e.m., and the shown *p*-values indicate results of a Wilcoxon signed rank test comparing small and big stimuli.

stimuli were similar for high contrasts regardless of stimulus size. However, for lower contrasts (5 and 10%), responses were weaker in the smaller stimuli than in the larger stimuli, again consistent with a sharpening of contrast sensitivity curves. We should also note here that for these population analyses, we accepted all neurons passing our explained variance tests for the curve fitting procedures (Materials and Methods). For one of these neurons, a c50 of 100% was observed (**Figure 2F**), which constituted an outlier when compared to the rest of the population for assessments of c50 effects. Removing this outlier resulted in significant c50 modulations across the population in **Figure 2F** ($p = 0.0029$, Wilcoxon signed rank test). This effect on c50 was still nonetheless consistent with our observation that the effect of stimulus size primarily acted through a change in SC response strengths for low contrast stimuli.

Higher Sustained Activity for Small Stimuli in Response Fields

The results above with small stimuli might suggest differences in local lateral interactions caused by an extended stimulus (Humphrey, 1968; Schiller and Koerner, 1971; Cynader and Berman, 1972; Goldberg and Wurtz, 1972; Updyke, 1974; Marrocco and Li, 1977). This idea was rendered clearer when inspecting sustained firing rates after the initial onset transient. In the sample neuron of **Figures 2A,B**, it can be seen that sustained activity was elevated for the small stimuli, even when the evoked response was itself weak. For example, for 10% stimulus contrast, even though the initial evoked response was much weaker in the small stimulus configuration than in the large stimulus configuration, the sustained activity was significantly higher in the small stimulus configuration than in the large stimulus configuration ($p = 0.0011$, two-sample *t*-test). This suggests that with the large stimulus, an inhibitory effect kicked in after the initial excitatory stimulus transient, even though the stimulus was contained within the classical RF boundaries and not extending outside as might be expected from surround suppression.

We also wanted to investigate whether the local population activity around our recording electrodes behaved similarly in this regard to our isolated single neurons or not (Zhang and Li, 2013). We therefore next analyzed LFP's, and we still observed evidence for such an inhibitory effect. For example, in **Figures 3A,B**, we plotted LFP evoked responses for different contrasts and different stimulus sizes from the same electrode penetration in which the sample neuron of **Figures 2A,B** was isolated. As can be seen, the sharpening of contrast sensitivity curves can be clearly seen in the LFP evoked responses. For example, for the small stimulus, the initial evoked LFP transient for 10% contrast was much weaker than with a large stimulus (compare the magenta curves of **Figures 3A,B**). On the other hand, the initial evoked responses for high contrast stimuli were very similar whether the stimuli were large or small. Interestingly, after the initial evoked transient had subsided, there was a bigger change in LFP amplitude between the transient and sustained response (labeled Δ in **Figures 3A,B**) for large stimuli than for small stimuli, suggesting a potential inhibitory effect kicking in after the initial excitation. Across the population of experiments, this effect of a bigger Δ with the big stimuli persisted (**Figure 3C**), and it was mirrored by higher sustained firing rates for small stimuli in the isolated neurons (**Figure 3D**). Naturally, these effects were weakest for the lowest stimulus contrast (5%), because this contrast evoked the weakest responses anyway (Chen et al., 2015).

Therefore, our experiments with small and large stimuli revealed potential local lateral interactions in and around classical SC RF's. These interactions are not identical to inhibitory surround interactions in V1 (Vaiceliunaite et al., 2013). For example, in our case, the bigger stimulus did not reduce the SC

response for high contrast stimuli as might be expected from surround suppression in V1 (Vaiceliunaite et al., 2013) suggesting that this stimulus was still within the classical RF boundaries in our experiments. Nonetheless, subsequent inhibition in neural responses during the sustained stimulus interval still occurred in our neurons.

Changes in First-Spike Latency for Small Stimuli in Response Fields

The above results suggest that for small stimuli, low contrast stimuli evoke weaker responses. This should also result in later evoked responses, since visual response latency tends to be correlated with visual response amplitude in the SC (Marino et al., 2012; Chen and Hafed, 2017). We confirmed this to be the case. We plotted first-spike latency as we had done earlier (Hafed and Chen, 2016), but now relating it to stimulus contrast. For 10% contrast in the presented gratings, our earlier results above (**Figure 2**) showed that visual responses were significantly different for small and big stimuli. We thus compared first-spike latencies at 10% contrast between the different stimulus sizes (**Figure 4**). For the small stimulus, first-spike latency at 10% contrast was significantly longer than for the big stimulus ($p = 0.022$, Wilcoxon rank sum test) consistent with the sharper decrease in response gain for this contrast with small stimuli (**Figure 4**). This effect was not significant for the higher stimulus contrasts ($p = 0.277$, 0.473, 0.787, and 0.600 for 5, 20, 40, and 80% contrast, respectively, Wilcoxon rank sum test), again consistent with our interpretation above (**Figure 2**) that stimulus size altered the slope of the contrast sensitivity curve of SC neurons without altering other parameters like semi-saturation contrast or maximal firing rate. It should be noted here that we used a stricter unpaired statistical test in this analysis, as opposed to a paired Wilcoxon signed rank test, because not all neurons in our population exhibited responses in both small and large stimuli (especially for low contrast stimuli). Therefore, we could not estimate first-spike latency in such cases (assigning an arbitrary value of infinity for no spiking responses might have biased our measurements unnecessarily).

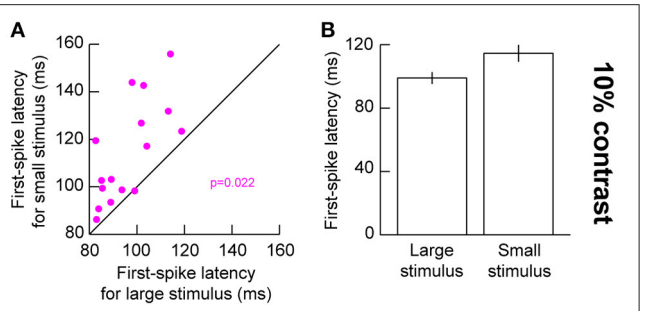

FIGURE 4 | Visual response latency for low contrast large and small stimuli. **(A)** First-spike latency for neurons when a 10% contrast grating was presented in their visual RF's. The x-axis shows first-spike latency with a large stimulus in the RF, and the y-axis shows first-spike latency with a small stimulus in the RF. **(B)** Summary of first-spike latency across our population as a function of stimulus size. The small stimulus was associated with a longer latency of visual responses. Error bars denote s.e.m.

Preference for Primarily 10–20 Hz Temporal Frequency by Primate SC Neurons

We next explored the temporal properties of SC neurons. We presented flickering gratings and varied the flicker frequency from trial to trial (Materials and Methods). The contrast of the gratings was gradually increased and then gradually decreased to minimize onset transients, so it was expected that neural responses would be time varying in this experiment; the logic of the experiment here was that the time variation with stimulus contrast would be also accompanied by time variation associated with the stimulus flicker (Materials and Methods). **Figure 5A** shows example results that we obtained from a sample neuron. At low flicker frequencies (e.g., 3 Hz), the neuron responded in a phasic manner to each stimulus onset event (in individual flicker cycles) and the phasic response reflected the gradual increases and decreases in stimulus contrast near the beginning and end, respectively, of a given trial (Materials and Methods). At higher frequencies (e.g., 20 Hz), the phasic events were less obvious than for low frequencies (e.g., 3 Hz), and they were replaced with a more sustained response. This means that 20 Hz was close to the critical flicker fusion frequency (Wells et al., 2001) of this neuron. Interestingly, increasing the frequency more to 60 Hz, resulted in a much weaker neural response even though the stimulus was practically constantly presented on the monitor for the entire duration of the trial. This means that the neuron exhibited tuning for temporal frequencies, and that 60 Hz was outside the neuron's preferred frequency range.

We assessed the sample neuron's frequency "tuning curve" as done in the previous literature for cortical visual neurons, for example in rats (Wells et al., 2001), by measuring the average firing rate during trials and plotting it as a function of stimulus flicker frequency. The logic of such tuning curves is similar to the logic of obtaining spatial frequency tuning curves as a function of grating spatial frequency, for example in our macaque SC neurons (Hafed and Chen, 2016). **Figure 5B** shows the temporal frequency tuning curve obtained for the same sample neuron as in **Figure 5A**, and the curve was obtained by fitting the data to a difference-of-Gaussians equation (Materials and Methods). As can be seen, the neuron was most sensitive to temporal frequencies of 10–20 Hz. We also assessed the amplitude of the neuron's sensitivity to a given frequency. As others have done for cortical visual neurons (Wells et al., 2001), we computed a so-called F1/F0 ratio. Briefly, we performed a Fourier transformation of firing rate observed when a given temporal flicker frequency was presented to the neuron (e.g., 10 Hz in **Figure 5C**). As expected, we obtained a primary harmonic at the stimulus frequency (F1; 10 Hz in **Figure 5C**). The amplitude of the harmonic was then divided by the mean firing rate (or the 0 Hz response of the neuron), and we repeated this for different stimulus frequencies that were presented. For the neuron in **Figure 5A**, this procedure resulted in the F1/F0 curve shown in **Figure 5D**. This curve means that the phasic response at 3 Hz was much stronger relative to

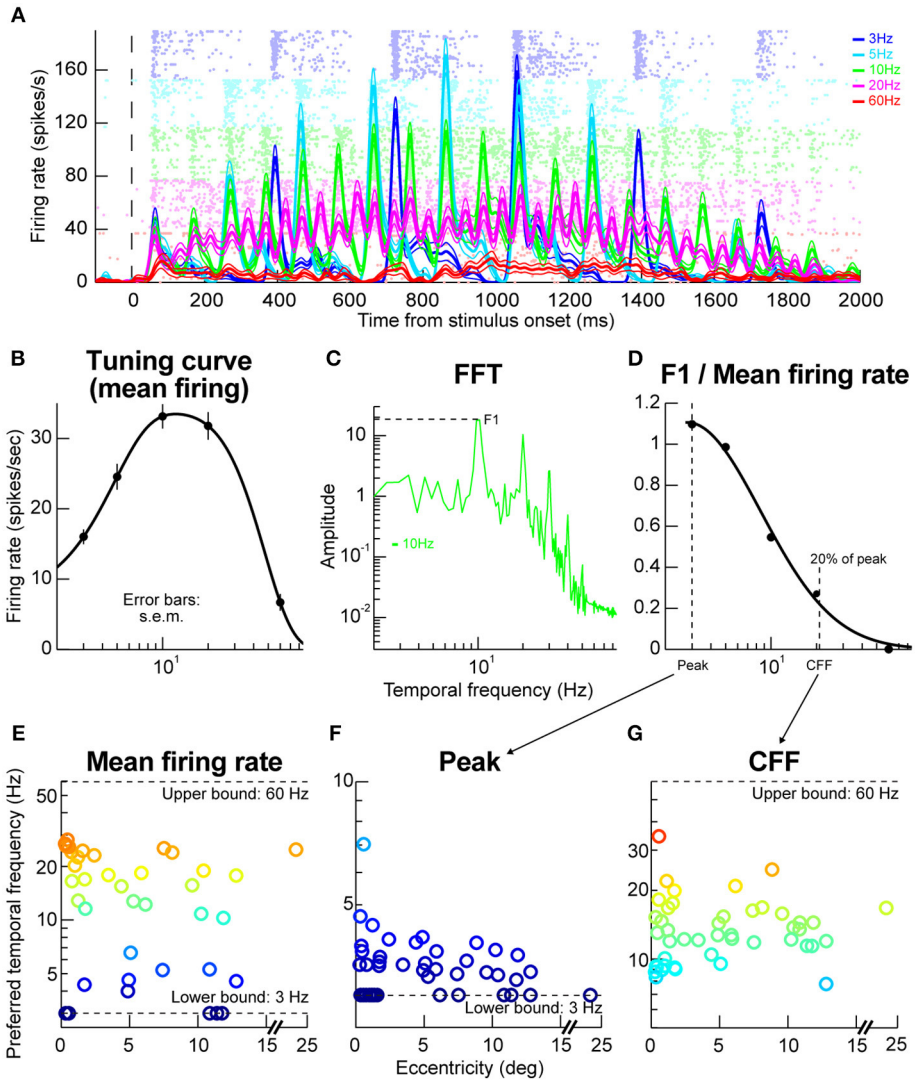

FIGURE 5 | Temporal frequency tuning by macaque SC. **(A)** Example firing rates and raster plots from a neuron exposed to flicker of different frequencies. At low frequencies, the neuron emitted phasic responses to individual stimulus events (e.g., at 3 Hz; blue curves and rasters). At higher frequencies, the individual phasic events started to merge or fuse (e.g., at 20 Hz; magenta curves and rasters). At even higher frequencies (e.g., 60 Hz; red curves and rasters), the neuron stopped responding completely even though the stimulus was practically almost permanently on the display. The formatting of this panel is similar to that described for **Figures 2A,B** above (i.e., for the faint dots describing action potentials and firing rate curves describing averages and s.e.m. boundaries), and error bars denote s.e.m. **(B)** The tuning curve of the neuron obtained by plotting mean firing rate as a function of temporal frequency. The neuron responded best for 10–20 Hz frequencies. **(C)** Fourier transform of firing rate for the same neuron with 10 Hz stimulus flicker. The neuron had a dominant harmonic at 10 Hz (F1) along with power at different frequencies (e.g., multiples of 10 Hz), including also DC (0 Hz), indicating a non-zero average response (sometimes referred to as F0). **(D)** We plotted the power at F1 divided by the mean response for this condition (or the DC response), to estimate how big the phasic response to individual stimulus events was relative to the overall average. For this same neuron, the phasic response at 3 Hz was very strong (also evident in **A)**. At near 20 Hz, the individual phasic responses (aligned to stimulus flicker) were much weaker compared to the overall average firing rate, suggesting "flicker fusion." We defined the critical flicker fusion frequency as the frequency for which F1/F0 was 20% of the peak. **(E)** Preferred temporal flicker frequencies of all neurons based on tuning curves like in **(B)**, and plotted as a function of each neuron's preferred retinotopic eccentricity. There was no apparent eccentricity dependence of temporal tuning. **(F,G)** the parameters of the curve in **(D)** across all our neurons. Most neurons had a critical flicker fusion frequency near 20 Hz. Error bars in all panels indicate s.e.m. Also, the colors in **(E–G)** are provided as a visual aid, and they go from cool to warm with increasing y-axis values.

the mean firing rate than, say, the phasic response at 10 Hz, which is also evident from inspecting **Figure 5A**. Additionally, this curve was used to define the flicker fusion frequency or the frequency at which the phasic response at the stimulus frequency was much reduced (to 20% of the peak). In the neuron of **Figure 5D**, this frequency was just above 20 Hz, again consistent with the raw data in **Figure 5A**. In other words, above ∼20 Hz, the neuron just emitted a more-or-less constant response as opposed to a phasic response to each stimulus cycle.

Across the population, our neurons temporal frequency tuning curves were relatively broad (**Figure 5E**), with a range of neurons preferring a range of flicker frequencies, but none of the neurons preferred >30 Hz. Similarly, most neurons had a critical flicker fusion frequency of ∼20 Hz (**Figures 5F,G**). These temporal SC properties are very similar to those observed in the visual capabilities of blindsight patients who lose portions of their primary visual cortex (Trevethan and Sahraie, 2003).

DISCUSSION

In this study, we explored visual properties of the rhesus macaque SC, as a continuation of our recent efforts in this regard (Chen et al., 2015, in press; Hafed and Chen, 2016; Chen and Hafed, 2017; Veale et al., 2017; Yoshida et al., 2017). We found that primate SC neurons exhibit mild orientation selectivity. We also found that within the boundaries of a classical RF of an SC neuron, increasing stimulus size can increase the size of the initial volley of stimulus-evoked action potential rates, but it also increases subsequent inhibition. The net result is that bigger stimuli can evoke stronger initial responses but weaker sustained responses. Finally, we explored the primate SC's temporal frequency tuning properties, and we found flicker fusion rates of ∼20 Hz. Thus, the SC's temporal response profile lies in an intermediate range between the slow rod-mediated component of vision at the level of the retina and the faster cone-mediated component.

Our results on orientation tuning are related to recent rodent SC work. For example, it was suggested that the mouse SC contains orientation columns (Feinberg and Meister, 2015), much like primate primarily visual cortex contains such columns. In other words, according to these authors, different regions of the SC topographic map might over-represent particular orientations, such that there is an additional "feature map" for orientation in the SC, in addition to this structure's topographic representation of space. Our results so far cannot fully address whether the primate SC would also contain such "feature maps" in addition to spatial topography. The clearest evidence that we have in our data for such potential feature maps may relate to **Figure 1F**, in which we observed that orthogonal gratings (relative to the line connecting the fovea to the RF location) evoked stronger visual responses than parallel ones. This suggests that orientation tuning properties in the primate SC can depend on a given neuron's RF location within the SC topographic map, and this is an interesting question that needs to be further investigated with significantly larger data sets. There was apparently also no indication of such feature mapping in recent marmoset monkey SC work (Tailby et al., 2012). In any case, given ecologically-driven large asymmetries in representing the upper and lower visual fields (Hafed and Chen, 2016), it is certainly conceivable that similar ecological constraints may indeed result in over-representation of certain orientation preferences in different parts of the primate SC's representation of visual field locations. Such asymmetries would most likely exist if they serve orienting behavior with rapid gaze shifts, since the primate SC is particularly relevant for such gaze shifts.

We also explored potential lateral interactions in and around RF's, and we explored temporal tuning properties. We believe that such experiments and results should be followed up on in subsequent studies, especially if one were to understand the broader contributions of the SC to active perception. For example, eye movements under natural conditions might be associated with different peri-saccadic perceptual phenomena depending on the prevalent scene statistics in natural images (Burr et al., 1994), and there is evidence that the SC plays a critical role in these perceptual phenomena (Chen and Hafed, 2017; Chen et al., in press). Given that individual cell types (like purely visual vs. visual-motor neurons) might be particularly dissociated in these kinds of phenomena (Chen and Hafed, 2017) even though it is a visual response that is ultimately modulated in all cases, there is a need to dissect the circuit mechanisms of the primate SC in much more detail, and specifically in terms of visual properties. Similarly, the role of the SC in target selection and attention (Li and Basso, 2005; Krauzlis et al., 2013; Basso and May, 2017; Crapse et al., 2018; Odegaard et al., 2018) would be even better understood than already present today if phenomena like lateral interactions and temporal response profiles were fully characterized. Finally, on top of all of the above, there still remains a distinct possibility that the SC contributes to coarse initial visual analysis of scenes, particularly to allow for efficient approach or evade responses by the organism. Indeed, combined with our earlier work, like (Hafed and Chen, 2016) and (Chen et al., in press) as well as other work, like (Nguyen et al., 2014), there is evidence that the visual properties of the SC may be relevant for behavior that is based on (at least coarse) scene understanding. We find this possibility intriguing and worthwhile for future research endeavors.

We also find our results intriguing because of how they may link to the role of the SC as a potential alternative visual pathway from the primary geniculo-cortical pathway that is used by primates. In particular, blindsight is a phenomenon that happens after lesion of the primary visual cortex, and it is characterized by an ability of patients, with very little or sometimes no awareness of a stimulus presented in the blind field, to perform discrimination tasks above chance level, especially if the stimulus is salient (Weiskrantz et al., 1974; Cowey and Stoerig, 1991; Ptito and Leh, 2007; Cowey, 2010; Leopold, 2012). The visual stimuli that are optimal for these patients are critical. Specifically, these patients perform the best with first-order low spatial frequency patches, with a cut off of around 3 cpd (Sahraie et al., 2002, 2010; Trevethan and Sahraie, 2003). Transient stimuli are usually better, with a range around 10–33 Hz, peaking at around 20 Hz. These tuning properties are very similar to what we found in our SC neurons, both in this study (for temporal frequency) and in earlier work (for spatial frequency) (Chen et al., in press). Patients can also perform color discrimination tasks (Boyer et al., 2005; Silvanto et al., 2008). It is also known that the pupillary reflex can be a reliable predictor of performance (Sahraie et al., 2002). Because the lateral geniculate nucleus (LGN) and pulvinar project directly to extrastriate cortex, and

because both of them also receive superficial SC and retinal input, it could be that blindsight reflects residual vision from this alternative visual pathway through LGN, SC, or pulvinar, or all of them to the extrastriate cortex (Cowey and Stoerig, 1991; Isa and Yoshida, 2009; Leopold, 2012). The remarkable observation based on our results is that the SC visual properties are quite similar to those of blindsight patients, which could add to the discussion on whether a collicular pathway is more or less important during blindsight than the other potential pathways.

AUTHOR CONTRIBUTIONS

C-YC and ZH designed the experiments, collected and analyzed the data, and wrote the manuscript.

FUNDING

We were funded by the Werner Reichardt Centre for Integrative Neuroscience (CIN), an Excellence Cluster (EXC307) funded by the Deutsche Forschungsgemeinschaft (DFG). We were also supported by the Hertie Institute for Clinical Brain Research, and the DFG-funded collaborative research centre Robust Vision (SFB 1233; project 11). We acknowledge the DFG and the Open Access Publishing Fund of the University of Tübingen for subsidizing publication costs.

ACKNOWLEDGMENTS

Parts of this manuscript have appeared in the Ph.D. Thesis of the first author (see Chen, 2017).

REFERENCES

Ahmadlou, M., and Heimel, J. A. (2015). Preference for concentric orientations in the mouse superior colliculus. *Nat. Commun.* 6:6773. doi: 10.1038/ncomms7773

Basso, M. A., and May, P. J. (2017). Circuits for action and cognition: a view from the superior colliculus. *Annu. Rev. Vis. Sci.* 3, 197–226. doi: 10.1146/annurev-vision-102016-061234

Bellet, J., Chen, C. Y., and Hafed, Z. M. (2017). Sequential hemifield gating of alpha and beta behavioral performance oscillations after microsaccades. *J. Neurophysiol.* 118, 2789–2805. doi: 10.1152/jn.00253.2017

Boyer, J. L., Harrison, S., and Ro, T. (2005). Unconscious processing of orientation and color without primary visual cortex. *Proc. Natl. Acad. Sci. U.S.A.* 102, 16875–16879. doi: 10.1073/pnas.0505332102

Burr, D. C., Morrone, M. C., and Ross, J. (1994). Selective suppression of the magnocellular visual pathway during saccadic eye movements. *Nature* 371, 511–513. doi: 10.1038/371511a0

Carandini, M., Heeger, D. J., and Movshon, J. A. (1997). Linearity and normalization in simple cells of the macaque primary visual cortex. *J. Neurosci.* 17, 8621–8644. doi: 10.1523/JNEUROSCI.17-21-08621.1997

Chen, C.-Y. (2017). *Seeing Through the Tectal Eye: Visual Representations in the Primate Superior Colliculus with and Without Eye Movements*. Ph.D. thesis, Tuebingen University.

Chen, C. Y., and Hafed, Z. M. (2013). Postmicrosaccadic enhancement of slow eye movements. *J. Neurosci.* 33, 5375–5386. doi: 10.1523/JNEUROSCI.3703-12.2013

Chen, C. Y., and Hafed, Z. M. (2017). A neural locus for spatial-frequency specific saccadic suppression in visual-motor neurons of the primate superior colliculus. *J. Neurophysiol.* 117, 1657–1673. doi: 10.1152/jn.00911.2016

Chen, C. Y., Ignashchenkova, A., Thier, P., and Hafed, Z. M. (2015). Neuronal response gain enhancement prior to microsaccades. *Curr. Biol.* 25, 2065–2074. doi: 10.1016/j.cub.2015.06.022

Chen, C.-Y., Sonnenberg, L., Weller, S., Witschel, T., and Hafed, Z. M. (in press). Spatial frequency sensitivity in macaque midbrain. *Nat. Commun*.

Cowey, A. (2010). The blindsight saga. *Exp. Brain Res.* 200, 3–24. doi: 10.1007/s00221-009-1914-2

Cowey, A., and Stoerig, P. (1991). The neurobiology of blindsight. *Trends Neurosci.* 14, 140–145. doi: 10.1016/0166-2236(91)90085-9

Crapse, T. B., Lau, H., and Basso, M. A. (2018). A role for the superior colliculus in decision criteria. *Neuron* 97, 181.e6–194.e6. doi: 10.1016/j.neuron.2017.12.006

Cynader, M., and Berman, N. (1972). Receptive-field organization of monkey superior colliculus. *J. Neurophysiol.* 35, 187–201. doi: 10.1152/jn.1972.35.2.187

Davidson, R. M., and Bender, D. B. (1991). Selectivity for relative motion in the monkey superior colliculus. *J. Neurophysiol.* 65, 1115–1133. doi: 10.1152/jn.1991.65.5.1115

Derrington, A. M., and Lennie, P. (1984). Spatial and temporal contrast sensitivities of neurones in lateral geniculate nucleus of macaque. *J. Physiol.* 357, 219–240. doi: 10.1113/jphysiol.1984.sp015498

Feinberg, E. H., and Meister, M. (2015). Orientation columns in the mouse superior colliculus. *Nature* 519, 229–232. doi: 10.1038/nature14103

Fuchs, A. F., and Robinson, D. A. (1966). A method for measuring horizontal and vertical eye movement chronically in the monkey. *J. Appl. Physiol.* 21, 1068–1070. doi: 10.1152/jappl.1966.21.3.1068

Gandhi, N. J., and Katnani, H. A. (2011). Motor functions of the superior colliculus. *Annu. Rev. Neurosci.* 34, 205–231. doi: 10.1146/annurev-neuro-061010-113728

Goldberg, M. E., and Wurtz, R. H. (1972). Activity of superior colliculus in behaving monkey. I. Visual receptive fields of single neurons. *J. Neurophysiol.* 35, 542–559. doi: 10.1152/jn.1972.35.4.542

Hafed, Z. M. (2011). Mechanisms for generating and compensating for the smallest possible saccades. *Eur. J. Neurosci.* 33, 2101–2113. doi: 10.1111/j.1460-9568.2011.07694.x

Hafed, Z. M., and Chen, C.-Y. (2016). Sharper, stronger, faster upper visual field representation in primate superior colliculus. *Curr. Biol.* 26, 1647–1658. doi: 10.1016/j.cub.2016.04.059

Hafed, Z. M., Chen, C.-Y., and Tian, X. (2015). Vision, perception, and attention through the lens of microsaccades: mechanisms and implications. *Front. Syst. Neurosci.* 9:167. doi: 10.3389/fnsys.2015.00167

Hafed, Z. M., and Ignashchenkova, A. (2013). On the dissociation between microsaccade rate and direction after peripheral cues: microsaccadic inhibition revisited. *J. Neurosci.* 33, 16220–16235. doi: 10.1523/JNEUROSCI.2240-13.2013

Hafed, Z. M., and Krauzlis, R. J. (2008). Goal representations dominate superior colliculus activity during extrafoveal tracking. *J. Neurosci.* 28, 9426–9439. doi: 10.1523/JNEUROSCI.1313-08.2008

Hansel, D., and van Vreeswijk, C. (2012). The mechanism of orientation selectivity in primary visual cortex without a functional map. *J. Neurosci.* 32, 4049–4064. doi: 10.1523/JNEUROSCI.6284-11.2012

Humphrey, N. K. (1968). Responses to visual stimuli of units in the superior colliculus of rats and monkeys. *Exp. Neurol.* 20, 312–340. doi: 10.1016/0014-4886(68)90076-9

Inayat, S., Barchini, J., Chen, H., Feng, L., Liu, X., and Cang, J. (2015). Neurons in the most superficial lamina of the mouse superior colliculus are highly selective for stimulus direction. *J. Neurosci.* 35, 7992–8003. doi: 10.1523/JNEUROSCI.0173-15.2015

Isa, T., and Yoshida, M. (2009). Saccade control after V1 lesion revisited. *Curr. Opin. Neurobiol.* 19, 608–614. doi: 10.1016/j.conb.2009.10.014

Judge, S. J., Richmond, B. J., and Chu, F. C. (1980). Implantation of magnetic search coils for measurement of eye position: an improved method. *Vis. Res.* 20, 535–538. doi: 10.1016/0042-6989(80)90128-5

Kato, R., Takaura, K., Ikeda, T., Yoshida, M., and Isa, T. (2011). Contribution of the retino-tectal pathway to visually guided saccades after lesion of the primary visual cortex in monkeys. *Eur. J. Neurosci.* 33, 1952–1960. doi: 10.1111/j.1460-9568.2011.07729.x

Krauzlis, R. J., Lovejoy, L. P., and Zenon, A. (2013). Superior colliculus and visual spatial attention. *Annu. Rev. Neurosci.* 36, 165–182. doi: 10.1146/annurev-neuro-062012-170249

Legendy, C. R., and Salcman, M. (1985). Bursts and recurrences of bursts in the spike trains of spontaneously active striate cortex neurons. *J. Neurophysiol.* 53, 926–939. doi: 10.1152/jn.1985.53.4.926

Leopold, D. A. (2012). Primary visual cortex: awareness and blindsight. *Annu. Rev. Neurosci.* 35, 91–109. doi: 10.1146/annurev-neuro-062111-150356

Li, X., and Basso, M. A. (2005). Competitive stimulus interactions within single response fields of superior colliculus neurons. *J. Neurosci.* 25, 11357–11373. doi: 10.1523/JNEUROSCI.3825-05.2005

Li, X., and Basso, M. A. (2008). Preparing to move increases the sensitivity of superior colliculus neurons. *J. Neurosci.* 28, 4561–4577. doi: 10.1523/JNEUROSCI.5683-07.2008

Ludwig, C. J., Gilchrist, I. D., and McSorley, E. (2004). The influence of spatial frequency and contrast on saccade latencies. *Vis. Res.* 44, 2597–2604. doi: 10.1016/j.visres.2004.05.022

Marino, R. A., Levy, R., Boehnke, S., White, B. J., Itti, L., and Munoz, D. P. (2012). Linking visual response properties in the superior colliculus to saccade behavior. *Eur. J. Neurosci.* 35, 1738–1752. doi: 10.1111/j.1460-9568.2012.08079.x

Marrocco, R. T., and Li, R. H. (1977). Monkey superior colliculus: properties of single cells and their afferent inputs. *J. Neurophysiol.* 40, 844–860. doi: 10.1152/jn.1977.40.4.844

Moors, J., and Vendrik, A. J. (1979). Responses of single units in the monkey superior colliculus to moving stimuli. *Exp. Brain Res.* 35, 349–369. doi: 10.1007/BF00236620

Nguyen, M. N., Matsumoto, J., Hori, E., Maior, R. S., Tomaz, C., Tran, A. H., et al. (2014). Neuronal responses to face-like and facial stimuli in the monkey superior colliculus. *Front. Behav. Neurosci.* 8:85. doi: 10.3389/fnbeh.2014.00085

Odegaard, B., Grimaldi, P., Cho, S. H., Peters, M. A. K., Lau, H., and Basso, M. A. (2018). Superior colliculus neuronal ensemble activity signals optimal rather than subjective confidence. *Proc. Natl. Acad. Sci. U.S.A.* 115, E1588–E1597. doi: 10.1073/pnas.1711628115

Ptito, A., and Leh, S. E. (2007). Neural substrates of blindsight after hemispherectomy. *Neuroscientist* 13, 506–518. doi: 10.1177/1073858407300598

Robinson, D. A. (1972). Eye movements evoked by collicular stimulation in the alert monkey. *Vis. Res.* 12, 1795–1808. doi: 10.1016/0042-6989(72)90070-3

Sahraie, A., Hibbard, P. B., Trevethan, C. T., Ritchie, K. L., and Weiskrantz, L. (2010). Consciousness of the first order in blindsight. *Proc. Natl. Acad. Sci. U.S.A.* 107, 21217–21222. doi: 10.1073/pnas.1015652107

Sahraie, A., Weiskrantz, L., Trevethan, C. T., Cruce, R., and Murray, A. D. (2002). Psychophysical and pupillometric study of spatial channels of visual processing in blindsight. *Exp. Brain Res.* 143, 249–256. doi: 10.1007/s00221-001-0989-1

Schiller, P. H., and Koerner, F. (1971). Discharge characteristics of single units in superior colliculus of the alert rhesus monkey. *J. Neurophysiol.* 34, 920–936. doi: 10.1152/jn.1971.34.5.920

Silvanto, J., Cowey, A., and Walsh, V. (2008). Inducing conscious perception of colour in blindsight. *Curr. Biol.* 18, R950–951. doi: 10.1016/j.cub.2008.08.016

Tailby, C., Cheong, S. K., Pietersen, A. N., Solomon, S. G., and Martin, P. R. (2012). Colour and pattern selectivity of receptive fields in superior colliculus of marmoset monkeys. *J. Physiol. Lond.* 590, 4061–4077. doi: 10.1113/jphysiol.2012.230409

Takaura, K., Yoshida, M., and Isa, T. (2011). Neural substrate of spatial memory in the superior colliculus after damage to the primary visual cortex. *J. Neurosci.* 31, 4233–4241. doi: 10.1523/JNEUROSCI.5143-10.2011

Tian, X., Yoshida, M., and Hafed, Z. M. (2016). A microsaccadic account of attentional capture and inhibition of return in posner cueing. *Front. Syst. Neurosci.* 10:23. doi: 10.3389/fnsys.2016.00023

Tian, X., Yoshida, M., and Hafed, Z. M. (2018). Dynamics of fixational eye position and microsaccades during spatial cueing: the case of express microsaccades. *J. Neurophysiol.* 119, 1962–1980. doi: 10.1152/jn.00752.2017

Trevethan, C. T., and Sahraie, A. (2003). Spatial and temporal processing in a subject with cortical blindness following occipital surgery. *Neuropsychologia* 41, 1296–1306. doi: 10.1016/S0028-3932(03)00049-6

Updyke, B. V. (1974). Characteristics of unit responses in superior colliculus of the Cebus monkey. *J. Neurophysiol.* 37, 896–909. doi: 10.1152/jn.1974.37.5.896

Vaiceliunaite, A., Erisken, S., Franzen, F., Katzner, S., and Busse, L. (2013). Spatial integration in mouse primary visual cortex. *J. Neurophysiol.* 110, 964–972. doi: 10.1152/jn.00138.2013

Veale, R., Hafed, Z. M., and Yoshida, M. (2017). How is visual salience computed in the brain? Insights from behaviour, neurobiology and modelling. *Philos. Trans. R. Soc. Lond. B Biol. Sci.* 372:20160113. doi: 10.1098/rstb.2016.0113

Weiskrantz, L., Warrington, E. K., Sanders, M. D., and Marshall, J. (1974). Visual capacity in the hemianopic field following a restricted occipital ablation. *Brain* 97, 709–728. doi: 10.1093/brain/97.1.709

Wells, E. F., Bernstein, G. M., Scott, B. W., Bennett, P. J., and Mendelson, J. R. (2001). Critical flicker frequency responses in visual cortex. *Exp. Brain Res.* 139, 106–110. doi: 10.1007/s002210100721

White, B. J., Berg, D. J., Kan, J. Y., Marino, R. A., Itti, L., and Munoz, D. P. (2017a). Superior colliculus neurons encode a visual saliency map during free viewing of natural dynamic video. *Nat. Commun.* 8:14263. doi: 10.1038/ncomms14263

White, B. J., Kan, J. Y., Levy, R., Itti, L., and Munoz, D. P. (2017b). Superior colliculus encodes visual saliency before the primary visual cortex. *Proc. Natl. Acad. Sci. U.S.A.* 114, 9451–9456. doi: 10.1073/pnas.1701003114

White, B. J., Stritzke, M., and Gegenfurtner, K. R. (2008). Saccadic facilitation in natural backgrounds. *Curr. Biol.* 18, 124–128. doi: 10.1016/j.cub.2007.12.027

Wurtz, R. H., and Optican, L. M. (1994). Superior colliculus cell types and models of saccade generation. *Curr. Opin. Neurobiol.* 4, 857–861. doi: 10.1016/0959-4388(94)90134-1

Yoshida, M., Hafed, Z. M., and Isa, T. (2017). Informative cues facilitate saccadic localization in blindsight monkeys. *Front. Syst. Neurosci.* 11:5. doi: 10.3389/fnsys.2017.00005

Yoshida, M., Takaura, K., Kato, R., Ikeda, T., and Isa, T. (2008). Striate cortical lesions affect deliberate decision and control of saccade: implication for blindsight. *J. Neurosci.* 28, 10517–10530. doi: 10.1523/JNEUROSCI.1973-08.2008

Zhang, L., and Li, B. (2013). Surround modulation characteristics of local field potential and spiking activity in primary visual cortex of cat. *PLoS ONE* 8:e64492. doi: 10.1371/journal.pone.0064492

Conflict of Interest Statement: The authors declare that the research was conducted in the absence of any commercial or financial relationships that could be construed as a potential conflict of interest.

frontiers in Neural Circuits

REVIEW
published: 21 June 2018
doi: 10.3389/fncir.2018.00046

Principles of Functional Circuit Connectivity: Insights From Spontaneous Activity in the Zebrafish Optic Tectum

Emiliano Marachlian[1], *Lilach Avitan*[2], *Geoffrey J. Goodhill*[2,3]* *and Germán Sumbre*[1]*

[1]*Institut de Biologie de l'Ecole Normale Supérieure (IBENS), Ecole Normale Supérieure, CNRS, INSERM, PSL Université Paris, Paris, France,* [2]*Queensland Brain Institute, The University of Queensland, Brisbane, QLD, Australia,* [3]*School of Mathematics and Physics, The University of Queensland, Brisbane, QLD, Australia*

The brain is continuously active, even in the absence of external stimulation. In the optic tectum of the zebrafish larva, this spontaneous activity is spatially organized and reflects the circuit's functional connectivity. The structure of the spontaneous activity displayed patterns associated with aspects of the larva's preferences when engaging in complex visuo-motor behaviors, suggesting that the tectal circuit is adapted for the circuit's functional role in detecting visual cues and generating adequate motor behaviors. Further studies in sensory deprived larvae suggest that the basic structure of the functional connectivity patterns emerges even in the absence of retinal inputs, but that its fine structure is affected by visual experience.

Keywords: zebrafish, optic tectum, spontaneous activity, functional connectivity, sensory experience, two-photon calcium imaging

OPEN ACCESS

Edited by:
Harald Luksch, Technische Universität München, Germany

Reviewed by:
Hernan Lopez-Schier, Helmholtz Zentrum München—Deutsches Forschungszentrum für Gesundheit und Umwelt, Germany
Martin Meyer, King's College London, United Kingdom

***Correspondence:**
Geoffrey J. Goodhill
g.goodhill@uq.edu.au
Germán Sumbre
sumbre@biologie.ens.fr

Received: *10 April 2018*
Accepted: *28 May 2018*
Published: *21 June 2018*

Citation:
Marachlian E, Avitan L, Goodhill GJ and Sumbre G (2018) Principles of Functional Circuit Connectivity: Insights From Spontaneous Activity in the Zebrafish Optic Tectum. Front. Neural Circuits 12:46. doi: 10.3389/fncir.2018.00046

INTRODUCTION

Sensory brain areas are continuously active even in the absence of external stimulation. This ongoing spontaneous activity, defined as the intrinsic brain activity not driven by sensory stimuli, was once considered to be merely biophysical noise which interferes with brain computations (Tolhurst et al., 1983; Faisal et al., 2008). However, this view has changed in recent years, as spontaneous activity has been found to be structured in space and time (Kenet et al., 2003; Fiser et al., 2004; Luczak et al., 2007, 2009; Smith and Kohn, 2008; Ringach, 2009; Kirkby et al., 2013; Jetti et al., 2014; Romano et al., 2015). In sensory brain areas, spontaneous activity can exhibit spatial patterns that match functional sensory maps (Kenet et al., 2003; Jetti et al., 2014; Romano et al., 2015).

This ongoing spontaneous activity could reflect any or all of: (1) top-down signals associated with cognitive process (e.g., attention, memory, Engel et al., 2001; Harris and Thiele, 2011); (2) preparatory activity associated with self-generated behaviors (e.g., readiness potential; Libet et al., 1983); (3) a readout of the functional connectivity of neural circuits (which neurons are connected and the strength of these connections); and (4) a Bayesian prior for expected patterns of sensory activity (Berkes et al., 2011). Therefore, patterns of spontaneous activity may contain information about the circuit's functional connectivity constraints and/or preferred states (Kenet et al., 2003; Miller et al., 2014; Romano et al., 2015).

The zebrafish larva is an excellent model to study these principles of functional connectivity through the interrogation of the brain's ongoing spontaneous activity. Its transparent skin,

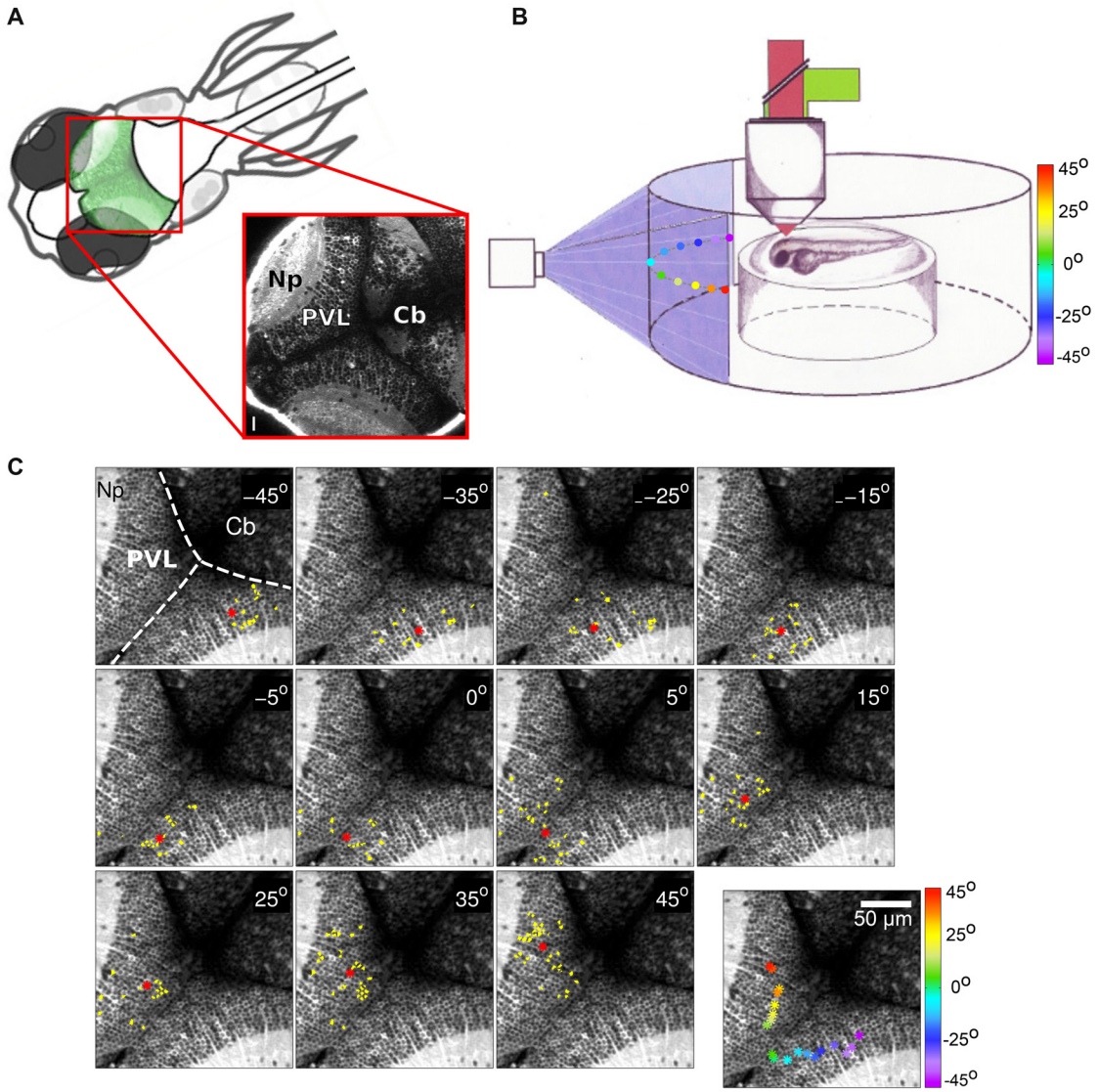

FIGURE 1 | (A) Top left: schematic dorsal view of an 8-days-post-fertilization (dpf) zebrafish larva. The optic tectum is indicated in green. Bottom right: optical section of a Tg(huC:GCaMP5G) zebrafish larva showing pan-neuronal GCaMP5 expression corresponding to the area in the top left scheme (red rectangle). The image was obtained using a two-photon microscope. PVZ, Periventricular layer; Np, neuropil; Cb, cerebellum. Scalebar: 15 µm (reproduced with permission from Pietri et al., 2017). **(B)** Schematic drawing of an agarose-embedded zebrafish larvae in the recording chamber. The colored dots represent the different stimuli positions projected on a screen (color scale). **(C)** Examples of neuronal groups consistently activated by light spots at different positions in the field of view of the larva (azimuth angle, top right corner). Activated neurons are colored in yellow, and the neuronal groups' centroids are depicted as red asterisks. Top left: anatomical landmarks. Dashed lines delineate the tectal-cerebellar and inter-hemispheric tectal boundaries. Cb, cerebellum; Np, tectal neuropil; PVL, periventricular layer. Bottom right panel: the centroids colored according to the azimuth angle (color bar on the right). The centroids evenly tile the contra-lateral rostro-caudal (reproduced with permission from Romano et al., 2015).

small size and cutaneous breathing, in combination with optogenetics and cutting-edge imaging approaches, such as 2-photon and SPIM, allow the dynamics of large neuronal populations to be monitored, with single-neuron resolution, in an intact, non-paralyzed, non-anesthetized behaving vertebrate (**Figure 1A**). From a behavioral point of view, upon hatching the larva needs to immediately catch prey and avoid predators in order to survive. These constraints force the larva to rapidly develop complex behaviors. However and despite their complexity, these behaviors are based on discrete bouts, thus facilitating their classification (Marques et al., 2018), analysis and correlation with different aspects of neuronal circuit dynamics.

In this review article, we discuss recent work analyzing spontaneous activity in the optic tectum (homologous to the superior colliculus in mammals) of the zebrafish larva, to

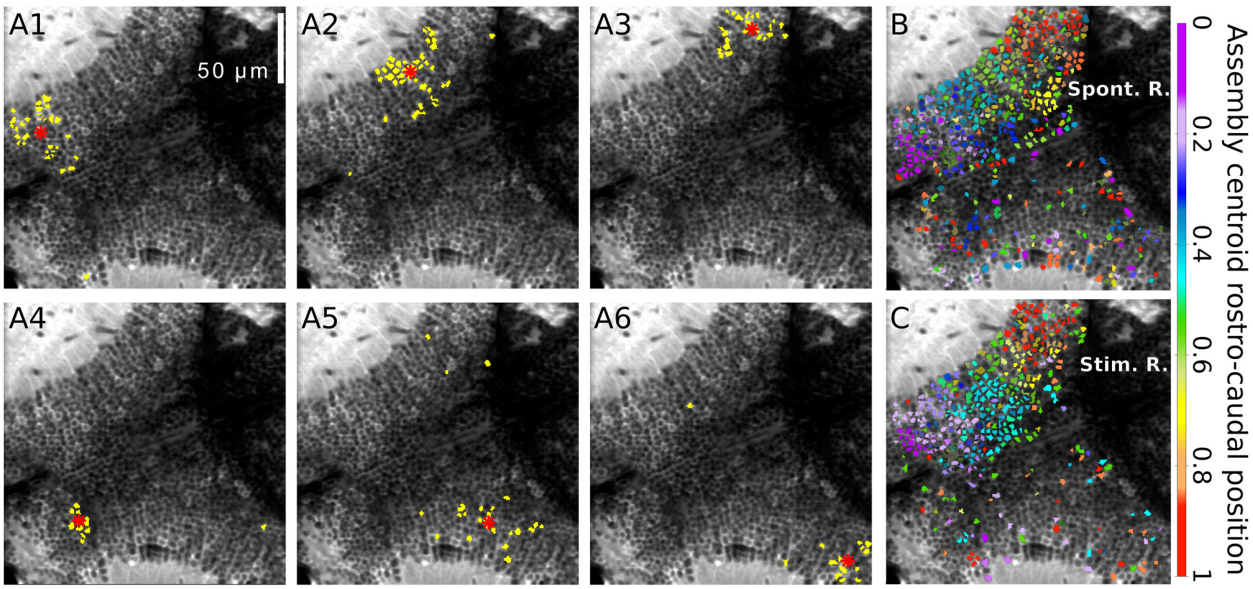

FIGURE 2 | Spontaneously emerging neuronal assemblies. **(A1–6)** Topographies of six examples of spontaneous neuronal assemblies. The neurons belonging to each of the assemblies are labeled in yellow. Red asterisks: assembly centroids. **(B)** Example of the spontaneously emerging spatial organization where all the spontaneous assemblies whose centroids lay on the right tectum. Neurons belonging to assemblies with similar topographic centroids were similarly colored. The colors represent the average normalized rostro-caudal centroid position of their assemblies. **(C)** The same representation for the light-spot-induced responses. Note the resemblance between **(B,C)**, showing a graded change in colors along the rostro-caudal axes. Scalebars: 50 µm (reproduced with permission from Romano et al., 2015).

shed light on its functional connectivity and the mechanisms underlying its emergence. Overall, these studies support the idea that spontaneous activity reveals important features of the functional role of neuronal circuits. If we consider the brain not just as a purely stimulus-driven data processor, but rather as an active system with rich intrinsic dynamics that interact with environmental sensory information, spontaneous activity could bias the response to sensory information, and thus confer a specific role for expectations in the animal's ability to interpret and respond rapidly to relevant external stimuli.

THE ZEBRAFISH OPTIC TECTUM: A MODEL FOR STUDYING FUNCTIONAL NEURONAL CIRCUITRY

In zebrafish the optic tectum receives mainly sensory inputs from the retina, but also from other modalities (Thompson et al., 2016; Pietri et al., 2017). Its main functional role is to detect sensory stimuli, process them, and thus generate appropriate motor behaviors such as prey capture (Gahtan et al., 2005; Krauzlis et al., 2013). Tectal neurons receive inputs from retinal ganglion cells (RGCs), exclusively from the contralateral eye, that synapse on the tectal neuropil (Np) creating a functional retinotopic tectal map of the contralateral visual field (Burrill and Easter, 1994; Niell and Smith, 2005; Romano et al., 2015). The elevation of the contralateral visual hemifields are represented in the dorso-ventral tectal axis, whereas the azimuth of the hemifields are mapped along the rostro-caudal tectal axis.

Neurons in the optic tectum are selective for different stimulus features in the visual field such as size (Preuss et al., 2014; Barker and Baier, 2015), position (Niell and Smith, 2005; Romano et al., 2015; **Figure 1B**), or direction (Gabriel et al., 2012; Hunter et al., 2013; Romano et al., 2015). Responses to visual cues in the optic tectum take the form of co-active neuronal groups, i.e., a population code (Georgopoulos, 1988; Niell and Smith, 2005). Some stimulus features, for instance direction selectivity, are represented with no apparent tectal spatial organization (Hunter et al., 2013; Romano et al., 2015). However, other features, such as position in the visual field, are represented by compact topographically organized groups of neurons, indicating a rough preservation of spatial relationship between the retina and the tectum (**Figure 1C**). It is often assumed that this topography of wiring is essential for the animal to decode the position of a given target in the visual field. To examine this Avitan et al. (2016) used evoked tectal neural activity to decode the positions of small spots presented to the larva. While the performance of a topography-based decoder was significantly better than chance, it was still inferior to performance obtained using methods that do not rely on the spatial position of tectal neurons, in particular a linear decoder and a maximum likelihood decoder. A computational model of the zebrafish visual system reproduced these results and confirmed that topography-based decoding performs well only for widely separated stimuli. Theory shows that a topography-based decoder can perform as well as a maximum likelihood decoder only when the map is perfect, i.e., dense, regular with little background noise (Snippe, 1996). However, these

conditions are usually violated in the tectum with only large-scale rough topography (Niell and Smith, 2005; Romano et al., 2015) and a substantial proportion of misplaced cells (Northmore, 2011). Thus while topography provides a convenient initial method for decoding, it could be replaced by more statistically sophisticated methods as the animal gains more experience in the world.

While structured activity of neuronal populations takes place in response to visual input, similar tectal activity is observed spontaneously in the absence of visual cues. The emergence of this activity may be guided by intrinsic retinal and/or tectal activity and visual experience. We now discuss recent studies which addressed these issues by recording spontaneous tectal activity over development, both in the presence and the absence of retinal input.

SPONTANEOUS ACTIVITY AS A PROXY FOR THE CIRCUIT'S FUNCTIONAL CONNECTIVITY

To learn about the functional connectivity of the optic tectum, Romano et al. (2015) monitored tectal spontaneous activity in the absence of any sensory stimulation. Neuronal populations displayed sparse basal activity, with low average neuronal activation frequencies (0.016 ± 0.015 Hz) and involving less than $\sim$1% of the imaged population simultaneously active at any one time. Nevertheless, the pair-wise temporal correlations were significantly larger than those for null models generated by permutation of the identity of neurons in each experiment. Interestingly, these highly correlated neurons displayed a spatially organized structure (groups of neurons that are topographically compact). These functional neuronal assemblies emerged in the absence of sensory stimulation but were spatially organized similarly to the neuronal groups evoked by small light-spots presented at different positions of the field of view. They were composed of neurons which share similar spatial tuning curves, but with no specific similarity in terms of their direction selectivity (Romano et al., 2015; **Figure 2**).

Given the retinotopic organization of the retinal inputs to the tectal Np, it is possible that the assemblies are the result of spontaneous activity relayed from the retina. However, physical removal of the RGCs (enucleations) 1–3 days prior to the spontaneous recordings did not significantly affect the assemblies and their spatial organization. This suggests that spontaneous neuronal assemblies of the optic tectum are not the simple outcome of correlated feed-forward inputs arriving from the retina, but rather are generated intrinsically in the tectum. However, as discussed later, early enucleation does have an effect on the development of the tectum.

The spontaneous activations of the neuronal assemblies showed a facilitatory effect, where neurons were more likely to be activated when the spontaneous network activation better resembled the pattern of the assembly they belong to. Thus, the spontaneous neuronal assembly patterns represent network states that are "preferred" by the assembly neurons. This is similar to pattern completion in attractor-like circuits (Knierim and Zhang, 2012), and acts like a prior on the stimulus distribution. This could help the larva to better detect prey in low-contrast environments, and cope with the observed variance of the stimulus in the natural environment.

Furthermore, the spontaneous tectal activity patterns matched, with significant cellular precision, those induced by visual stimulation. More precisely, they were similar to neuronal responses induced by visual stimuli of a size matching that of the natural prey of the larva (e.g., Paramecia), rather than visual stimuli of larger sizes. This implies that the assemblies are highly similar to those evoked by the visual stimuli, supporting their biological relevance. This suggests that the tectal functional circuit connectivity is adapted to respond preferentially to visual stimuli of biological relevance for the survival of the animal (e.g., the larva's prey), and therefore, that the tectal circuitry is adapted for its functional role (Romano et al., 2015).

Similarity between evoked and spontaneous patterns of neural activity has been observed in several species (Kenet et al., 2003; Berkes et al., 2011; Miller et al., 2014; Romano et al., 2015). While this similarity could also emerge due to circuitry constraints, it is much higher for behaviorally relevant stimuli than for non-behaviorally relevant ones (Berkes et al., 2011; Romano et al., 2015), suggesting that these adaptations reflect a general principle governing circuit organization.

EMERGENCE AND DEVELOPMENT OF THE TECTAL FUNCTIONAL CIRCUITRY

An important question in neuroscience is to understand the role of sensory experience and genetic factors in the development of neuronal circuits. To help address this, two recent articles (Avitan et al., 2017; Pietri et al., 2017) investigated the emergence of neural assemblies in the tectum during a critical developmental time window (4–9 days-post-fertilization, and 2.5–8 dpf, respectively). From 48 h post-fertilization RGCs begin to connect with the tectal Np. At 3 dpf the optokinetic response is already established, by 5 dpf larvae are capable of tracking and capturing prey, and by 8 dpf the optic tectum is structurally and functionally relatively mature (Niell and Smith, 2005). Pietri et al. (2017) reported that the frequency, the duration, the amplitude of calcium events of tectal neurons and the temporal correlations between them change abruptly between 2.5 dpf and 3 dpf, the period at which the retina establishes a functional connection with the optic tectum (Niell and Smith, 2005; Pietri et al., 2017).

In the zebrafish optic tectum, the size of the visual receptive fields increases from 4 dpf to 6 dpf and then refines to the same size as that at 4 dpf by 8–9 dpf (Zhang et al., 2011). The excitatory components of the receptive field play a more important role in determining this developmental profile than the inhibitory components. During this developmental period, GABAergic responses most likely switch from depolarizing to hyperpolarizing currents, and thus functional pruning of feedforward inputs is likely the most important factor in receptive field refinement (Zhang et al., 2011). When monitoring the spatial structure of the spontaneous activity, Pietri et al. (2017) found that

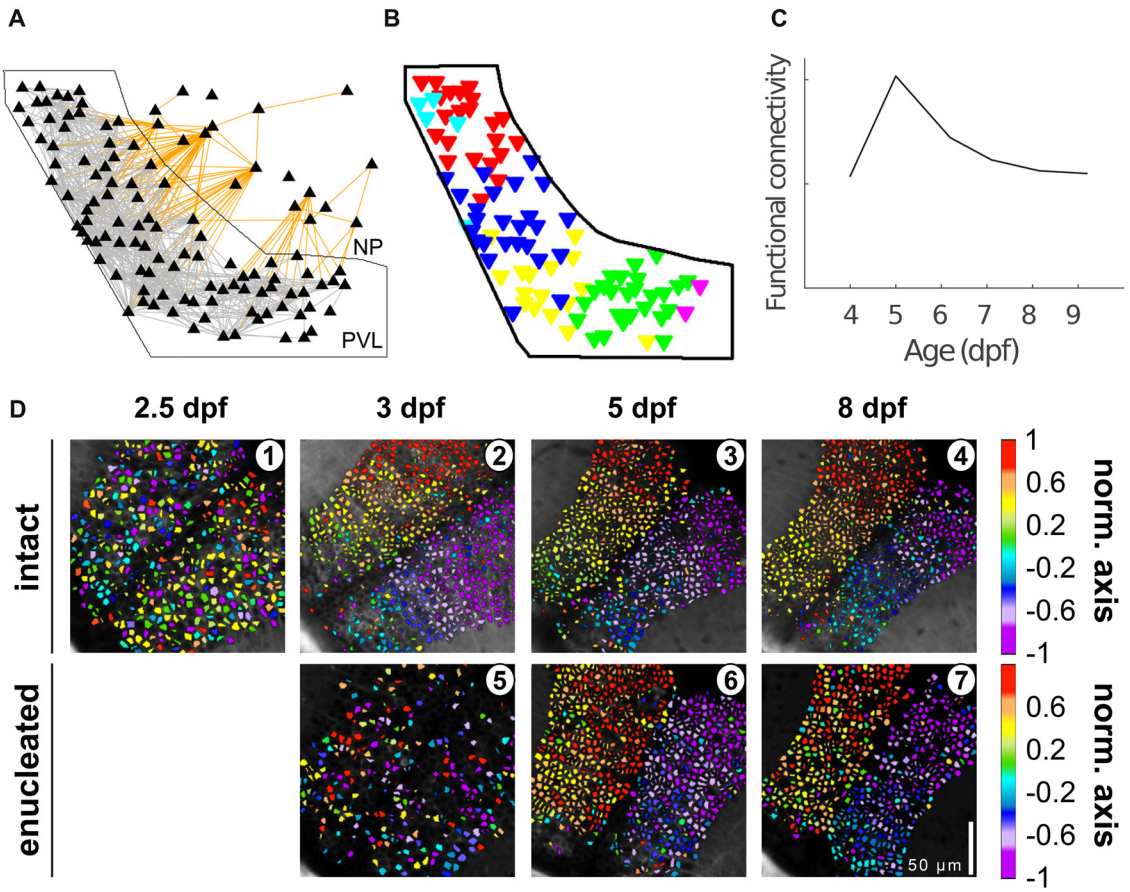

FIGURE 3 | Tectal functional connectivity and neuronal assembly characteristics change over development. **(A)** Representation of the optic tectum as a graph. Each node (triangle) represents a neuron, and each edge represents correlation exceeding a threshold, i.e., functional connectivity between two neurons (gray lines for intra-PVL edges and orange lines for edges involving NP neurons). The solid black outline shows the boundary of the PVL. **(B)** Six communities (color coded) were detected in the graph presented in **(A)**. **(C)** Functional connectivity metrics peaked at 5 dpf and declined afterwards. **(D)** Examples of the spatial organization of the spontaneous activity along the caudo-rostral axis of an intact (1–4) and enucleated larva (5–7) at different developmental stages. Scale bar represents 100 mm. Color bar: position along the caudo-rostral axis (the neurons are color coded according to the centroid azimuthal position of the assembly to which they belong; reproduced with permission from Avitan et al., 2017; Pietri et al., 2017).

the spatial organization of the neuronal assemblies followed similar dynamics as those observed for the development of the receptive fields of single neurons (Zhang et al., 2011).

Avitan et al. (2017) also showed changes over development in the characteristics of tectal spontaneous activity at the single cell and population level (**Figure 3**). At 5–6 dpf both single-neuron event frequency and correlation at the population level increased while the dimensionality of the population activity decreased. These changes were then reversed by 8 dpf, showing similar values to those observed at 4 dpf. These authors studied the functional organization of the tectum by treating the tectum as a graph, a mathematical structure composed of a set of nodes (representing neurons) joined together in pairs by edges (representing pair-wise correlation; Rubinov and Sporns, 2010). These tectal graphs were studied using metrics whose changes over development revealed corresponding modifications in the functional connectivity reorganization, with most measures (graph mean degree, clustering coefficient and global efficiency) peaking at 5 dpf and declining afterwards. At all ages inspected (4–9 dpf) graph degree distribution followed a power law, a topological feature of a network often called "scale free," which indicates a high proportion of neurons with low connectivity and low proportion of "hub" neurons with higher connectivity than expected. Thus, although the underlying topology of tectal functional networks remains robust, over development tectal functional connectivity substantially refines.

DEPENDENCE OF TECTAL FUNCTIONAL CIRCUITRY ON VISUAL EXPERIENCE

To assess the role of visual experience in the development of the tectal functional circuit, Pietri et al. (2017) studied the development of spontaneous activity in tecta deprived of visual inputs (bi-lateral enucleations performed at 54–58 hpf). Under

these conditions, the amplitude, frequency and synchronization of calcium events showed a significant increase compared to the intact larvae. The excitatory retinal inputs that normally commence at 3 dpf therefore seem to play a major role in the maturation of tectal responses. The temporal structure (the pair-wise correlations between the activity of the neurons) was also significantly impacted, displaying lower correlation levels at 3 dpf with respect to intact larvae. Surprisingly, by 5 dpf, the significant pair-wise correlations in enucleated larvae increased by ∼120% and remained at this level to 8 dpf. In contrast, the development of the spatial structure of the spontaneous activity was initially delayed, but by 8 dpf, when the tectal circuitry is functionally mature (Niell and Smith, 2005; Romano et al., 2015), it reached similar values to those of intact larvae.

Avitan et al. (2017) further tested the role of retinal activity (both evoked and spontaneous) in shaping the development of spontaneous activity, by performing bilateral and unilateral enucleation at 24 hpf and recording tectal spontaneous activity at 6 dpf. In the developing zebrafish, spontaneous retinal waves were observed during 2.5–3.5 dpf (Zhang et al., 2016) and hence in the enucleated larvae, the tectal circuit did not sense either spontaneous retinal waves nor evoked retinal input. Deprived tecta in the bilateral enucleation case and both the intact and deprived tecta in the unilateral enucleation case were examined. Neural assemblies were still present in the unilaterally and bilaterally deprived tecta, although they were slightly fewer in number and showed slightly less spatial organization, suggesting that their formation is at least partially driven endogenously. The correlation structure of intact tecta in the unilateral enucleation case was much more similar to the structure of the deprived tecta from both unilateral and bilateral enucleations than to the tecta of intact larvae at the same age, indicating a role for interhemispheric connections in transfer of information to the deprived tectum.

Besides enucleations, Avitan et al. (2017) also studied the role of visual input in shaping tectal spontaneous activity and instructing behavior by rearing the fish in the dark until 6 dpf, keeping spontaneous retinal activity intact while preventing visual experience (**Figure 3**). While measures at the single-neuron level such as event frequency were similar to the normally reared fish (Niell and Smith, 2005; Avitan et al., 2017), there were substantial changes in population level characteristics of spontaneous activity (such as correlations between pairs of neurons) of spontaneous activity, with a lower number of neuronal assemblies and reduced functional connectivity in dark-reared fish. This difference in the statistics of spontaneous activity was reflected in altered visually guided behavior, where dark-reared fish hunted fewer Paramecia compared to the normally-reared fish. This difference persisted also after exposing dark-reared fish to normal rearing conditions from 6 dpf to 9 dpf, suggesting that early visual experience has a long-lasting effect on visually guided behavior.

Together these findings support the hypotheses that: (i) neither visual experience nor spontaneous activity in the retina are essential for the establishment of spatially compact neural assemblies in the optic tectum; but (ii) retinal activity does play at least some role in shaping functional connectivity in the tectum. The emergence of spatial structure in spontaneous activity is likely determined by a pre-programmed mechanism that organizes the circuit architecture of the optic tectum, but activity-dependent mechanisms may further refine these spatial structures.

THE ROLE OF THE TECTAL SPONTANEOUS ACTIVITY IN MOTOR BEHAVIOR

To investigate the functional role of tectal neuronal assemblies Romano et al. (2015) compared several assembly properties with behavioral characteristics during prey-capture behaviors, e.g., the relative position of the prey (Paramecia) and its angular size at the time of detection. They showed that the assemblies emerging in areas of the optic tectum that represent lateral positions of the visual field of the larva (caudal regions of the optic tectum), are composed of neurons with significantly narrower spatial tuning curves and higher activation levels than those situated in areas that represent rostral positions. Consistently, larvae detected prey more often when they were at the lateral positions of the visual field of the larva. The angular size of Paramecia at the moment of detection represented ∼5° on the larva's retina. Remarkably, neuronal groups induced by similarly-sized light spots were over-represented among the spontaneous neuronal assemblies.

In addition, it was found that the activation of some spatially compact assemblies was associated with brief episodes of tail movements. Notably, when the activation of a spontaneous assembly preceded a tail flip with kinematics that indicated a turning movement, the assembly corresponded to the contralateral tectal hemisphere in 93% of the cases. Thus, the spontaneous activations of tectal assemblies can be interpreted as a latent state that allows a better response to events that are biologically meaningful (e.g., visual stimuli resembling prey).

DISCUSSION AND PERSPECTIVES

Overall, the studies discussed here show that the spontaneous activity of the optic tectum, far from being noise, presents activity patterns (neuronal assemblies) that emerge from the intrinsic dynamics of the tectal circuit. These assemblies mimic the spatial organization of visually induced responses associated with the larva's prey, and are organized according to the tectum's retinotopic map. Neither visual experience nor intrinsic retinal activity are essential for the basic functional development of the tectal network. This pre-programmed innate mechanism could be an advantageous strategy in species without parental care, enabling the prompt execution of vital behaviors soon after hatching, without requiring prior visual experience. However, visual experience is important for further fine tuning the tectal network. This hypothesis is supported by a recent study which also shows that neuronal assemblies could be generated via artificially induced Hebbian plasticity (Carrillo-Reid et al., 2016).

Tectal circuitry thus appears to be adapted for the biologically relevant statistics of the environment (expectations or priors). This salience of biologically relevant stimuli could

be interpreted as a biased "attentional-like" process imposed by the circuit's functional connectivity. In other words, the tectal circuitry is more sensitive to biologically relevant objects (e.g., prey) in comparison to objects that are less relevant for the survival of the larva. Moreover, the spontaneous activity structure reflects the tectal connectivity based on preferred local circuit states with attractor-like dynamics. This mechanism may help increase the signal-to-noise ratio for stimulus detection in low-contrast backgrounds, suggesting that the tectal network is wired for its functional role. Some assemblies are capable of predicting specific self-generated motor behaviors, potentially underlying internal decision making.

Performing similar experiments in others brain areas could shed light on the brain's basic principles underlying information processing. In addition, future studies on zebrafish models for human neurological diseases (Best and Alderton, 2008; Sager et al., 2010), may contribute to the understanding of neuronal anomalies in functional connectivity underlying neurological disorders, such as Rett's syndrome (Panier et al., 2013), or autism (Stewart et al., 2014).

AUTHOR CONTRIBUTIONS

EM, LA, GG and GS wrote the manuscript.

FUNDING

This work was supported by European Research Council (ERC) CoG 726290 awarded to GS. Australian Research Council Discovery grants DP150101152, DP170102263, DP180100636 awarded to GG.

REFERENCES

Avitan, L., Pujic, Z., Hughes, N. J., Scott, E. K., and Goodhill, G. J. (2016). Limitations of neural map topography for decoding spatial information. *J. Neurosci.* 36, 5385–5396. doi: 10.1523/jneurosci.0385-16.2016

Avitan, L., Pujic, Z., Mölter, J., Van De Poll, M., Sun, B., Teng, H., et al. (2017). Spontaneous activity in the zebrafish tectum reorganizes over development and is influenced by visual experience. *Curr. Biol.* 27, 2407–2419.e4. doi: 10.1016/j.cub.2017.06.056

Barker, A. J., and Baier, H. (2015). Sensorimotor decision making in the Zebrafish tectum. *Curr. Biol.* 25, 2804–2814. doi: 10.1016/j.cub.2015.09.055

Berkes, P., Orbán, G., Lengyel, M., and Fiser, J. (2011). Spontaneous cortical activity reveals hallmarks of an optimal internal model of the environment. *Science* 331, 83–87. doi: 10.1126/science.1195870

Best, J. D., and Alderton, W. K. (2008). Zebrafish: an *in vivo* model for the study of neurological diseases. *Neuropsychiatr. Dis. Treat.* 4, 567–576. doi: 10.2147/ndt.s2056

Burrill, J. D., and Easter, S. S. (1994). Development of the retinofugal projections in the embryonic and larval zebrafish (*Brachydanio rerio*). *J. Comp. Neurol.* 346, 583–600. doi: 10.1002/cne.903460410

Carrillo-Reid, L., Yang, W., Bando, Y., Peterka, D. S., and Yuste, R. (2016). Imprinting cortical ensembles. *Science* 353, 691–694. doi: 10.1126/science.aaf7560

Engel, A. K., Fries, P., and Singer, W. (2001). Dynamic predictions: oscillations and synchrony in top-down processing. *Nat. Rev. Neurosci.* 2, 704–716. doi: 10.1038/35094565

Faisal, A. A., Selen, L. P. J., and Wolpert, D. M. (2008). Noise in the nervous system. *Nat. Rev. Neurosci.* 9, 292–303. doi: 10.1038/nrn2258

Fiser, J., Chiu, C., and Weliky, M. (2004). Small modulation of ongoing cortical dynamics by sensory input during natural vision. *Nature* 431, 573–578. doi: 10.1038/nature02907

Gabriel, J. P., Trivedi, C. A., Maurer, C. M., Ryu, S., and Bollmann, J. H. (2012). Layer-specific targeting of direction-selective neurons in the zebrafish optic tectum. *Neuron* 76, 1147–1160. doi: 10.1016/j.neuron.2012.12.003

Gahtan, E., Tanger, P., and Baier, H. (2005). Visual prey capture in larval zebrafish is controlled by identified reticulospinal neurons downstream of the tectum. *J. Neurosci.* 25, 9294–9303. doi: 10.1523/jneurosci.2678-05.2005

Georgopoulos, A. P. (1988). Neural integration of movement: role of motor cortex in reaching. *FASEB J.* 2, 2849–2857. doi: 10.1096/fasebj.2.13.3139485

Harris, K. D., and Thiele, A. (2011). Cortical state and attention. *Nat. Rev. Neurosci.* 12, 509–523. doi: 10.1038/nrn3084

Hunter, P. R., Lowe, A. S., Thompson, I. D., and Meyer, M. P. (2013). Emergent properties of the optic tectum revealed by population analysis of direction and orientation selectivity. *J. Neurosci.* 33, 13940–13945. doi: 10.1523/jneurosci.1493-13.2013

Jetti, S. K., Vendrell-Llopis, N., and Yaksi, E. (2014). Spontaneous activity governs olfactory representations in spatially organized habenular microcircuits. *Curr. Biol.* 24, 434–439. doi: 10.1016/j.cub.2014.01.015

Kenet, T., Bibitchkov, D., Tsodyks, M., Grinvald, A., and Arieli, A. (2003). Spontaneously emerging cortical representations of visual attributes. *Nature* 425, 954–956. doi: 10.1038/nature02078

Kirkby, L. A., Sack, G. S., Firl, A., and Feller, M. B. (2013). A role for correlated spontaneous activity in the assembly of neural circuits. *Neuron* 80, 1129–1144. doi: 10.1016/j.neuron.2013.10.030

Knierim, J. J., and Zhang, K. (2012). Attractor dynamics of spatially correlated neural activity in the limbic system. *Annu. Rev. Neurosci.* 35, 267–285. doi: 10.1146/annurev-neuro-062111-150351

Krauzlis, R. J., Lovejoy, L. P., and Zénon, A. (2013). Superior colliculus and visual spatial attention. *Annu. Rev. Neurosci.* 36, 165–182. doi: 10.1146/annurev-neuro-062012-170249

Libet, B., Gleason, C. A., Wright, E. W., and Pearl, D. K. (1983). Time of conscious intention to act in relation to onset of cerebral activity (readiness-potential). The unconscious initiation of a freely voluntary act. *Brain* 106, 623–642. doi: 10.1093/brain/106.3.623

Luczak, A., Barthó, P., and Harris, K. D. (2009). Spontaneous events outline the realm of possible sensory responses in neocortical populations. *Neuron* 62, 413–425. doi: 10.1016/j.neuron.2009.03.014

Luczak, A., Barthó, P., Marguet, S. L., Buzsáki, G., and Harris, K. D. (2007). Sequential structure of neocortical spontaneous activity *in vivo*. *Proc. Natl. Acad. Sci. U S A* 104, 347–352. doi: 10.1073/pnas.0605643104

Marques, J. C., Lackner, S., Félix, R., and Orger, M. B. (2018). Structure of the zebrafish locomotor repertoire revealed with unsupervised behavioral clustering. *Curr. Biol.* 28, 181–195.e5. doi: 10.1016/j.cub.2017.12.002

Miller, J.-E. K., Ayzenshtat, I., Carrillo-Reid, L., and Yuste, R. (2014). Visual stimuli recruit intrinsically generated cortical ensembles. *Proc. Natl. Acad. Sci. U S A* 111, E4053–E4061. doi: 10.1073/pnas.1406077111

Niell, C. M., and Smith, S. J. (2005). Functional imaging reveals rapid development of visual response properties in the zebrafish tectum. *Neuron* 45, 941–951. doi: 10.1016/j.neuron.2005.01.047

Northmore, D. (2011). "The optic tectum," in *The Encyclopedia of Fish Physiology: From Genome to Environment*, ed. A. Farrell (San Diego, CA: Academic Press), 131–142.

Panier, T., Romano, S., Olive, R., Pietri, T., Sumbre, G., Candelier, R., et al. (2013). Fast functional imaging of multiple brain regions in intact zebrafish larvae using selective plane illumination microscopy. *Front. Neural Circuits* 7:65. doi: 10.3389/fncir.2013.00065

Pietri, T., Romano, S. A., Pérez-Schuster, V., Boulanger-Weill, J., Candat, V., and Sumbre, G. (2017). The emergence of the spatial structure of tectal spontaneous activity is independent of visual inputs. *Cell Rep.* 19, 939–948. doi: 10.1016/j.celrep.2017.04.015

Preuss, S. J., Trivedi, C. A., Vom Berg-Maurer, C. M., Ryu, S., and Bollmann, J. H. (2014). Classification of object size in retinotectal microcircuits. *Curr. Biol.* 24, 2376–2385. doi: 10.1016/j.cub.2014.09.012

Ringach, D. L. (2009). Spontaneous and driven cortical activity: implications for computation. *Curr. Opin. Neurobiol.* 19, 439–444. doi: 10.1016/j.conb.2009.07.005

Romano, S. A., Pietri, T., Pérez-Schuster, V., Jouary, A., Haudrechy, M., and Sumbre, G. (2015). Spontaneous neuronal network dynamics reveal circuit's functional adaptations for behavior. *Neuron* 85, 1070–1085. doi: 10.1016/j.neuron.2015.01.027

Rubinov, M., and Sporns, O. (2010). Complex network measures of brain connectivity: uses and interpretations. *Neuroimage* 52, 1059–1069. doi: 10.1016/j.neuroimage.2009.10.003

Sager, J. J., Bai, Q., and Burton, E. A. (2010). Transgenic zebrafish models of neurodegenerative diseases. *Brain Struct. Funct.* 214, 285–302. doi: 10.1007/s00429-009-0237-1

Smith, M. A., and Kohn, A. (2008). Spatial and temporal scales of neuronal correlation in primary visual cortex. *J. Neurosci.* 28, 12591–12603. doi: 10.1523/JNEUROSCI.2929-08.2008

Snippe, H. P. (1996). Parameter extraction from population codes: a critical assessment. *Neural Comput.* 8, 511–529. doi: 10.1162/neco.1996.8.3.511

Stewart, A. M., Nguyen, M., Wong, K., Poudel, M. K., and Kalueff, A. V. (2014). Developing zebrafish models of autism spectrum disorder (ASD). *Prog. Neuropsychopharmacol. Biol. Psychiatry* 50, 27–36. doi: 10.1016/j.pnpbp.2013.11.014

Thompson, A. W., Vanwalleghem, G. C., Heap, L. A., and Scott, E. K. (2016). Functional profiles of visual-, auditory- and water flow-responsive neurons in the Zebrafish tectum. *Curr. Biol.* 26, 743–754. doi: 10.1016/j.cub.2016.01.041

Tolhurst, D. J., Movshon, J. A., and Dean, A. F. (1983). The statistical reliability of signals in single neurons in cat and monkey visual cortex. *Vision Res.* 23, 775–785. doi: 10.1016/0042-6989(83)90200-6

Zhang, R. W., Li, X. Q., Kawakami, K., and Du, J. L. (2016). Stereotyped initiation of retinal waves by bipolar cells via presynaptic NMDA autoreceptors. *Nat. Commun.* 7:12650. doi: 10.1038/ncomms12650

Zhang, M., Liu, Y., Wang, S.-Z., Zhong, W., Liu, B.-H., and Tao, H. W. (2011). Functional elimination of excitatory feedforward inputs underlies developmental refinement of visual receptive fields in zebrafish. *J. Neurosci.* 31, 5460–5469. doi: 10.1523/jneurosci.6220-10.2011

Conflict of Interest Statement: The authors declare that the research was conducted in the absence of any commercial or financial relationships that could be construed as a potential conflict of interest.

frontiers in Cellular Neuroscience

ORIGINAL RESEARCH
published: 19 June 2018
doi: 10.3389/fncel.2018.00163

Transformation of Feature Selectivity From Membrane Potential to Spikes in the Mouse Superior Colliculus

Xuefeng Shi[1,2], *Yanjiao Jin*[1,3] *and Jianhua Cang*[1,4]*

[1]*Department of Neurobiology, Northwestern University, Evanston, IL, United States,* [2]*Tianjin Eye Hospital, Tianjin Key Laboratory of Ophthalmology and Visual Science, Tianjin Eye Institute, Clinical College of Ophthalmology, Tianjin Medical University, Tianjin, China,* [3]*General Hospital, Tianjin Medical University, Tianjin, China,* [4]*Department of Biology and Department of Psychology, University of Virginia, Charlottesville, VA, United States*

Neurons in the visual system display varying degrees of selectivity for stimulus features such as orientation and direction. Such feature selectivity is generated and processed by intricate circuit and synaptic mechanisms. A key factor in this process is the input-output transformation from membrane potential (V_m) to spikes in individual neurons. Here, we use *in vivo* whole-cell recording to study V_m-to-spike transformation of visual feature selectivity in the superficial neurons of the mouse superior colliculus (SC). As expected from the spike threshold effect, direction and orientation selectivity increase from V_m to spike responses. The degree of this increase is highly variable, and interestingly, it is correlated with the receptive field size of the recorded neurons. We find that the relationships between V_m and spike rate and between V_m dynamics and spike initiation are also correlated with receptive field size, which likely contribute to the observed input-output transformation of feature selectivity. Together, our findings provide useful information for understanding information processing and visual transformation in the mouse SC.

Keywords: superior colliculus, feature selectivity, receptive field, membrane potential, spike rate

OPEN ACCESS

Edited by:
Karl Farrow, Neuroelectronics Research Flanders, Belgium

Reviewed by:
J. Alexander Heimel, Netherlands Institute for Neuroscience (KNAW), Netherlands
Martin Meyer, King's College London, United Kingdom

***Correspondence:**
Jianhua Cang
cang@virginia.edu

Received: *23 April 2018*
Accepted: *25 May 2018*
Published: *19 June 2018*

Citation:
Shi X, Jin Y and Cang J (2018) Transformation of Feature Selectivity From Membrane Potential to Spikes in the Mouse Superior Colliculus. Front. Cell. Neurosci. 12:163. doi: 10.3389/fncel.2018.00163

INTRODUCTION

Each neuron functions as an information processing unit that transforms synaptic input to spiking output. How individual neurons convert membrane potential (V_m) dynamics to spiking activity in this transformation process is a key factor in determining how they encode sensory stimuli or motor commands. Several biophysical factors underlying V_m-to-spike transformation have been revealed to contribute to response selectivity in the visual cortex, where neurons are tuned to features such as stimulus orientation and motion direction (Hubel and Wiesel, 1959, 1962; Ferster and Miller, 2000; Priebe, 2016). For example, spiking threshold enhances feature selectivity of the spike response over that of the membrane potential (Carandini and Ferster, 2000; Priebe and Ferster, 2008, 2012; Tan et al., 2011). Interestingly, spiking threshold is not a fixed value, but depends on the rate of V_m depolarization and firing history (Azouz and Gray, 2000; Wester and Contreras, 2013; Fontaine et al., 2014). In addition, trial-to-trial response variability and dendritic processing are also known to play important roles in enhancing feature selectivity of neuronal output in visual cortex (Anderson et al., 2000; Miller and Troyer, 2002; Carandini, 2007; Finn et al., 2007; Smith et al., 2013).

In recent years, the mouse superior colliculus (SC) has become a productive model for investigating neural processing in the brain (Cang et al., 2018; Ito and Feldheim, 2018). Neurons in its superficial layers, including the stratum griseum superficiale (SGS) and stratum opticum (SO),

display diverse visual feature selectivity (Wang et al., 2010; Gale and Murphy, 2014; Inayat et al., 2015). Importantly, even though direction and orientation selectivity are seen in the mouse SC, their underlying circuit and synaptic mechanisms are likely different from those in the visual cortex. Orientation and direction selectivity in cat V1 arise from the precise alignment of non-selective thalamic receptive fields (RFs; Ferster and Miller, 2000; Lampl et al., 2001; Priebe and Ferster, 2005, 2008). A similar feedforward model seems to also underlie orientation selectivity in layer 4 of mouse V1 (Li et al., 2013; Lien and Scanziani, 2013), even though many of the thalamic inputs are already selective (Marshel et al., 2012; Piscopo et al., 2013; Scholl et al., 2013; Zhao et al., 2013a; Sun et al., 2016). In contrast, in the mouse SC, we recently revealed that the direction selectivity (DS) in the SC originates from the direction selective ganglion cells in the retina (Shi et al., 2017). In addition, another prominent characteristic of the SC is that it contains a much higher proportion of inhibitory neurons than in cortex (Mize, 1988, 1992; Endo et al., 2003; Inayat et al., 2015). Together, these important differences between visual cortex and the SC argue for the need to study V_m-to-spike transformation in the mouse SC and how it contributes to feature selectivity.

In this study, we set out to describe the feature selectivity transformation from V_m to spikes in mouse SGS neurons and to reveal underlying contributing factors. With *in vivo* whole-cell recording, we show that the transformation of direction and orientation selectivity from V_m to spikes is highly variable in the mouse SGS. Interestingly, the degree of this variable transformation is correlated with RF size. Several biophysical factors, including V_m-to-spike-rate relationship and the V_m-rising slope for spike initiation, but not dendritic processing, are correlated with RF size and likely contribute to the observed input-output transformation of feature selectivity. Together, these findings provide useful information for understanding information processing and visual transformation in the SC.

MATERIALS AND METHODS

Animal Preparation

C57BL/6 wild type (n = 23) and transgenic mice (n = 18) of both sexes between postnatal day 45 and 90 were used in this study. *Gad2-IRES-cre* (Stock no. 010802) and Ai32 (*RCL-ChR2(H134R)/EYFP*, Stock no. 012569) mice were acquired from Jackson Laboratory and crossed to generate heterozygous offspring that express ChR2 in glutamate decarboxylase 2 positive ($GAD2^+$) cells for *in vivo* optogenetic experiments. All mice were kept on a 12 h light:12 h dark cycle, 1–5 mice per cage. All experimental procedures were approved by the Northwestern University Institutional Animal Care and Use Committee.

Mice were anesthetized with urethane (1.2 g/kg in 10% saline solution, i.p.) and then sedated by chlorprothixene (10 mg/kg in water, i.m.) as described before (Zhao et al., 2014; Shi et al., 2017). Atropine (0.3 mg/kg in 10% saline) and dexamethasone (2 mg/kg in 10% saline) were administrated subcutaneously. The animal's body temperature was monitored through a rectal thermos-probe and maintained at 37°C through a feedback heater control module (Frederick Haer Company, Bowdoinham, ME, USA). Additional urethane (0.2–0.3 g/kg) was administered when necessary according to the depth of anesthesia monitored with toe-pinch reflex test during experiments. After the mice were anesthetized, the scalp was shaved and skin removed to expose the skull. A metal plate was mounted on top of the skull with Metabond (Parkell, Edgewood, NY, USA) mixed with black ink. The plate was then mounted to a steel stand on the vibration isolation table. A thin layer of silicon oil was applied on both eyes to prevent from drying. A craniotomy ($\sim$4.0 $\times$ 2.0 mm^2) was performed on the left hemisphere, and the tissues including the entire V1 overlaying the SC was removed by aspiration to expose the SC.

In Vivo Whole-Cell Recording

Blind whole-cell patch clamp was performed to record SGS neurons intracellularly, following procedures previously described (Shi et al., 2017). K^+-based internal solution used in this study contained 135 mM K-gluconate, 7 mM KCl, 0.5 mM EGTA, 10 mM HEPES, 10 mM Na-phosphocreatine, 4 mM Mg-ATP, 0.4 mM Na-GTP and 0.5% biocytin with pH adjusted to 7.25. Glass pipettes were advanced perpendicularly to the horizontal plane of the mouse head until just touching the SC surface. 2% agarose in artificial cerebrospinal fluid solution (ACSF, containing 140 mM NaCl, 2.5 mM KCl, 11 mM Glucose, 20 mM HEPES, 2.5 mM $CaCl_2$, 3 mM $MgSO_4$, 1 mM NaH_2PO_4) was then added onto the exposed SC. Pipettes were then inserted into the SC.

Electrical signals were amplified using MultiClamp 700B (Axon Instruments, CA, USA), and acquired with System 3 workstation (Tucker Davis Technologies, Alachua, FL, USA) at 10 kHz. Pipette capacitance and the electrode resistance were compensated initially. Only responsive cells with stable resting membrane potentials and series resistances lower than 80 MΩ across the duration of the recordings were included in this study. The depths of recorded cells (reading from the micromanipulator) were between 0 μm and 300 μm from the point where the pipette broke into the thin membrane on the SC.

After recordings, mice were euthanized with 50 mg/kg pentobarbital and perfused with PBS and then 4% paraformaldehyde (PFA). The brain was immersed in 4% PFA overnight. Coronal slices of 150 μm were cut from the fixed brain using a vibrating blade microtome (VT1000S, Leica Microsystems). The labeled cells were revealed by visualizing biocytin with streptavidin-Alex Fluor 488 conjugate (Invitrogen). Images were captured using a Zeiss LSM5 Pascal confocal microscope (Carl Zeiss, Jena, Germany).

Visual Stimulation

Visual stimuli were generated with Matlab Psychophysics toolbox on a CRT monitor (40 cm $\times$ 30 cm, 60 Hz, $\sim$35 cd/m^2 luminance). The monitor was placed 25 cm away from the right eye (contralateral to the recording site), and slightly adjusted for each cell so that its RF was completely covered. The left eye was covered throughout the experiments. Sweeping white bars on a gray background, 5° wide drifting at a speed of

30°/s, were used in the experiments to determine the direction selectivity or orientation selectivity. The drifting directions were varied between 0° and 330° (12 steps, 30° spacing), which were presented in a pseudorandom sequence together with a "blank stimulus" (gray screen at the mean luminance). The inter-stimulus interval was 0.5 or 1 s. Each stimulus was repeated 5–8 times.

Optogenetic Determination of Cell Types

An optic fiber (0.2 mm core diameter) driven by a blue LED (470 nm, Doric Lenses) was placed ∼0.5 mm above the exposed SC to photostimulate ChR2-expressing cells. The intensity of LED light was ∼160 mW/mm^2 at the tip of the optic fiber in all recordings, which was confirmed to be reliably effective in activating ChR2-expressing neurons (Shi et al., 2017).

Data Analysis

Whole-cell recording data were first analyzed using a custom MATLAB program (Shi et al., 2017). Briefly, spikes were detected when the first derivative of raw voltage traces (dV/dt) reached a manually set positive threshold. Individual traces were carefully inspected to ensure proper spike detection. To precisely determine the start of a spike (spike initiation), the second derivative of raw voltage traces (d^2V/dt^2) were calculated. The spike initiation time point was the time of the first peak of d^2V/dt^2 of the spike (Platkiewicz and Brette, 2010). The peri-stimulus spike time histograms (PSTHs) were calculated by trial-averaging the spike counts in each 50 ms time bin. Subthreshold V_m were extracted by removing spikes from the raw voltage traces by a 6 ms median filter. The subthreshold V_m traces were trial-averaged for each stimulus condition. The trial-averaged V_m trace for the blank stimulus (i.e., gray screen) was used to calculate the V_m baseline and the standard deviation of spontaneous V_m fluctuations. The V_m baseline was then subtracted from the trial-averaged V_m trace for each visual stimulus condition.

For analyzing V_m, we determined time windows of responses to the sweeping bars as described in a previous article (Shi et al., 2017). Briefly, we first calculated a cutoff threshold, which was the V_m level 2 standard deviations away from the baseline fluctuation. The widest segment of the traces that were above the threshold was determined as the response time window for each stimulus condition. This time window was expanded if there were any short above-threshold segments within 150 ms of the two sides. Next, the conditions that evoked wider time windows were used to guide the analysis of other conditions, to ensure that the estimation of response window was not too conservative or inaccurate for non-preferred directions. Specifically, for conditions where the window was narrower than 1/3 of the widest window of this cell (or 333 ms if the widest window is bigger than 1 s), the response time window determined from the opposite direction, reversed in timing, was used. All traces were checked visually to confirm that the time windows were determined properly. Peak V_m and spike rate were calculated for the response time window of each stimulus condition, subtracting the mean values of blank condition. The RF size was determined using the widest time window of all the 12 stimulus conditions, i.e., the size of the long axis of the RF. We also calculated the area of RF using a fitting method and observed similar correlations as using the width of the long axis. These analyses were thus not presented in the article.

To quantify the degree of direction selectivity and orientation selectivity, we calculated a global direction selectivity index (gDSI) and a global orientation selectivity index (gOSI). gDSI or gOSI is the vector sum of responses normalized by the scalar sum of responses in 12 directions or six orientations (Mazurek et al., 2014; Inayat et al., 2015; Shi et al., 2017): $gDSI = \left|\frac{\sum R_\theta e^{i\theta}}{\sum R_\theta}\right|$, $gOSI = \left|\frac{\sum R_\theta e^{i2\theta}}{\sum R_\theta}\right|$, where R_θ is the response magnitude of spikes or V_m, at θ direction of bars. DS transformation index (DSTI) is the difference of gDSI of spike rate and V_m: DSTI = gDSI-Spike − gDSI-V_m. OS transformation index (OSTI) is the difference of gOSI of spike rate and V_m: OSTI = gOSI-Spike − gOSI-V_m.

To quantify the relationship between V_m and spike rate, we fitted the data with a power law function (Hansel and van Vreeswijk, 2002; Miller and Troyer, 2002; Priebe et al., 2004): $R(V_m) = k(V_m - V_{rest})^p$, where R($V_m$) is the average spike rate at V_m, k is a gain factor, V_{rest} is the resting membrane potential, and p is the exponent of the fitted function, referred to as power-law index in this study.

Statistics

All pooled data were presented as mean ± SEM unless otherwise stated. Statistical significance was calculated using two-sided student's *t* test or non-parametric, two-sided, Kolmogorov-Smirnov (K-S) test as mentioned in the text. All analyses and graph plotting were performed in MATLAB (MathWorks) or Prism (GraphPad Software Inc). No statistical methods were used to predetermine sample sizes, but our sample sizes are similar to those reported in the field.

RESULTS

Feature Selectivity Transformation From V_m to Spike Rate in SGS Neurons

To study how membrane potential (V_m)-to-spike transformation in SGS neurons impact their feature selectivity, we carried out *in vivo* intracellular whole-cell recording in urethane-anesthetized mice. We recorded SGS neurons under current clamp to reveal their spiking and the underlying V_m changes in response to sweeping bars in different directions (**Figures 1A–D**). As described in previous studies (Wang et al., 2010; Inayat et al., 2015), SGS neurons displayed diverse feature selectivity. To moving bars, some cells showed orientation selectivity (OS; **Figure 1C**), and others showed DS (**Figure 1D**). We separately analyzed the recorded cells' V_m and spike responses and examined their tuning properties (see "Materials and Methods" section for details; e.g., **Figures 1E–H**). Using the normalized vector sum as an index (see "Materials and Methods" section for details), which we refer to as gDSI and gOSI, we quantified the degree of DS and OS of spiking and V_m responses, respectively, of the recorded SGS neurons. As

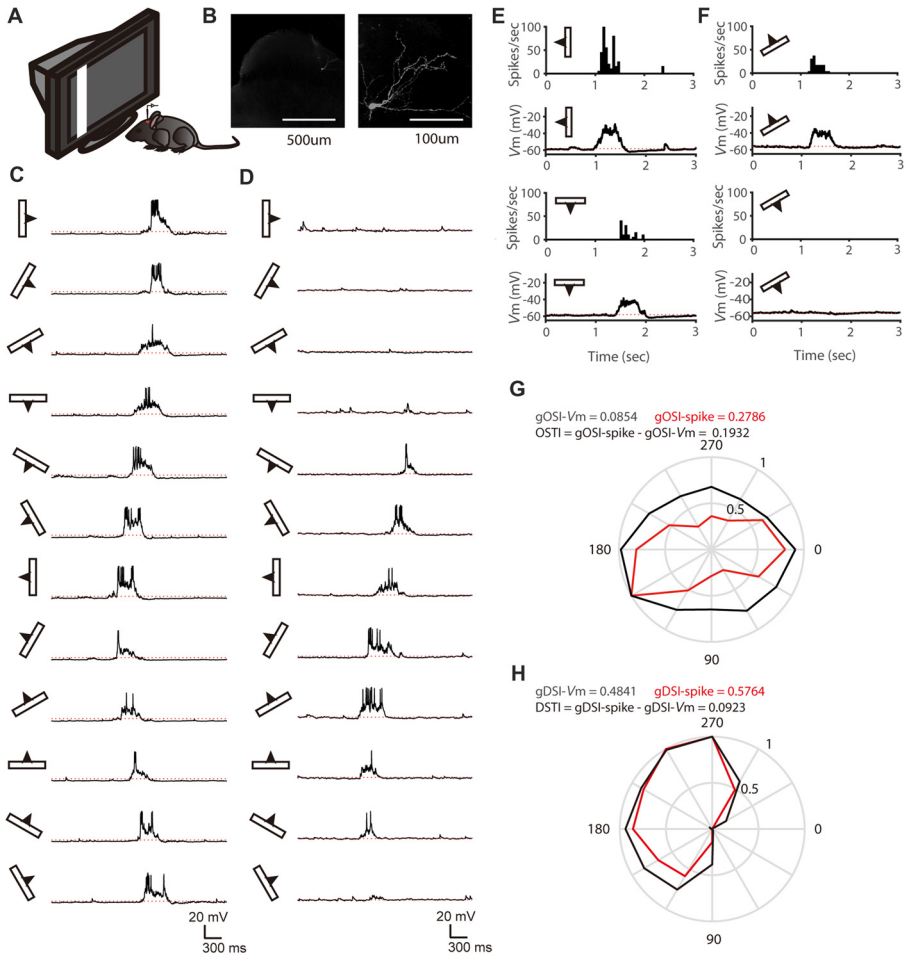

FIGURE 1 | *In vivo* whole-cell recording of stratum griseum superficiale (SGS) neurons. **(A)** A schematic of the experimental setup. **(B)** Morphology of an example SGS neuron with low (left) and high (right) magnification. **(C,D)** Membrane potential (V_m) traces of an orientation selectivity (OS) cell **(C)** and a direction selectivity (DS; **D)** cell in response to sweeping bars. The movement direction is diagramed by the bar and arrow to the left of each trace. Action potentials are truncated at −10 mV to better reveal visually-evoked V_m responses. The red dotted lines indicate the resting membrane potential of −58 mV in the OS cell and −56 mV in the DS cell. **(E)** The mean spike and V_m responses to bars moving along its preferred and opposite orientations of the same cell in **(C)**. Peri-stimulus spike time histograms (top) and trial-averaged V_m (bottom) are shown. The red dotted lines indicate the resting V_m. **(F)** The mean spike and V_m responses to bars moving along its preferred and opposite directions of the same cell in **(D)**. **(G)** Orientation tuning for peak V_m (black) and spike rate (red) of the same cell in **(C)**. **(H)** Direction tuning for peak V_m (black) and spike rate (red) of the same cell in **(D)**.

expected from the thresholding effect (Carandini and Ferster, 2000), the gDSI or gOSI of spiking responses were greater than those of V_m responses for individual cells (e.g., **Figures 1G,H**) and across the population (**Figures 2A–D**).

We then quantified the transformation of direction/orientation selectivity from V_m to spiking responses by calculating a DS transformation index (DSTI = gDSI-Spike − gDSI-V_m) and an OS transformation index (OSTI = gOSI-Spike − gOSI-V_m). Most of OSTI and DSTI were positive, reflecting the sharpening of OS and DS from SGS neurons' input (V_m) to output (spikes). Furthermore, the degree of this sharpening was highly variable among the recorded cells, with OSTI ranging from −0.04 to 0.31, and DSTI from −0.02 to 0.27, respectively. No correlation between DSTI and gDSI-V_m or OSTI and gOSI-V_m were found in the recorded cells (**Figures 2E,F**), suggesting that the feature selectivity of input itself does not determine the degree of its transformation from input to output.

Receptive Field Size Constrains V_m-to-Spike Transformation of Feature Selectivity

We next asked whether other characteristic of the input (as reflected by V_m) constrains the feature selectivity transformation from V_m to spikes. One possibility is that the RF size of input may have an impact on the DS or OS transformation from V_m to spiking responses, since cells with big or small RF may take different roles in visual processing. To explore this possibility, we measured the RF size of V_m of each recorded neuron (see "Materials and Methods" section), which

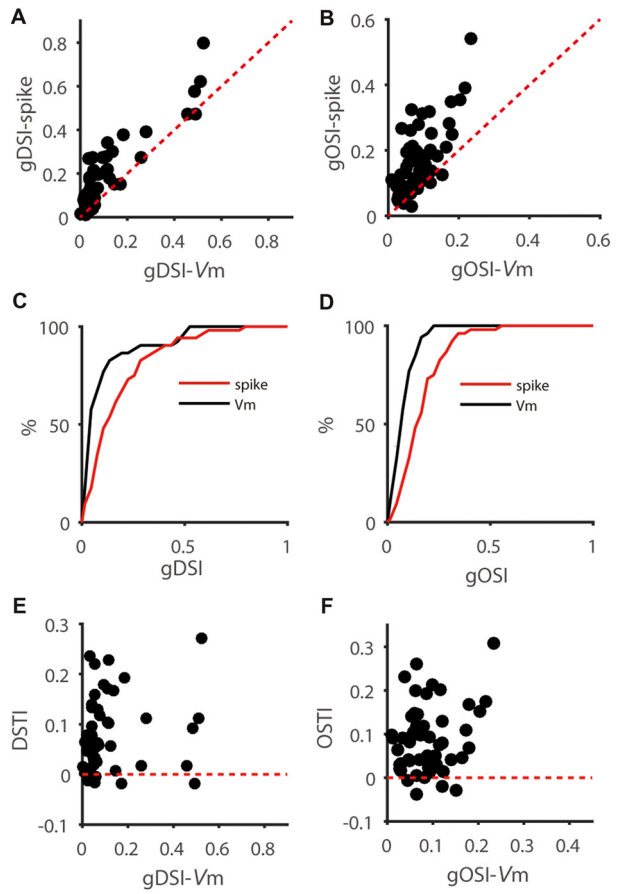

FIGURE 2 | Feature selectivity transformation from V_m to spikes is highly variable in SGS neurons. **(A)** Scatter plot of global direction selectivity index (gDSI)-Spike vs. gDSI-V_m (n = 52 cells from 41 mice). The red dotted line is the line of unity. Note that this plot is adapted from Figure 1F of Shi et al., 2017. **(B)** Scatter plot of global orientation selectivity index (gOSI)-Spike vs. gOSI-V_m of the same neurons. The red dotted line is the line of unity. **(C,D)** Cumulative distributions of gDSI **(C)** and gOSI **(D)** for V_m and spike rate, indicating that spike rate has higher gDSI and gOSI values than V_m ($P < 0.0001$ for gDSI and <0.0001 for gOSI, K-S statistic = 0.46 for gDSI and 0.5 for gOSI, Kolmogorov-Smirnov test; n = 52 cells from 41 mice). **(E)** Scatter plot of gDSI for V_m vs. DS transformation index (DSTI). The red dotted line is the line of zero. Note that the DSTI is highly variable for different degree of gDSI. **(F)** Scatter plot of gOSI for V_m vs. OS transformation index (OSTI). The red dotted line is the line of zero.

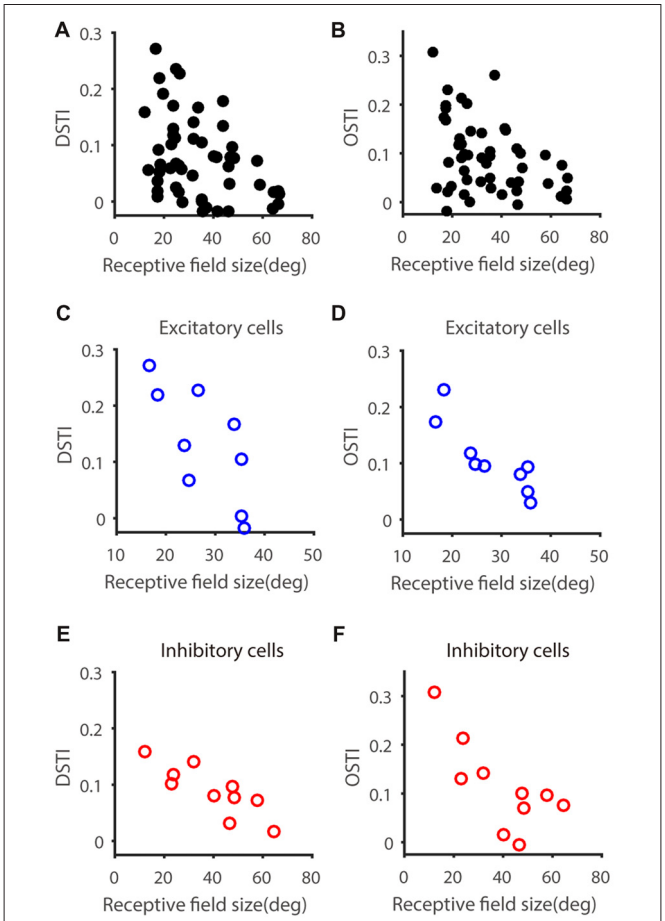

FIGURE 3 | Relationship between feature transformation and receptive field (RF) size. **(A,B)** Scatter plot of RF size vs. V_m-to-spike-rate DSTI **(A)** and OSTI **(B)**, indicating significant correlation (n = 52 cells from 41 mice, $r = -0.40$, $P < 0.01$ for panel **A**, $r = -0.37$, $P < 0.01$ for panel **B**). **(C,D)** Scatter plot of RF size vs. DSTI **(C)** and OSTI **(D)** of identified excitatory cells (n = 9; $r = -0.74$, $P < 0.05$ for panel **C**, $r = -0.87$, $P < 0.01$ for panel **D**). **(E,F)** Scatter plot of RF size vs. DSTI **(E)** and OSTI **(F)** of identified inhibitory cells (n = 10; $r = -0.84$, $P < 0.01$ for panel **E**, $r = -0.73$, $P < 0.05$ for panel **F**).

is larger than that of spiking responses and reflect the full range of visual field to which the recorded neurons respond, including subthreshold responses. Neither gDSI or gOSI itself was significantly correlated with RF size (gDSI-Spike, $r = -0.26$, $P = 0.07$; gDSI-V_m, $r = -0.10$, $P = 0.48$; gOSI-Spike, $r = -0.25$, $P = 0.07$; gOSI-V_m, $r = 0.04$, $P = 0.76$), but the increase of gDSI and gOSI (i.e., the "transformation index", DSTI and OSTI) were negatively correlated with the RF size in the recorded cells (DSTI: $r = -0.40$, $P < 0.01$, **Figure 3A**; OSTI: $r = -0.38$, $P < 0.01$, **Figure 3B**; n = 52 cells from 41 mice). Furthermore, using transgenic mice that expressed Channelrhodopsin-2 (ChR2) in GABAergic inhibitory neurons, we were able to identify whether the recorded cells were excitatory or inhibitory by their responses to LED photoactivation (Shi et al., 2017). The correlation between RF size and the transformation index was seen for both cell types and for both DSTI ($r = -0.74$, $P < 0.05$ for excitatory cells, n = 9 cells from 8 mice, **Figure 3C**; $r = -0.84$, $P < 0.01$ for inhibitory cells, n = 10 cells from 10 mice, **Figure 3E**) and OSTI ($r = -0.87$, $P < 0.01$ for excitatory cells, **Figure 3D**; $r = -0.72$, $P < 0.05$ for inhibitory cells, **Figure 3F**).

V_m-Spike Relationship in SGS Neurons

We next sought insights on what biophysical properties might contribute to the observed correlation between feature selectivity transformation and RF size. Previous studies in visual cortex have shown that V_m-spike transformation follows a power-law nonlinearity (Priebe and Ferster, 2008) and neurons with higher power-law index tended to have a greater OSI increase from V_m to spike rate than neurons with lower index (Tan et al., 2011).

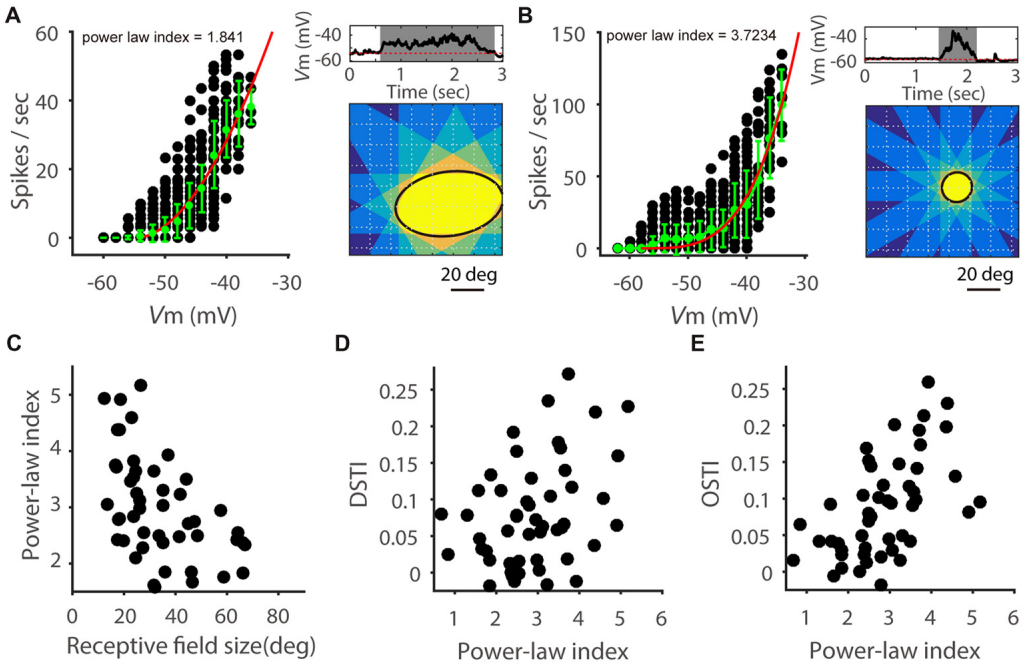

FIGURE 4 | Power-law relationship of V_m-to-spike transformation. **(A,B)** Relationship between V_m and spike rate in two example SGS neurons. On the left of each panel, each black point represents the spike rate and corresponding V_m response (grouped in 2 mV intervals) for one 50 ms epoch of a trial-averaged response. Green points and error bars are means and STDs of all the black points in the corresponding V_m range. Red curve is a fit of the green points to a power-law function. Right up: trial-averaged V_m response with the widest time window to the sweeping bar. Gray shadow indicates the response time window. Red dotted line indicates the resting V_m. Right bottom: ellipse fitted RF (black solid line) measured with superimposed time windows of responses to 12 directions of moving bars. Note that the power-law index of the cell in panel **(A)** is smaller than that of **(B)**, and its RF size is larger than that of the cell in panel **(B)**. **(C)** Scatter plot of power-law index vs. RF size, indicating negative correlation ($n = 52$ cells from 41 mice, $r = -0.45$, $P < 0.001$). **(D)** Scatter plot of DSTI vs. power law index ($r = 0.38$, $P < 0.01$). **(E)** Scatter plot of OSTI vs. power-law index ($r = 0.62$, $P < 0.0001$).

We thus examined this factor by fitting power-law functions to the data of spike rate vs. V_m (see "Materials and Methods" section). As in previous studies, we used the exponent of the fitted function, referred to as power-law index (Priebe and Ferster, 2008; Tan et al., 2011), to quantify the V_m-spike transformation (**Figures 4A,B**). No significant difference in the power law index was seen between excitatory (3.38 ± 0.33, $n = 9$) and inhibitory cells (3.01 ± 0.41, $n = 10$; $t = 0.70$; $P = 0.49$). Interestingly, the power-law index was indeed negatively correlated with the RF size (**Figure 4C**, $r = -0.45$, $P < 0.001$), where cells with larger RFs tended to have smaller exponents (e.g., **Figure 4A**) and smaller RFs larger exponents (e.g., **Figure 4B**). Consequently, both DSTI (**Figure 4D**, $r = 0.38$, $P < 0.01$) and OSTI (**Figure 4E**, $r = 0.61$, $P < 0.0001$) were positively correlated with the power-law index.

In performing this analysis, we noted that not all V_m-spike relationship could be best fitted by the power-law nonlinearity, possibly due to sublinear effects at more depolarized V_m (Zhao et al., 2013b). We thus carried out additional analysis and separated the recorded cells into "superlinear" and "sublinear" cells based on their behavior at the most depolarized membrane potentials. Specifically, we calculated spike rate change in the two most depolarized V_m ranges (shown as red arrows in **Figures 5A,B**). Cells with increasing rate change with V_m were considered "superlinear cells" (e.g., **Figure 5A**) and cells with decreasing rate changes were "sublinear cells" (e.g., **Figure 5B**). Overall, the "superlinear cells" had smaller RFs than the "sublinear cells" (**Figure 5C**). The above analyses thus suggest that the V_m-spike relationship in SGS cells is correlated with their RF size, and likely contributes to the RF-dependent feature selectivity transformation.

Spike Initiation in SGS Neurons

The spike threshold is highly variable *in vivo* (Azouz and Gray, 2000; Fontaine et al., 2014), which could be stimulus dependent and affect feature selectivity in cortical neurons (Wilent and Contreras, 2005). Moreover, spike initiation not only depends on the absolute V_m level but also on other features such as the rate of V_m change (Wester and Contreras, 2013). We thus calculated the slope of the V_m during the 1 ms window before each spike (**Figure 6A**) for individual neurons. For each cell, we plotted the distribution of this "pre-spike slope" (**Figure 6B**) and saw no obvious segregation of these distributions according to RF size. Similarly, distributions of spike initiating V_m also showed no difference between the two groups (**Figure 6C**). We then averaged the pre-spike slopes of all the spikes for each cell. Again, no correlation was observed between the average pre-spike slope and RF size; and the pre-spike slope in the cells with small RF was not different from that of the cells with large RF (**Figure 6D**). Accordingly, the DS and OS transformation index (DSTI and

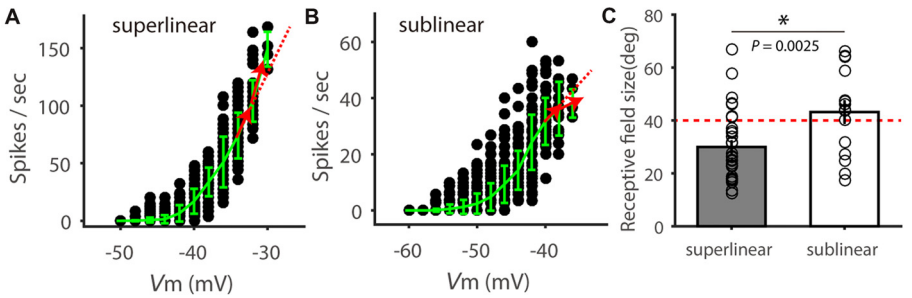

FIGURE 5 | Superlinear and sublinear V_m-spike transformation in SGS neurons. **(A)** Relationship between V_m and spike rate in an example SGS neuron. Red arrows show the instant change of spike rate with V_m increasing, which is higher than that at lower V_m (dotted red line), indicating superlinear change of spike rate with V_m. **(B)** Relationship between V_m and spike rate in another example SGS neuron, indicating sublinear change of spike rate at the more depolarized V_m. **(C)** Comparison of RF size between SGS neurons with superlinear and sublinear V_m-spike-transformation. There is significant difference between these two groups (t = 3.18, $P < 0.01$). Note that most "superlinear" cells (80.0%, 28/35) had RF size smaller than 40 degrees (red dotted line), and most "sublinear" cells (64.7%, 11/17) had RF size larger than 40 degrees. Error bars represent STD in **(A,B)** and SEM in **(C)**. * represents $P < 0.01$.

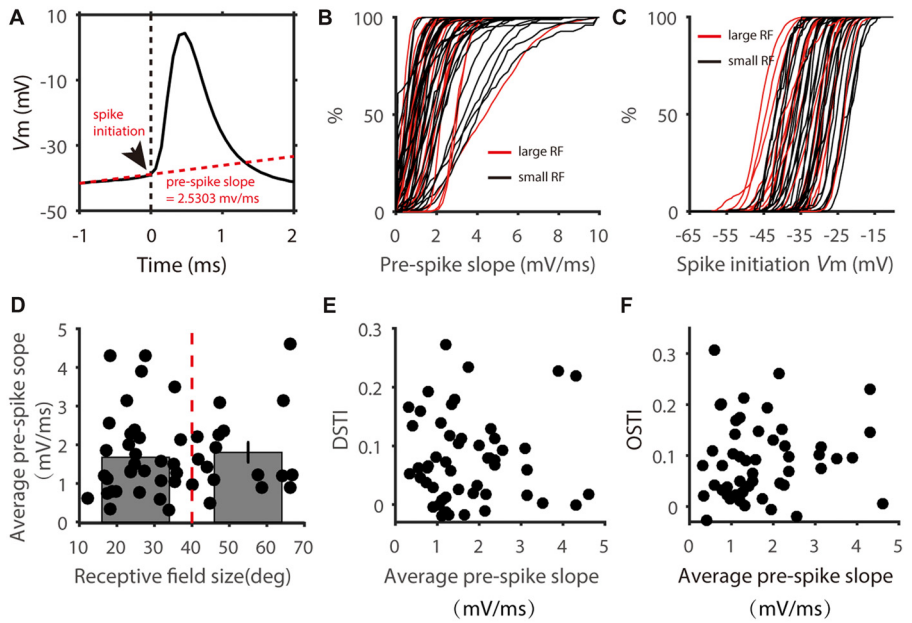

FIGURE 6 | Distribution of pre-spike V_m slopes. **(A)** Calculation of pre-spike V_m slope. Arrow head shows the point of spike initiation. The slope of the red dotted line shows the mean pre-spike V_m slope during the 1 ms window before spike onset. **(B)** Cumulative distributions of pre-spike V_m slope of cells with small (black) and large (red) RFs. Each line represent all spikes from one cell. **(C)** Cumulative distributions of spike initiating V_m of the two groups of cells. **(D)** Scatter plot of average pre-spike slope vs. RF size. The average pre-spike slopes of two groups divided at 40 degrees of RF size (red dotted line) showed no significant difference (t = 0.37, P = 0.71). **(E,F)** Scatter plot of DSTI **(E)** and OSTI **(F)** vs. average pre-spike slope.

OSTI) did not show correlation with pre-spike slope in the recorded SGS cells (**Figures 6E,F**). Because small pre-spike slope is often associated with dendritic spikes which has been found in wide-field SGS cells (Gale and Murphy, 2016), our results suggest that it is unlikely that dendritic processing has much effect on feature selectivity transformation from V_m to spikes in mouse SGS neurons.

Finally, we analyzed the relationship between pre-spike slope and spike-initiating V_m for each cell. In some cells, a negative correlation was seen between the pre-spike slope and V_m threshold (e.g., **Figure 7A**), indicating a faster V_m rise is needed for spike initiation at more hyperpolarized V_m. In other cells, their relationship is rather flat (e.g., **Figure 7B**). To quantify this relationship, we compared the average pre-spike slopes between the 0%–25% and 75%–100% of the observed V_m range for spike initiation (red circles in **Figures 7A,B**), and normalized their difference by the corresponding V_m difference. Notably, this "slope-changing rate" was well correlated with the RF size (r = 0.60, $P < 0.0001$, **Figure 7C**). Most cells with smaller RFs had negative values (**Figure 7A** for an example

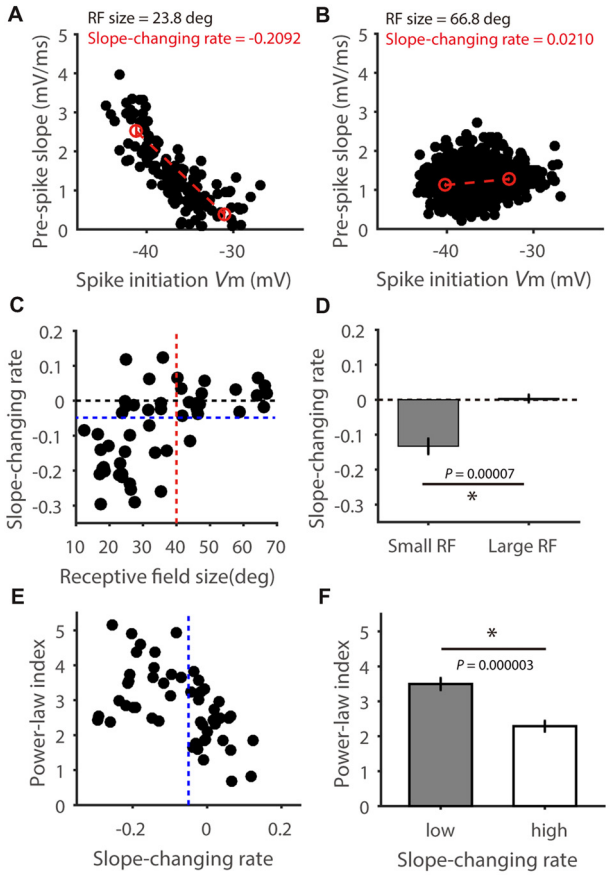

FIGURE 7 | The relationship between pre-spike V_m slope and spike-initiating V_m. **(A,B)** Relationship between pre-spike V_m slope and spike initiating V_m level in two example cells, one with small RF **(A)** and the other large **(B)**. Red circles indicate average pre-spike slopes for all spikes in the 0%–25% and 75%–100% spike initiating V_m range. Red dotted lines indicate the pre-spike slope changing rates. **(C)** Scatter plot of the "slope-changing rate" vs. RF size, indicating positive correlation between them ($r = 0.60$, $P < 0.0001$). Note that most of the cells (31/34, 91.2%) with RF smaller than 40 degrees (red dotted line) had values smaller than zero, and most of the cells with larger RFs (17/18, 94.4%) had values around zero and larger than −0.5 (blue dotted line). **(D)** The "slope-changing rate" is significantly different between the two groups of cells ($t = 4.35$, $P < 0.0001$). **(E)** Scatter plot of power-law index vs. slope changing rate, indicating negative correlation between them ($r = 0.49$ $P = 0.0002$), and **(F)** the means were significantly different between cells with high and low changing rate ($t = 5.29$, $P < 0.0001$). Error bars represent SEM. * represents $P < 0.0001$.

cell, **Figures 7C,D** for the population), while cells with larger RFs had values around zero (**Figure 7B** for an example cell, **Figures 7C,D** for the population; $t = 4.35$, $P < 0.0001$ for comparison between the two groups). In other words, for cells with smaller RFs, their spike initiation would become "easier" at more depolarized V_m because smaller V_m rise rate is needed, which would then contribute to their superlinear behavior in V_m-spike transformation (**Figure 5C**) and higher power-law index than bigger RF neurons (**Figures 7E,F**). Overall, these results suggest that RF-size-dependent spike initiation is another factor contributing to feature selectivity transformation from V_m to spikes.

DISCUSSION

Feature selectivity is a fundamental property that allows neurons in the sensory systems to extract and encode external information. The circuit and synaptic mechanisms underlying feature selectivity have been extensively studied in the visual system, where neurons are tuned to specific stimulus orientation or moving direction. These studies have revealed precise neural circuits that give rise to orientation and direction selectivity in different visual structures. For example, direction selective ganglion cells (DSGCs) in the retina acquire their selectivity from the intricate spatial and temporal interactions between synaptic excitation and inhibition (Wei and Feller, 2011; Vaney et al., 2012). Similarly, orientation selectivity in the visual cortex arises from the excitatory thalamic inputs that are precisely aligned in their spatial RFs (Ferster and Miller, 2000; Priebe and Ferster, 2008; Priebe, 2016). On the other hand, we have recently discovered that SGS neurons in the SC inherit their direction selectivity from the retina by precisely converging inputs of similarly-tuned DSGCs (Shi et al., 2017).

In addition to the precise circuit connectivity, the transformation from synaptic input to spike output is another key mechanism in processing feature selectivity. Here, we performed *in vivo* whole cell recording of mouse SGS neurons to study factors important for orientation and direction selectivity transformation from V_m to spikes. We found that the selectivity increased from the V_m to spike responses, and the degree of this increase was highly variable among different neurons. Interestingly, the variability was not random, but correlated with the size of the neurons' RFs. Our subsequent analyses indicate that the power-law relationship between V_m and spike rate and the relationship between V_m dynamics and spike initiation, but not dendritic processing, are RF size dependent and likely contribute to the observed input-output transformation of feature selectivity.

The power-law index, i.e., the exponent of the fitted power-law function, has been used to estimate the degree of V_m-to-spike transformation in previous studies (Finn et al., 2007; Priebe and Ferster, 2008, 2012; Tan et al., 2011). Similar as in visual cortex (Tan et al., 2011), our studies showed that the power-law index is positively correlated with the level of increase of feature selectivity from V_m to spikes. In other words, the higher the index, the greater degree of the V_m-to-spike sharpening of orientation/direction selectivity will be. Previous studies in cat V1 demonstrated that the power-law relationship between V_m and spike rate could be explained by trial-to-trial response variability (Hansel and van Vreeswijk, 2002; Miller and Troyer, 2002; Carandini, 2004; Priebe et al., 2004). Our finding that the power-law index is correlated with RF size, which would not affect response variability, suggests that additional mechanisms may be also involved. One possible factor is the relationship between spike initiating V_m and the required depolarizing rate, which we found to be correlated with RF size in mouse SGS neurons. Cells with smaller RFs display a negative correlation, where spike initiation becomes "easier" at more depolarized V_m because smaller V_m rise rate is needed. These

cells would likely show higher power-law index and superlinear behavior in V_m-spike transformation. In contrast, cells with larger RFs require similar depolarization rate for spike initiation at different V_m, thus displaying smaller power-law index than smaller RF cells.

What causes the differences in the relationship between V_m and spike rate and between V_m dynamics and spike initiation among cells with different RF sizes is still unknown. One possibility is that cells with different RFs may represent distinct cell types. We were not able to distinguish the recorded cells into subtypes because of the limited dataset in reconstructed morphology. But it was shown that narrow field (NF) vertical cells, wide field (WF) vertical and stellate cells are the three types of excitatory cells and they show different RF size (Gale and Murphy, 2014). It is possible that these cells have different biophysical features in their membrane properties that underlie their difference in V_m-to-spike transformation. On the other hand, horizontal cells represent possibly the only inhibitory cell type in the mouse SGS (Gale and Murphy, 2014), and our optogenetic experiments demonstrate that they also display RF-size-dependent V_m-to-spike transformation. This result suggests that additional factors within a cell type could contribute to the observed difference as well.

Finally, the RF-dependent differences in V_m-to-spike transformation may have functional implications. For small visual objects such as a prey that is best responded to by cells with small RFs, a higher input-output transformation could augment the saliency of the objects. For large visual stimuli such as a moving background, a lower transformation could maintain the wider tuning of the input, potentially helping keep the fidelity of the signal. These speculations may be testable one day under more natural conditions with ethologically-relevant visual stimulation. Our current study thus provides the basic information for future studies that will attempt to link sensory input to behavioral output.

AUTHOR CONTRIBUTIONS

XS and JC designed the experiments. XS performed *in vivo* whole-cell recording experiments and analyzed the data. YJ performed histology. JC guided data analysis and oversaw the project. All authors discussed the results and wrote the manuscript.

ACKNOWLEDGMENTS

We thank Xinyu Zhao and Hui Chen for their help with data analysis. This research was supported by US National Institutes of Health (NIH) grants (R01EY026286 and R01EY020950 to JC), National Natural Science Foundation of China (NSFC) grant (81371049 and 81770956 to XS), and Tianjin Science Fund for Distinguished Young Scholars (17JCJQJC46000 to XS).

REFERENCES

Anderson, J. S., Lampl, I., Gillespie, D. C., and Ferster, D. (2000). The contribution of noise to contrast invariance of orientation tuning in cat visual cortex. *Science* 290, 1968–1972. doi: 10.1126/science.290.5498.1968

Azouz, R., and Gray, C. M. (2000). Dynamic spike threshold reveals a mechanism for synaptic coincidence detection in cortical neurons *in vivo*. *Proc. Natl. Acad. Sci. U S A* 97, 8110–8115. doi: 10.1073/pnas.130200797

Cang, J., Savier, E., Barchini, J., and Liu, X. (2018). Visual Function, Organization, and Development of the Mouse Superior Colliculus. *Annu. Rev. Vis. Sci.* doi: 10.1146/annurev-vision-091517-034142 [Epub ahead of print].

Carandini, M. (2004). Amplification of trial-to-trial response variability by neurons in visual cortex. *PLoS Biol.* 2:E264. doi: 10.1371/journal.pbio.0020264

Carandini, M. (2007). Melting the iceberg: contrast invariance in visual cortex. *Neuron* 54, 11–13. doi: 10.1016/j.neuron.2007.03.019

Carandini, M., and Ferster, D. (2000). Membrane potential and firing rate in cat primary visual cortex. *J. Neurosci.* 20, 470–484. doi: 10.1523/JNEUROSCI.20-01-00470.2000

Endo, T., Yanagawa, Y., Obata, K., and Isa, T. (2003). Characteristics of GABAergic neurons in the superficial superior colliculus in mice. *Neurosci. Lett.* 346, 81–84. doi: 10.1016/s0304-3940(03)00570-6

Ferster, D., and Miller, K. D. (2000). Neural mechanisms of orientation selectivity in the visual cortex. *Annu. Rev. Neurosci.* 23, 441–471. doi: 10.1146/annurev.neuro.23.1.441

Finn, I. M., Priebe, N. J., and Ferster, D. (2007). The emergence of contrast-invariant orientation tuning in simple cells of cat visual cortex. *Neuron* 54, 137–152. doi: 10.1016/j.neuron.2007.02.029

Fontaine, B., Peña, J. L., and Brette, R. (2014). Spike-threshold adaptation predicted by membrane potential dynamics *in vivo*. *PLoS Comput. Biol.* 10:e1003560. doi: 10.1371/journal.pcbi.1003560

Gale, S. D., and Murphy, G. J. (2014). Distinct representation and distribution of visual information by specific cell types in mouse superficial superior colliculus. *J. Neurosci.* 34, 13458–13471. doi: 10.1523/JNEUROSCI.2768-14.2014

Gale, S. D., and Murphy, G. J. (2016). Active dendritic properties and local inhibitory input enable selectivity for object motion in mouse superior colliculus neurons. *J. Neurosci.* 36, 9111–9123. doi: 10.1523/JNEUROSCI.0645-16.2016

Hansel, D., and van Vreeswijk, C. (2002). How noise contributes to contrast invariance of orientation tuning in cat visual cortex. *J. Neurosci.* 22, 5118–5128. doi: 10.1523/JNEUROSCI.22-12-05118.2002

Hubel, D. H., and Wiesel, T. N. (1959). Receptive fields of single neurones in the cat's striate cortex. *J. Physiol.* 148, 574–591. doi: 10.1113/jphysiol.1959.sp006308

Hubel, D. H., and Wiesel, T. N. (1962). Receptive fields, binocular interaction and functional architecture in the cat's visual cortex. *J. Physiol.* 160, 106–154. doi: 10.1113/jphysiol.1962.sp006837

Inayat, S., Barchini, J., Chen, H., Feng, L., Liu, X., and Cang, J. (2015). Neurons in the most superficial lamina of the mouse superior colliculus are highly selective for stimulus direction. *J. Neurosci.* 35, 7992–8003. doi: 10.1523/JNEUROSCI.0173-15.2015

Ito, S., and Feldheim, D. A. (2018). The mouse superior colliculus: an emerging model for studying circuit formation and function. *Front. Neural Circuits* 12:10. doi: 10.3389/fncir.2018.00010

Lampl, I., Anderson, J. S., Gillespie, D. C., and Ferster, D. (2001). Prediction of orientation selectivity from receptive field architecture in simple cells of cat visual cortex. *Neuron* 30, 263–274. doi: 10.1016/s0896-6273(01)00278-1

Li, Y. T., Ibrahim, L. A., Liu, B. H., Zhang, L. I., and Tao, H. W. (2013). Linear transformation of thalamocortical input by intracortical excitation. *Nat. Neurosci.* 16, 1324–1330. doi: 10.1038/nn.3494

Lien, A. D., and Scanziani, M. (2013). Tuned thalamic excitation is amplified by visual cortical circuits. *Nat. Neurosci.* 16, 1315–1323. doi: 10.1038/nn.3488

Marshel, J. H., Kaye, A. P., Nauhaus, I., and Callaway, E. M. (2012). Anterior-posterior direction opponency in the superficial mouse lateral geniculate nucleus. *Neuron* 76, 713–720. doi: 10.1016/j.neuron.2012.09.021

Mazurek, M., Kager, M., and Van Hooser, S. D. (2014). Robust quantification of orientation selectivity and direction selectivity. *Front. Neural Circuits* 8:92. doi: 10.3389/fncir.2014.00092

Miller, K. D., and Troyer, T. W. (2002). Neural noise can explain expansive, power-law nonlinearities in neural response functions. *J. Neurophysiol.* 87, 653–659. doi: 10.1152/jn.00425.2001

Mize, R. R. (1988). Immunocytochemical localization of γ-aminobutyric acid (GABA) in the cat superior colliculus. *J. Comp. Neurol.* 276, 169–187. doi: 10.1002/cne.902760203

Mize, R. R. (1992). The organization of GABAergic neurons in the mammalian superior colliculus. *Prog. Brain Res.* 90, 219–248. doi: 10.1016/s0079-6123(08)63616-x

Piscopo, D. M., El-Danaf, R. N., Huberman, A. D., and Niell, C. M. (2013). Diverse visual features encoded in mouse lateral geniculate nucleus. *J. Neurosci.* 33, 4642–4656. doi: 10.1523/JNEUROSCI.5187-12.2013

Platkiewicz, J., and Brette, R. (2010). A threshold equation for action potential initiation. *PLoS Comput. Biol.* 6:e1000850. doi: 10.1371/journal.pcbi.1000850

Priebe, N. J. (2016). Mechanisms of orientation selectivity in the primary visual cortex. *Annu. Rev. Vis. Sci.* 2, 85–107. doi: 10.1146/annurev-vision-111815-114456

Priebe, N. J., and Ferster, D. (2005). Direction selectivity of excitation and inhibition in simple cells of the cat primary visual cortex. *Neuron* 45, 133–145. doi: 10.1016/j.neuron.2004.12.024

Priebe, N. J., and Ferster, D. (2008). Inhibition, spike threshold, and stimulus selectivity in primary visual cortex. *Neuron* 57, 482–497. doi: 10.1016/j.neuron.2008.02.005

Priebe, N. J., and Ferster, D. (2012). Mechanisms of neuronal computation in mammalian visual cortex. *Neuron* 75, 194–208. doi: 10.1016/j.neuron.2012.06.011

Priebe, N. J., Mechler, F., Carandini, M., and Ferster, D. (2004). The contribution of spike threshold to the dichotomy of cortical simple and complex cells. *Nat. Neurosci.* 7, 1113–1122. doi: 10.1038/nn1310

Scholl, B., Tan, A. Y., Corey, J., and Priebe, N. J. (2013). Emergence of orientation selectivity in the Mammalian visual pathway. *J. Neurosci.* 33, 10616–10624. doi: 10.1523/JNEUROSCI.0404-13.2013

Shi, X., Barchini, J., Ledesma, H. A., Koren, D., Jin, Y., Liu, X., et al. (2017). Retinal origin of direction selectivity in the superior colliculus. *Nat. Neurosci.* 20, 550–558. doi: 10.1038/nn.4498

Smith, S. L., Smith, I. T., Branco, T., and Häusser, M. (2013). Dendritic spikes enhance stimulus selectivity in cortical neurons *in vivo*. *Nature* 503, 115–120. doi: 10.1038/nature12600

Sun, W., Tan, Z., Mensh, B. D., and Ji, N. (2016). Thalamus provides layer 4 of primary visual cortex with orientation- and direction-tuned inputs. *Nat. Neurosci.* 19, 308–315. doi: 10.1038/nn.4196

Tan, A. Y., Brown, B. D., Scholl, B., Mohanty, D., and Priebe, N. J. (2011). Orientation selectivity of synaptic input to neurons in mouse and cat primary visual cortex. *J. Neurosci.* 31, 12339–12350. doi: 10.1523/JNEUROSCI.2039-11.2011

Vaney, D. I., Sivyer, B., and Taylor, W. R. (2012). Direction selectivity in the retina: symmetry and asymmetry in structure and function. *Nat. Rev. Neurosci.* 13, 194–208. doi: 10.1038/nrn3165

Wang, L., Sarnaik, R., Rangarajan, K., Liu, X., and Cang, J. (2010). Visual receptive field properties of neurons in the superficial superior colliculus of the mouse. *J. Neurosci.* 30, 16573–16584. doi: 10.1523/JNEUROSCI.3305-10.2010

Wei, W., and Feller, M. B. (2011). Organization and development of direction-selective circuits in the retina. *Trends Neurosci.* 34, 638–645. doi: 10.1016/j.tins.2011.08.002

Wester, J. C., and Contreras, D. (2013). Biophysical mechanism of spike threshold dependence on the rate of rise of the membrane potential by sodium channel inactivation or subthreshold axonal potassium current. *J. Comput. Neurosci.* 35, 1–17. doi: 10.1007/s10827-012-0436-2

Wilent, W. B., and Contreras, D. (2005). Stimulus-dependent changes in spike threshold enhance feature selectivity in rat barrel cortex neurons. *J. Neurosci.* 25, 2983–2991. doi: 10.1523/JNEUROSCI.4906-04.2005

Zhao, X., Chen, H., Liu, X., and Cang, J. (2013a). Orientation-selective responses in the mouse lateral geniculate nucleus. *J. Neurosci.* 33, 12751–12763. doi: 10.1523/JNEUROSCI.0095-13.2013

Zhao, X., Liu, M., and Cang, J. (2013b). Sublinear binocular integration preserves orientation selectivity in mouse visual cortex. *Nat. Commun.* 4:2088. doi: 10.1038/ncomms3088

Zhao, X., Liu, M., and Cang, J. (2014). Visual cortex modulates the magnitude but not the selectivity of looming-evoked responses in the superior colliculus of awake mice. *Neuron* 84, 202–213. doi: 10.1016/j.neuron.2014.08.037

Conflict of Interest Statement: The authors declare that the research was conducted in the absence of any commercial or financial relationships that could be construed as a potential conflict of interest.

frontiers in Neuroscience

ORIGINAL RESEARCH
published: 11 June 2018
doi: 10.3389/fnins.2018.00396

Visual Neurons in the Superior Colliculus Discriminate Many Objects by Their Historical Values

Whitney S. Griggs[1], Hidetoshi Amita[1], Atul Gopal[1] and Okihide Hikosaka[1,2]*

[1] *Laboratory of Sensorimotor Research, National Eye Institute, National Institutes of Health, Bethesda, MD, United States,*
[2] *National Institute on Drug Abuse, National Institutes of Health, Baltimore, MD, United States*

The superior colliculus (SC) is an important structure in the mammalian brain that orients the animal toward distinct visual events. Visually responsive neurons in SC are modulated by visual object features, including size, motion, and color. However, it remains unclear whether SC activity is modulated by non-visual object features, such as the reward value associated with the object. To address this question, three monkeys were trained (>10 days) to saccade to multiple fractal objects, half of which were consistently associated with large rewards while other half were associated with small rewards. This created historically high-valued ('good') and low-valued ('bad') objects. During the neuronal recordings from the SC, the monkeys maintained fixation at the center while the objects were flashed in the receptive field of the neuron without any reward. We found that approximately half of the visual neurons responded more strongly to the good than bad objects. In some neurons, this value-coding remained intact for a long time (>1 year) after the last object-reward association learning. Notably, the neuronal discrimination of reward values started about 100 ms after the appearance of visual objects and lasted for more than 100 ms. These results provide evidence that SC neurons can discriminate objects by their historical (long-term) values. This object value information may be provided by the basal ganglia, especially the circuit originating from the tail of the caudate nucleus. The information may be used by the neural circuits inside SC for motor (saccade) output or may be sent to the circuits outside SC for future behavior.

Keywords: superior colliculus, object-value learning, value coding, long-term memory, rhesus monkey

OPEN ACCESS

Edited by:
Tadashi Isa,
Kyoto University, Japan

Reviewed by:
Shunsuke Kobayashi,
Fukushima Medical University, Japan
Paul Geoffrey Overton,
University of Sheffield,
United Kingdom

****Correspondence:***
Whitney S. Griggs
wsgriggs@gmail.com

Specialty section:
This article was submitted to Decision Neuroscience, a section of the journal Frontiers in Neuroscience

Received: *28 February 2018*
Accepted: *23 May 2018*
Published: *11 June 2018*

Citation:
Griggs WS, Amita H, Gopal A and Hikosaka O (2018) Visual Neurons in the Superior Colliculus Discriminate Many Objects by Their Historical Values. Front. Neurosci. 12:396. doi: 10.3389/fnins.2018.00396

INTRODUCTION

The superior colliculus (SC) is an important brain region of mammals that allows them to precisely control their gaze direction and orient toward relevant and salient objects in their surrounding world. These functions are facilitated by the SC's involvement with visual spatial attention and its role in generating a retinotopic priority map for target selection (Fecteau and Munoz, 2006; Krauzlis et al., 2013; Wolf et al., 2015; Crapse et al., 2018). Specific visual features of objects, including size, color, and motion, modulate the activity in SC and contribute to perceptual decisions (Cynader and Berman, 1972; Moors and Vendrik, 1979; Horwitz et al., 2004; Hall and Colby, 2016; Herman and Krauzlis, 2017). Task-dependent variables, including saccade target probability or covert attention allocation, also modulate the activity of SC neurons

(Basso and Wurtz, 1998; Ignashchenkova et al., 2004). Visual responses in SC neurons are higher when the monkey is covertly attending to the future visual object location (Ignashchenkova et al., 2004), further suggesting that activity in specific SC locations may reflect a spatial attention signal. More recently, researchers used a color-change task to show that event-related SC activity encodes the behavioral significance of visual objects, even for object features not commonly attributed to the SC (Herman and Krauzlis, 2017). As the authors discuss, this suggests that SC plays an important role in action selection and attention by helping choose what sensory information is most relevant to future actions. To help form this priority map, signals from many cortical and subcortical regions converge on the SC and modulate the activity of its neurons (see review Krauzlis et al., 2013).

Despite the research exploring how SC neurons respond to different visual features, it remains unclear how non-visual features, such as reward history, affect the activity of SC neurons. We have shown earlier that visual responses of SC neurons are influenced by short-term reward history associated with specific visual locations (Ikeda and Hikosaka, 2003). In this study, we extended this result further by testing whether long-term reward history associated with specific visual objects would modulate activity of SC neurons.

In this study, we explored this question by testing whether SC neurons respond differently to objects previously associated with different amounts of reward value (high or low volume of juice). We trained three monkeys to discriminate a large number of visual objects that were associated with a consistent small or large juice reward. After multiple days of training with these visual objects, we recorded from SC neurons as each monkey completed a Passive Viewing task where they fixated on a center dot as the visual objects were sequentially shown in the neuron's receptive field without the associated reward. We found that many neurons clearly discriminated between visual objects associated with a large juice reward history or small juice reward history.

MATERIALS AND METHODS

General Procedure

Many of the methods used in this paper have been described in detail in a previous paper (Yasuda et al., 2012). All animal care and experimental procedures were approved by the National Eye Institute Animal Care and Use Committee and followed the Public Health Service Policy on the Humane Care and Use of Laboratory Animals. The raw data supporting the conclusions of this manuscript will be made available by the authors, without undue reservation, to any qualified researcher. We used three monkeys (*Macaca mulatta*, male, 8–10 kg; monkeys R, S, and D). Under general anesthesia and sterile conditions, we implanted a head post, scleral search coil, and recording chamber for each monkey. The recording chamber was positioned directly over the occipito-parietal cortex. For monkeys R and S, we used scleral search coil to record eye movements at 1000 Hz. For monkey D, we recorded eye movements at 1000 Hz using an infrared high-speed camera (EyeLink 1000 Plus) during the initial sessions while the final sessions were recorded using a scleral search coil.

Visual Stimuli

In this experiment, we used visual fractal objects with several randomly determined features (size, colors, and shape), which were generated for each monkey (Miyashita et al., 1991; Yamamoto et al., 2012). This ensured that the monkeys had no previous perceptual exposures to these objects. To avoid differences in physical salience from systemically influencing our results, we used a large number of distinct visual stimuli for each monkey and randomly assigned the visual stimuli to different reward groups. On average, the fractal size was $\sim 7^\circ \times 7^\circ$, but varied between $5^\circ - 10^\circ$.

Behavioral Tasks

Behavioral tasks were controlled by BLIP, a custom VC++ based software[1]. The monkey sat head-fixed in a primate chair positioned 30 cm away from a frontoparallel screen. Stimuli were back-projected on to the screen using an active-matrix liquid crystal display projector (PJ550, ViewSonic). Monkeys received diluted apple juice as rewards for successful task completion.

We used three different behavioral tasks: Delayed Saccade task for training, Free Viewing task for behavioral testing, and Passive Viewing task for neuronal testing. The Delayed Saccade task was initially used to train the monkeys to associate each visual object with a fixed reward outcome (large or small). After this initial training, we periodically used the Delayed Saccade task to maintain each monkey's memory of the object-reward associations. After the initial 10 days of training with the Delayed Saccade task, we began testing the preference for objects using two tasks: Free Viewing (for behavioral preference) and Passive Viewing (for neuronal preference). There were two important features in these testing tasks: (1) During these two tasks, the reward outcome was uncorrelated with the presented objects, unlike the Delayed Saccade task; (2) These tasks were used at least 1 day after the most recent training. Therefore, any behavioral/neuronal preference was 'automatic' and was based on the old object-reward association, which is attributed to 'long-term memory.'

Delayed Saccade Task for Object-Value Association Training (Figure 1A)

A set of eight visual objects were randomly split into four 'good' (large reward) objects and four 'bad' (small-reward) objects (**Figure 1C**). These object-reward associations were consistent across all training sessions. The monkey initiated each trial by fixating on a center white dot for 900 ± 200 ms. As the monkey maintained fixation on the center dot, a visual object appeared in the periphery at one of eight positions. The object was chosen pseudo-randomly from a set of eight objects. After 400 ms, the center fixation dot disappeared and the monkey was free to make a saccade to the visual object. After fixating the visual object for 500 ± 100 ms, the monkey received the juice reward associated

[1] www.robilis.com/blip/

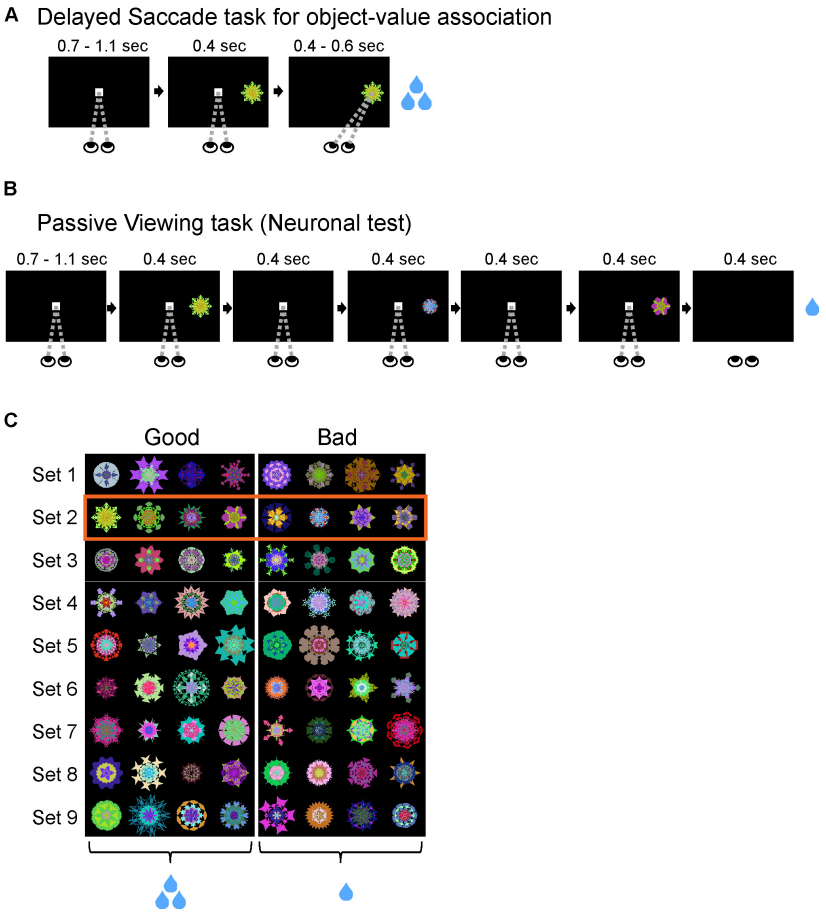

FIGURE 1 | Training task and neuronal test. **(A)** Delayed Saccade task for object-reward association training. Subjects completed a Delayed Saccade task where they made saccades to a visual object after an overlap period for the center dot and peripheral object. Each object was associated with a consistent small or large reward delivered after successfully fixating on the object. **(B)** Passive Viewing task for neuronal test. Subjects fixated on a center dot as 1–6 objects were sequentially displayed in the neuron's RF. At the end of a trial, subjects received a consistent reward not associated with any objects viewed during trial. This task was done on separate days from the Delayed Saccade task to avoid confounds from short-term learning. **(C)** Well-learned objects used with monkey R. Each row corresponds to one set of 8 objects. The first four objects (left of the dividing line) were consistently associated with large reward ('good' objects) while last four objects (right of the dividing line) with small reward ('bad' objects). Each set was trained >10 days before being used in the Passive Viewing task. Box with orange outline shows an example set used for tasks in this figure and **Figure 2**.

with the object (small/large reward: 100/300 ms for monkey D; 66/200 ms for monkey R; 80/250 ms for monkey S). If the monkey failed to maintain fixation on the center white dot or avoided looking at a visual object, then it received no reward and the same trial was repeated until successfully completed. Each block consisted of 80 trials with each visual object used in 10 trials. The start of each trial was preceded by an inter-trial interval (ITI) of 1250 ± 250 ms with a blank screen. Many sets of objects (n = 9, 9, 12 for monkeys R, S, D) were used repeatedly (>10 sessions) for this learning task. To test for learning of object-reward associations, we occasionally used a variant of this task that had interspersed binary choice trials (20% of all trials in a block). On a choice trial, the task structure was identical to a normal trial, except that two objects were presented instead of one object. After the good and bad objects were randomly presented at opposite locations on the screen and the overlap period ended, the monkey was free to choose which object to look at. After choosing an object and looking at the object for 500 ± 100 ms, the monkey received the reward associated with that object.

Passive Viewing Task for Neuronal Testing (Figure 1B)

The monkey initiated each trial by fixating on a center white dot for 900 ± 200 ms. As the monkey maintained fixation within the central fixation window (10° × 10°), 1–6 objects chosen pseudorandomly from a set of eight objects were sequentially presented in the receptive field of the neuron (400 ms for monkeys R and D; 300 ms for monkey S). Each object was followed by an intra-trial interval where only the fixation dot was present on the screen (400 ms for monkeys R and D; 300 ms for monkey S). At the end of a trial, the monkey received a fixed reward that was independent of the objects seen in the trial (monkey R: 200 ms; monkey S: 200 ms; monkey D: 300 ms). If the monkey broke fixation during the trial, then it received no reward

and a new trial was initiated with different pseudorandomly chosen objects from the same set of 8 objects. The start of the next trial was preceded by an ITI of 1250 ± 250 ms with a blank screen.

Free Viewing Task for Behavioral Testing (Figure 2A)

Each block of trials consisted of 30 trials with all objects drawn from the same set of eight objects. During each trial, four objects were presented on the screen in one of two configurations (square or diamond) with each object equidistant from the center of the screen. The four objects were pseudo-randomly chosen from the set of eight objects and could be any possible combination, i.e., 0–4 good objects combined with 0–4 bad objects. The objects were presented on the screen for 3 s and the monkey was free to look at or ignore the objects during that time. After a 600 ± 100 ms interval after the objects were turned off, a white fixation dot appeared in one of eight radial positions. The monkey received a fixed reward after maintaining fixation on the white dot for 1 s. The reward was not contingent on objects in the trial or monkey's behavior in the trial. The start of the next trial was preceded by an ITI of 1250 ± 250 ms with a blank screen.

Training and Testing Procedure

Before any behavioral or neural testing, we first taught each monkey the object-reward associations using Delayed Saccade task for 10 days. On each day, we used 80 trials per set, with each object being associated with its consistent reward 10 times. After these 10 days of initial training for a set, we occasionally refreshed each set using a single block of 40 or 80 trials. The gap between refreshing a specific set varied from 1 days to >450 days, with usually >1 week between training sessions. Following the initial 10 days of training, we started to use the Free Viewing task for behavioral test and Passive Viewing task for neuronal test. These tests were never done if the same objects had been used for a training session (object-value association) on the same day to avoid any possible confounds from short-term learning.

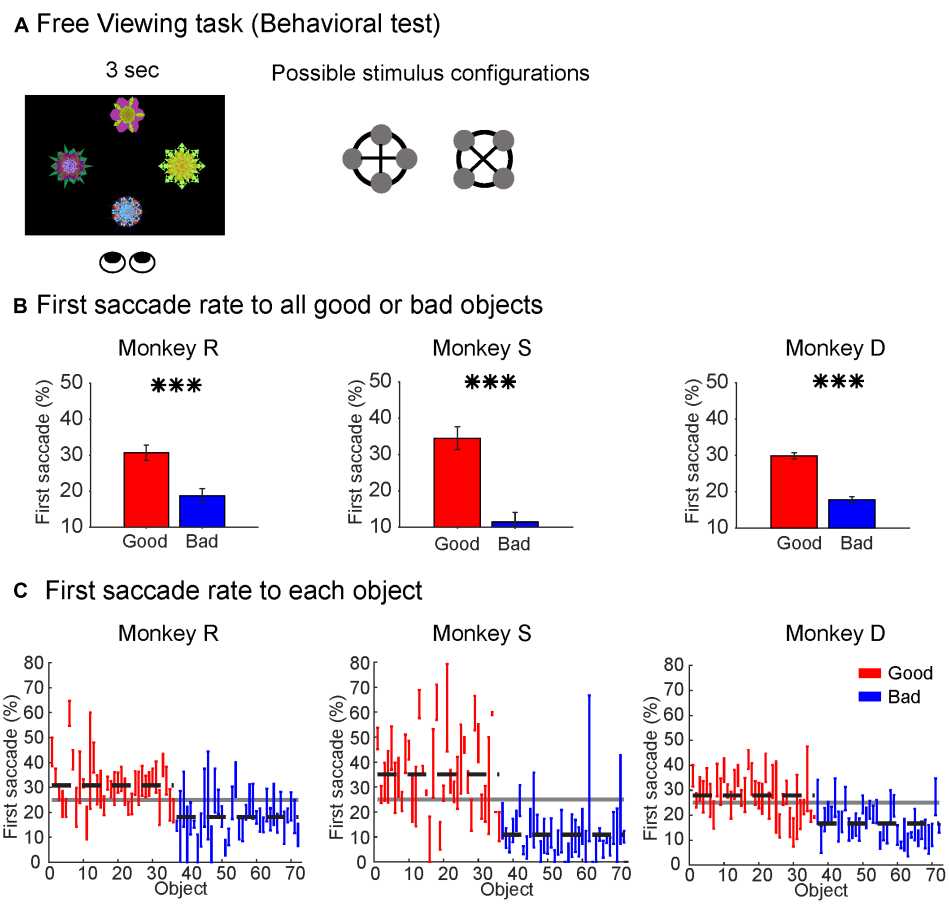

FIGURE 2 | Monkeys showed behavioral bias to good objects. **(A)** Free Viewing task for behavioral test. Four objects pseudorandomly drawn from a set of eight objects were presented in one of two configurations (square or diamond) with all objects equidistant from center of screen (15°). Objects presented on any given trial could contain 0, 1, 2, 3, or 4 good objects. Subject was free to look anywhere on the screen for duration of object presentations. **(B)** Behavioral preference for good objects in the Free Viewing task. All subjects made significantly more first saccades to good objects than bad objects despite no associated reward (***$p < 0.001$). **(C)** Behavioral preference for individual objects shown as first saccade rate to each object. Horizontal dashed lines represent group mean for good (red) and bad (blue) objects. Solid gray horizontal line represents chance rate (25%) for first saccade to one object among four objects.

Recording Procedures

We used tungsten microelectrodes (Alpha Omega, 1 MΩ at 10 kHz) to record single-units in the SC. We used a grid with 1 mm × 1 mm holes to record across multiple locations within the SC. To determine the top of the SC, we advanced the microelectrode until we heard clear visual activity in the SC and let the microelectrode settle for >5 min. We then slowly retracted the microelectrode until no more SC activity was heard. This final position was used as the top of the SC. During recording of each neuron, we mapped the receptive field using the Passive Viewing task with the visual objects being projected at various locations on the contralateral visual field to the hemisphere being recorded from. After identifying the visual location that evoked the strongest visual responses, we used this location for all subsequent object presentations. The final histology has not been conducted on these animals, thus the location of the recorded SC neurons has not been verified histologically.

Data Analysis

We used MATLAB 2015b for all analyses, including behavioral analyses and neuronal analyses. For behavioral analysis, the gaze locations and saccades (>0.5°) were calculated for each trial. We considered an object fixated when the gaze location was within 6° of the center of the object and the gaze location was stationary. We used the gaze locations and saccades to calculate percentage of first saccades to each object following object presentation.

For generating spike density functions (SDF), we used a kernel bandwidth of 10 ms. To assess saccade responsiveness, we compared each neuron's response during a baseline period (100 - 200 ms before saccade) and a response period (0–100 ms before saccade) while the monkey completed the Delayed Saccade task. We assessed statistical significance of the difference between the response and baseline periods using the Wilcoxon rank-sum test.

To assess visual responsiveness, we compared each neuron's response during a baseline period before the cue onset (0–200 ms before object onset) and a response period following each object presentation (0–200 after object onset). We assessed the statistical significance of the difference between the response and baseline periods using the Wilcoxon rank-sum test. To calculate the net visual response for each neuron, we defined the baseline activity as the average firing in a time window before object presentation (50–250 ms before object onset) and the gross visual response as the average firing in a time window after object presentation (100–300 ms after object onset). We then subtracted the base activity from the gross visual response to calculate the net visual response for each neuron. We computed the net visual response separately for good and bad objects.

To assess the strength of the neuronal discrimination of object-value association, we measured each neuron's response to different fractal objects by summing the number of spikes within a test window (100–300 ms after object presentation) for each object presentation. We then calculated the area under the receiver operating characteristic (AUROC) based upon the responses to good objects versus bad objects. To calculate this value discrimination score (AUROC), we compared the number of spikes in each test window for all good objects (objects 1–4) against the number of spikes in each test window for all bad objects (objects 5–8). The statistical significance of this value discrimination score was assessed using Wilcoxon rank-sum test.

To determine when the differences in response to good and bad objects began, we used a sliding time window method after pooling all the neurons from each monkey. In this method, we found when the averaged neuronal responses to good and bad objects were statistically different from each other in five consecutive overlapping time windows (50 ms time windows shifted by 5 ms). For example, the value discrimination began at 120 ms if the response differences in the following five time windows were all statistically significant: 70–120, 75–125, 80–130, 85–135, and 90–140. To calculate statistical significance for this method, we used the Wilcoxon signed-rank test. To determine when the value discrimination ended, we used the same method except we used the lower bound of the first time window where the difference in responses was no longer statistically significant. For example, the value difference would end at 400 ms if the 400–450 ms time window and all subsequent time windows were statistically non-significant.

To determine the net visual response to each of the object presentation number within the trial (1st, 2nd, 3rd, 4th, or 5th, object presented in a given trial), we compared the responses in a common response window (100–300 ms after object presentation). We limited this analysis to the first five objects shown in any given trial because monkey S used a modified Passive Viewing task with only 1–5 objects shown per trial. To calculate the value discrimination score (using AUROC) for good vs. bad objects for each of these object presentations, we used the same response window (100–300 ms after object presentation).

To calculate the value bias score for individual objects, we first compared the response of one neuron to 1 object (e.g., good) with the same neuron's averaged responses to four objects with the opposite value (e.g., bad) within the same set of eight objects. For this value bias score, we calculated AUROC based on the number of spikes within a response window (100–300 ms after object presentation). We compared the number of spikes in each test window for the designated object (e.g., Object 3) against the number of spikes in each test window for all the opposite objects (e.g., Objects 5–8). To correct for comparing one object against four objects, we used the average number of spikes within the response window for the four opposite-value objects. We then averaged the score across all neurons in which the same object was tested. This is similar to the method we used to calculate the value discrimination score for each neuron but differs in two ways. For the value discrimination score, we compared all good objects vs. all bad objects, but for the value bias score for each object, we compared one object against all of the opposite value objects. Second, the value discrimination score was based upon only data from a single neuron while the value bias score was averaged across all neurons for which the designated object was used.

Significance Levels

Error bars in all plots show standard error of the mean (SEM) unless otherwise noted. Significance thresholds for all tests in this

study were $\alpha = 0.05$. $^{*}p < 0.05$, $^{**}p < 0.01$, $^{***}p < 0.001$, *ns*: non-significant.

RESULTS

To test whether long-term reward history of visual objects affected the visual response of SC neurons, we performed experiments in three phases in this study. We used separate tasks in each phase. First, each monkey learned object-reward associations for multiple sets of eight objects using the Delayed Saccade task (**Figure 1A**). In each set, four objects were consistently associated with a large juice reward ('good' objects) and the remaining four objects were consistently associated with a small juice reward ('bad' objects) (**Figure 1A**). Each monkey learned the association for at least nine sets of visual objects (>72 objects) to control for effects of physical salience from different luminosity, shape, size, or colors of different visual objects (**Figure 1C**). To assess each monkey's learning of the object-reward associations, we used a variant of the Delayed Saccade task that had interspersed binary-choice trials (20% of all trials). On those choice trials, the monkey had to choose between a good and bad object. The monkey then received the associated outcome of the object they chose. We found that just after 5 days of training, across all objects, each monkey chose the good object >97% of the time, demonstrating that each monkey had successfully learned the consistent reward associated with most, if not all, of the objects (Supplementary Figure S1).

Secondly, to test whether the monkeys discriminated good objects from bad objects without reward association after learning, we used a Free Viewing task (**Figure 2**). In this task, four objects drawn from a set of eight objects were simultaneously presented on the screen in either a diamond or square configuration (**Figure 2A**). We found that all three monkeys showed a significant bias in making the first saccade to the good objects (**Figure 2B**), which is consistent with our previous studies (Yasuda et al., 2012; Ghazizadeh et al., 2016a).

We then assessed the first saccade rate to each individual object to test whether the clear gaze bias was limited to a subset of the good objects. We found that most good objects had first-saccade rates above chance-level (25%) while most bad objects had first-saccade rates below chance level (**Figure 2C**). This demonstrated that all three monkeys successfully learned the reward value associated with different objects and automatically discriminated the objects based on their reward histories.

Thirdly, to test whether SC neurons discriminated good from bad objects, we recorded activity of SC neurons using a Passive Viewing task (**Figure 1B**), in which 1–6 previously trained visual objects were sequentially presented in the neuron's receptive field (RF). We recorded from a total of 92 neurons across three monkeys with this Passive Viewing task. Of those 92 neurons, 84 neurons were visually responsive (91%; $p < 0.05$, Wilcoxon rank-sum test).

Many of the 84 visually responsive neurons responded differently to good and bad objects. The activity of a representative value-coding neuron in monkey R is shown in Supplementary Figure S2 and **Figure 3**. The neuron's response was more prolonged to good objects than bad objects, largely independent of object identities (Supplementary Figure S2). Overall, it responded more strongly to the four good objects than the four bad objects (**Figure 3B**), although there was some variability across the objects in each group (**Figure 3A**).

Of the 84 visually responsive neurons, we determined whether each neuron discriminated good and bad objects by comparing the gross visual response of each neuron to good vs. bad objects in a response window (100–300 ms after object presentation). We then assessed the statistical significance of the difference between responses to good and bad objects using Wilcoxon rank-sum test. We found that 41 of the 84 visually responsive neurons responded differently to good and bad objects (49%; $p < 0.05$, Wilcoxon rank-sum test). We then examined their net response (visual response minus baseline firing) to good versus bad objects. We found that all of the value-modulated neurons had stronger net responses to good objects than bad objects (**Figure 4A**) and were thus 'positive-coding.' To quantify the strength of each neuron's discrimination for good and bad objects (value discrimination score), we calculated the area under the ROC (AUROC) for each recorded neuron (**Figure 4B**).

Next, to compare the value-modulation of SC among three monkeys, we pooled the neuronal data within each monkey and calculated each monkey's population average (**Figure 5A**). All three monkey's population averages showed significantly higher responses to the good than bad objects. The timing and magnitude of this difference differed slightly between monkeys (**Table 1**). For all monkeys, the value difference began after the peak visual response and lasted for at least 100 ms. In monkeys R and S, the value difference lasted until approximately 130–150 ms after the object was no longer presented. In monkey D, the value difference ended >100 ms before the object was extinguished.

We then analyzed the neuronal and behavioral discrimination of individual objects by their values (**Figure 5B**). The behavioral discrimination (i.e., first saccade to each object) was shown in **Figure 2C**, which is now shown in the ordinate. Here, we added the neuronal discrimination (i.e., averaged value bias of SC neurons to each object) shown in the abscissa. Most of the good objects were chosen by the first saccade more often than average (i.e., 1 out of 4 objects presented in the Free Viewing task = 25% in ordinate), while most of the bad objects were chosen less often than average. Most of the good objects caused SC neurons to respond more strongly than average (i.e., 0.5 in abscissa), while most of the bad objects caused SC neurons to respond more weakly than average. Similar effects occurred in the all monkeys. These data suggest that visual neurons in SC contribute to the behavioral choice of objects by their values.

Having established that SC neurons discriminated good from bad objects, we were curious if the value-modulation was affected by other parameters (i.e., object order, time since the last training session, RF eccentricity, saccadic activity, and depth of neuron). First, we analyzed the effect of object order within a trial, separately for good and bad objects (**Figure 6A**). See Supplementary Figure S2 for example trials. For each monkey, the visual response was strongest to the first object and diminished for later object presentations in a trial (**Figure 6B**). Despite this reduced visual response for later trials, the value difference

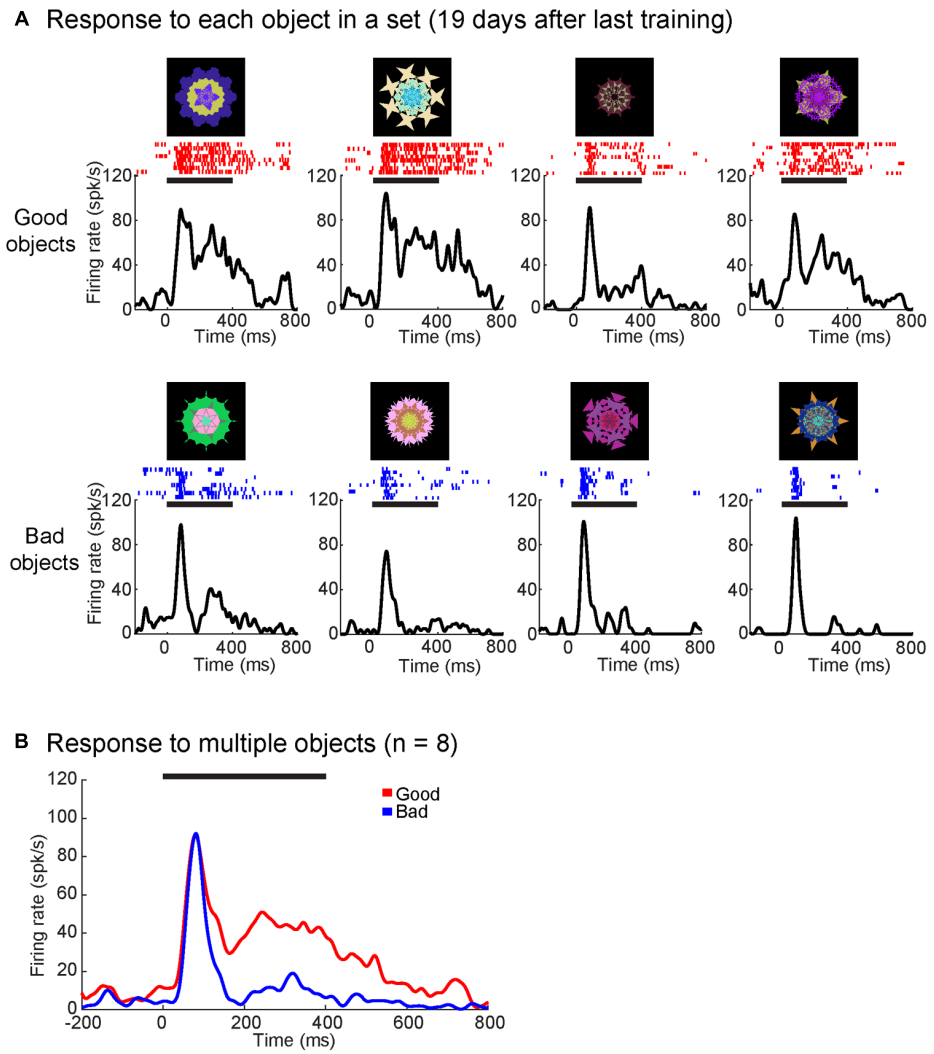

FIGURE 3 | Superior colliculus (SC) neuron showed more excitatory responses to good objects than bad. **(A)** Average responses to each object from one object set (19 days since the last training) shown as SDF and raster plots aligned to object onset (in monkey R). Upper row are good objects while lower row are bad objects. **(B)** SC neuron showed significantly higher responses to good objects than bad ($p < 0.01$). Average response to good (red) and bad (blue) objects displayed as SDF aligned to object onset. Solid horizontal lines represent the duration of the object presentations (0–400 ms). Neuron depth: 1000 um; RF (r,Θ): 9°,0°. Value discrimination score: 0.84 ($p < 0.01$).

remained even on late trials (black line in **Figure 6A**). For all monkeys, the later objects in a trial had smaller visual responses ($p < 0.05$, Wilcoxon signed rank test) while the value difference (calculated via value discrimination score) remained unchanged ($p > 0.05$, Wilcoxon signed rank test) (**Figure 6B**). To examine the changes in these later trials, we generated SDFs for the early object presentations and later object presentations separated by value of the objects (Supplementary Figure S3). We found later object presentations to evoke similar neuronal responses as early object presentations, but reduced in magnitude (Supplementary Figure S3), suggesting an overall reduction in visual response without any reduction in value difference.

Secondly, we tested whether time from the last training session decreased the strength of the value modulation. **Figure 7** shows that a single SC neuron in monkey D discriminated good and bad objects after 2 months (58 days) since the last training (value discrimination score: 0.69; $p < 0.001$, Wilcoxon rank-sum test). The time course of value-coding also showed little change (compared with **Figure 5A**). Supplementary Figure S4 shows the cumulative activity of several neurons in the superficial layer of SC in monkey D that discriminated good and bad objects for an object set after 470 days since the last training (value discrimination score: 0.63; $p < 0.01$, Wilcoxon rank-sum test).

By letting each monkey learn many sets of objects at separate temporal stages (i.e., different amounts of time since last training session for each set), we found SC neurons with significant value-coding at all memory periods tested (**Figure 8A**). There was no significance between the value discrimination score and the time since the last training [$F(2,168) = 0.38$, $p > 0.7$, Pearson's

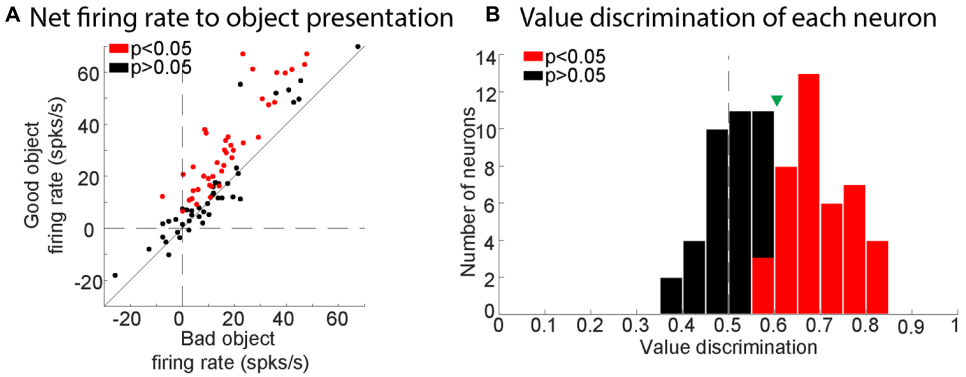

FIGURE 4 | Value-modulation of SC neurons in all three monkeys. **(A)** Comparison between net response to good and bad objects. Plots for each neuron (dots) are the net visual responses to good objects (ordinate) and bad objects (abscissa). Each net visual response was calculated as the difference between a response period and a baseline period. Red and black dots indicate neurons with significant value coding ($p < 0.05$) and non-significant value coding ($p > 0.05$), respectively. **(B)** Histogram showing the distribution of value discrimination score (AUROC) for all neurons recorded. Red and black bars represent neurons with significant value-coding ($p < 0.05$) and with non-significant value-coding ($p > 0.05$), respectively. Green triangle shows mean value discrimination score for all visually responsive neurons.

$r = 0.03$]. To explore this further, we split the data into six groups: <3 days, 4–10 days, 11–30 days, 31–100 days, 101–365 days, and >365 days since last training session (**Figure 8B**): the value-coding remained significant at all points, although it may have diminished after 1 year.

Thirdly, we examined whether the value-coding of SC neurons depended on the eccentricity of their RF (**Figure 9**). We found a non-significant relationship between value discrimination score and RF eccentricity (**Figure 9A**) [$F(2,82) = 0.22$, $p > 0.8$; Pearson's $r = 0.02$]. Receptive fields outside of the central 10 degrees are commonly considered part of peripheral visual field which is associated with poor discriminability (Strasburger et al., 2011). Yet, there was no significant difference in the strength of the value-coding between central vision (RF $\leq 10°$) and peripheral vision (RF $> 10°$) (**Figure 9B**) ($p > 0.8$, Wilcoxon rank-sum test). This suggests that SC neurons discriminated good objects from bad objects independent of their RF eccentricities.

Fourthly, we examined saccadic properties of the recorded visual neurons. Of the 84 visual neurons recorded, 18 neurons were also tested using the delayed saccade task. Of those 18 neurons, only 2 showed saccadic activity (11%; $p < 0.05$, Wilcoxon rank-sum test), which we defined as a rise in firing rate <100 ms before the saccade. Because of insufficient numbers, we did not further analyze any saccadic properties of the recorded neurons.

Finally, we examined whether the strength of the value coding depended on the dorso-ventral positions of neurons in SC (**Figure 10**). Most of our recorded neurons were within 2 mm from the surface of SC. Among them, high value-coding neurons tended to be in the ventral region. A significant regression equation was found [$F(2,81) = 2.01$, $p < 0.05$], with a Pearson's 'r' of 0.22 (**Figure 10**). This suggests that SC neurons in the ventral superficial layer showed stronger value-coding. Although all of these neurons are visually responsive, a minority of them (2 out of 18 neurons tested for saccadic activity) displayed pre-saccadic activity, suggesting that our recordings extended into the dorsal intermediate layer (though not examined histologically).

DISCUSSION

Value-Based Discrimination of Visual Objects by SC

Our data indicate that many neurons in the superficial layer of SC discriminate visual objects by their historical values, higher responses to good objects (i.e., objects previously associated with a large reward) than bad objects [i.e., objects previously associated with a small reward (**Figures 3,4**)]. Initially, these objects were completely new, but then they were repeatedly associated with fixed amounts of reward (large or small). Therefore, the ability of SC neurons to discriminate object was purely based on learning.

There are two important features of this learning. First, the learning resulted in long-term memory. After the object-value association learning, SC neurons were able to discriminate objects by their values, even when the objects had not been shown for a long time (**Figure 8**). Second, the memory includes peripheral vision. SC neurons discriminated objects by their values, even when they were located in periphery (>10°) (**Figure 9**).

These features together are crucial to find good objects. In real life, many objects, which have been experienced previously, may appear randomly. If short-term memory is used, their values may not be recognized if they have not been shown recently. Moreover, these objects may appear simultaneously. If peripheral vision does not work well [as often assumed (Strasburger et al., 2011)], gaze must be directed to many of the objects (with saccades) before a good object is recognized, even when long-term memories are available. This suggests that SC neurons may play an important role in recognizing the value of objects located in periphery, so that the subject can find good objects wherever they are located.

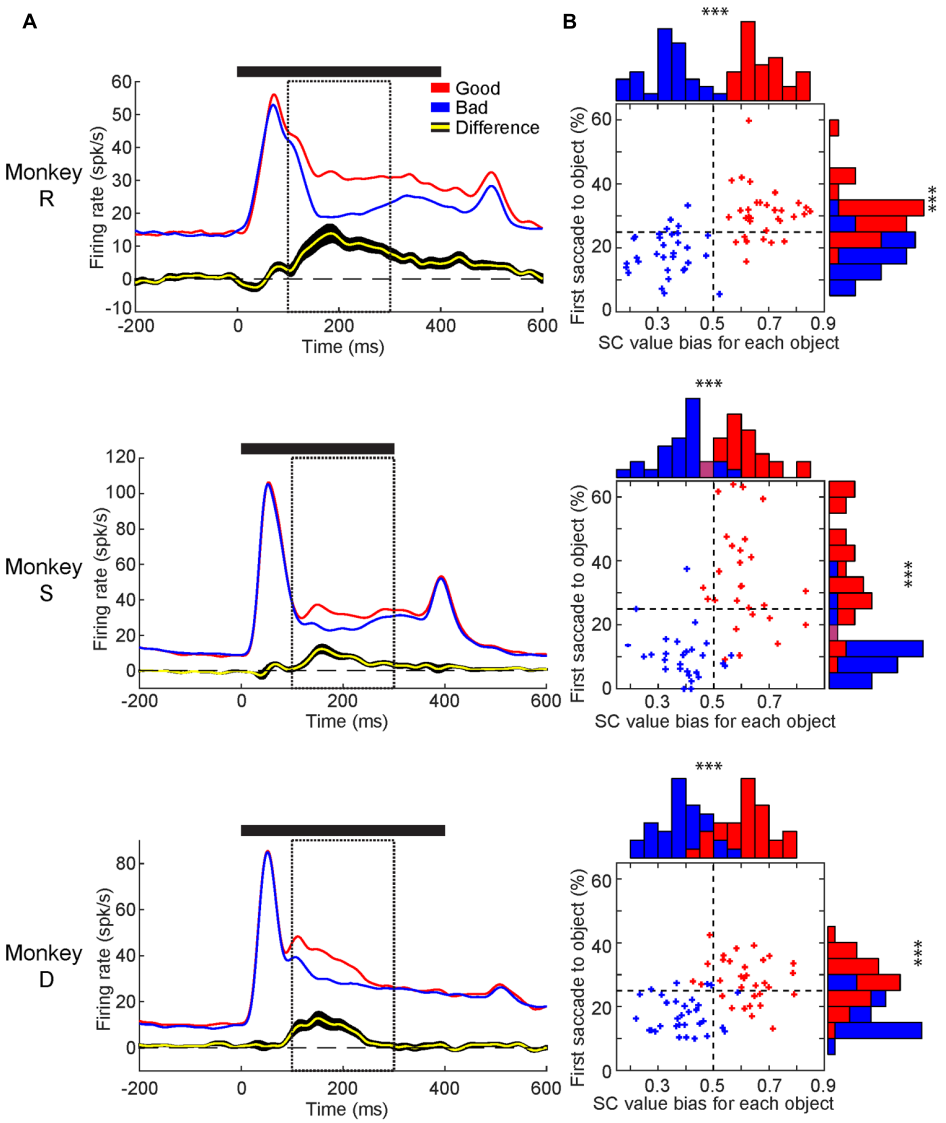

FIGURE 5 | Value-modulation of SC neurons in individual monkeys and individual objects. **(A)** Average neuronal response to good objects (red) and bad objects (blue) displayed as SDF aligned to object onset for each monkey. Below: the average difference across neurons between the responses to good and bad objects (yellow: average, black: SEM). Solid horizontal line represents duration of object presentations. Dashed boxes represent the response window used for calculating value discrimination score (100–300 ms). **(B)** Comparison between behavioral and neuronal preference for each object used. Behavioral preference measured by first saccade rate (ordinate) and neuronal preference measured by value bias score (abscissa). Good and Bad objects shown in red and blue, respectively. Purple bars in histogram represent red and blue bars of equal height. Horizontal dashed line shows chance level for first-saccade (25%). Vertical dashed line shows chance level for value bias score (0.5). ***$p < 0.001$.

TABLE 1 | Timing of visal responses.

Monkey	Peak visual response (ms)	Start of value difference (ms)	End of value difference (ms)
R	72	95	540
S	56	145	315
D	59	110	230

This is actually what happened in the Free Viewing task (**Figure 2**). In this task, four objects appeared in different positions, which means that most of them were located away from gaze position (i.e., periphery). The monkeys usually made the first saccade directly to a good object (**Figure 2B**). This motor output – saccade – is a typical way to find good objects. This visual-motor transformation can be accomplished by the connection from the superficial layer of SC (visual layer) to the intermediate layer of SC (saccade layer) (Isa et al., 1998; Ozen et al., 2000). Previous studies from our lab has also shown that these high-value objects are more salient than low-value objects and automatically attract the subject's attention (Ghazizadeh et al., 2016a). Given the role of the SC in generating priority maps for the visual environment, our data suggest that automatic

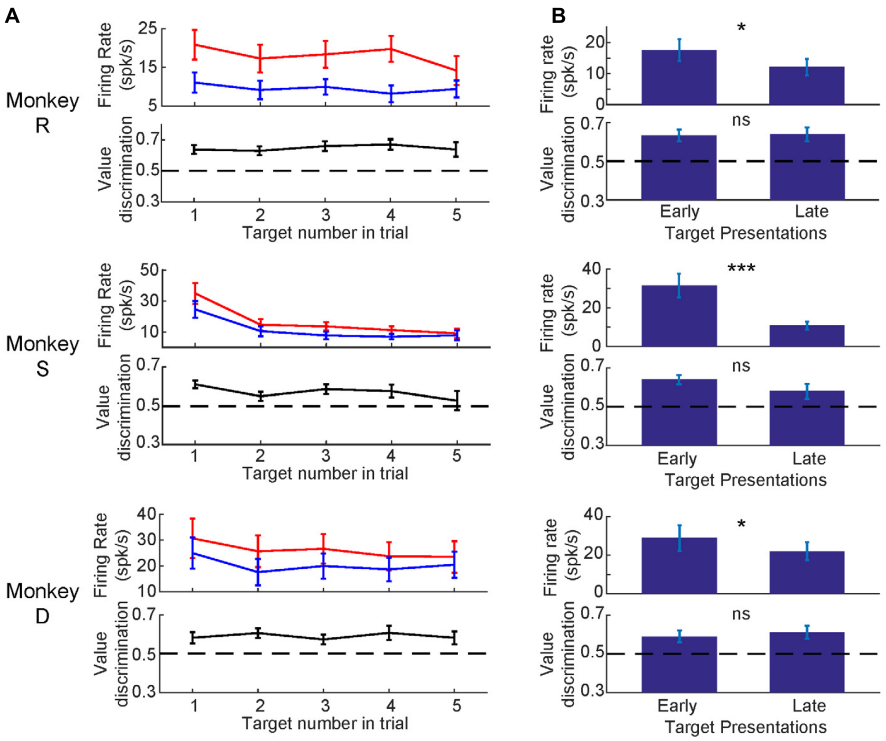

FIGURE 6 | Visual response diminished for later object presentations while value-modulation remained. **(A)** Average neuronal responses at 1st, 2nd, 3rd, 4th, or 5th presentation of objects in each trial. Top: firing rates (mean and SEM) for good objects (red) and bad objects (blue). Bottom: value-modulation measured by value discrimination score (with SEM). **(B)** Comparison between the early (1st) or late (4th and 5th) object presentations. Error bars: SEM. *$p < 0.05$, ***$p < 0.001$, *ns*: non-significant.

attention to good objects may be a direct consequence of the SC value-coding.

Rapidly and accurately recognizing peripheral objects and their associated ecological history is also important for goal-directed behavior. We previously tested a visual search task using the same type of fractal objects: One good object and several bad objects were presented simultaneously, all of which were chosen randomly from many objects (>20) (Ghazizadeh et al., 2016b). The monkeys (including monkey R) made rapid and accurate saccades to the good object, often directly, and obtained a large reward. This perfect goal-directed behavior required long-term object-value memories with high capacity, which is actually represented by SC visual neurons as shown in our study.

Inputs From the Basal Ganglia for Stable Object Values

The object value information in SC neurons may originate from the basal ganglia, especially the caudal-ventral part. Previous studies in our group showed that neurons in the tail of the caudate nucleus (CDt) respond to visual objects (i.e., fractals) very selectively, even when they are completely new (Yamamoto et al., 2012). CDt has a very localized output to the substantia nigra pars reticulata (i.e., caudal-dorsal-lateral part, cdlSNr) (Saint-Cyr et al., 1990; Kim et al., 2017), which predominantly projects to SC (Yasuda and Hikosaka, 2015). CDt has another localized output to the globus pallidus externus (i.e., caudal-ventral part, cvGPe), which then projects to cdlSNr (Kim et al., 2017). CDt-cdlSNr circuit and CDt-cvGPe-cdlSNr circuit act as the direct and indirect pathways. Due to the selective connections, most neurons in cdlSNr and cvGPe are highly sensitive to visual objects (Yasuda et al., 2012; Kim et al., 2017).

Importantly, most neurons in CDt-circuits discriminate visual objects by their values (Hikosaka et al., 2014), similarly to SC neurons in this study. CDt neurons, overall, were value-sensitive (Yamamoto et al., 2013), but this is often unclear for individual neurons because their responses are highly object-selective. In contrast, value-coding becomes stronger in cvGPe and cdlSNr neurons (Yasuda et al., 2012; Kim et al., 2017) for two reasons. First, object-selectivity becomes weaker, so that value-coding becomes clearer in individual neurons. Second, good objects are largely processed by the direct pathway, while bad objects are largely processed by the indirect pathway (Kim et al., 2017). Since all of these neurons (CDt, cvGPe, cdlSNr) are GABAergic inhibitory, the final output of the CDt-circuit sends distinct value information: cdlSNr neurons are inhibited by good objects and excited by bad objects (Yasuda et al., 2012).

Notably, visual neurons in SC are typically activated by the inputs from the retina and the primary visual cortex (Wurtz and Albano, 1980; Berson, 1988; May, 2006) with short latencies as shown in **Figure 5** and **Table 1**. Such excitatory visual responses would then be modulated by the object-value information from

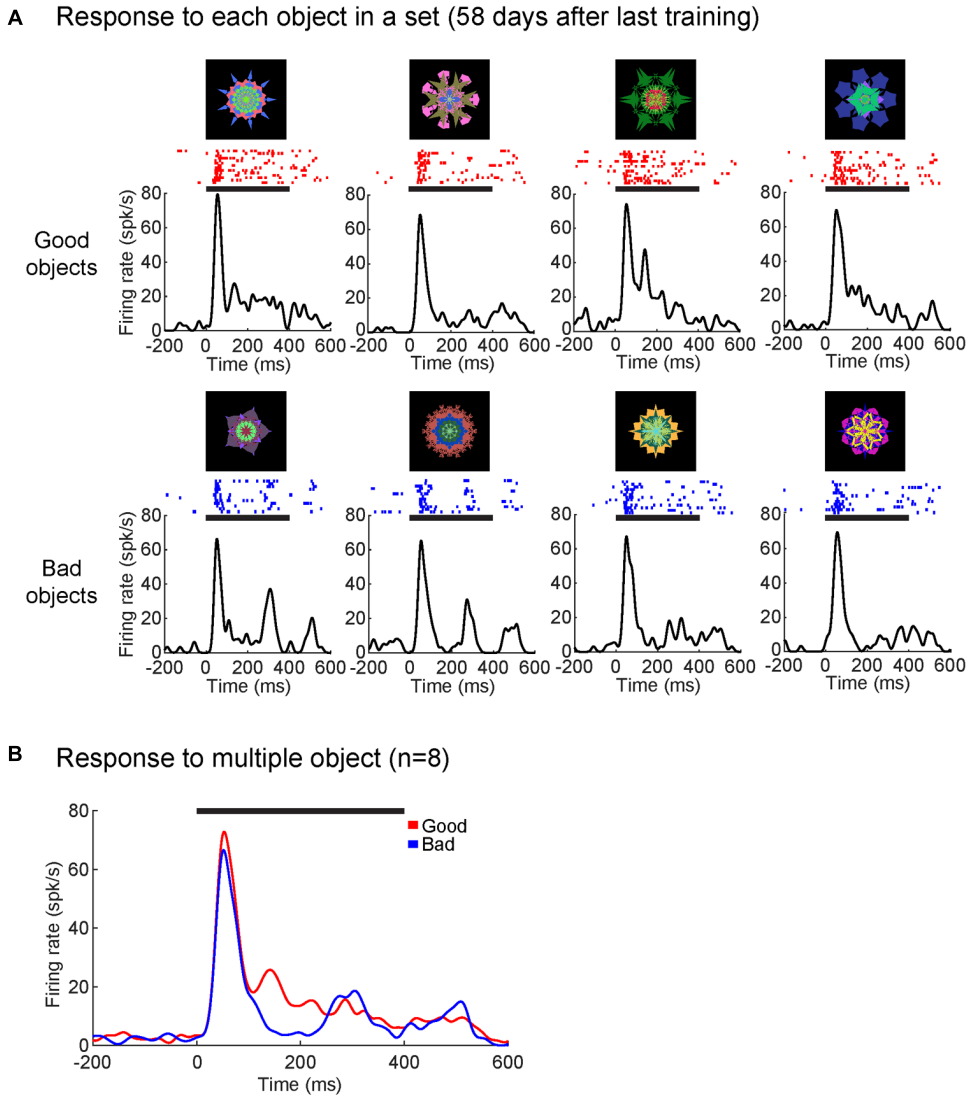

FIGURE 7 | Superior colliculus neuron retained value-coding after 2 month since the last training. **(A)** Average responses to each object from one object set (58 days since the last training) shown as SDF and raster plots aligned to object onset (in monkey D). **(B)** SC neuron showed significantly higher responses to good objects than bad ($p < 0.001$). Average response to good (red) and bad (blue) objects displayed as SDF aligned to object onset. Solid horizontal lines represent the duration of the object presentations (0–400 ms). Neuron depth: 800 um; RF (r, Θ): 20°, –20°. Value discrimination score: 0.69 ($p < 0.001$).

cdlSNr neurons: increase (due to disinhibition) by good objects; decrease (due to enhanced inhibition) by bad objects. This is exactly what we observed (**Figure 4**).

Possible Inputs From the Cortex for Stable Object Values

However, it is possible that other brain areas also contribute to the value-coding of SC neurons. A fMRI study from our lab used similar methods and found regions across the brain that responded differently to stable high-value or low-value objects even after several months without training (Ghazizadeh et al., 2018). Many of the value-coding cortical areas identified in that study have been shown to have projections to the SC, including the ventral-lateral prefrontal cortex (vlPFC; areas 12r and 46vc), ventral premotor area F5, frontal eye field (FEF), and lateral intraparietal area (LIP) (Pare and Wurtz, 2001; Lock et al., 2003; Borra et al., 2014; Distler and Hoffmann, 2015). This suggest cortical areas may complement the value-coding information coming from the basal ganglia. Interestingly though, most of these cortical areas have been found to project to intermediate and deep layers with minimal, if any, projections to the superficial layer of the SC. Although it has not been confirmed histologically, we believe that most of our recorded SC neurons were located within the ventral superficial layer of the SC based upon depth and visual response properties. Future experiments will be needed to explore the anatomical and functional contributions of these different cortical areas to the SC.

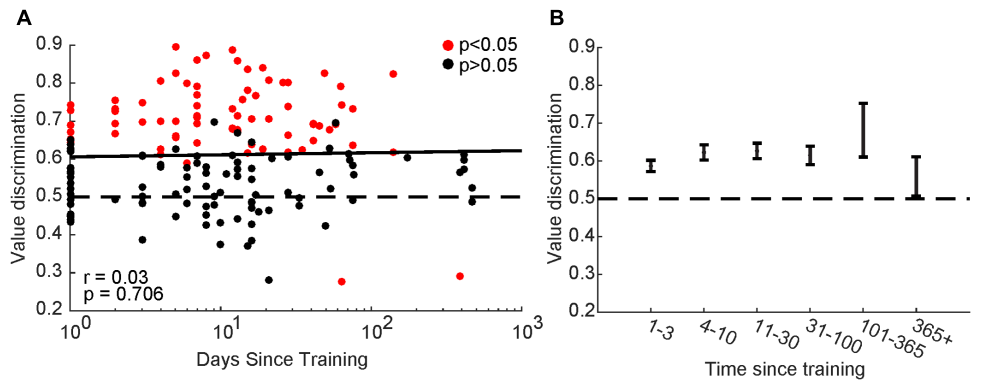

FIGURE 8 | Superior colliculus neurons retained object values even after long periods without training. **(A)** Comparison between value-coding measured by value discrimination score (ordinate) and days since the last training of object values shown by log scale (abscissa). Each dot indicates each value-coding neuron for a set of objects. Red and black dots indicate significant value-coding ($p < 0.05$) and non-significant value-coding ($p > 0.05$), respectively. For linear regression, Pearson's correlation '*r*' and significance '*p*' are shown. **(B)** Average value discrimination score for sets with different retention periods. Error bars: SEM.

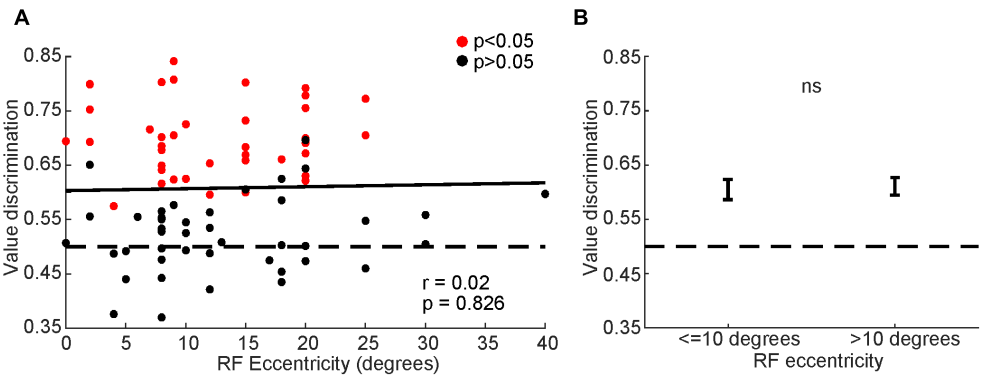

FIGURE 9 | Superior colliculus neurons encoded object values even in peripheral field. **(A)** Comparison between value-coding (ordinate) and RF eccentricities (abscissa). Red and black dots indicate significant value-coding ($p < 0.05$) and non-significant value-coding ($p > 0.05$), respectively. For linear regression, Pearson's correlation '*r*' and significance '*p*' are shown. **(B)** Average value discrimination score for neurons with near (≤10 degrees) or far (>10 degrees) eccentricity RFs. Error bars: SEM. *ns*, non-significant.

Timing of Visual and Value Responses Within SC

Notably, the value-coding of SC neurons started significantly later than the beginning of their visual responses (**Figure 5** and **Table 1**). This suggests that two kinds of visual input arrive in SC neurons differently in timing: elementary visual input (mostly <100 ms) and value-based visual input (mostly >100 ms). In fact, the value-coding of CDt-circuit (CDt, cvGPe, and cdlSNr) starts around 100 ms (Yasuda et al., 2012; Yamamoto et al., 2013), which may cause the second peak of visual response in SC neurons.

Effects of Object Values Within SC

Superior colliculus is the main and common target of SNr in various vertebrates examined (Reiner et al., 1998; Smeets et al., 2000), probably because finding good objects is crucial for animal life. Notably, axons of SNr neurons terminate mainly in the intermediate layer of SC (Graybiel, 1978; Hikosaka and Wurtz, 1983; Karabelas and Moschovakis, 1985) where most neurons control saccades by sending a burst signal to the brainstem saccade generator (Miyashita and Hikosaka, 1996; Takahashi et al., 2005). Thus, SNr neurons can control saccade initiation with this direct connection to saccadic neurons. However, some neurons in SNr, especially visual neurons, project also to the superficial layer of SC (Hikosaka and Wurtz, 1983). This needs to be examined in future.

Notably, the object-value coding was more prominent in the deeper part of the superficial layer (**Figure 10**). This might indicate that a spatial gradient of the SNr input within SC, which has not been analyzed well. In any case, this may indicate a

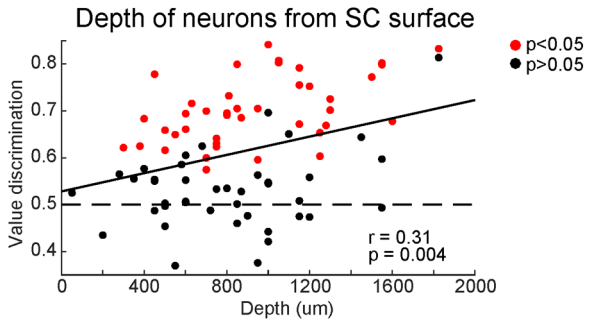

FIGURE 10 | Superior colliculus neurons showed stronger value-coding along the depth. Comparison between value-coding (ordinate) and the depth from the top of SC (abscissa). Red and black dots indicate significant value-coding ($p < 0.05$) and non-significant value-coding ($p > 0.05$), respectively. For linear regression, Pearson's correlation '*r*' and significance '*p*' are shown.

functional gradient from visual to motor (saccade) across the layers in SC. Visual neurons with value-coding in the superficial layer are physically close to the intermediate layer so that they may be able to modulate the activity of saccadic neurons.

Stable vs. Flexible Value Mechanism

So far, we have suggested that the value information in SC neurons originate from CDt-circuit and cortical circuits. However, these may not be the only sources. In fact, previous studies showed that SC also receives value-related inputs from different regions of the basal ganglia, especially the head of the caudate nucleus (CDh). CDh neurons changed their visual responses completely and quickly when the predicted reward is changed (Kawagoe et al., 1998; Kim and Hikosaka, 2013). CDh neurons project to the rostral-ventral-medial part of SNr (rvmSNr) (Yasuda and Hikosaka, 2015), which is separate from cdlSNr. Some neurons in rvmSNr also project to SC (Yasuda and Hikosaka, 2015). Accordingly, the flexible value information in CDh is mediated by rvmSNr, then to SC (Yasuda and Hikosaka, 2015). In fact, the visual response of SC neurons increases if it is immediately followed by a reward and decreases if it is followed by no reward (Ikeda and Hikosaka, 2003).

In contrast, the value information from CDt-circuit is stable. CDt, cvGPe, and cdlSNr neurons respond to visual objects differently based on the previous reward association, not predicted reward association (Hikosaka et al., 2014). Our current study showed that SC neurons encode stable values, unlike the previous study showing flexible value-coding of SC neurons (Ikeda and Hikosaka, 2003). Moreover, both stable and flexible value-coding neurons are more common in the deeper part of the superficial layer: **Figure 10** for stable value, Figure 7 in Ikeda and Hikosaka (2003) for flexible value. These results suggest that visual neurons in SC can encode both stable and flexible values by receiving inputs from both CDt-circuit and CDh-circuit.

In real life, many objects may be either good or bad for a life-long time (e.g., my favorite or hated food), but some of them may change their values (e.g., getting food poisoning after eating favorite food). In this sense, CDt-input and CDh-input are both important, but their opinions can be different if the values of some object have changed (Abraham and Robins, 2005). In that case, one of them should be chosen to make the final decision. This raises an important issue: CDt-circuit and CDh-circuit send their selective opinions to SC, but they may not be aware which opinion will be chosen. This issue may suggest another function of SC, as described below.

Role of SC Visual Neurons in Value Learning – Hypothesis

According to a traditional theory, synaptic plasticity occurs at the cortico-striatal glutamatergic synapses based on dopaminergic inputs (Reynolds and Wickens, 2002). The downstream circuits, including SC, modulate motor behavior by simply following the change in the striatum. However, there may be other mechanisms than this unidirectional sequential mechanism. Neurons in SC project to many brain areas (Harting et al., 1980; Coizet et al., 2007), in addition to its downstream area (brainstem saccade generator) (Takahashi et al., 2005). Some of the connections are directed to the basal ganglia, directly to dopamine neurons (Comoli et al., 2003) and indirectly to the striatum (including CDt and CDh) (Sadikot et al., 1992; Ichinohe and Shoumura, 1998).

If the learning and decision making are made by the downstream circuits, why is the upstream circuit necessary? As described above, CDt-circuit, CDh-circuit, and cortical circuits send their selective opinions to SC, but they may not be aware which opinion will be chosen. Instead, SC neurons are likely to represent the final decision. It would then be crucial for CDt, CDh, and cortical areas to be notified with the outcome; otherwise, they cannot proceed to the next behavior quickly. In this sense, the message from the final decision-maker (e.g., SC) would be essential, which may be relevant to 'corollary discharge' (Crapse and Sommer, 2008).

The connection from SC neurons to dopamine neurons may be important for value-based learning (Redgrave and Gurney, 2006). Dopamine neurons are activated by reward (juice or water for our monkey subjects), which is a primary reinforcer for behavior (Hollerman and Schultz, 1998). Dopamine neurons then become sensitive to an event that precedes the reward, which is called conditioned reinforcer (Kelleher and Gollub, 1962). The sensitivity of SC neurons to good objects, which are based on both stable and flexible values, would be ideal for the conditioned reinforcement.

AUTHOR CONTRIBUTIONS

WG, HA, and AG performed the neuronal recordings. WG analyzed the data with input from OH. WG and OH wrote the paper with input from HA and AG.

FUNDING

This research was supported by the Intramural Research Program at the National Eye Institute, National Institutes of Health.

ACKNOWLEDGMENTS

We thank members of the Hikosaka lab for valuable discussions and D. Parker, M. K. Smith, G. Tansey, J. W. McClurkin, A. M. Nichols, T. W. Ruffner, and A. V. Hays for technical assistance.

SUPPLEMENTARY MATERIAL

The Supplementary Material for this article can be found online at: https://www.frontiersin.org/articles/10.3389/fnins.2018.00396/full#supplementary-material

REFERENCES

Abraham, W. C., and Robins, A. (2005). Memory retention–the synaptic stability versus plasticity dilemma. *Trends Neurosci.* 28, 73–78. doi: 10.1016/j.tins.2004.12.003

Basso, M. A., and Wurtz, R. H. (1998). Modulation of neuronal activity in superior colliculus by changes in target probability. *J. Neurosci.* 18, 7519–7534. doi: 10.1523/JNEUROSCI.18-18-07519.1998

Berson, D. M. (1988). Retinal and cortical inputs to cat superior colliculus: composition, convergence and laminar specificity. *Prog. Brain Res.* 75, 17–26. doi: 10.1016/S0079-6123(08)60462-8

Borra, E., Gerbella, M., Rozzi, S., Tonelli, S., and Luppino, G. (2014). Projections to the superior colliculus from inferior parietal, ventral premotor, and ventrolateral prefrontal areas involved in controlling goal-directed hand actions in the macaque. *Cereb. Cortex* 24, 1054–1065. doi: 10.1093/cercor/bhs392

Coizet, V., Overton, P. G., and Redgrave, P. (2007). Collateralization of the tectonigral projection with other major output pathways of superior colliculus in the rat. *J. Comp. Neurol.* 500, 1034–1049. doi: 10.1002/cne.21202

Comoli, E., Coizet, V., Boyes, J., Bolam, J. P., Canteras, N. S., Quirk, R. H., et al. (2003). A direct projection from superior colliculus to substantia nigra for detecting salient visual events. *Nat. Neurosci.* 6, 974–980. doi: 10.1038/nn1113

Crapse, T. B., Lau, H., and Basso, M. A. (2018). A role for the superior colliculus in decision criteria. *Neuron* 97, 181.e6–194.e6. doi: 10.1016/j.neuron.2017.12.006

Crapse, T. B., and Sommer, M. A. (2008). Corollary discharge across the animal kingdom. *Nat. Rev. Neurosci.* 9, 587–600. doi: 10.1038/nrn2457

Cynader, M., and Berman, N. (1972). Receptive-field organization of monkey superior colliculus. *J. Neurophysiol.* 35, 187–201. doi: 10.1152/jn.1972.35.2.187

Distler, C., and Hoffmann, K. P. (2015). Direct projections from the dorsal premotor cortex to the superior colliculus in the macaque (*macaca mulatta*). *J. Comp. Neurol.* 523, 2390–2408. doi: 10.1002/cne.23794

Fecteau, J. H., and Munoz, D. P. (2006). Salience, relevance, and firing: a priority map for target selection. *Trends Cogn. Sci.* 10, 382–390. doi: 10.1016/j.tics.2006.06.011

Ghazizadeh, A., Griggs, W., and Hikosaka, O. (2016a). Ecological origins of object salience: reward, uncertainty, aversiveness, and novelty. *Front. Neurosci.* 10:378. doi: 10.3389/fnins.2016.00378

Ghazizadeh, A., Griggs, W., and Hikosaka, O. (2016b). Object-finding skill created by repeated reward experience. *J. Vis.* 16:17. doi: 10.1167/16.10.17

Ghazizadeh, A., Griggs, W., Leopold, D. A., and Hikosaka, O. (2018). Temporal-prefrontal cortical network for discrimination of valuable objects in long-term memory. *Proc. Natl. Acad. Sci. U.S.A.* 115, E2135–E2144. doi: 10.1073/pnas.1707695115

Graybiel, A. M. (1978). Organization of the nigrotectal connection: an experimental tracer study in the cat. *Brain Res.* 143, 339–348. doi: 10.1016/0006-8993(78)90573-5

Hall, N. J., and Colby, C. L. (2016). Express saccades and superior colliculus responses are sensitive to short-wavelength cone contrast. *Proc. Natl. Acad. Sci. U.S.A.* 113, 6743–6748. doi: 10.1073/pnas.1600095113

Harting, J. K., Huerta, M. F., Frankfurter, A. J., Strominger, N. L., and Royce, G. J. (1980). Ascending pathways from the monkey superior colliculus: an autoradiographic analysis. *J. Comp. Neurol.* 192, 853–882. doi: 10.1002/cne.901920414

Herman, J. P., and Krauzlis, R. J. (2017). Color-change detection activity in the primate superior colliculus. *eNeuro* 4:ENEURO.0046-17.2017. doi: 10.1523/ENEURO.0046-17.2017

Hikosaka, O., Kim, H. F., Yasuda, M., and Yamamoto, S. (2014). Basal ganglia circuits for reward value-guided behavior. *Annu. Rev. Neurosci.* 37, 289–306. doi: 10.1146/annurev-neuro-071013-013924

Hikosaka, O., and Wurtz, R. H. (1983). Visual and oculomotor functions of monkey substantia nigra pars reticulata. IV. Relation of substantia nigra to superior colliculus. *J. Neurophysiol.* 49, 1285–1301. doi: 10.1152/jn.1983.49.5.1285

Hollerman, J. R., and Schultz, W. (1998). Dopamine neurons report an error in the temporal prediction of reward during learning. *Nat. Neurosci.* 1, 304–309.

Horwitz, G. D., Batista, A. P., and Newsome, W. T. (2004). Representation of an abstract perceptual decision in macaque superior colliculus. *J. Neurophysiol.* 91, 2281–2296. doi: 10.1152/jn.00872.2003

Ichinohe, N., and Shoumura, K. (1998). A di-synaptic projection from the superior colliculus to the head of the caudate nucleus via the centromedian-parafascicular complex in the cat: an anterograde and retrograde labeling study. *Neurosci. Res.* 32, 295–303. doi: 10.1016/S0168-0102(98)00095-9

Ignashchenkova, A., Dicke, P. W., Haarmeier, T., and Thier, P. (2004). Neuron-specific contribution of the superior colliculus to overt and covert shifts of attention. *Nat. Neurosci.* 7, 56–64. doi: 10.1038/nn1169

Ikeda, T., and Hikosaka, O. (2003). Reward-dependent gain and bias of visual responses in primate superior colliculus. *Neuron* 39, 693–700. doi: 10.1016/S0896-6273(03)00464-1

Isa, T., Endo, T., and Saito, Y. (1998). The visuo-motor pathway in the local circuit of the rat superior colliculus. *J. Neurosci.* 18, 8496–8504. doi: 10.1523/JNEUROSCI.18-20-08496.1998

Karabelas, A. B., and Moschovakis, A. K. (1985). Nigral inhibitory termination on efferent neurons of the superior colliculus: an intracellular horseradish peroxidase study in the cat. *J. Comp. Neurol.* 239, 309–329. doi: 10.1002/cne.902390305

Kawagoe, R., Takikawa, Y., and Hikosaka, O. (1998). Expectation of reward modulates cognitive signals in the basal ganglia. *Nat. Neurosci.* 1, 411–416. doi: 10.1038/1625

Kelleher, R. T., and Gollub, L. R. (1962). A review of positive conditioned reinforcement. *J. Exp. Anal. Behav.* 5, 543–597. doi: 10.1901/jeab.1962.5-s543

Kim, H. F., Amita, H., and Hikosaka, O. (2017). Indirect pathway of caudal basal ganglia for rejection of valueless visual objects. *Neuron* 94, 920.e3–930.e3. doi: 10.1016/j.neuron.2017.04.033

Kim, H. F., and Hikosaka, O. (2013). Distinct basal ganglia circuits controlling behaviors guided by flexible and stable values. *Neuron* 79, 1001–1010. doi: 10.1016/j.neuron.2013.06.044

Krauzlis, R. J., Lovejoy, L. P., and Zenon, A. (2013). Superior colliculus and visual spatial attention. *Annu. Rev. Neurosci.* 36, 165–182. doi: 10.1146/annurev-neuro-062012-170249

Lock, T. M., Baizer, J. S., and Bender, D. B. (2003). Distribution of corticotectal cells in macaque. *Exp. Brain Res.* 151, 455–470. doi: 10.1007/s00221-003-1500-y

May, P. J. (2006). The mammalian superior colliculus: laminar structure and connections. *Prog. Brain Res.* 151, 321–378. doi: 10.1016/S0079-6123(05)51011-2

Miyashita, N., and Hikosaka, O. (1996). Minimal synaptic delay in the saccadic output pathway of the superior colliculus studied in awake monkey. *Exp. Brain Res.* 112, 187–196. doi: 10.1007/BF00227637

Miyashita, Y., Higuchi, S., Sakai, K., and Masui, N. (1991). Generation of fractal patterns for probing the visual memory. *Neurosci. Res.* 12, 307–311. doi: 10.1016/0168-0102(91)90121-E

Moors, J., and Vendrik, A. J. H. (1979). Responses of single units in the monkey superior colliculus to moving stimuli. *Exp. Brain Res.* 35, 349–369.

Ozen, G., Augustine, G. J., and Hall, W. C. (2000). Contribution of superficial layer neurons to premotor bursts in the superior colliculus. *J. Neurophysiol.* 84, 460–471. doi: 10.1152/jn.2000.84.1.460

Pare, M., and Wurtz, R. H. (2001). Progression in neuronal processing for saccadic eye movements from parietal cortex area lip to superior colliculus. *J. Neurophysiol.* 85, 2545–2562. doi: 10.1152/jn.2001.85.6.2545

Redgrave, P., and Gurney, K. (2006). The short-latency dopamine signal: a role in discovering novel actions? *Nat. Rev. Neurosci.* 7, 967–975. doi: 10.1038/nrn2022

Reiner, A., Medina, L., and Veenman, C. L. (1998). Structural and functional evolution of the basal ganglia in vertebrates. *Brain Res. Brain Res. Rev.* 28, 235–285. doi: 10.1016/S0165-0173(98)00016-2

Reynolds, J. N., and Wickens, J. R. (2002). Dopamine-dependent plasticity of corticostriatal synapses. *Neural Netw.* 15, 507–521. doi: 10.1016/S0893-6080(02)00045-X

Sadikot, A. F., Parent, A., and François, C. (1992). Efferent connections of the centromedian and parafascicular thalamic nuclei in the squirrel monkey: A PHA-L study of subcortical projections. *J. Comp. Neurol.* 315, 137–159. doi: 10.1002/cne.903150203

Saint-Cyr, J. A., Ungerleider, L. G., and Desimone, R. (1990). Organization of visual cortical inputs to the striatum and subsequent outputs to the pallido-nigral complex in the monkey. *J. Comp. Neurol.* 298, 129–156. doi: 10.1002/cne.902980202

Smeets, W. J., Marin, O., and Gonzalez, A. (2000). Evolution of the basal ganglia: new perspectives through a comparative approach. *J. Anat.* 196(Pt 4), 501–517. doi: 10.1046/j.1469-7580.2000.19640501.x

Strasburger, H., Rentschler, I., and Juttner, M. (2011). Peripheral vision and pattern recognition: a review. *J. Vis.* 11:13. doi: 10.1167/11.5.13

Takahashi, M., Sugiuchi, Y., Izawa, Y., and Shinoda, Y. (2005). Synaptic inputs and their pathways from fixation and saccade zones of the superior colliculus to inhibitory burst neurons and pause neurons. *Ann. N. Y. Acad. Sci.* 1039, 209–219. doi: 10.1196/annals.1325.020

Wolf, A. B., Lintz, M. J., Costabile, J. D., Thompson, J. A., Stubblefield, E. A., and Felsen, G. (2015). An integrative role for the superior colliculus in selecting targets for movements. *J. Neurophysiol.* 114, 2118–2131. doi: 10.1152/jn.00262.2015

Wurtz, R. H., and Albano, J. E. (1980). Visual-motor function of the primate superior colliculus. *Annu. Rev. Neurosci.* 3, 189–226. doi: 10.1146/annurev.ne.03.030180.001201

Yamamoto, S., Kim, H. F., and Hikosaka, O. (2013). Reward value-contingent changes of visual responses in the primate caudate tail associated with a visuomotor skill. *J. Neurosci.* 33, 11227–11238. doi: 10.1523/JNEUROSCI.0318-13.2013

Yamamoto, S., Monosov, I. E., Yasuda, M., and Hikosaka, O. (2012). What and where information in the caudate tail guides saccades to visual objects. *J. Neurosci.* 32, 11005–11016. doi: 10.1523/JNEUROSCI.0828-12.2012

Yasuda, M., and Hikosaka, O. (2015). Functional territories in primate substantia nigra pars reticulata separately signaling stable and flexible values. *J. Neurophysiol.* 113, 1681–1696. doi: 10.1152/jn.00674.2014

Yasuda, M., Yamamoto, S., and Hikosaka, O. (2012). Robust representation of stable object values in the oculomotor Basal Ganglia. *J. Neurosci.* 32, 16917–16932. doi: 10.1523/JNEUROSCI.3438-12.2012

Conflict of Interest Statement: The authors declare that the research was conducted in the absence of any commercial or financial relationships that could be construed as a potential conflict of interest.

frontiers in Neural Circuits

ORIGINAL RESEARCH
published: 04 May 2018
doi: 10.3389/fncir.2018.00035

Parvalbumin and GABA Microcircuits in the Mouse Superior Colliculus

Claudio A. Villalobos[1], Qiong Wu[1], Psyche H. Lee[1], Paul J. May[2] and Michele A. Basso[1]**

[1] Fuster Laboratory of Cognitive Neuroscience, Department of Psychiatry and Biobehavioral Sciences – Department of Neurobiology, Semel Institute for Neuroscience and Human Behavior – Brain Research Institute, David Geffen School of Medicine, University of California, Los Angeles, Los Angeles, CA, United States, [2] Department of Neurobiology and Anatomical Sciences, University of Mississippi Medical Center, Jackson, MS, United States

The mammalian superior colliculus (SC) is a sensorimotor midbrain structure responsible for orienting behaviors. Although many SC features are known, details of its intrinsic microcircuits are lacking. We used transgenic mice expressing reporter genes in parvalbumin-positive (PV^+) and gamma aminobutyric acid-positive ($GABA^+$) neurons to test the hypothesis that PV^+ neurons co-localize GABA and form inhibitory circuits within the SC. We found more PV^+ neurons in the superficial compared to the intermediate SC, although a larger percentage of PV^+ neurons co-expressed GABA in the latter. Unlike PV^+ neurons, $PV^+/GABA^+$ neurons showed predominantly rapidly inactivating spiking patterns. Optogenetic activation of PV^+ neurons revealed direct and feedforward GABAergic inhibitory synaptic responses, as well as excitatory glutamatergic synapses. We propose that PV^+ neurons in the SC may be specialized for a variety of circuit functions within the SC rather than forming a homogeneous, GABAergic neuronal subtype as they appear to in other regions of the brain.

Keywords: superior colliculus (SC), parvalbumin, mouse, optogenetics, GABAergic neurons, orienting movements, attention

OPEN ACCESS

Edited by:
Tadashi Isa,
Kyoto University, Japan

Reviewed by:
Andreas Antonios Kardamakis,
Karolinska Institute, Sweden
Yasuhiko Saito,
Nara Medical University, Japan

****Correspondence:***
Claudio A. Villalobos
cavillalobos@mednet.ucla.edu
Michele A. Basso
mbasso@mednet.ucla.edu

Received: *02 February 2018*
Accepted: *16 April 2018*
Published: *04 May 2018*

Citation:
Villalobos CA, Wu Q, Lee PH, May PJ and Basso MA (2018) Parvalbumin and GABA Microcircuits in the Mouse Superior Colliculus. Front. Neural Circuits 12:35. doi: 10.3389/fncir.2018.00035

INTRODUCTION

The mammalian superior colliculus (SC) is a midbrain structure specializing in translating sensory information into commands for orienting movements and redirecting attention (reviewed in, Basso and May, 2017). With the development of new molecular tools and transgenic mouse lines, we are now well-poised to unravel the neuronal microcircuits within the SC underlying these complex behaviors. Here, we took advantage of transgenic mice expressing a reporter gene in neurons containing the Ca^{2+}-binding protein, parvalbumin (PV) and mice expressing the light-activated ion channel channelrhodopsin-2 (ChR2) in molecularly identified parvalbumin-positive (PV^+) neurons to determine the features and influence of PV^+ neuronal activation on SC microcircuits.

In all areas of the cerebral cortex studied thus far, as well as in hippocampus and striatum, PV appears almost exclusively in a subpopulation of GABAergic neurons (Gonchar et al., 2008; Klausberger and Somogyi, 2008; Tremblay et al., 2016). In cortex, these GABAergic neurons exhibit fast-spiking patterns and form direct inhibitory synapses with the somata, proximal dendrites, and initial segments of cortical pyramidal neurons (Kawaguchi et al., 1987; Kawaguchi, 1993; Kawaguchi and Kubota, 1993, 1997; Gupta, 2000; Markram et al., 2004; Taniguchi et al., 2011; Taniguchi, 2014; Tremblay et al., 2016). These GABAergic PV^+ neurons thus play a key role in intrinsic inhibitory microcircuits in cortical and subcortical regions (Cardin et al., 2009;

Sohal et al., 2009; Chen et al., 2017). Impairments of inhibitory processes related to the function of PV^+ neurons are associated with disorders ranging from autism to schizophrenia, highlighting the importance of PV^+ neurons in mechanisms underlying higher cognitive functions (Lewis et al., 2012; Wöhr et al., 2015; Chung et al., 2016; Hashemi et al., 2017; Kim et al., 2017). We sought to determine whether PV^+ neurons play a similar role in SC circuits.

The mammalian SC is a layered structure. The superficial layers (sSC) participate in visual functions and the intermediate layers (iSC) contribute to the control of orienting behaviors; thus, we often refer to these as visuosensory and motor layers, respectively. The sSC contains neurons expressing a variety of Ca^{2+}-binding proteins, including PV (Behan et al., 1992; Mize et al., 1992; Leuba and Saini, 1996; Lee et al., 2006). Specific calcium binding properties may characterize individual streams for SC visual information processing. For example, $calbindin^+$ neurons in sSC receive inputs from K-type ganglion cells, whereas PV^+ neurons receive input from M-type ganglion cells, as well as from cortical neurons with M-like properties (Mize et al., 1991; Casagrande, 1994; Mize, 1999). These two types of neuron inhabit different strata within the sSC, with PV^+ neurons lying in the lower superficial layer (SGS) and stratum opticum (SO) (Illing et al., 1990). These PV^+ neurons in turn, project to the lateral posterior nucleus of the thalamus, indicating that at least some PV^+ neurons in the SC are projection neurons, as opposed to interneurons (Casagrande, 1994; Mize, 1996). A recent report using transgenic mouse models provides further support for the idea that PV^+ neurons in the sSC form extrinsic excitatory circuits (Shang et al., 2015). These authors discovered that sSC PV^+ neurons form excitatory connections with the parabigeminal nucleus, which in turn projects to the amygdala. Activation of this pathway produces fear responses, including escape and freezing behaviors. Together, the work in sSC suggests that collicular PV^+ neurons play a different role than that proposed for PV^+ local circuit neurons in the cerebral cortex.

We designed a series of experiments to test the hypotheses that PV^+ neurons in the SC can form intralaminar inhibitory circuits, in addition to their known role in extrinsic excitatory circuits. Inhibitory microcircuits modulate the flow of retinal information from the sSC to the iSC (Hall and Lee, 1997; Lee et al., 1997; Isa et al., 1998) and are thought to play a key role in circuit interactions leading to eye movement choices (reviewed in, Basso and May, 2017). Therefore, understanding how inhibitory neuronal microcircuits act within the SC will provide valuable insight into understanding how the brain controls behavior. To this end, we performed immunohistochemical experiments comparing PV and GABA expression throughout the rostral-caudal extent of the SC. In brain slices from transgenic mice expressing a reporter gene (tdTomato) in PV^+ neurons, we characterized the morphology, as well as the biophysical and electrophysiological properties of SC PV^+ neurons. We crossed the Ai9;PV-Cre mouse line with the GAD67-EGFP knock-in mouse to create a new mouse expressing both tdTomato and EGFP reporters exclusively in $PV^+/GABA^+$ neurons and assessed the distribution and electrophysiological properties of these neurons throughout the SC. Finally, we crossed the PV-IRES-Cre mouse line with the Ai32 mouse line to express ChR2 in PV^+ neurons. Using optogenetic stimulation, we tested the functional connectivity of the synapses formed by PV^+ neurons within the SC. Our results demonstrate that $PV^+/GABA^+$ neurons exist in the SC, form functional inhibitory circuits within the SC, and show physiological properties that differ from those in cerebral cortex, hippocampus and striatum. We conclude that PV^+ neurons in the SC likely play different roles in collicular function than they do in cortex.

MATERIALS AND METHODS

All experimental protocols involving animals were approved by the UCLA Chancellor's Animal Research Committee and complied with standards set by the Public Health Service policy on the humane care and use of laboratory animals, as well as all state and local guidelines. To identify parvalbumin containing neurons (PV^+) in the SC, we used Ai9;PV-Cre transgenic mice generated from crossing of PV-IRES-Cre knock-in females (Jackson Laboratories, stock no. 008069) and male Ai9-tdTomato reporter knock-in mice (Jackson Laboratories, stock no. 007905). All experimental mice were heterozygous for the transgenes on a C57BL/6 background. To identify PV^+ and $GABA^+$ neurons in the SC, we used an Ai9;PV-Cre;GAD67 transgenic mice generated by crossing Ai9;PV-Cre females and GAD67-GFP males (Jackson Laboratories, stock no. 007677). These experimental mice were homozygous for tdTomato, heterozygous for PV-Cre and hemizigous for GAD67-GFP on a C57BL/6 background. Optogenetic experiments were carried out using Ai32;PV-Cre mice generated from PV-IRES-Cre knock-in female mice crossed with Ai32 males [Ai32(RCL-ChR2(H134R)/EYFP); Jackson Laboratories, stock no. 012569].

Immunohistochemistry

Ai9;PV-Cre mice brain sections were used to determine the co-expression of PV and GABA in neurons of the SC. Mice were deeply anesthetized with isoflurane/O_2 (1 L/min) and perfused transcardially with 4% paraformaldehyde in 0.12 M phosphate buffer (PB), pH 7.3. The brains were removed and post-fixed for 2 h in 4% paraformaldehyde PB. After rinsing, the brains were cryoprotected in a 30% sucrose phosphate buffer saline (PBS) overnight at room temperature, embedded in Tissue-Tek® optical cutting temperature compound (Sakura Finetek), frozen on dry ice, and cryo-sectioned coronally (30 μm thickness). Sections were then labeled with antibodies for GABA (Sigma A2052). Briefly, sections were rinsed in 0.1M Tris-buffered saline (TBS) and then incubated in TBS containing 5% donkey serum and 1% Triton X-100 for 2 h to block non-specific staining and enhance penetration. The tissue was rinsed three times with TBS between all subsequent steps in the immunohistochemical procedures. Sections were incubated in primary antibody, rabbit anti-GABA (1:1000), overnight at room temperature. Next, the tissue was incubated overnight at room temperature in a secondary antibody, donkey anti-rabbit IgG conjugated with

Alexa Fluor 488 (1:500) (Jackson ImmunoResearch), to which Neurotrace® (1:500) (Thermo Fisher Scientific) was added as a counterstain. After thorough rinsing, sections were mounted on slides and cover-slipped with Prolong Diamond Antifade mounting medium (P36970). All sections were scanned with a LSM 800 (Carl Zeiss) confocal microscope, and confocal images were analyzed with Zen 2.3 lite imaging software (Carl Zeiss).

Neuronal Quantification

Processed tissue was scanned for neurons in the superficial and intermediate layers of the SC (sSC and iSC, respectively), as well as for neurons in primary visual cortex (Cx). Z-stack images (18–25 sections, ∼0.6 μm thickness) were acquired from the sSC and iSC at locations across the mediolateral extent of the layers containing abundant PV^+ neurons. Images were taken while alternating between three channels (excitation spectra 488, 561, and 640 nm for PV^+, $GABA^+$, and Neurotrace labels, respectively) throughout the Z-stack. Images from three to six regions from either rostral, middle or caudal SC were obtained from four mice (255 μm × 255 μm) and single- and double-labeled neurons, positive for either tdTomato and/or the immunohistochemical label for GABA, were identified and quantified within the selected regions. Verification of immuno-positive neurons was done by sliding through the optical z-sections, and all PV^+ cells were determined to be neurons by counterstaining with Neurotrace® (**Supplementary Figure S1**). Specifically, under the tdTomato filter and corresponding excitation spectra, PV^+ neurons were individually identified in each of the z-stack images of a section. Then, under the AF488 filter and excitation, each of the previously selected neurons was checked for GABA labeling. In this manner, PV^+ or $PV^+/GABA^+$ neurons were quantified in each of the sections. Quantification of double-labeled neurons from sections through cortex processed at the same time were used as a control.

Acute Brain Slice Preparation

Coronal brain slices of 250–300 μm in thickness that included the SC were prepared as follows: mice (P30-45) were anesthetized with isoflurane, decapitated and their brains were quickly removed and cooled (4°C) in high sucrose artificial cerebrospinal fluid (sucrose ACSF) containing (in mM): 240 sucrose, 7 D-glucose, 7 $MgCl_2$, 1.25 NaH_2PO_4, 2.5 KCl, 25 $NaHCO_3$, 0.5 $CaCl_2$, that was bubbled to saturation with 95% O_2 – 5% CO_2. The isolated brain was then affixed to the specimen plate using cyanoacrylate glue, and cut using a vibratome (Leica VT 1200S). Coronal slices were subsequently transferred to a recovery chamber containing standard ACSF (in mM: 126 NaCl, 2.5 KCl, 26 NaHCO3, 1.25 NaH2PO4, 2 $CaCl_2$, 2 $MgCl_2$, and 10 glucose) at 35°C for at least an hour before recording.

Electrophysiological Recordings

Brain slices were transferred to a submerged recording chamber on the stage of an upright Zeiss (Axio Examiner D1) or a Nikon (Eclipse E600) microscope. Slices were superfused (2–3 ml/min) with standard ACSF and maintained at ∼30°C using an in-line heater controller (TC-324C, Warner Instruments). Individual PV^+ or $PV^+/GABA^+$ neurons from the sSC or iSC were identified under DIC or fluorescence with a Hamamatsu Cooled CCD camera (C11440-42U). Recordings were obtained using 3–4 MΩ electrodes filled with intracellular solution (in mM: 150 K-Gluconate, 15 KCl, 1.5 $MgCl_2$, 10 HEPES, 0.1 EGTA, 2 Na-ATP, and 0.5 Na-GTP; 290 mOsm; pH 7.3). In some cases, recorded neurons were labeled by injecting either Lucifer Yellow or biocytin added to the intracellular solution. Signals were amplified using a Multiclamp 700B amplifier (Molecular Devices, San Jose, CA, United States), digitized and stored on a PC. Series resistance and whole-cell capacitance were automatically compensated. Total resistance values ($R_t = R_a + R_m$) where R_t is total resistance, R_a is access resistance and R_m is membrane resistance, for each recording was obtained immediately after breaking into the neuron from the Membrane Test Window of the *Clampfit 10* software. The R_t values are calculated based on a series of known voltage pulses applied to the neuron and measuring the corresponding current values obtained right after breaking the gigaseal. All electrophysiological data were analyzed using the *Clampfit 10* software. All chemicals were purchased from Sigma-Aldrich. Optogenetic experiments were carried out using brain slices obtained from the Ai32;PV-Cre mice. We visualized PV^- neurons with infrared differential interference contrast (IR-DIC) microscopy. We excited PV^+ neurons by illuminating the SC through the objective with a 470 nm LED light (Mightex). To prevent firing of action potentials, QX-314 (2.5 mM) was added to the intracellular solution. Traces recorded from collicular PV^- neurons depicting postsynaptic currents are shown as the averaged responses of three consecutive light pulses. All recorded neurons were deemed healthy by assessing V_m magnitude and stability, and maximum spike voltage (e.g., < -50 mV and > 0 mV, respectively).

Morphology

To identify and categorize the morphology of PV^+ or $PV^+/GABA^+$ neurons in the SC, individual neurons were patched and recorded using pipettes filled with either Lucifer Yellow CH dipotassium (1 mg/ml, Sigma) or biocytin 0.5% added to the intracellular solution. Recordings were made from acute slices obtained from either Ai9;PV-Cre or Ai9;PV-Cre;GAD67 mice to assess the morphology of PV^+ and $PV^+/GABA^+$ neurons, respectively. After 10–30 min, the slices were fixed with 4% paraformaldehyde for 24 h and then stored in a 0.1M PBS/0.06% NaN_3 solution. After three rinses with PBS, the slices were incubated with streptavidin conjugated with Alexa Fluor 647 (1:500) (Thermo Fisher Scientific S32357) overnight at room temperature. After thorough rinsing, slices were mounted on slides and cover-slipped with Fluoro-Gel in TES buffer mounting medium (Electron Microscopy Sciences). Images of the recorded neurons were obtained using a LSM 800 (Carl Zeiss) confocal microscope.

Classification of neuronal morphology is a daunting task due to the fact that different authorities have used different

terminologies and focused on different characteristics. In addition, different methodologies including Golgi staining (Langer and Lund, 1974; Norita, 1980; Ma et al., 1990), *in vivo* intracellular staining and serial reconstruction (Mooney et al., 1985; Moschovakis and Karabelas, 1985; Moschovakis et al., 1988a,b), and *in vitro* intracellular staining (Hall and Lee, 1997; Edwards et al., 2002; Lee et al., 2007) provide different types of information, and these studies have been performed in a variety of species, e.g., mouse, hamster, cat, and monkey. For this study, we adopted a simplified classification system similar to that of Edwards et al. (2002). In the sSC, we used the term narrow field vertical for any neurons whose dendritic fields were taller than were wide and <100 μm across. This included classical narrow field vertical neurons, which displayed long apical dendrites and short basal dendrites, as well as neurons which had primary dendrites extending at a variety of points from their somata, but which nevertheless had a columnar dendritic field shape. This category also included up-side-down examples where the soma was near the surface and most of the dendritic field extended ventrally. We used the term horizontal, for neurons in which the dendritic field was clearly non-symmetrical, with the long axis oriented parallel to the collicular surface. These neurons had either fusiform or spherical somata, and they sometimes had primary dendrites that initially extended in the dorsoventral direction, but which then turned parallel to the surface. We used the term wide field vertical, for neurons whose dendritic fields, unlike those of the horizontal neurons, extended toward the collicular surface. This type of neuron was discriminated from narrow field vertical type by the fact that the dendritic field was greater than 150 μm across. (It should be noted that due to the fact these were stained in slices, we could not see the entire extent of their dendritic field.) In theory, this class includes pyriform neurons (Langer and Lund, 1974), having funnel-shaped dendritic fields and no basal dendrites, that have been described previously (Mooney et al., 1985; Luksch et al., 1998; Lee et al., 2001; May, 2006). In the present case, only non-pyriform neurons that displayed both dorsally and ventrally extending dendrites were observed. The final sSC category that we observed were stellate neurons. Stellate neurons were characterized by primary dendrites that extended in all directions from the soma and which formed a roughly symmetric dendritic field with no obvious orientation. Using this neuronal classification scheme, we observed four different neuronal types within the sSC, as did a previous study using a cell-type clustering analysis of filled neurons (Gale and Murphy, 2014). The iSC contains a number of different multipolar cell types (Norita, 1980; Ma et al., 1990). In the present experiment, we divided the stained neuronal population into just two classes: horizontal and radial-stellate. The iSC horizontal neuronal population had essentially the same features as those seen in the sSC. The iSC radial-stellate neurons had roughly spherical dendritic fields like sSC stellates. However, iSC radial-stellate dendritic fields were much larger and the dendrites branched far less than sSC stellate neurons. Neurons of this type have been variously termed small multipolar, stellate and radial by others (Langer and Lund, 1974; Norita, 1980; Laemle, 1981).

RESULTS

Parvalbumin-Positive (PV^+) Neurons Co-localize GABA in the SC

The stratum zonale, the stratum griseum superficiale (SGS) and the SO comprise the superficial, visuosensory layers of the SC (sSC), and below these layers is the stratum griseum intermediale, which we refer to as the intermediate or motor layers (iSC). **Figure 1A** shows the SC viewed with differential interference contrast (DIC) microscopy, as it appears in the recording chamber. The borders of the layers are demarcated with dashed white lines. **Figure 1B** shows the distribution of PV-positive (PV^+) neurons in the SC from the Ai9;PV-Cre mouse. Most of the red (tdTomato) PV^+ neurons and neuropil in the sSC lie in a band located in the lower portion of the SGS. Scattered neurons are present dorsal to this lamina and ventrally, in SO. PV expression also appears throughout the iSC, and it includes both neurons and neuropil (**Figure 1B**). Unlike the sSC laminar pattern, the iSC pattern is patchy, with the densest labeling in the lateral-most aspect. The appearance of the PV labeling in the Ai9;PV-Cre mouse (**Figure 1B**, white arrows), is similar to

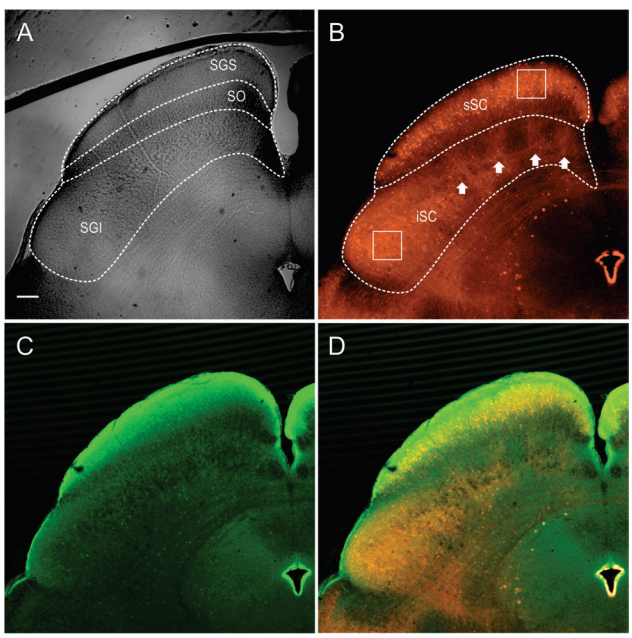

FIGURE 1 | Distribution of PV and GABA in the Ai9;PV-Cre mouse SC. **(A)** Differential interference contrast (DIC) image from an Ai9;PV-Cre mouse showing the left side of a 300 μm slice through the SC and the layers (SGS; stratum griseum superficiale; SO, stratum opticum; sSC, superficial/visuosensory layers; iSC, intermediate/motor layer; SGI, stratum griseum intermediale). **(B)** Confocal image of the same section showing the distribution of PV^+ neurons and neuropil in both layers of the SC as visualized by tdTomato fluorescence. Squares on sections within the layers are shown in expanded view in **Figure 2A**. White arrows highlight the patchy distribution of PV^+ labeling in iSC. **(C)** Confocal image depicting the distribution of $GABA^+$ neurons and neuropil in the same section detected by GFP immunofluorescence using anti-GABA antibody. **(D)** Merged PV^+ and $GABA^+$ confocal images **(B,C)**. Scale bar: 200 μm.

that observed in rats using immunohistochemistry (Illing et al., 1990).

To investigate whether PV^+ neurons in the SC also express gamma-aminobutyric acid (GABA) as they do in cerebral cortex (Celio, 1986), we used an antibody to GABA on sections from four Ai9;PV-Cre mice. **Figure 1C** shows the distribution of GABA labeling from the same section shown in **Figure 1B**. GABA antibody densely labels the SC, primarily in the upper superficial layer with comparatively less label observed in SO and in iSC. The lower SGS lamina seen with PV staining is not evident. A merged view of the PV^+ and $GABA^+$ images (**Figure 1D**) shows that double-labeled neurons are sparsely distributed in the two layers.

The appearance of double label in the section shown in **Figure 1D** was consistent across our sample of four mice. We obtained 40× magnification confocal images of similar sections throughout the sSC and the iSC, and performed counts of the yellow neurons containing both tdTomato and GABA. **Figure 2A** shows example images taken from regions of the sSC (A_1) and iSC (A_2) marked by the white squares in **Figure 1B**, and a similarly sized region of visual cortex (A_3; Cx). In both layers, we observed singly labeled $GABA^+$ and PV^+ neurons (**Figure 2A**, arrows and arrowheads, respectively) and double labeled $PV^+/GABA^+$ neurons (**Figure 2A**, circles). In visual cortex, the majority of PV^+ neurons expressed GABA (**Figure 2A$_3$**). The Venn diagrams in **Figure 2A** show schematically what is quantified in **Figure 2B** based on sample counts from 13 to 20 brain sections from four mice. The number of neurons co-localizing PV and GABA with respect to the total PV^+ neuronal population (36 ± 3% sSC, 81 ± 4% iSC, and 90 ± 2% Cx; $^*p < 0.05$, paired *t*-test), demonstrates clear differences in the proportions of PV^+ neurons expressing GABA (**Figure 2B**). These differences remain when sorting the slices into rostral, middle and caudal collicular regions (**Figure 2C**). Like the cortex, iSC had a high proportion of $PV^+/GABA^+$ neurons, although the overall number of PV^+ neurons in the iSC was significantly less than found in sSC and Cx (**Figure 2D**; $^*p < 0.05$, Mann–Whitney).

Physiological and Morphological Features of PV^+ Neurons in the SC

Transgenic mouse lines allow for targeted recordings of specific visually identified neurons. In cerebral cortex, PV^+ neurons are

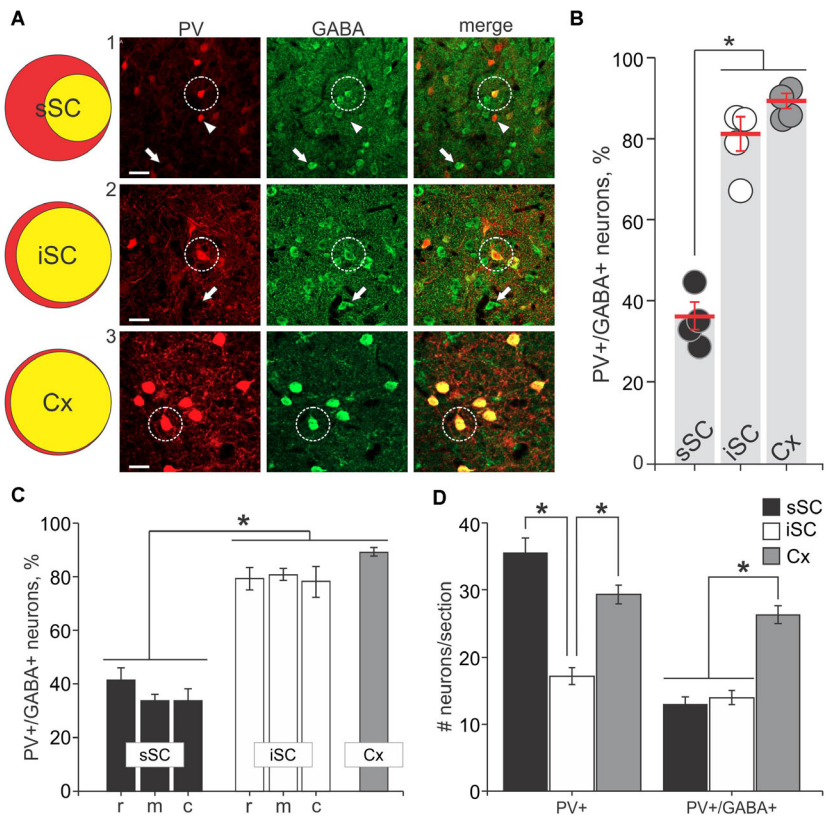

FIGURE 2 | PV^+ neurons contain $GABA^+$ in the SC. **(A)** Far left, Venn diagrams representing the proportion of $PV^+/GABA^+$ neurons (yellow) of the total number of PV^+ neurons (red) from sections of sSC, iSC and V1 of cerebral cortex (Cx). Right panels, confocal images of sections from sSC, iSC, and Cx (row **A$_{1-3}$**, respectively) showing PV^+ (left column), $GABA^+$ (middle), and the merged images (right). White arrowheads indicate examples of PV^+ neurons. White arrows show examples of $GABA^+$ neurons and white circles highlight $PV^+/GABA^+$ neurons. Scale bar: 20 μm. **(B)** Percentage of $PV^+/GABA^+$ neurons of the total number PV^+ neurons counted in sSC, iSC, and Cx for each of the mice ($n = 4$). Red line, mean ± SE. **(C)** Mean percentage of double-labeled $PV^+/GABA^+$ neurons in sections from sSC (black), iSC (white) obtained from rostral (r), middle (m) or caudal (c) SC brain slices and from Cx (gray). $^*p < 0.05$, Kruskal–Wallis. Bar: mean ± SE. **(D)** Mean ± SE number of PV^+ and double labeled $PV^+/GABA^+$ neurons per section (4–8 sections/mouse) from sSC, iSC, and Cx. $^*p < 0.05$, Mann–Whitney.

known to be GABA$^+$ and fast-spiking, with high-frequency trains of action potentials that display little adaptation (Kawaguchi et al., 1987; Cauli et al., 1997; Kawaguchi and Kubota, 1997; Xu and Callaway, 2009; Taniguchi, 2014). We asked whether PV$^+$ neurons in the colliculus show similar characteristics by recording visually identified PV$^+$ neurons in whole-cell configuration from slices obtained from Ai9;PV-Cre mice (**Figure 3A**). **Figure 3B** shows representative traces obtained from PV$^+$ neurons in response to +100 pA (black) and −100 pA (gray) current injections. **Table 1** reports electrophysiological measurements from our sample of neurons. We found that PV$^+$ neurons in the SC showed a variety of firing profiles, including fast-spiking (**Figure 3B$_1$**), regular spiking (**Figure 3B$_2$**) rapidly inactivating (**Figure 3B$_3$**), burst spiking (**Figure 3B$_4$**), and non-spiking (**Figure 3B$_5$**) patterns. Thus, in contrast to cerebral cortex, where most PV$^+$ neurons are fast-spiking, SC PV$^+$ neurons exhibit heterogeneous electrophysiological properties.

To obtain an unbiased classification of SC PV$^+$ neurons, we analyzed the firing pattern of each recorded neuron in response to a series of injected current amplitudes to create a series of current versus spike frequency (I/F) plots. The slope of these functions and the R^2 values allowed us to assign most neurons into one of three major classes: fast-spiking, regular spiking or rapidly inactivating. **Figure 3C** depicts the mean and SE of the spike rate measured for each current step for each of the three classes of neuron. We defined fast-spiking neurons as having $a > 150$ spikes/sec rate in response to positive current steps with little spike frequency adaptation. Fast-spiking neurons (gray circles, $n = 74$) showed the steepest rate of I/F (slope = 0.33; $R^2 = 0.94$). We defined regular spiking neurons as those displaying continuous spiking

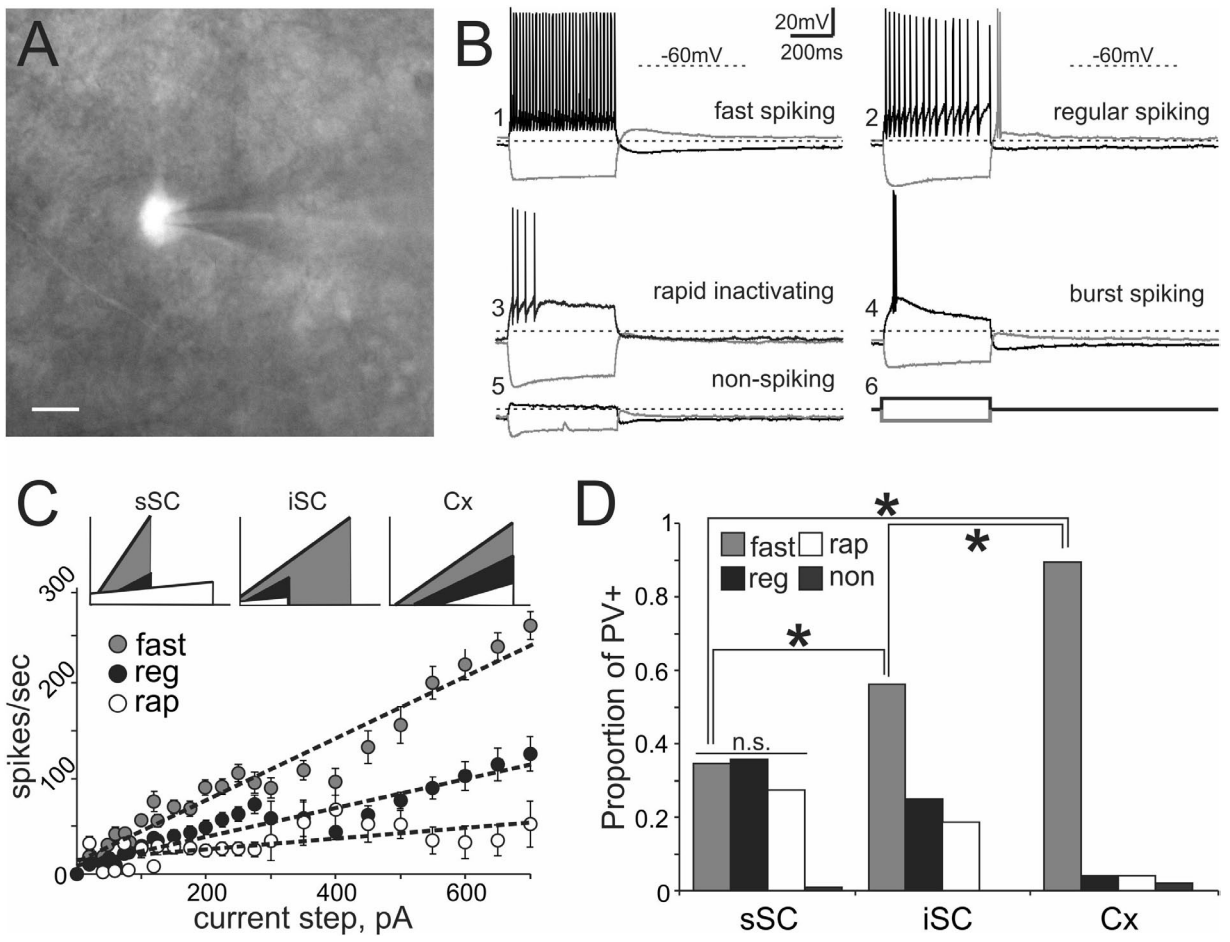

FIGURE 3 | PV$^+$ neurons in the SC show a variety of electrophysiological properties. **(A)** Visually identified and recorded PV$^+$ neuron from a brain slice of an Ai9;PV-Cre mouse. Scale bar: 10 μm. **(B)** Representative traces from whole-cell patch-clamp recordings obtained from PV$^+$ neurons in the SC. **(B$_1$)** Shows fast spiking, **(B$_2$)** regular spiking, **(B$_3$)** rapidly inactivating, **(B$_4$)** burst spiking and **(B$_5$)** non-spiking. Gray and black traces represent voltages resulting from injection of negative and positive step currents (–100 pA/+100 pA, **B$_6$**), respectively. Dotted line, –60 mV applies to all five traces. Scale bar: 20 mV/200 ms. **(C)** Mean values of step current vs. spikes/sec (I/F) curves calculated from all recorded PV$^+$ neurons showing the most common spiking classes; fast (gray circles), regular (black circles) and rapidly inactivating (open circles). Dotted lines represent the linear regression computed for each of the classes. The I/F plots at the top provide a comparison of the linear regressions calculated for fast (gray), regular (black), and rapidly inactivating neurons (white) recorded from sSC (left), iSC (middle), and Cx (right). **(D)** Proportion of fast, regular, rapidly inactivating and non-spiking PV$^+$ neurons recorded in sSC, iSC, and Cx. *$p < 0.05$, z-test.

TABLE 1 | Electrophysiological parameters from PV^+ neurons in the SC.

		V_m	R_t	C_m	sAHP	I_h
sSC	Reg	60.64 ± 1.12	293.79 ± 41.24	53.62 ± 8.17	−1.30 ± 1.54	4.46 ± 0.74∗
	Rap	60.76 ± 2.13	415.56 ± 56.8	37.81 ± 3.83	0.22 ± 0.66	3.43 ± 1.04∗
	Fast	58.39 ± 1.36	338.17 ± 59.09	37.84 ± 5.9	1.86 ± 1.53	7.08 ± 1.33∗
iSC	Reg	61.27 ± 2.11	412.88 ± 39.21	44.34 ± 6.69	2.50 ± 1.28	5.22 ± 1.88∗
	Rap	55.98 ± 3.17	432.94 ± 136.52	54.86 ± 9	−1.57 ± 0.79	0.97 ± 0.93∗
	Fast	57.76 ± 1.84	410.33 ± 56.1	45.46 ± 6.43	2.76 ± 0.91	3.68 ± 0.87∗
Cx	Reg	73.98 ± 0.22	109.25 ± 1.45∗	57.12 ± 4.85	1.50 ± 0	0.9 ± 0.7
	Rap	65.1 ± 7.95	121.85 ± 41.95∗	84.82 ± 0	0.30 ± 0.10	1.25 ± 1.05
	Fast	69.21 ± 0.71	135.01 ± 9.26∗	60.42 ± 4.04	1.21 ± 0.58	0.74 ± 0.17

*Mean values for resting potential (V_m), total resistance (R_t), membrane capacitance (C_m), slow afterhyperpolarization (sAHP), and hyperpolarization-activated current (I_h) found in PV+ neurons in SC and Cx. *Represent whether I_h-dependent depolarization after the current step triggered spikes in the recordings.*

in response to positive current, with marked spike frequency adaptation. Regular spiking neurons (black circles, n = 28) showed increasing spike attenuation, reflected as a lower slope (slope = 0.15; R^2 = 0.90). Rapidly inactivating neurons fired only a few action potentials in response to positive current injection. These neurons (open circles, n = 27) showed the lowest slope and reached a spiking plateau at currents >125 pA (slope = 0.056; R^2 = 0.47). The differences between the slopes were statistically significant ($^*p < 0.05$, Mann–Whitney) and support the classification of most PV^+ neurons into these three classes (**Table 2**). This classification was also consistent for PV^+ neurons across different regions: sSC, iSC, and Cx (upper plots, **Figure 3C** and **Table 3**). Finally, the three main neuron types were equally represented within the sSC (**Figure 3D**; not statistically different (n.s.); p = 0.23; p = 0.88; p = 0.29, z-test). However, the fast firing type was the most common in iSC, as seen in Cx ($^*p < 0.05$, z-test). This distribution of the various neuronal types occurred throughout the medio-lateral extent of the SC (**Supplementary Figure S2**).

To investigate the morphology of PV^+ neurons in the colliculus, we filled recorded SC PV^+ neurons with either biocytin or lucifer yellow (n = 38) and classified them according to their dendritic morphology (see Materials and Methods). **Figures 4A–D** shows examples of neuronal cell types observed: stellate (**Figure 4A**), narrow field vertical (**Figure 4B**) and horizontal (**Figure 4C**) in the sSC, and radial-stellate neurons (**Figure 4D**) in iSC. Panel E summarizes the results of the morphological analysis of PV^+ neurons in the SC with respect to their electrophysiological profiles. In the sSC, PV^+ neurons showed a variety of morphologies, stellate, narrow field vertical, and horizontal (**Figures 4A–C,E**; black bars). Wide field vertical neurons were rarely encountered. In the iSC, the predominant morphology of PV^+ neurons was radial-stellate, although a few horizontal neurons were encountered (**Figures 4D,E**, white bars). These results indicate that PV^+ neurons in the sSC show a variety of morphologies and electrophysiological profiles, whereas PV^+ neurons in the iSC are less heterogeneous. Most were fast-spiking, radial-stellate neurons (cf., **Figure 4E** black and white bars).

TABLE 2 | I/F parameters.

	Linear regression			Mean values	
	Slope	Intercept	R^2	Slope	R^2
Fast	0.33	11.8	0.94	0.69*	0.94
Reg	0.15	11.13	0.9	0.34*	0.96
Rap	0.056	14.91	0.47	0.08*	0.58*

*Left columns, slope, intercept and R^2 derived from the linear regression computed from the mean I/F data for each neuronal type according to their firing patterns. Right columns, mean I/F parameters obtained from the individual slope and R^2 values from I/F curves for each neuron. *$p < 0.05$.*

Ai9;PV-Cre;GAD67 Mouse

To determine the relationship between GABA content and the physiological features of PV^+ neurons, we crossed the Ai9;PV-Cre mouse with the GAD67-EGFP knock in mouse to create a new mouse containing both tdTomato and EGFP in $PV^+/GABA^+$ neurons. The GAD67-GFP knock in mouse labels the PV^+ subset of GABA neurons in cerebral cortex (Chattopadhyaya, 2004). Consistent with this, the cerebral cortex of this mouse line contained only yellow neurons, indicating $PV^+/GABA^+$ co-labeling (**Supplementary Figure S3B$_3$**).

TABLE 3 | I/F parameters.

		Linear regression			Mean values	
		Slope	Intercept	R^2	Slope	R^2
sSC	Fast	0.59	0.15	0.99	0.65*	0.93
	Reg	0.19	3.92	0.90	0.32*	0.92
	Rap	0.036	24.5	0.26	0.13*	0.67*
iSC	Fast	0.36	21.7	0.97	0.65*	0.97
	Reg	0.27	0.72	0.98	0.36*	0.97
	Rap	0.049	7.15	0.20	0.08*	0.62*
Cx	Fast	0.34	−11.14	0.91	0.71*	0.93
	Reg	0.25	−32.75	0.90	0.44*	0.95
	Rap	0.15	−46.41	0.70	0.11*	0.74*

*Left columns, slope, intercept and R^2 derived from the linear regression computed from the mean I/F data for each neuronal type according to their firing patterns and location. Right columns mean I/F parameters obtained from the individual slope and R^2 values from I/F curves for each recorded neuron. *$p < 0.05$.*

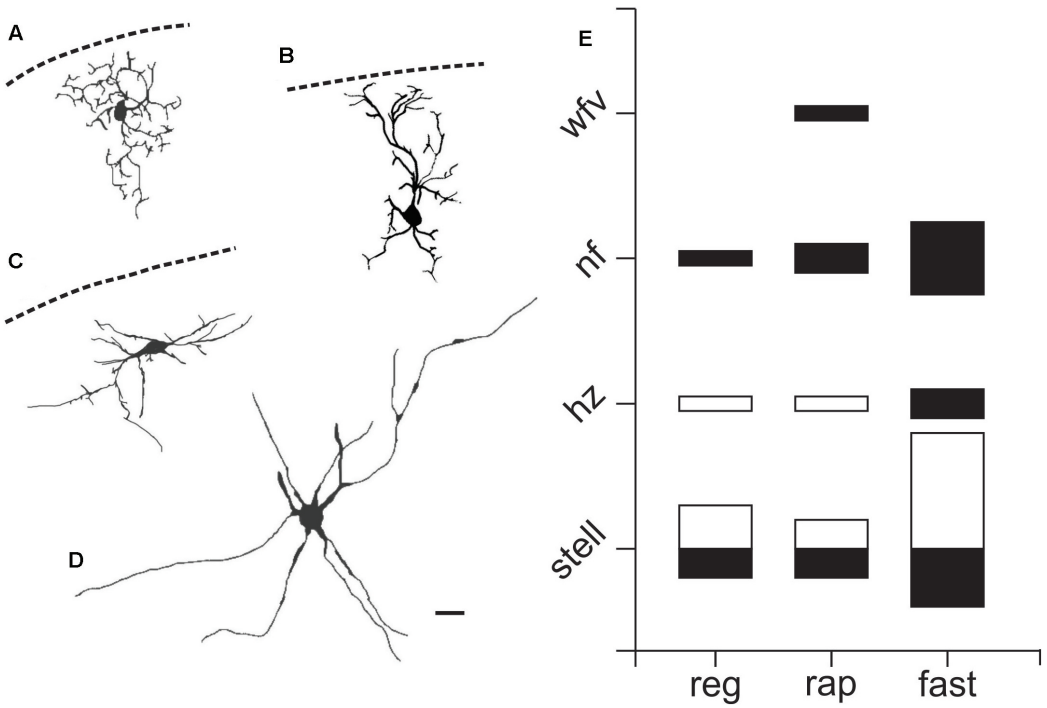

FIGURE 4 | PV$^+$ neurons in the SC show a variety of morphological properties. Drawings from visually identified PV$^+$ neurons filled with Lucifer yellow or biocytin in the SC from slices obtained from Ai9;PV-Cre mice. **(A)** sSC stellate. **(B)** sSC narrow field vertical. **(C)** sSC horizontal. **(D)** iSC radial stellate. Scale bar: 20 μm. **(E)** Quantification of PV$^+$ neurons according to their morphology and electrophysiological features for both sSC (black) and iSC (white). The size of the squares indicates number of PV$^+$ neurons on each of the categories.

Figure 5A shows a low magnification confocal image of a slice obtained from an Ai9;PV-Cre;GAD67 mouse showing the distributions of PV$^+$ and GABA$^+$ neurons in the SC. The distribution of PV$^+$ (red, **Figure 5A$_1$**), GABA$^+$ (green, **Figure 5A$_2$**), as well as PV$^+$/GABA$^+$ neurons (yellow, **Figure 5A$_3$**), were similar to those observed in the Ai9;PV-Cre mouse treated with antibody against GABA (cf., **Figures 1D**, **5A**). The proportion of double-labeled PV$^+$/GABA$^+$ neurons in the Ai9;PV-Cre;GAD67 was similar to that found in the Ai9;PV-Cre mouse double-labeled with GABA antibody (sSC = 43 ± 4%; iSC = 73 ± 7%; Cx = 98 ± 1%; cf., **Supplementary Figure S3A** and **Figure 2B**; $p = 0.71$, $p = 0.82$, $p = 0.26$, respectively; *t*-test). **Figures 5A$_{1-3}$** display high magnification confocal images from the region highlighted by the white square in **Figure 5A** and show the presence of PV$^+$ (arrowhead), GABA$^+$ (arrows) and PV$^+$/GABA$^+$ neurons (circles) in the sSC. We obtained whole-cell recordings from 30, visually identified PV$^+$/GABA$^+$ neurons from both collicular layers, many of which we filled with biocytin. Surprisingly, most PV$^+$/GABA$^+$ neurons tended to display rapidly inactivating spiking patterns, as illustrated in the recording trace from a sSC neuron (**Figure 5B**; yellow star, inset), and they were found throughout the mediolateral and dorsoventral extent of both SC layers (**Figure 5B**, inset, circles). Quantitative analysis revealed that 88% of the PV$^+$/GABA$^+$ neurons in sSC and 64% in the iSC showed rapidly inactivating firing (**Figure 5B** inset, white circles; **Figure 5C**, white bars, rap). The other 12% in the sSC showed non-spiking profiles in response to positive currents steps (500 ms, −100 to +700 pA; **Figure 5B** inset, black circles, **Figure 5C**, black bars, non). In the iSC, 14% were non-spiking and 21% fast-spiking (**Figure 5B** inset, gray circles and **Figure 5C**, gray bars, fast). The physiological differences between PV$^+$ and PV$^+$/GABA$^+$ neurons did not result from a systematic bias in recording locations between mouse lines, since the distributions of recorded neurons were found throughout the SC (**Supplementary Figure S3** and **Figure 5B**, inset). It seems likely that PV$^+$/GABA$^+$ neurons are smaller on average than PV$^+$ neurons, and so these rapidly inactivating neurons were sampled less frequently (**Figure 3D**). Consistent with this idea, we found that the mean total resistance of PV$^+$ and PV$^+$/GABA$^+$ neurons as measured from the membrane test window of the *Clampfit 10* software, were statistically different (286.1 ± 19 MΩ; 527 ± 54 MΩ, respectively; $p < 0.05$ paired *t*-test). Our visual inspection of the neurons during recordings as well as in confocal imaging, corroborated the hypothesis that PV$^+$/GABA$^+$ neurons were on average smaller than PV$^+$ neurons overall. Based on these results, we conclude that most PV$^+$/GABA$^+$ neurons exhibit a unique physiological phenotype in both the sSC and iSC; namely, a rapidly inactivating firing pattern. As we found with PV$^+$ neurons, PV$^+$/GABA$^+$ neurons showed a variety of different morphologies. **Figures 5D$_{1-4}$** show examples of filled PV$^+$/GABA$^+$ neurons and **Figure 5D$_5$** indicates the locations of these neurons within the SC. PV$^+$/GABA$^+$

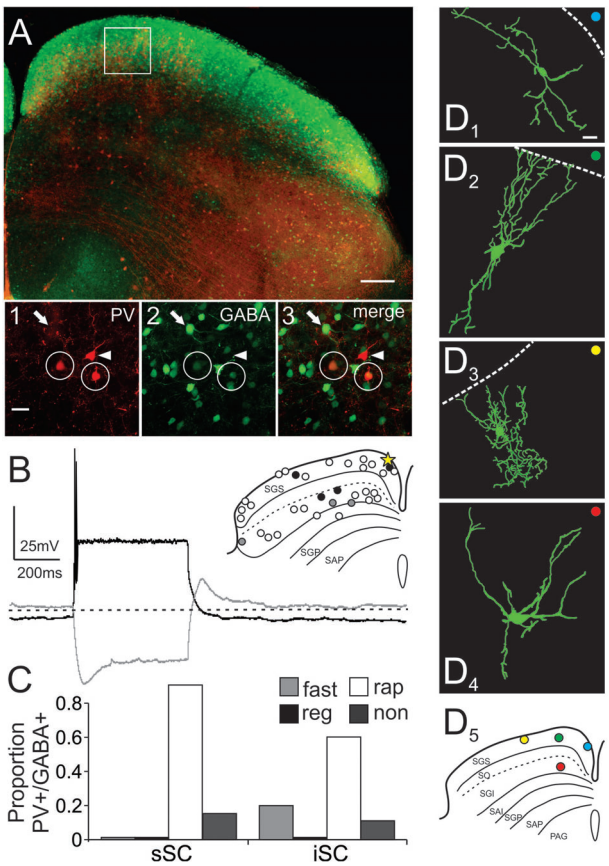

FIGURE 5 | PV$^+$/GABA$^+$ neurons in the SC are predominantly stellate and rapidly inactivating neurons. **(A)** Low magnification confocal image of a slice from an Ai9;PV-Cre;GAD67 mouse depicting PV$^+$ (tdTomato) and GABA$^+$ neurons (eGFP) in the SC. Scale bar: 200 μm. White box shows the area selected for further visual analysis. **(A_{1-3})** High magnification confocal images showing PV$^+$ (white arrowhead), GABA$^+$ (white arrow), and double-labeled PV$^+$/GABA$^+$ (white circle) neurons imaged from the location shown in the white box in **(A)**. Scale bar: 20 μm. **(B)** Representative traces of a single PV$^+$/GABA$^+$ neuron recorded from sSC (inset, yellow star). The white (rap; rapidly inactivating), black (non; non-spiking), and gray (fast; fast spiking) circles in the inset depict the location and corresponding firing pattern for each of the recorded neurons. **(C)** Proportion of PV$^+$/GABA$^+$ neurons according to their firing patterns from sSC and iSC. **(D)** Drawings of PV$^+$/GABA$^+$ neurons; **(D_1)** horizontal, **(D_2)** narrow field vertical, **(D_3)** stellate in sSC, and **(D_4)** stellate in iSC. Scale bar: 20 μm. **(D_5)** Shows the locations of the neurons shown in **(D_{1-4})**. Note that all these neurons are portrayed in the inset in **(B)** and were rapidly inactivating (white circles).

neurons displayed horizontal (**Figure 5D$_1$**), narrow field vertical (**Figure 5D$_2$**), and stellate morphologies (**Figure 5D$_3$**) in sSC, and radial-stellate morphology in iSC (**Figure 5D$_4$**). The variety of PV$^+$/GABA$^+$ neuronal morphologies observed is similar to that observed in PV$^+$ neurons, even though most neurons showed the rapidly inactivating physiological profile. Thus, PV$^+$/GABA$^+$ neurons in the SC constitute a particular neuronal subclass with heterogeneous morphology and rapidly inactivating spiking features, a considerably different profile than PV$^+$ neurons in cerebral cortex, hippocampus and striatum.

PV$^+$/GABA$^+$ Neurons in SC Make Functional GABAergic Synapses

We next asked whether PV$^+$ neurons made functional GABAergic synapses with PV$^-$ neurons in the SC. To do this, we crossed Ai32 and PV-IRES-Cre mice to express ChR2-EYFP specifically in PV$^+$ neurons. We obtained brain slices from this crossed mice (Ai32;PV-Cre) and recorded from collicular PV$^-$ neurons (**Figure 6A**, white), while stimulating PV$^+$ neurons (**Figure 6A**, red). Pulses of blue light (2 ms, 470 nM) produced sufficient membrane depolarization to evoke action potentials in PV$^+$ neurons, indicating effective activation of ChR2 (**Supplementary Figure S4A**). This stimulation generated reliable post-synaptic currents (PSCs) in sSC PV$^-$ neurons. We were unable to record PSCs from iSC PV$^-$ neurons, in spite of effective PV$^+$ neuronal stimulation (**Supplementary Figure S5**). The lack of postsynaptic responses in the iSC with PV$^+$ ChR2 activation may be due to the scarcity of iSC PV$^+$ neurons, thus rendering little and/or weak postsynaptic activity within this layer. An alternative, not mutually exclusive explanation is that few or no iSC PV$^+$ neurons project within the layer, and that they instead project mostly to regions outside the SC. Or less likely, that we failed to record from neurons receiving PV$^+$ input. Note however, that the lack of inhibitory responses in iSC with PV$^+$ stimulation, suggests that local inhibition within the iSC (Helms et al., 2004; Lee and Hall, 2006; Lee et al., 2007) is mediated by circuits other than those involving PV$^+$ neurons, such as somatostatin interneurons. Since we did not drive iSC neurons postsynaptically, all of the postsynaptic activation data come from recordings in the sSC.

Figure 6B$_1$ shows that 2 ms light stimulation (blue squares) evoked a biphasic response in a PV$^-$ neuron when the holding voltage (V_h) was −20 mV; an outward current followed by a large inward current (**Figure 6B$_1$**, black trace). Similar stimulation resulted in a large inward current when V_h was −80 mV (**Figure 6B$_1$**, gray trace). We plotted the I/V curve obtained by measuring the peaks of postsynaptic currents evoked in PV$^-$ neurons held at different V_h (−100 to +40 mV) in response to light activation of PV$^+$ neurons (**Figure 6B$_1$**, inset). To investigate the neurotransmitters involved in these currents, we applied the glutamate receptor antagonists D-(-)-2-amino-5-phosphonopentanoic acid (APV) and 6-cyano-7-nitroquinoxaline-2,3-dione (CNQX). Bath application of these antagonists resulted in loss of the light-activated inward currents seen at both −80 mV and −20 mV, demonstrating the glutamatergic nature of the inward currents and isolating a PV$^+$ driven outward current at −20 mV (**Figure 6B$_2$**, top). After washout (**Supplementary Figure S4B**), subsequent application of the $GABA_A$ receptor antagonist bicuculline eliminated the outward current (**Figure 6B$_3$**), confirming its GABAergic origin.

Quantification of the EPSCs and IPSCs evoked by PV$^+$ stimulation across our sample of 45 neurons revealed inward currents seen with V_h at −80 mV. About 95% of the recorded PV$^-$ neurons showed inward currents with a mean amplitude of −355 ± 67 pA (**Figure 6C**, black circles and red bar), whereas only 10% of the neurons showed outward currents at −80 mV with a mean amplitude of 5.41 ± 0.66 pA (**Figure 6C**, white

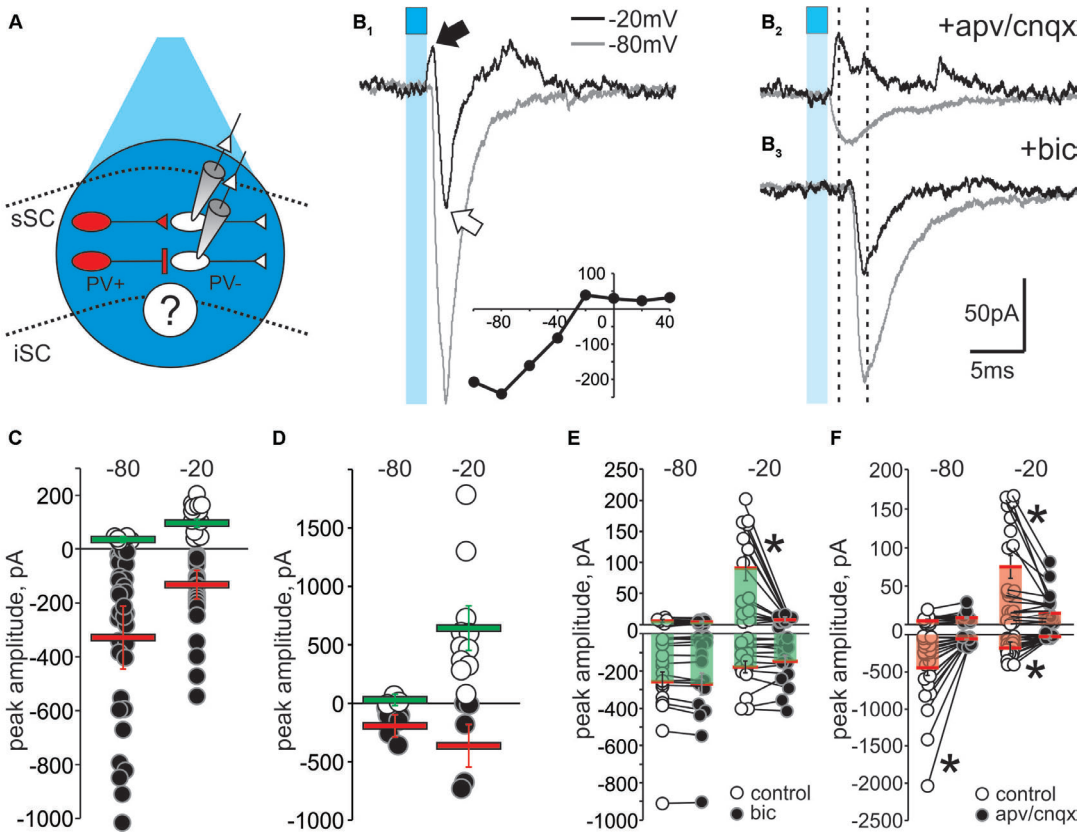

FIGURE 6 | Optogenetic activation of PV$^+$ neurons reveals functional GABAergic synapses in the SC. **(A)** Schematic diagram depicting the experimental design. Whole-cell recordings from PV$^-$ neurons (white) were obtained from visually identified neurons using IR-DIC in slices from Ai32;PV-Cre mice. To stimulate PV$^+$ neurons (red), pulses of blue light from a LED source were triggered through the objective (cyan circle, ~5–10 mW). **(B_1)** 2 ms pulses of LED stimulation (cyan square) elicited inward currents when the holding voltage (V_h) of PV$^-$ neurons was set at –80 mV (gray traces). With V_h set at –20 mV (black traces), light stimulation evoked a biphasic response, with an outward current (black arrow) preceding an inward current (white arrow). Inset, I/V curve. **(B_2)** Bath application of APV/CNQX (50 μM/10 μM) diminished the light-evoked EPSC at V_h –80 mV and –20 mV and isolated the light-evoked outward current at –20 mV (black). **(B_3)** After washout, bath application of bicuculline (10 μM) eliminated the IPSC at V_h –20 mV (black), thus isolating the EPSCs. **(C,D)** Peak amplitude plotted for all recorded IPSCs (white circles) and EPSCs (black circles) evoked in PV$^-$ neurons by optogenetic activation of PV+ neurons in sSC **(C)** and in Cx **(D)**. Red bars: EPSC mean ± SE; green bars: IPSC mean ± SE. **(E)** Peak amplitudes of light-evoked current measured in PV$^-$ neurons of sSC before (*o*) and after (•) bath application of bicuculline, which exclusively inhibited the light-induced outward currents recorded in PV$^-$ neurons at –20 mV. *$p < 0.05$, paired *t*-test. **(F)** Peak amplitude currents before (*o*) and after (•) bath application of APV/CNQX.

circles and green bar). With V_h set to −20 mV, closer to the reversal potential for Na^{2+}, light pulses were more likely to evoke IPSCs. In fact, 73% of the PV$^-$ neurons showed IPSCs with a mean amplitude of 64 ± 11 pA (**Figure 6C**, white circles and green bar). For comparison, and to confirm the efficacy of the ChR2 expression in PV$^+$ neurons, we also performed similar recordings in cortex. As expected, light activation predominantly resulted in large amplitude IPSCs (mean = 639 ± 152 pA) at V_h −20 mV (**Figure 6D**).

To directly test whether activation of ChR2 in PV$^+$ neurons triggers GABAergic or glutamatergic synapses, we bath applied bicuculline or APV/CNQX and measured the amplitude of the evoked PSCs before and after bath application. **Figure 6E** shows that bicuculline failed to reduce the EPSC amplitude recorded at either −80 mV (control: −258 ± 53 pA; bic: −269 ± 56 pA; $p = 0.18$) or −20 mV (control: −178 ± 31 pA; bic: −150 ± 33 pA; $p = 0.33$), but significantly reduced the IPSCs observed at −20 mV (control: 90.49 ± 19.84 pA; bic: 2.96 ± 1.29 pA; *$p < 0.05$), demonstrating the GABAergic nature of these synapses. Most IPSCs recorded at −80 mV were small and not affected by bicuculline (control: 3.92 ± 0.39 pA; bic; 3.55 ± 0.50 pA, $p = 0.58$). On the other hand, bath application of APV/CNQX significantly reduced the EPSCs at both −80 mV (control: −447 ± 100 pA; apv/cnqx: −43 ± 9 pA; *$p < 0.05$) and −20 mV (control: −173 ± 29 pA; apv: −21 ± 2 pA; *$p < 0.05$; **Figure 6F**), supporting the idea that these inward currents are mediated by glutamatergic receptors. We also found that some of the outward currents recorded at −20 mV were significantly inhibited by APV/CNQX, suggesting that glutamatergic PV$^+$ synapses in the SC are also driving some of the IPSCs (control: 74 ± 15; apv: 14 ± 4, $p < 0.05$). Taken together, these results provide evidence for the existence of both PV$^+$ GABAergic and PV$^+$ glutamatergic synaptic transmission capable of driving inhibitory circuits within the SC.

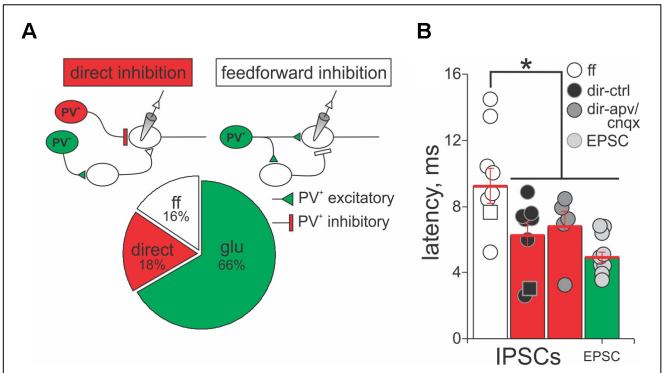

FIGURE 7 | PV^+ neurons form direct and feedforward inhibitory circuits in the SC. **(A)** Top panel, schematic diagrams of the PV^+ driven inhibitory circuits, direct and feedforward, found in our recordings. PV^+, red circles; PV^-, white circles. Triangles depict excitatory terminals and bars depict inhibitory terminals. Lower panel, percentage of recordings providing evidence for direct inhibition (18%), feedforward inhibition (16%), and excitatory (66%) circuits resulting from optogenetic activation of PV^+ neurons. **(B)** Latency of the peak outward currents classified as feedforward (ff, white circles), direct inhibition before (dir-ctrl, black circles), and after APV/CNQX application (dir-apv/cnqx, gray circles). The latency of the peak inward currents in neurons showing feedforward inhibition is also shown (EPSC, light gray circles). Red bar: mean ± SE.

PV^+ Neurons Form Direct Inhibitory and Feedforward Inhibitory Circuits in SC

The results shown in **Figure 6** suggest that PV^+ neurons in the SC form excitatory and inhibitory synaptic connections with PV^- neurons, consistent with our anatomical results showing that some, but not all PV^+ neurons in the SC co-localize GABA. Therefore, we quantified the nature and kinetics of light-evoked PSCs in the presence of APV/CNQX or bicuculline for our sample of 45 PV^- neurons recorded from the Ai32;PV-Cre mouse. The upper panels in **Figure 7A** show schematic drawings of hypothetical synaptic circuits that could explain the outward currents obtained in response to optogenetic stimulation of PV^+ neurons, as shown in **Figure 6B** and **Supplementary Figure S4C**. The IPSCs were classified as feedforward inhibition if bath application of APV/CNQX abolished the light-evoked outward current or as direct inhibition if APV/CNQX failed to abolish the outward current. Again, to corroborate their GABAergic nature, after washout, bath application of bicuculline eliminated the outward currents in all neurons displaying feedforward and direct inhibitory currents. The pie chart in **Figure 7A** shows that 34% of our recordings showed PV^+ neurons driving inhibitory circuits; of these 18% corresponded to APV/CNQX-insensitive outward currents, inhibited by bicuculline, and thus resulted from PV^+ driven direct inhibitory synapses. The rest, 16% corresponded to APV/CNQX sensitive outward currents, consistent with feedforward inhibitory circuity. From our recordings, 66% showed APV/CNQX-sensitive inward currents, consistent with direct excitation via glutamatergic synapses.

A signature feature of feedforward inhibitory circuits is that IPSCs are recorded later compared to directly activated inward currents. Therefore, we measured the latency of isolated currents as the times from the beginning of the light pulse to the peak of the evoked PSC, to assess whether they were well explained by direct or feedforward circuits. **Figure 7B** shows the mean latency of the peak amplitude of IPSCs and EPSCs recorded from PV^- neurons in response to light activation of PV^+ neurons, when sorted by whether the currents were classified as direct or feedforward inhibition, according to their APV/CNQX-sensitivity. For the neurons showing feedforward inhibitory profile, the mean latency of the peak outward current was 9.25 ms ± 1.07 ms with a minimum of 5.24 ms and a maximum of 14.49 ms (white circles and bar). The mean value was significantly longer than the mean latency calculated for the currents classified as direct inhibition (6.24 ms ± 0.80 ms with a minimum of 2.59 ms and a maximum of 14.49 ms, black circles and bars; Mann–Whitney $p = 0.032$), as well as for the EPSCs (4.08 ms ± 0.32 ms with a minimum of 3.00 ms and a maximum of 5.88 ms; light gray circles and bars; Mann–Whitney $p = 0.002$). This longer latency outward current is therefore consistent with a feedforward mechanism. In addition, the mean latency of direct inhibitory and excitatory currents (6.24 ms versus 4.08 ms) did not differ significantly (**Figure 7B**, cf., black and light gray circles and bars, Mann–Whitney $p = 0.83$). To ensure that the inward currents did not confound the measurements of the outward currents, we measured the latency of direct outward currents before and after application of APV/CNQX and found that these values showed no statistical differences (cf., black and gray circles and bars, Mann–Whitney $p = 0.84$). These results demonstrate that PV^+ neurons can form excitatory, as well as two types of inhibitory, circuits with PV^- neurons, with direct and feedforward inhibition, occurring in equal proportions.

DISCUSSION

We took advantage of a mouse line genetically engineered to express the reporter gene (tdTomato) in PV^+ neurons to determine their distribution and electrophysiological properties within the SC. Consistent with previous reports, we found strong PV expression concentrated in a discrete sublamina of the visuosensory layer (sSC) and weaker PV^+ expression, with a patch-like appearance, in the motor layer (iSC) (Illing et al., 1990; Mize et al., 1992; Cork et al., 1998; Jeong et al., 2014; Lee et al., 2014). While PV marks a very specific subclass of GABAergic fast-spiking inhibitory interneurons in the cerebral cortex, striatum and hippocampus (Hu et al., 2014), our results showed that PV^+ neurons in the sSC present heterogeneous spiking profiles and morphologies, and only a fraction contain GABA. On the other hand, a higher proportion of the relatively sparse PV^+ population in the iSC showed the presence of GABA. Furthermore, most of these neurons showed a fast-spiking profile and radial-stellate morphology. Crossing of the GAD67-EGFP mouse with the Ai9;PV-Cre mouse to identify $PV^+/GABA^+$ neurons in the SC confirmed our immunohistological results showing that in the iSC, a larger proportion of PV^+ neurons express GABA, compared to the sSC. Surprisingly, the majority of $PV^+/GABA^+$ neurons, in both SC layers, showed rapidly

inactivating spiking patterns, an entirely different profile from that seen in cortex, striatum or hippocampus. Finally, activation of PV^+ neurons expressing ChR2 revealed three main types of connections with PV^- neurons in the SC, direct excitatory, direct inhibitory and feedforward inhibitory synaptic connections. Taken together, our immunohistological, electrophysiological and optogenetic results indicate that the PV^+ subclass of neuron plays multiple roles in SC circuits, and these roles are most likely different from those played by PV^+ neurons in cortical, striatal or hippocampal areas (Gray et al., 2014; Chen et al., 2017).

Comparison to Previous Findings in the SC Superficial Layers (sSC)

The pattern of PV staining observed in the transgenic Ai9;PV-Cre mouse sSC (**Figures 1**, **2**) was similar to that observed previously using immunohistochemistry (Illing et al., 1990; Mize et al., 1992; Cork et al., 1998; González-Soriano et al., 2000; Behan et al., 2002; Kang et al., 2002), with a predominant band of labeled neurons in the lower SGS, and others scattered across the sSC. Interestingly, this band pattern is not obvious in the monkey sSC, where the distribution appears homogeneous (Soares et al., 2001).

An outstanding feature of sSC PV^+ neurons, especially when compared with their cortical homologs, is the degree of heterogeneity of their physiological properties. Within this population, we found 5 different spiking classes, as previously described (Lee et al., 2001; Edwards et al., 2002). We observed that these classes appear to sort independently of their morphology, in agreement with previous *in vitro* studies of sSC neurons (Edwards et al., 2002). Others have suggested that some intrinsic biophysical properties are correlated to specific neuronal type (Gale and Murphy, 2014), however, our data do not support this idea. Previous studies have suggested the existence of a link between cellular Ca^{2+}-binding protein expression and neuronal excitability (Celio, 1986; Gall et al., 2003; Roussel et al., 2006). In fact, theoretical work suggests that the excitability of fast-spiking neurons in the striatum depends on PV concentration and the presence of Ca^{2+}-activated K^+ channels, such as SK channels (Bischop et al., 2012). In contrast, our results show that sSC PV^+ neurons display a variety of spiking profiles and that $PV^+/GABA^+$ neurons show a very consistent, rapidly inactivating spiking profile. Possible explanations for these differences include; SC PV^+ neurons express different kinetic relationships between PV and SK channels, they have other Ca^{2+}-activated K^+ channels that allow them to buffer Ca^{2+} at different concentrations or they have Ca^{2+}-activated K^+ channels with slower kinetics.

Rapidly inactivating $PV^+/GABA^+$ neurons would provide a fast, transient inhibitory input to their targets in response to retinal stimulation. It seems reasonable to propose that non-spiking activity might be found in inhibitory neurons that lack axons and instead, produce inhibition using dendrodendritic synapses, similar to retinal horizontal cells. Dendrodendritic synapses are known to modulate retinal inputs in the sSC (Mize et al., 1982; Mize, 1992). In this case, the inhibitory inputs would arrive soon after retinal excitation, in a tonic fashion, like that provided by fast-spiking neurons. Together, these signals would cause the sSC $PV^+/GABA^+$ neurons to function more as event detectors, looking for transient changes in the visual scene (Kaneda and Isa, 2013). More recent experiments, using transgenic and knock-in mice, assessed the features of sSC neurons containing glutamic acid decarboxylase (GAD; GAD67-GFP or Gad2-Cre mice). These studies indicate that only horizontal neurons are positive for GAD (Endo et al., 2003; Gale and Murphy, 2014). Since the stellate and narrow field vertical neurons we observed were not labeled in these studies, it suggests that the GAD mice reveal only a subset of the inhibitory neurons present in the sSC (Whyland et al., 2017).

Comparison to Previous Findings in the Motor Layers (iSC)

Parvalbumin expression in the iSC is densest laterally, and appears patchy medio-laterally, similar to that descriptions using immunohistochemistry and may be due to the presence of PV^+ terminal puffs (Illing et al., 1990; Mize et al., 1992; Cork et al., 1998; González-Soriano et al., 2000; Behan et al., 2002). PV^+ neurons in iSC displayed more homogeneity compared to sSC, with most neurons showing a fast-spiking profile and radial-stellate morphology. These findings mirror immunohistochemical descriptions of iSC PV^+ neurons in other species, although the terms used to describe these neurons vary (Mize et al., 1992; González-Soriano et al., 2000). There is evidence that many PV^+ multipolar neurons supply the crossed tectoreticular and tectotectal projections (Mize, 1992). The tectotectal projection is known to contain a strong inhibitory component in the cat (Takahashi et al., 2005, 2010). It seems likely then, that the radial-stellate neurons observed in the present paper are similar to the multipolar neurons others have observed supplying the tectotectal projection (Rhoades et al., 1986; Olivier et al., 1998). It would be quite surprising if the crossed tectoreticular neurons supplying the paramedian pontine reticular formation were GABAergic. However, others have suggested that GABAergic neurons in the iSC do have targets outside the colliculus, as well as ascending interlaminar projections (Sooksawate et al., 2011). Our difficulty in recording IPSCs in iSC PV^- neurons after ChR2 activation of PV^+ neurons is consistent with the possibility that they are projection cells, not local circuit neurons.

PV^+ Circuit Motifs in the Visuosensory SC

Our immunohistochemical and optogenetic experiments provide important constraints on sSC circuit models. Although PV is commonly associated with GABAergic neurons, in the sSC it does not appear to be an exclusive marker of inhibitory neurons nor of a particular electrophysiological phenotype, as it does in cortex, striatum or hippocampus. Rather, PV may be a marker for a functional circuit that includes both excitatory and inhibitory neurons. It has been proposed that PV^+ neurons integrate and transmit Y-type retinal ganglion cell information and cortical Y-like information to thalamic nuclei and to the

pontine gray (Casagrande, 1994; Mize, 1996). In this model, PV^+ neurons are exclusively excitatory. Similarly, recent work using transgenic mice showed an excitatory circuit from the sSC to the amygdala via the parabigeminal nucleus (Shang et al., 2015). Our results are largely consistent with those of Shang et al. (2015), but extend them in important ways. Our optogenetic experiments suggest that PV^+ neurons form at least three types of intrinsic circuits with sSC PV^- neurons: direct excitation, direct inhibition and feedforward inhibition. It will be interesting to determine whether these circuits arise from different neuronal cell types. For example, the direct excitatory projection may emanate from the axon collaterals of glutaminergic narrow field vertical neurons (Hall and Lee, 1997), the GABAergic, direct inhibitory projection may originate from the horizontal and stellate neurons, and the feedforward inhibitory projection may originate from intrinsic circuits or activation of retinal ganglion cell axons terminating on a PV^- subclass of inhibitory interneuron (Schmidt et al., 2001; Edwards and Platt, 2003).

We believe that intrinsic $PV^+/GABA^+$ circuits, rather than external sources mediate the feedforward inhibitory currents seen in the sSC for the following reasons. First, activation of retinal axons generally results in triphasic responses in target neurons with an initial inward current, followed by an outward current and a third inward current, suggestive of recurrent excitation (Isa et al., 1998). Our results show that ChR2 activation in PV^+ neurons evoked biphasic currents, indicative of intrinsic feedforward inhibition. Second, we do not believe the direct inhibitory currents we measured resulted from activation of external sources of GABA, such as the substantia nigra pars reticulata, whose neurons co-localize PV^+ (White et al., 1994; Lee and Tepper, 2007). Although our current results do not allow us to rule this out definitively, we think that activation of nigral afferents is an unlikely explanation due to the small size of the inhibitory currents we measured compared to the large-sized potentials that stimulation of the nigra evokes in SC neurons (Karabelas and Moschovakis, 1985). Furthermore, in all species so far examined, the input from the nigra to the sSC is less prominent than that to the motor layers (Harting et al., 2001). It is noteworthy that, in our model, activation of $PV^+/GABA^+$ neurons from the substantia nigra pars reticulata (SNr) did not elicit inhibitory influence over collicular neurons. Ongoing experiments in which viral injections carrying ChR2 that target the SNr will help to further elucidate the role of SNr activation on the collicular circuitry.

CONCLUSION

We provide novel evidence that some PV^+ neurons in the SC co-localize GABA in both the visuosensory and motor layers, with the latter being more prominent. PV^+ neurons in the sSC have heterogeneous morphology and firing properties allowing them to respond selectively to different inputs and support varied functions, whereas most PV^+ neurons in the iSC show fast-spiking activity and radial-stellate morphology. Unlike PV^+ neurons elsewhere in the brain, most SC neurons that co-localize PV and GABA displayed rapidly inactivating firing properties. Furthermore, these neurons form both feedforward and direct inhibitory circuits within the SC. These properties indicate that PV^+ neurons in the SC perform unique circuit functions that are different from the canonical roles described in other areas of the brain, and may be specialized for different functions in the different layers of the SC.

AUTHOR CONTRIBUTIONS

CV, PL, PM, and MB designed the experiments. CV and QW collected the data. CV, QW, PL, and PM analyzed the data. CV wrote the first draft of the manuscript. CV, PL, PM, and MB contributed to manuscript revision, read, and approved the submitted version.

FUNDING

This work was supported by NIH EY019963 (MB and PM) and NIH EY024153 (MB).

ACKNOWLEDGMENTS

We are grateful to Marianne Cilluffo in the Brain Research Institute core facility for advice and assistance with immunostaining and Dr. Carolyn Houser for her advice using the GABA antibodies.

SUPPLEMENTARY MATERIAL

The Supplementary Material for this article can be found online at: https://www.frontiersin.org/articles/10.3389/fncir.2018.00035/full#supplementary-material

FIGURE S1 | Histological sections through the sSC **(A)** and iSC **(B)** of an Ai9;PV-Cre mouse. Cells labeled with Neurotrace® appear in green (pseudo-colored) and PV^+ cells (with tdTomato, red) appear as yellow. All PV^+ cells co-localized with Neurotrace® indicating they are neurons.

FIGURE S2 | Distribution of PV^+ neurons in the SC layers recorded in brain slices obtained from the Ai9;PV-Cre mouse. Each circle corresponds to individually recorded PV+ neurons and the color shows their respective electrophysiological phenotype (gray, fast spiking; white; rapidly inactivating; black, regular spiking).

FIGURE S3 | The percentage of $PV^+/GABA^+$ neurons from the total number of PV^+ neurons in the Ai9;PV-Cre;GAD67 mouse are similar to those found in the Ai9;PV-Cre mouse using a GABA antibody. **(A)** Mean percentage of $PV^+/GABA^+$ vs. PV^+ neurons calculated from slices obtained from the Ai9;PV-Cre mouse using a GABA antibody (white bars, **Figure 2B**) compared to the mean percentage of $PV^+/GABA^+$ neurons found in three Ai9;PV-Cre;GAD67 mice (gray bars); sSC = 42 ± 4% (black circles), iSC = 73 ± 7% (white circles), Cx = 98 ± 2%; n = 34 (gray circles). **(B)** PV^+ (tdTomato), $GABA^+$ (GFP) and merge panels showing high magnification confocal images from sections of sSC **(B_1)**, iSC **(B_2)**, and Cx **(B_3)** obtained from an Ai9;PV-Cre;GAD67 mouse. Examples of double-labeled $PV^+/GABA^+$ neurons are highlighted on each of the images (white circles). Red bar: mean ± SE.

FIGURE S4 | (A) Brief LED blue light pulses (cyan square, 2 ms) effectively evoked action potentials in PV^+ neurons recorded in slices from Ai32;PV-Cre mice. Representative trace of a PV^+ neuron (red trace) from sSC recorded in current-clamp configuration without QX-314 in the pipette (dashed lines, 0 mV and −60 mV). **(B)** Light-evoked EPSCs recorded at −80 mV (black trace) were blocked by APV/CNQX (50 μM/10 μM) (green trace). After ∼15 min washout, the EPSC amplitude was almost completely recovered (red trace). Bicuculline application (10 μM) did not affect the EPSC amplitude (orange trace). **(C)** Representative traces showing a PV^+ driven inhibitory circuits classified as feedforward inhibition. Bath application of APV/CNQX diminished PSCs evoked at −80 and −20 mV. After washout, bicuculline selectively inhibited the outward current. Scale: 100 pA/5 ms.

FIGURE S5 | Optogenetic stimulation of PV^+ neurons failed to evoke PSCs in PV^- neurons recorded in iSC. **(A)** Fluorescent image (40×, GFP) showing a PV^+ neuron in iSC (white arrow) of a brain slice from the Ai32;PV-Cre mouse. Scale: 20 μm. **(B)** DIC image showing the location of the recorded PV^+ neuron. Scale: 200 μm. **(C)** Upper panel: Schematic illustration showing the recording of PV^- (1) and PV^+ (2) neurons in the iSC. Bottom panel: Representative traces of a recorded PV^- neuron showing no significant current evoked upon 2 ms light stimulation in voltage-clamp configuration. Note the spontaneous IPSC evoked long after the light pulse when voltage is held at −20 mV (white arrow). Scale: 10 pA/5 ms. **(D)** Light stimulation elicited in a PV^+ neuron a large and short latency APV/CNQX-insensitive inward current at −80 mV. Application of 1 μM TTX eliminated the inward current. The recording pipette contained QX-314 hence the absence of spikes. Scale: 100 pA/5 ms. **(E)** Light pulses of increasing length failed to evoke PSCs in iSC PV^- neurons at either −80 mV or −20 mV V_m. **(F)** a train of 10 light pulses (5 ms in length) failed to evoke PSCs in iSC PV^- neurons. Five consecutive traces are superimposed.

REFERENCES

Basso, M. A., and May, P. J. (2017). Circuits for action and cognition: a view from the superior colliculus. *Annu. Rev. Vis. Sci.* 3, 197–226. doi: 10.1146/annurev-vision-102016-061234

Behan, M., Jourdain, A., and Bray, G. M. (1992). Calcium binding protein (calbindin D28k) immunoreactivity in the hamster superior colliculus: ultrastructure and lack of co-localization with GABA. *Exp. Brain Res.* 89, 115–124. doi: 10.1007/BF00229008

Behan, M., Steinhacker, K., Jeffrey-Borger, S., and Meredith, M. A. (2002). Chemoarchitecture of GABAergic neurons in the ferret superior colliculus. *J. Comp. Neurol.* 452, 334–359. doi: 10.1002/cne.10378

Bischop, D. P., Orduz, D., Lambot, L., Schiffmann, S. N., and Gall, D. (2012). Control of neuronal excitability by calcium binding proteins: a new mathematical model for striatal fast-spiking interneurons. *Front. Mol. Neurosci.* 5:78. doi: 10.3389/fnmol.2012.00078

Cardin, J. A., Carlén, M., Meletis, K., Knoblich, U., Zhang, F., Deisseroth, K., et al. (2009). Driving fast-spiking cells induces gamma rhythm and controls sensory responses. *Nature* 459, 663–667. doi: 10.1038/nature08002

Casagrande, V. A. (1994). A third parallel visual pathway to primate area V1. *Trends Neurosci.* 17, 305–310. doi: 10.1016/0166-2236(94)90065-5

Cauli, B., Audinat, E., Lambolez, B., Angulo, M. C., Ropert, N., Tsuzuki, K., et al. (1997). Molecular and physiological diversity of cortical nonpyramidal cells. *J. Neurosci.* 17, 3894–3906. doi: 10.1523/JNEUROSCI.17-10-03894.1997

Celio, M. R. (1986). Parvalbumin in most γ-aminobutyric acid-containing neurons of the rat cerebral cortex. *Science* 231, 995–997. doi: 10.1126/science.3945815

Chattopadhyaya, B. (2004). Experience and activity-dependent maturation of perisomatic GABAergic innervation in primary visual cortex during a postnatal critical period. *J. Neurosci.* 24, 9598–9611. doi: 10.1523/JNEUROSCI.1851-04.2004

Chen, G., Zhang, Y., Li, X., Zhao, X., Ye, Q., Lin, Y., et al. (2017). Distinct inhibitory circuits orchestrate cortical beta and gamma band oscillations. *Neuron* 96, 1403.e6–1418.e6. doi: 10.1016/j.neuron.2017.11.033

Chung, D. W., Fish, K. N., and Lewis, D. A. (2016). Pathological basis for deficient excitatory drive to cortical parvalbumin interneurons in schizophrenia. *Am. J. Psychiatry* 173, 1131–1139. doi: 10.1176/appi.ajp.2016.16010025

Cork, R. J., Baber, S. Z., and Mize, R. R. (1998). Calbindin(D28k)- and parvalbumin-immunoreactive neurons form complementary sublaminae in the rat superior colliculus. *J. Comp. Neurol.* 394, 205–217. doi: 10.1002/(SICI)1096-9861(19980504)394:2<205::AID-CNE5>3.0.CO;2-6

Edwards, M. D., and Platt, B. (2003). Sometimes you see them, sometimes you don't: IPSCs in the rat superficial superior colliculus. *Exp. Brain Res.* 149, 331–339. doi: 10.1007/s00221-002-1368-2

Edwards, M. D., White, A. M., and Platt, B. (2002). Characterisation of rat superficial superior colliculus neurones: firing properties and sensitivity to GABA. *Neuroscience* 110, 93–104. doi: 10.1016/S0306-4522(01)00558-9

Endo, T., Yanagawa, Y., Obata, K., and Isa, T. (2003). Characteristics of GABAergic neurons in the superficial superior colliculus in mice. *Neurosci. Lett.* 346, 81–84. doi: 10.1016/S0304-3940(03)00570-6

Gale, S. D., and Murphy, G. J. (2014). Distinct representation and distribution of visual information by specific cell types in mouse superficial superior colliculus. *J. Neurosci.* 34, 13458–13471. doi: 10.1523/JNEUROSCI.2768-14.2014

Gall, D., Roussel, C., Susa, I., D'Angelo, E., Rossi, P., Bearzatto, B., et al. (2003). Altered neuronal excitability in cerebellar granule cells of mice lacking calretinin. *J. Neurosci.* 23, 9320–9327. doi: 10.1523/JNEUROSCI.23-28-09320.2003

Gonchar, Y., Wang, Q., and Burkhalter, A. (2008). Multiple distinct subtypes of GABAergic neurons in mouse visual cortex identified by triple immunostaining. *Front. Neuroanat.* 1:3. doi: 10.3389/neuro.05.003.2007

González-Soriano, J., González-Flores, M. L., Contreras-Rodríguez, J., Rodríguez-Veiga, E., and Martínez-Sainz, P. (2000). Calbindin D28k and parvalbumin immunoreactivity in the rabbit superior colliculus: an anatomical study. *Anat. Rec.* 259, 334–346. doi: 10.1002/1097-0185(20000701)259:3<334::AID-AR100>3.0.CO;2-K

Gray, D. T., Engle, J. R., Rudolph, M. L., and Recanzone, G. H. (2014). Regional and age-related differences in GAD67 expression of parvalbumin- and calbindin-expressing neurons in the rhesus macaque auditory midbrain and brainstem. *J. Comp. Neurol.* 522, 4074–4084. doi: 10.1002/cne.23659

Gupta, A. (2000). Organizing principles for a diversity of GABAergic interneurons and synapses in the neocortex. *Science* 287, 273–278. doi: 10.1126/science.287.5451.273

Hall, W. C., and Lee, P. (1997). Interlaminar connections of the superior colliculus in the tree shrew. III: the optic layer. *Vis. Neurosci.* 14, 647–661. doi: 10.1017/S095252380001261X

Harting, J. K., Updyke, B. V., and Van Lieshout, D. P. (2001). The visual-oculomotor striatum of the cat: functional relationship to the superior colliculus. *Exp. Brain Res.* 136, 138–142. doi: 10.1007/s002210000606

Hashemi, E., Ariza, J., Rogers, H., Noctor, S. C., and Martínez-Cerdeño, V. (2017). The number of parvalbumin-expressing interneurons is decreased in the medial prefrontal cortex in autism. *Cereb. Cortex* 27, 1931–1943. doi: 10.1093/cercor/bhw021

Helms, M. C., Özen, G., and Hall, W. C. (2004). Organization of the intermediate gray layer of the superior colliculus. i. intrinsic vertical connections. *J. Neurophysiol.* 91, 1706–1715. doi: 10.1152/jn.00705.2003

Hu, H., Gan, J., and Jonas, P. (2014). Fast-spiking, parvalbumin+ GABAergic interneurons: from cellular design to microcircuit function. *Science* 345:1255263. doi: 10.1126/science.1255263

Illing, R.-B., Vogt, D. M., and Spatz, W. B. (1990). Parvalbumin in rat superior colliculus. *Neurosci. Lett.* 120, 197–200. doi: 10.1016/0304-3940(90)90037-A

Isa, T., Endo, T., and Saito, Y. (1998). The visuo-motor pathway in the local circuit of the rat superior colliculus. *J. Neurosci.* 18, 8496–8504. doi: 10.1523/JNEUROSCI.18-20-08496.1998

Jeong, S.-J., Kim, H.-H., Lee, W.-S., and Jeon, C.-J. (2014). Immunocytochemical localization of calbindin D28K, calretinin, and parvalbumin in bat superior colliculus. *Acta Histochem. Cytochem.* 47, 113–123. doi: 10.1267/ahc.14004

Kaneda, K., and Isa, T. (2013). GABAergic mechanisms for shaping transient visual responses in the mouse superior colliculus. *Neuroscience* 235, 129–140. doi: 10.1016/j.neuroscience.2012.12.061

Kang, Y. S., Park, W. M., Lim, J. K., Kim, S. Y., and Jeon, C. J. (2002). Changes of calretinin, calbindin D28K and parvalbumin-immunoreactive neurons in the superficial layers of the hamster superior colliculus following monocular enucleation. *Neurosci. Lett.* 330, 104–108. doi: 10.1016/S0304-3940(02)00723-1

Karabelas, A. B., and Moschovakis, A. K. (1985). Nigral inhibitory termination on efferent neurons of the superior colliculus: an intracellular horseradish peroxidase study in the cat. *J. Comp. Neurol.* 239, 309–329. doi: 10.1002/cne.902390305

Kawaguchi, Y. (1993). Physiological, morphological, and histochemical characterization of three classes of interneurons in rat neostriatum. *J. Neurosci.* 13, 4908–4923. doi: 10.1523/JNEUROSCI.13-11-04908.1993

Kawaguchi, Y., Katsumaru, H., Kosaka, T., Heizmann, C. W., and Hama, K. (1987). Fast spiking cells in rat hippocampus (CA1 region) contain the calcium-binding protein parvalbumin. *Brain Res.* 416, 369–374. doi: 10.1016/0006-8993(87)90921-8

Kawaguchi, Y., and Kubota, Y. (1993). Correlation of physiological subgroupings of nonpyramidal cells with parvalbumin- and calbindinD28k-immunoreactive neurons in layer V of rat frontal cortex. *J. Neurophysiol.* 70, 387–396. doi: 10.1152/jn.1993.70.1.387

Kawaguchi, Y., and Kubota, Y. (1997). GABAergic cell subtypes and their synaptic connections in rat frontal cortex. *Cereb. Cortex* 7, 476–486. doi: 10.1093/cercor/7.6.476

Kim, J., Kim, Y., Nakajima, R., Shin, A., Jeong, M., Park, A. H., et al. (2017). Inhibitory basal ganglia inputs induce excitatory motor signals in the thalamus. *Neuron* 95, 1181.e8–1196.e8. doi: 10.1016/j.neuron.2017.08.028

Klausberger, T., and Somogyi, P. (2008). Neuronal diversity and temporal dynamics: the unity of hippocampal circuit operations. *Science* 321, 53–57. doi: 10.1126/science.1149381

Laemle, L. K. (1981). A Golgi study of cellular morphology in the superficial layers of superior colliculus of man, Saimiri, and Macaca. *J. Hirnforsch.* 22, 253–263.

Langer, T. P., and Lund, R. D. (1974). The upper layers of the superior colliculus of the rat: a Golgi study. *J. Comp. Neurol.* 158, 405–435. doi: 10.1002/cne.901580404

Lee, C. R., and Tepper, J. M. (2007). Morphological and physiological properties of parvalbumin- and calretinin-containing γ-aminobutyric acidergic neurons in the substantia nigra. *J. Comp. Neurol.* 500, 958–972. doi: 10.1002/cne.21220

Lee, J.-Y., Choi, J.-S., Ahn, C.-H., Kim, I.-S., Ha, J.-H., and Jeon, C.-J. (2006). Calcium-binding protein calretinin immunoreactivity in the dog superior colliculus. *Acta Histochem. Cytochem.* 39, 125–138. doi: 10.1267/ahc.06008

Lee, J.-Y., Jeong, S.-J., and Jeon, C.-J. (2014). Parvalbumin-Immunoreactive cells in the superior colliculus in dog: distribution, colocalization with GABA, and effect of monocular enucleation. *Zoolog. Sci.* 31, 748–757. doi: 10.2108/zs140073

Lee, P., and Hall, W. C. (2006). An *in vitro* study of horizontal connections in the intermediate layer of the superior colliculus. *J. Neurosci.* 26, 4763–4768. doi: 10.1523/JNEUROSCI.0724-06.2006

Lee, P. H., Helms, M. C., Augustine, G. J., and Hall, W. C. (1997). Role of intrinsic synaptic circuitry in collicular sensorimotor integration. *Proc. Natl. Acad. Sci. U.S.A.* 94, 13299–13304. doi: 10.1073/pnas.94.24.13299

Lee, P. H., Schmidt, M., and Hall, W. C. (2001). Excitatory and inhibitory circuitry in the superficial gray layer of the superior colliculus. *J. Neurosci.* 21, 8145–8153. doi: 10.1523/JNEUROSCI.21-20-08145.2001

Lee, P. H., Sooksawate, T., Yanagawa, Y., Isa, K., Isa, T., and Hall, W. C. (2007). Identity of a pathway for saccadic suppression. *Proc. Natl. Acad. Sci. U.S.A.* 104, 6824–6827. doi: 10.1073/pnas.0701934104

Leuba, G., and Saini, K. (1996). Calcium-binding proteins immunoreactivity in the human subcortical and cortical visual structures. *Vis. Neurosci.* 13, 997–1009. doi: 10.1017/S0952523800007665

Lewis, D. A., Curley, A. A., Glausier, J. R., and Volk, D. W. (2012). Cortical parvalbumin interneurons and cognitive dysfunction in schizophrenia. *Trends Neurosci.* 35, 57–67. doi: 10.1016/j.tins.2011.10.004

Luksch, H., Cox, K., and Karten, H. J. (1998). Bottlebrush dendritic endings and large dendritic fields: motion-detecting neurons in the tectofugal pathway. *J. Comp. Neurol.* 396, 399–414. doi: 10.1002/(SICI)1096-9861(19980706)396:3<399::AID-CNE9>3.0.CO;2-Y

Ma, T. P., Cheng, H.-W., Czech, J. A., and Rafols, J. A. (1990). Intermediate and deep layers of the macaque superior colliculus: A golgi study. *J. Comp. Neurol.* 295, 92–110. doi: 10.1002/cne.902950109

Markram, H., Toledo-Rodriguez, M., Wang, Y., Gupta, A., Silberberg, G., and Wu, C. (2004). Interneurons of the neocortical inhibitory system. *Nat. Rev. Neurosci.* 5, 793–807. doi: 10.1038/nrn1519

May, P. J. (2006). The mammalian superior colliculus: Laminar structure and connections. *Prog. Brain Res.* 151, 321–378. doi: 10.1016/S0079-6123(05)51011-2

Mize, R. R. (1992). The organization of GABAergic neurons in the mammalian superior colliculus. *Prog. Brain Res.* 90, 219–248. doi: 10.1016/S0079-6123(08)63616-X

Mize, R. R. (1996). Neurochemical microcircuitry underlying visual and oculomotor function in the cat superior colliculus. *Prog. Brain Res.* 112, 35–55. doi: 10.1016/S0079-6123(08)63319-1

Mize, R. R. (1999). Calbindin 28kD and parvalbumin immunoreactive neurons receive different patterns of synaptic input in the cat superior colliculus. *Brain Res.* 843, 25–35. doi: 10.1016/S0006-8993(99)01847-8

Mize, R. R., Jeon, C.-J., Butler, G. D., Luo, Q., and Emson, P. C. (1991). The calcium binding protein calbindin-D 28K reveals subpopulations of projection and interneurons in the cat superior colliculus. *J. Comp. Neurol.* 307, 417–436. doi: 10.1002/cne.903070307

Mize, R. R., Luo, Q., Butler, G., Jeon, C.-J., and Nabors, B. (1992). The calcium binding proteins parvalbumin and calbindin-D 28K form complementary patterns in the cat superior colliculus. *J. Comp. Neurol.* 320, 243–256. doi: 10.1002/cne.903200208

Mize, R. R., Spencer, R. F., and Sterling, P. (1982). Two types of GABA-accumulating neurons in the superficial gray layer of the cat superior colliculus. *J. Comp. Neurol.* 206, 180–192. doi: 10.1002/cne.902060207

Mooney, R. D., Klein, B. G., and Rhoades, R. W. (1985). Correlations between the structural and functional characteristics of neurons in the superficial laminae and the hamster's superior colliculus. *J. Neurosci.* 5, 2989–3009. doi: 10.1523/JNEUROSCI.05-11-02989.1985

Moschovakis, A. K., and Karabelas, A. B. (1985). Observations on the somatodendritic morphology and axonal trajectory of intracellularly HRP-Labeled efferent neurons located in the deeper layers of the superior colliculus of the cat. *J. Comp. Neurol.* 239, 276–308. doi: 10.1002/cne.902390304

Moschovakis, A. K., Karabelas, A. B., and Highstein, S. M. (1988a). Structure-function relationships in the primate superior colliculus. I. Morphological classification of efferent neurons. *J. Neurophysiol.* 60, 232–262. doi: 10.1152/jn.1988.60.1.232

Moschovakis, A. K., Karabelas, A. B., and Highstein, S. M. (1988b). Structure-function relationships in the primate superior colliculus. II. Morphological identity of presaccadic neurons. *J. Neurophysiol.* 60, 263–302.

Norita, M. (1980). Neurons and synaptic patterns in the deep layers of the superior colliculus of the cat. A Golgi and electron microscopic study. *J. Comp. Neurol.* 190, 29–48. doi: 10.1002/cne.901900104

Olivier, E., Porter, J. D., and May, P. J. (1998). Comparison of the distribution and somatodendritic morphology of tectotectal neurons in the cat and monkey. *Vis. Neurosci.* 15, 903–922. doi: 10.1017/S095252389815513X

Rhoades, R. W., Mooney, R. D., Szczepanik, A. M., and Klein, B. G. (1986). Structural and functional characteristics of commissural neurons in the superior colliculus of the hamster. *J. Comp. Neurol.* 253, 197–215. doi: 10.1002/cne.902530207

Roussel, C., Erneux, T., Schiffmann, S. N., and Gall, D. (2006). Modulation of neuronal excitability by intracellular calcium buffering: From spiking to bursting. *Cell Calcium* 39, 455–466. doi: 10.1016/j.ceca.2006.01.004

Schmidt, M., Boller, M., Özen, G., and Hall, W. C. (2001). Disinhibition in rat superior colliculus mediated by GABAC receptors. *J. Neurosci.* 21, 691–699. doi: 10.1523/JNEUROSCI.21-02-00691.2001

Shang, C., Liu, Z., Chen, Z., Shi, Y., Wang, Q., Liu, S., et al. (2015). A parvalbumin-positive excitatory visual pathway to trigger fear responses in mice. *Science* 348, 1472–1477. doi: 10.1126/science.aaa8694

Soares, J. G., Botelho, E. P., and Gattass, R. (2001). Distribution of calbindin, parvalbumin and calretinin in the lateral geniculate nucleus and superior colliculus in *Cebus apella* monkeys. *J. Chem. Neuroanat.* 22, 139–146. doi: 10.1016/S0891-0618(01)00123-5

Sohal, V. S., Zhang, F., Yizhar, O., and Deisseroth, K. (2009). Parvalbumin neurons and gamma rhythms enhance cortical circuit performance. *Nature* 459, 698–702. doi: 10.1038/nature07991

Sooksawate, T., Isa, K., Behan, M., Yanagawa, Y., and Isa, T. (2011). Organization of GABAergic inhibition in the motor output layer of the superior colliculus. *Eur. J. Neurosci.* 33, 421–432. doi: 10.1111/j.1460-9568.2010.07535.x

Takahashi, M., Sugiuchi, Y., Izawa, Y., and Shinoda, Y. (2005). Commissural excitation and inhibition by the superior colliculus in tectoreticular neurons projecting to omnipause neuron and inhibitory burst neuron regions. *J. Neurophysiol.* 94, 1707–1726. doi: 10.1152/jn.00347.2005

Takahashi, M., Sugiuchi, Y., and Shinoda, Y. (2010). Topographic organization of excitatory and inhibitory commissural connections in the superior colliculi and their functional roles in saccade generation. *J. Neurophysiol.* 104, 3146–3167. doi: 10.1152/jn.00554.2010

Taniguchi, H. (2014). Genetic dissection of GABAergic neural circuits in mouse neocortex. *Front. Cell. Neurosci.* 8:8. doi: 10.3389/fncel.2014.00008

Taniguchi, H., He, M., Wu, P., Kim, S., Paik, R., Sugino, K., et al. (2011). A resource of cre driver lines for genetic targeting of GABAergic neurons in cerebral cortex. *Neuron* 71, 995–1013. doi: 10.1016/j.neuron.2011.07.026

Tremblay, R., Lee, S., and Rudy, B. (2016). GABAergic interneurons in the neocortex: from cellular properties to circuits. *Neuron* 91, 260–292. doi: 10.1016/j.neuron.2016.06.033

White, L. E., Hodges, H. D., Carnes, K. M., Price, J. L., and Dubinsky, J. M. (1994). Colocalization of excitatory and inhibitory neurotransmitter markers in striatal projection neurons in the rat. *J. Comp. Neurol.* 339, 328–340. doi: 10.1002/cne.903390303

Whyland, K. L., Masterson, S. P., Slusarczyk, A. S., Govindaiah, G., Guido, W., and Bickford, M. E. (2017). *Feedforward inhibitory Circuits within the Mouse Superior Colliculus. Program No. 228.08/CC21 2017 Neuroscience Meeting Planner*. Washington, DC: Society for Neuroscience.

Wöhr, M., Orduz, D., Gregory, P., Moreno, H., Khan, U., Vörckel, K. J., et al. (2015). Lack of parvalbumin in mice leads to behavioral deficits relevant to all human autism core symptoms and related neural morphofunctional abnormalities. *Transl. Psychiatry* 5:e525. doi: 10.1038/tp.2015.19

Xu, X., and Callaway, E. M. (2009). Laminar specificity of functional input to distinct types of inhibitory cortical neurons. *J. Neurosci.* 29, 70–85. doi: 10.1523/JNEUROSCI.4104-08.2009

Conflict of Interest Statement: The authors declare that the research was conducted in the absence of any commercial or financial relationships that could be construed as a potential conflict of interest.

frontiers in Neuroanatomy

ORIGINAL RESEARCH
published: 17 January 2018
doi: 10.3389/fnana.2017.00135

Hypothalamic Projections to the Optic Tectum in Larval Zebrafish

*Lucy A. Heap[1], Gilles C. Vanwalleghem[1], Andrew W. Thompson[1], Itia Favre-Bulle[2], Halina Rubinsztein-Dunlop[2] and Ethan K. Scott[1,3]**

[1]School of Biomedical Sciences, The University of Queensland, St. Lucia, QLD, Australia, [2]School of Maths and Physics, The University of Queensland, St. Lucia, QLD, Australia, [3]The Queensland Brain Institute, The University of Queensland, St. Lucia, QLD, Australia

The optic tectum of larval zebrafish is an important model for understanding visual processing in vertebrates. The tectum has been traditionally viewed as dominantly visual, with a majority of studies focusing on the processes by which tectal circuits receive and process retinally-derived visual information. Recently, a handful of studies have shown a much more complex role for the optic tectum in larval zebrafish, and anatomical and functional data from these studies suggest that this role extends beyond the visual system, and beyond the processing of exclusively retinal inputs. Consistent with this evolving view of the tectum, we have used a Gal4 enhancer trap line to identify direct projections from rostral hypothalamus (RH) to the tectal neuropil of larval zebrafish. These projections ramify within the deepest laminae of the tectal neuropil, the stratum album centrale (SAC)/stratum griseum periventriculare (SPV), and also innervate strata distinct from those innervated by retinal projections. Using optogenetic stimulation of the hypothalamic projection neurons paired with calcium imaging in the tectum, we find rebound firing in tectal neurons consistent with hypothalamic inhibitory input. Our results suggest that tectal processing in larval zebrafish is modulated by hypothalamic inhibitory inputs to the deep tectal neuropil.

Keywords: zebrafish, hypothalamus, tectum, superior colliculus, SPIM (selective plane illumination microscopy), optogenetics

OPEN ACCESS

Edited by:
Keisuke Yonehara, Aarhus University, Denmark

Reviewed by:
Pierre-Yves Risold, University of Franche-Comté, France
James A. Carr, Texas Tech University, United States
Manuel A. Pombal, University of Vigo, Spain

****Correspondence:***
Ethan K. Scott
ethan.scott@uq.edu.au

Received: *14 September 2017*
Accepted: *20 December 2017*
Published: *17 January 2018*

Citation:
Heap LA, Vanwalleghem GC, Thompson AW, Favre-Bulle I, Rubinsztein-Dunlop H and Scott EK (2018) Hypothalamic Projections to the Optic Tectum in Larval Zebrafish. Front. Neuroanat. 11:135. doi: 10.3389/fnana.2017.00135

INTRODUCTION

In vertebrates, the superior colliculus, or optic tectum, is a highly laminated structure located in the midbrain (Sparks, 1988; Robinson and McClurkin, 1989; Sparks and Hartwich-Young, 1989; Meek and Nieuwenhuys, 1998; May, 2006; Krauzlis et al., 2013). In mammals, the superior colliculus receives afferent inputs from multiple sensory regions of the brain, and contains intricate and overlapping topographic maps of the sensory world (Lane et al., 1973; Dräger and Hubel, 1976; Knudsen, 1982; Druga and Syka, 1984; Jay and Sparks, 1987; Sparks, 1988; Withington-Wray et al., 1990; King et al., 1996; Crish et al., 2003; Chabot et al., 2013). In contrast to mammals, amphibians and fish lack a visual cortex (Lázár, 1973; Streidter and Northcutt, 1989). Instead, they have a proportionally larger tectum that is hypothesized to carry out some of the visual processing that the cortex performs in mammals (Nevin et al., 2010; Orger, 2016). In teleost fish, tectal afferents arrive in the tectal neuropil, which comprises (from dorsal to ventral): the *stratum fibrosum marginale* (SM), which does not receive direct retinal inputs, the *stratum opticum* (SO), *stratum fibrosum et griseum superficiale* (SFGS), *stratum griseum centrale* (SGC) and the *stratum album centrale* and *stratum griseum periventriculare* (SAC/SPV; Vanegas et al., 1974; Meek, 1983; Sas and Maler, 1986; Meek and Nieuwenhuys, 1998). The laminae

spanning from the SO to the SAC/SPV are demarcated by robust innervation from the axons of retinal ganglion cells (RGCs), which convey visual information to the tectum (Fiebig et al., 1983; Struermer, 1988; Streidter and Northcutt, 1989; Niell and Smith, 2005; Corbo et al., 2012; Udin, 2012). In contrast, the SM receives axonal projections from the torus longitudinalis (Meek and Schellart, 1978; Perry et al., 2010), and lacks direct retinal inputs. As in birds and mammals, this visual projection is highly topographically organized, and in fish arises solely from the contralateral eye (Struermer, 1988; Easter and Nicola, 1996; Niell and Smith, 2005; Kita et al., 2015). In a variety of adult fish, nonretinal tectal afferents have been described anatomically. These have been shown to come from a variety of neural structures including the pretectum, the anterior and ventromedial thalamic nuclei (Northcutt, 1982; Fiebig et al., 1983; Meek and Nieuwenhuys, 1998), the hypothalamus (Amemiya, 1983; Fiebig et al., 1983; de Arriba and Pombal, 2007), the torus longitudinalis, torus semicircularis and nucleus ruber (Northcutt, 1982; Meek and Nieuwenhuys, 1998; Xue et al., 2001; Fame et al., 2006; Folgueira et al., 2007), as well as from hindbrain structures including the nucleus isthmi, reticular formation, dorsal funicular nucleus, eurydendroid cells in the cerebellum, and the trigeminal nuclei (Northcutt, 1982; Fiebig et al., 1983; Meek and Nieuwenhuys, 1998).

In zebrafish, the tectum's fundamental structure and cellular composition form early in development. In larvae at 3 days post fertilization (dpf), RGC axons begin arriving and the tectal neuropil's laminae have formed, as has the densely populated periventricular layer (PVL; Struermer, 1988). Nonretinal projections from the Raphe nucleus (Yokogawa et al., 2012; Filosa et al., 2016) and cerebellum (Heap et al., 2013) also innervate the neuropil. The tectal neuropil contains axons of these afferent structures, the dendrites of PVL neurons, and the axons of PVL interneurons. It is also sparsely populated with GABAergic superficial inhibitory neurons (SINs) that are located in the SO, and that have been described both anatomically and functionally (Del Bene et al., 2010; Robles et al., 2011; Dunn et al., 2016). PVL neurons are morphologically diverse, including both tectal interneurons and projection neurons (Scott and Baier, 2009; Robles et al., 2011). The tectal circuits arising from these cells are necessary for high-acuity vision (Gahtan et al., 2005), and for distinguishing between small prey items and larger visual features that may represent predators (Del Bene et al., 2010; Preuss et al., 2014; Semmelhack et al., 2014; Bianco and Engert, 2015; Dunn et al., 2016). Anatomical and functional studies have suggested that visual information principally enters the SO of the neuropil, and is progressively filtered by SINs and then PVL interneurons, before being relayed to other brain regions by the PVL projection neurons, the dendrites of which occupy the deep sublaminae of the neuropil (Scott and Baier, 2009; Del Bene et al., 2010; Robles et al., 2011; Gabriel et al., 2012; Preuss et al., 2014; Semmelhack et al., 2014; Barker and Baier, 2015; Temizer et al., 2015).

Inputs from the Raphe and cerebellum notwithstanding, the larval zebrafish tectum is viewed as a dominantly retinorecipient structure that is involved almost exclusively in visual processing. The list of described nonretinal inputs remains short in comparison to the diverse inputs received by the tectum in adult fish and the superior colliculus in mammals and birds. Nonetheless, larval zebrafish show behaviors that imply the integration of visual input with more complex state traits such as hunger (Filosa et al., 2016), and tectal neurons respond to auditory and water-flow stimuli (Thompson et al., 2016; Vanwalleghem et al., 2017). This implies that the larval zebrafish's tectum has more numerous and diverse inputs, and more nuanced circuitry, than has thus far been described.

Decisions based on the metabolic state of an animal are largely driven by the hypothalamus, a region of the brain that controls the metabolic and endocrine processes through the hypothalamic—pituitary—adrenal axis (Smith and Vale, 2006; Ulrich-Lai and Herman, 2009). In mammals, the hypothalamus has been shown to play a role in a multitude of such behaviors (Kokoeva et al., 2005; Bolborea and Dale, 2013), and elements of the underlying circuitry have been described. These include inhibitory hypothalamic projections to the intermediate laminae of the superior colliculus, which are hypothesized to assist in the role that the superior colliculus plays in visual attention tasks (Pityk, 1979; Rieck et al., 1986; Gandhi and Katnani, 2011).

Recently, contributions of the hypothalamus to behaviors in larval zebrafish have been described. Populations of dopaminergic hypothalamic neurons have been shown to regulate light seeking and motor behaviors (Fernandes et al., 2012; McPherson et al., 2016), feeding (Yokobori et al., 2011, 2012) and sleep cycles (Chiu and Prober, 2013). Additionally, serotonergic neurons in the Raphe nucleus, which are targeted by hypothalamic neurons, have been shown to work with visual information to mediate the classification of visual stimuli as either appetitive or predatory based on the feeding state of an individual animal (Filosa et al., 2016).

In larval zebrafish, hypothalamic nuclei are not yet spatially differentiated; instead, the expression of numerous hypothalamic neuropeptides allow for the general identification of hypothalamic nuclei (Herget et al., 2014). On this basis, the homologs of mammalian hypothalamic nuclei have been identified in larval zebrafish, including the paraventricular nucleus and preoptic area (Herget et al., 2014), and the dopaminergic A11 group and subpallial dopaminergic neural populations (Tay et al., 2011).

Combined, the anatomical and functional connections that have been described in adult fish, and tetrapods, the functions that the hypothalamus plays in larval zebrafish, and the flexibility of tectal responses to visual stimuli, suggest that the hypothalamus may be influencing tectal activity directly or indirectly in larval zebrafish. In this study, we have used a transgenic Gal4 line with expression in the hypothalamus to map previously undescribed projections into the tectal neuropil of zebrafish larvae, and to identify the laminae and sublaminae of the tectal neuropil in which these projections terminate. We have then used optogenetics and sculpted light to drive activity selectively in the hypothalamus while performing calcium imaging in the tectal PVL, thus identifying

the nature and magnitude of the hypothalamus' influence on tectal activity.

MATERIALS AND METHODS

Generation of Animals

All experiments were performed with approval from and in accordance with the University of Queensland Animal Welfare Unit (approval SBMS/378/16). Adult zebrafish (*Danio rerio*) were housed in a commercial RAS aquarium (Tecniplast S.p.A., Varese, Italy), in 28°C water (pH 7.5 ± 0.26, conductivity 992 ± 35 μS/cm^2, Ammonia 0–0.25 ppm, GH 83 ± 25 ppm, Ca2+ 76 ± 26 ppm) on a 14:10 h light:dark photoperiod, with 310,000 μJs/cm^2 UV disinfection. Fish were fed twice daily with a mixed commercial diet of O.range Wean and NRD at a 1:1 ratio, with a dusting of Spirulina powder (100g/kg; INVE Aquaculture Thailand) at a rate of approximately 5% body mass per day. Fish were housed at a stocking density of 10 fish per liter. Larval fish were reared in a 3 per-ml rotifer polyculture, based on the method described in Best et al. (2010), before being weaned to an exclusive dry food diet by 30 dpf. Adult zebrafish were mated as previously described to generate larvae for experiments (Westerfield, 2000). All experiments were performed in animals homozygous for the *nacre* mutation of the Tupfel long fin (TLN) strain (Lister et al., 1999).

The ChR2(ET/TC)-mCherry plasmid (Berndt et al., 2011) was provided by K. Deisseroth (Stanford University). All subcloning for transgenesis was performed using the Gateway Tol2 transgenesis system (Kwan et al., 2007). pME-MCS (construct 237, Tol2kit v1.2) was altered to include additional cloning sites with the forward primer CCCGGGACCGGTAGATCTTGATCAGGATCC and the reverse primer GGATCCTGATCAAGATCTACCGGTCCCGGG, creating the plasmid pME-MCS_linker. ChR2(ET/TC)-mCherry was cloned into the middle entry vector pME-MCS_linker using a blunt ApaI and XbaI sites, creating PME_ChR2(ET/TC)-mCherry. This was combined with a 10.5X UAS 5′ entry vector (construct 327, Tol2kit v1.2), a 3′ polyA containing vector (construct 302, Tol2kit v1.2) and a pDestTol2pA2 destination vector (construct 394, Tol2kit v1.2) using LR Clonase II Plus (Life Technologies) in a multi-site Gateway reaction. This generated the plasmid pDest_10.5XUAS:ChR2(ET/TC)-mCherry, which was confirmed by sequencing (AGRF, The University of Queensland, St. Lucia, QLD, Australia).

For transgenesis, plasmids were injected into single cell embryos within 40 min of fertilization, with an injection mix containing 75 ng/μL Tol2 transposase RNA and 100 ng/μL plasmid DNA. Injections were carried out in embryos obtained from crosses where a *Gal4*^{s1168t};*UAS:Kaede* (Scott and Baier, 2009) animal was mated to an animal homozygous for the *nacre* mutation (Lister et al., 1999). Injected embryos were screened for transient expression of the protein at 48 h post fertilization, and were then raised to adulthood. Founders with offspring containing the desired transgene were identified using fluorescence microscopy, and were then outcrossed to TLN animals to create stable transgenic lines.

Generation and Analysis of Averaged Transgene Expression Data for the Z-brain Atlas

Animals expressing *UAS:Kaede* under the control of the *Gal4*^{s1113t} transgene (Scott et al., 2007) were fixed, stained with the tERK antibody (Cell Signaling, ID 4696), and imaged as previously described (Randlett et al., 2015). Multiple tiles were stitched using the Pairwise Stitching ImageJ plugin (Preibisch et al., 2009). Image registration of Kaede expression was performed against a model of anti-tERK expression in the nervous system of larval zebrafish. This was performed with CMTK[1] using the command string -awr 010203 -T 8 -X 52 -C 8 -G 80 -R 3 -A "--accuracy 0.4" -W "--accuracy 1.6". Multiple (n = 9) registered animals were combined to create an average model of Kaede expression in *Gal4*^{s1113t};*UAS:Kaede* animals, which was incorporated into a local version of the Z-Brain atlas. Analysis of the location of expression of a given transgenic line was performed using the Z-Brain toolbox (Randlett et al., 2015).

Confocal Microscopy

Animals expressing the desired fluorescent proteins, under the control of the *Gal4*^{s1113t} were mated and raised as outlined above. All Kaede photoconversion experiments were carried out in 6 dpf animals, which were screened for desired fluorescence at 2 dpf and raised in the dark to avoid unwanted photoconversion. At 6 dpf, animals were mounted dorsal side down in 2% low melt agarose (Progen Biosciences, Murrarie, QLD, Australia) in 50 mm glass bottom dishes (MatTek Corporation, Ashland, MA, USA), which were then filled with E3 media.

Photoconversions were performed on an Olympus BX61 upright confocal microscope, using 405 nm light focused into a 10 μm region of interest (ROI), which was scanned across the cell bodies of neurons expressing *UAS:Kaede*. After conversions, animals were left for 1 h at 28.5°C in the dark, to allow photoconverted Kaede to diffuse from converted somae into axons. Fish were then imaged on an inverted Yokogawa 3i spinning disc confocal, using a 488 nm laser to image unconverted (green) Kaede, and a 561 nm laser to image converted (red) Kaede. Z-stacks were taken at 40× magnification, with a 0.2 μm slice interval.

Other fluorescent microscopy of the Gal4^{s1113t} line was performed on a Zeiss-LSM 710 inverted confocal microscope, using a 561 nm laser to image red fluorescence, and a 488 nm laser to image green fluorescence, and using either 10× or 20× objectives.

Deconvolution

Deconvolution of images acquired using the spinning disc confocal was performed with Huygens Professional Plus Deconvolution (Scientific Volume Imaging, Hilversum, Netherlands). A theoretical point spread function (PSF) was used, calculated from the parameters used for image acquisition. The signal to noise ratio (SNR) was calculated separately for each channel for each image by comparing the fluorescence intensity of a ROI to the fluorescence intensity

[1]http://www.nitrc.org/projects/cmtk/

of the background. Deconvolution was performed with a total image change threshold of 0.01, with single block processing on and a maximum iteration value of 60.

Spatial Analysis

Spatial analysis of neuropil laminae was performed using Imaris v8.1 (Bitplane, Zurich, Switzerland). Surfaces of both the red and green channels in the neuropil were created using the "surface creation" plugin, where the neuropil was highlighted as a ROI. To remove any out-of-focus light remaining after deconvolution, a background subtraction of 0.2 μm was used. Thresholding of the image was performed so that only axons in the neuropil were included in the surface reconstruction. Once surfaces were completed, clipping planes were used to section out a 20 μm slice through the medial region of the rostral-caudal axis. To calculate the average intensity of the red and green channels, measurements of the fluorescence intensity was taken in three evenly spaced points, which were averaged to get the mean fluorescent intensity over the depth of the neuropil.

Optogenetic Experiments

Animals used for optogenetic experiments were generated by crossing animals carrying *Gal4*^{s1113t} to animals carrying *Gal4*^{s1168t}*;UAS:ChR2-mCherry, HuC:H2B-GCaMP6s*, creating larvae with the genotype *Gal4*^{s1113t}*;UAS:ChR2-mCherry, HuC:H2B-GCaMP6s*. Animals were screened for the desired fluorescent pattern at 2 dpf, and were raised until 6 dpf as described above. Animals were mounted dorsal side up in 2% low melt agarose and immobilized using 100 μM tubocurarine (tubocurarine hydrochloride pentahydrate, Sigma-Aldrich). Larvae were mounted in a custom built glass sided imaging chamber and were allowed to acclimate for 30 min prior to imaging on a house-built selective planar illumination microscope (SPIM; Thompson et al., 2016). Optogenetic experiments were performed by splitting a 488 nm laser between a spatial light modulator (SLM; HOLOEYE Photonics, Germany) and the illumination tube of the SPIM. To avoid off target optogenetic activation of ChR2, a 0.975 neutral density filter was added to the SPIM path upstream of the beam expander.

Imaging was performed at 5 Hz, for 70 s (350 time points), at a depth of 50 μm under the skin of the animal, with imaging focused on the tectum. The activation of the hypothalamic nuclei was performed at time points 50, 150 and 250, and with pulses lasting for either 100 ms for "short" experiments, or 5000 ms for "long" experiments. The hologram displayed on the SLM was iteratively calculated using the Gerchberg-Saxton algorithm (Gerchberg and Saxton, 1972; Whyte and Courtial, 2005), resulting in a 2D illumination source at a chosen depth. In relatively low-scattering medium we theorized that a 10 μm disc would be very thin (Lutz et al., 2008), however by scanning the 10 μm disc at the depth of the hypothalamus (125 μm below the skin), we determined that the light spread in the z-plane was approximately 15 μm above and below the focal point (Favre-Bulle et al., 2015). Sibling controls not expressing ChR2 were subjected to identical experimental conditions to control for illumination.

Optogenetic Image Analysis

For movies taken during optogenetic experiments, we first deleted all frames in which the SLM was active; this resulted in movies containing frames 1–50, 77–150, 177–250 and 277–350 for long SLM experiments and frames 1–50, 53–150, 153–250 and 253–350 for short SLM experiments. This was done to avoid artifacts produced by the reflected SLM light. Images were then registered to eliminate drift in the X- and Y-axes using the "Align_slices_in_stack" ImageJ plugin[2]. To create an individual ROI for each cell in the PVL and neuropil, an average Z-projection of the image sequence was generated and then cropped to the border of the PVL and neuropil. A mask of this image was created using the Morphological Segmentation Plugin in ImageJ with a watershed function tolerance of 18 (Meyer and Beucher, 1990; Legland et al., 2016). Oversegmenting was tolerated, as the merging of erroneously split cells was performed during subsequent MATLAB analysis of these data.

Analysis of all data was performed using a custom written MATLAB code. Data were imported as a 16 BIT .tiff series, which were then transformed into a 2-dimensional data matrix, containing the gray values of every pixel in the 350-frame time series. Using the mask created above, the mean values of all pixels within each ROI were calculated for each time point. To measure the activity of individual neurons, the baseline fluorescence for each ROI was calculated by averaging the first ten time points for each individual ROI (F0). The raw gray value of every time point (FI) minus the baseline, was then divided by the baseline giving us the fluorescent change over time, which was then multiplied by 100 to give us percentage change over time:

$$\Delta F/F = ((FI - F0)/F0) * 100$$

After the ΔF/F of each ROI was calculated, ROIs with a correlation coefficient of above 0.97 were removed from the data using the corrcoeff MATLAB function. After duplicates had been removed, for each ROI at each SLM event, neural activity resulting from the SLM was identified by calculating the correlation of four time points before the SLM, and six time points after the SLM to three model profiles of GCaMP events. These were calculated by averaging 50 individual GCaMP signals over five separate movies (10 per movie) where cells were qualitatively excited or inhibited by the SLM illumination. For an ROI to be deemed either excited or inhibited, the minimum Pearson's correlation coefficient of all three SLM events to a model GCaMP profile had to be greater than 0.6, and the maximum probability value was required to be below 0.001. Every ROI that passed the above criteria was included as either an excited or an inhibited ROI, depending on which model spike it was correlated to. ROIs that did not meet these criteria were not included in the analysis. This analysis was performed on all experimental and control data. To compare the number of active cells between groups, an unpaired Student's *t*-test was performed (significance < 0.05), as data were normally distributed (one sample *t*-test).

[2]https://sites.google.com/site/qingzongtseng/template-matching-ij-plugin

RESULTS

The Transgenic Line *Gal4*^{s1113t} Expresses Gal4 in Rostral Hypothalamic Neurons with Projections to the Tectal Neuropil

Through preliminary screening of an existing collection of Gal4 enhancer trap lines (Scott et al., 2007; Scott and Baier, 2009), we identified the transgenic line *Gal4*^{s1113t} as containing apparent projections into the tectal neuropil in 6 dpf larvae. An initial assessment of the anatomy of the line was performed using the transgenic line *UAS:Kaede* (Scott et al., 2007). Animals with the genotype *Gal4*^{s1113t}*;UAS:Kaede* were used to create a model of the average expression pattern of the *Gal4*^{s1113t} transgenic line, which was then registered against the annotated Z-Brain atlas of the zebrafish brain (Randlett et al., 2015), and also compared with the the Atlas of Early Zebrafish Development (Mueller and Wullimann, 2005). Assessment against the Zebrafish Brain Atlas suggested expression within a small number of neurons in the vicinity of the rostral hypothalamus (RH), with sparse labeling of neurons in the rhombencephalon and telencephalon (**Figure 1**). Neurites originating from the labeled neurons in the vicinity of the RH were seen in the midbrain and hindbrain (**Figure 1H**). The most notable concentration of neurites was found in the tectal neuropil, where Kaede was concentrated toward the medial (and therefore, deep) laminae. Outside of the vicinity of the

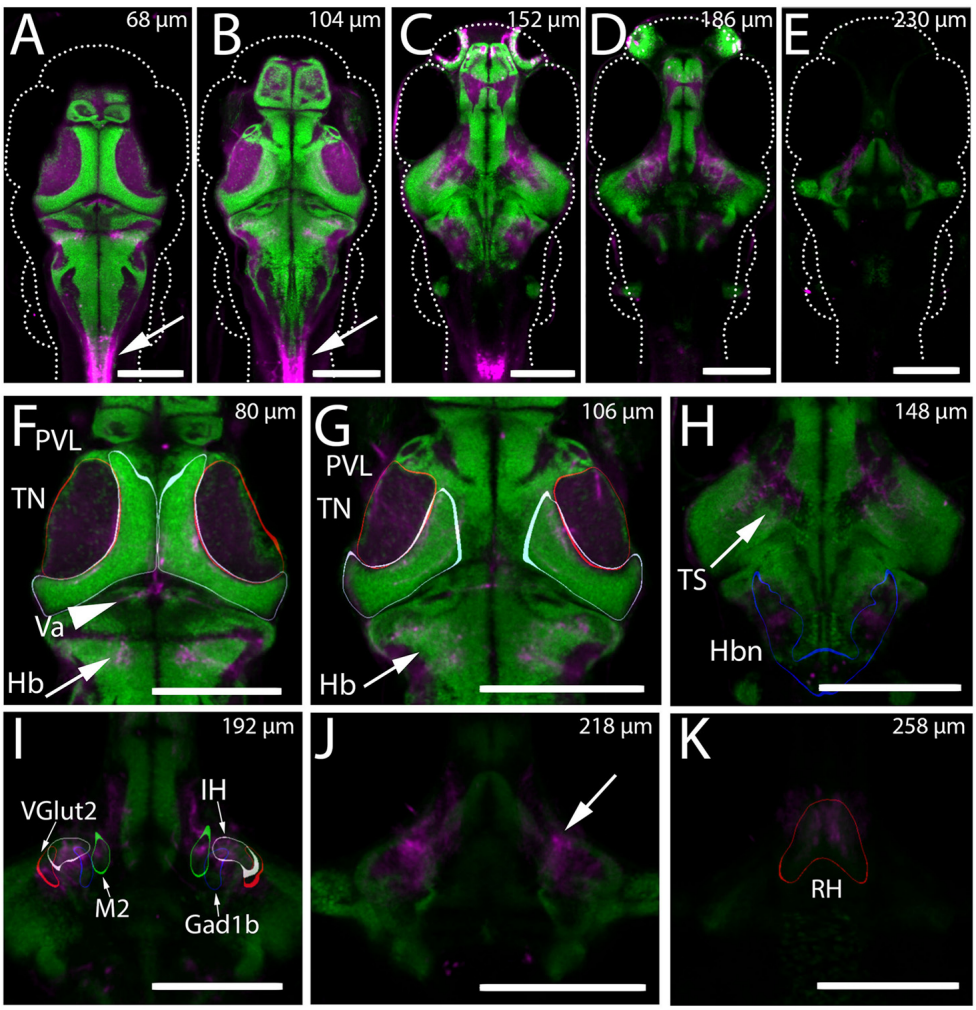

FIGURE 1 | Expression of Kaede in the *Gal4*^{s1113t} ET line. **(A–K)** The mean intensity, resulting from registering and averaging the expression pattern across nine animals, of the genotype *Gal4*^{s1113t}*;UAS:Kaede* is shown in magenta, overlaid with a pan-neuronal (HuC) H2B-RFP label (green). **(A–E)** Whole brain images at five dorsal-ventral depths separated by 15–21 microns. Arrows in **(A,B)** indicate expression in the spinal cord of these animals. **(F)** In the dorsal brain, *Gal4*^{s1113t} axons are present in the tectal neuropil (TN; red outline), tectal periventricular layer (PVL; cyan outline), valvula (Va) cerebellum (arrowhead) and hindbrain (Hb; arrow). **(G)** Axonal expression in the tectal neuropil (red outline) and sparse expression is seen in tectal periventricular neurons (cyan outline). Axons are present in the hindbrain (arrows). **(H)** Further ventral, expression is seen in the neuropil areas medial to the torus semicircularis (arrow) and in hindbrain neuropil (Hbn) regions (blue outline). **(I)** Axonal expression in the diffuse nucleus of the intermediate hypothalamus (IH; gray outline), a hypothalamic Gad1b cluster (blue outline) and hypothalamic Vglut2 cluster (red outline), and the migrated posterior tubercular area (M2; green outline). **(J)** Axonal labeling (arrow) of neurons with cell bodies located in the rostral hypothalamus (RH; outlined in red in **K**). Scale bars equal 200 µm.

RH, we observed labeled neurites in the valvula cerebellum (**Figure 1F**), within neuropil regions of the hindbrain caudal to the cerebellum, and also in a region medial to the torus semicircularis (**Figure 1H**). Observations of Kaede expression in individual *Gal4*^{s1113t}; *UAS:Kaede* animals supported these conclusions (**Figure 2**).

Overall, this analysis suggests that the majority of cell bodies labeled within *Gal4*^{s1113t} are located within the vicinity of the RH, with additional sparse labeling in the forebrain and hindbrain (**Figures 2A,B**). This, in turn, implies that the neurites visualized in these animals likely belong to these RH neurons. To confirm that the neurites observed in the tectal neuropil are sending synapses to the neuropil, we created *Gal4*^{s1113t}; *UAS:synaptophysin-GFP* larvae (Heap et al., 2013; Hines et al., 2015), in which the presynaptic terminals of Gal4-positive neurons are labeled. Following photoconversion of Kaede in the whole animal, we observed dense GFP labeling of presynaptic terminals throughout the deep laminae of the tectal neuropil (**Figure 2C**), suggesting that these neurites are axons, and that they are forming synapses in, rather than simply passing through, the tectal neuropil.

Hypothalamic Output Targets Specific Laminae of the Tectal Neuropil

The above data establish that neurons expressing Gal4 under the control of *Gal4*^{s1113t} transgene project axons into the tectal neuropil, but they do not conclusively demonstrate that the Gal4-positive RH neurons are the source of those axons. To address this, we performed targeted photoconversion of Kaede in the RH of *Atoh7:Gal4; Gal4*^{s1113t}, *UAS:Kaede* larvae, which express Kaede both in RGCs and throughout the *Gal4*^{s1113t} expression pattern (arrow, **Figure 3A**). Following targeted photoconversion of RH neurons, red Kaede diffused down the axons of these neurons, arriving in the deep sublaminae of the tectal neuropil (**Figure 3B**). Kaede in RGC axons remained unconverted, assuring that off-target photoconversion was negligible (**Figures 3B,C**). Combined with the previous data, this confirms that the Gal4-positive neurons in the RH are the source of the observed presynaptic terminals in the tectal neuropil.

In light of this, and since functionally distinct laminae are an important part of tectal visual processing, we next undertook a detailed analysis of the neuropil laminae into which the RH axons project. The tectal neuropils of *Atoh7:Gal4; Gal4*^{s1113t}, *UAS:Kaede* larvae with targeted RH photoconversion contain both the axons of RGCs (green, labeling the SO, SFGS, SGC, and SAC/SPV), and the axons of RH projection neurons (containing photoconverted red Kaede). This provides a scaffold in green that allows us to register our RH afferents against the retinorecipient laminae of the neuropil. The strongest signal from RH projection neurons was in the deepest neuropil lamina: the SAC/SPV (arrows, **Figures 3C–F**). Other RH projections were present in the SFGS (arrowhead, **Figures 3C,D,F**), and a non-retinorecipient sublamina located between the SGC and SAC/SPV (asterisks, **Figures 3E,F**). This shows that RH projection neurons target multiple discrete depths of the tectal neuropil, including both retinorecipient and non-retinorecipient laminae (**Figure 3G**).

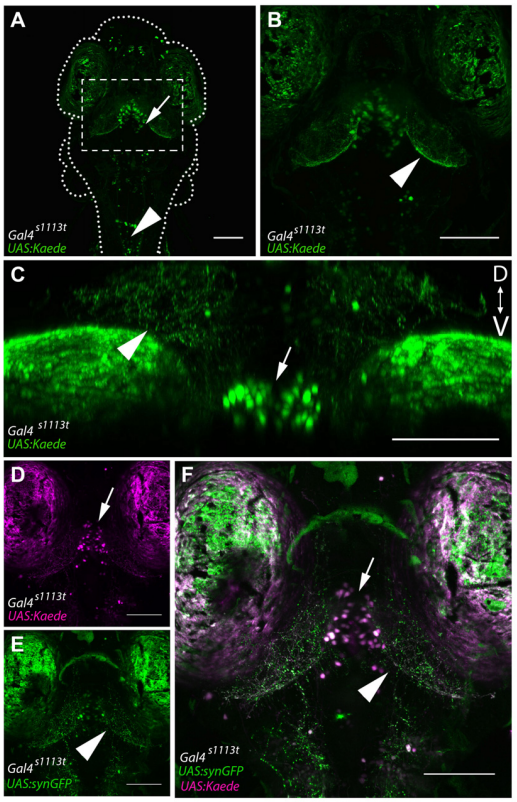

FIGURE 2 | Gal4-positive hypothalamic neurons project axons to the tectal neuropil. **(A)** Maximum projection of a 6 dpf *Gal4*^{s1113t}*;UAS:Kaede* larva in which expression is strongest in a small number of neurons in the ventral diencephalon, located in the RH (arrow). **(B)** shows a closeup of the box in **(A)**. Neurites are evident in the tectal neuropil (arrowhead) suggesting that hypothalamic projections may be targeting the tectum. **(C)** A coronal rotation through an animal with the genotype *Gal4*^{s1113t}*;UAS:Kaede*. The location of labeled cell bodies is indicated with an arrow, and projections to the tectal neuropil are labeled with an arrowhead. **(D,E)** Images from a *Gal4*^{s1113t}*;UAS:Kaede, UAS:syn-GFP* showing the cell bodies of the RH neurons with photoconverted red Kaede (arrowhead, **D**) and the green presynaptic terminals of their axons in the tectal neuropil (arrow, **E**). These channels are merged in **(F)**. Scale bars equal 100 μm.

Functional Properties of Hypothalamic Inputs to the Tectum

In order to gauge the functional relevance of these RH projections, we next observed the calcium responses that tectal neurons have to optogenetic RH stimulation. To do this, we used larvae with the genotype *Gal4*^{s1113t}*;UAS:Channelrhodopsin2(ET/TC)-mCherry, HuC:H2B-GCaMP6s* (Chen et al., 2013; Vladimirov et al., 2014). It is worth noting that in these experiments, the imaging plane was significantly more dorsal than the ChR2-expressing neurons in the RH. The result is that the illumination plane, although

it is at 488 nm, does not lead to any observable activation of ChR2-expressing neurons on the RH.

To determine whether projections from the RH are excitatory or inhibitory in the tectum, we performed experiments where neurons expressing ChR2 were excited with a short (100 ms)

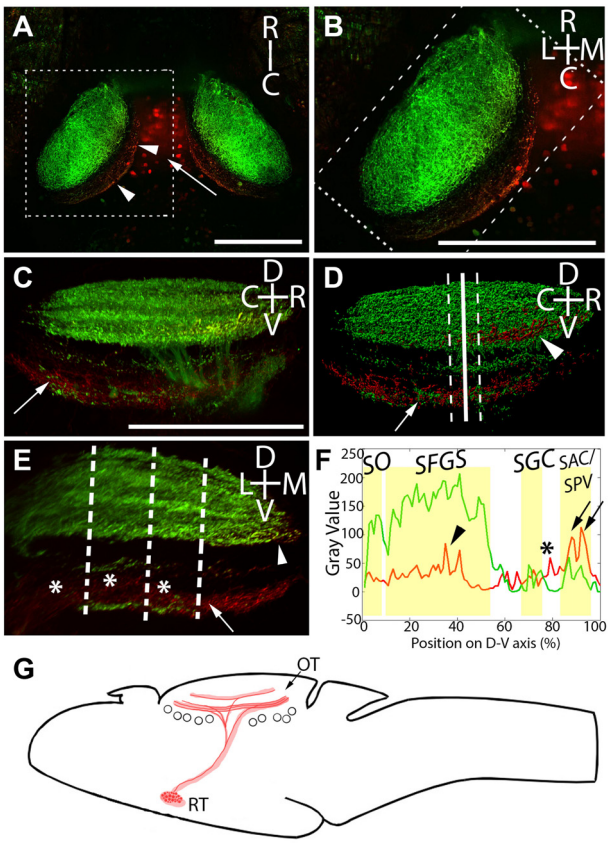

FIGURE 3 | Laminar structure of hypothalamic projections in the tectal neuropil. By expressing *UAS:Kaede* under the control of *Atoh7:Gal4* and *Gal4*^{s1113t}, we have identified the neuropil laminae targeted by hypothalamic projection neurons. **(A)** Maximum intensity projection of a single larva at 20× magnification, showing red photoconverted cells in the hypothalamus (arrow), as well as their neurites in the tectal neuropil (arrowheads). **(B)** An expanded view of the box in **(A)**, showing the relative positions of the retinal ganglion cells (RGC; green) and RH (red) axons. **(C)** A rotated view of the box in **(B)**, with the medial edge of the neuropil perpendicular to the field of view. The arrow indicates hypothalamic axons in the stratum album centrale (SAC)/stratum griseum periventriculare (SPV). **(D)** An Imaris 3D rendering of **(C)**. The solid line indicates the medial-lateral center point of the tectal neuropil, and dashed lines show the boundaries that were used in creating the coronal perspective in **(E)**. The arrow indicates hypothalamic output to the SAC/SPV, arrowhead indicates hypothalamic output in the stratum fibrosum et griseum superficiale (SFGS). **(E)** A coronal perspective of the tectal neuropil labeling all laminae formed by the RGC axons (green) and hypothalamic inputs (red). To assess which sublaminae of the neuropil the hypothalamus targets, the fluorescent intensities of retinal and hypothalamic inputs were sampled at three evenly-spaced positions, indicated by dashed lines. **(F)** Hypothalamic inputs specifically targeted regions of the SFGS (arrowhead) and SAC/SPV (arrows) in the tectal neuropil. Additionally, hypothalamic projections frequently targeted a lamina devoid of retinal input between the stratum griseum centrale (SGC) and SAC/SPV (asterisks, **E,F**). Scale bar represents 100 μm. **(G)** A schematic of the projection from the RH to the optic tectum in the *Gal4*^{s1113t} transgenic line.

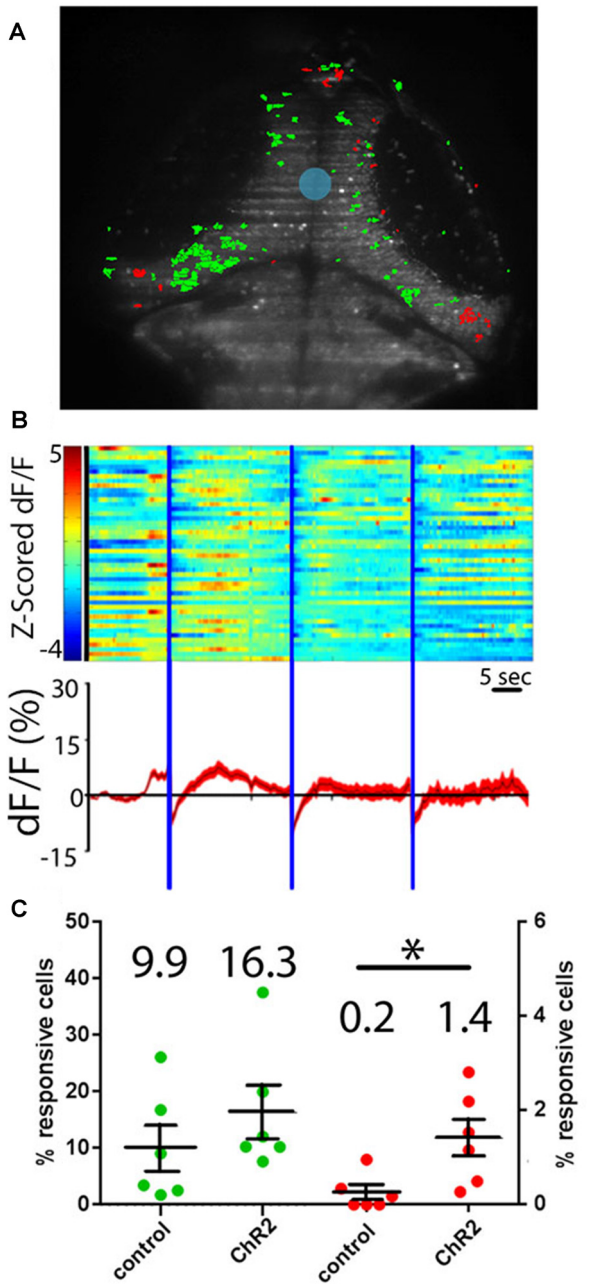

FIGURE 4 | Hypothalamic projection neurons deliver inhibitory inputs to the tectum. **(A)** Activation of ChR2-expressing neurons in the RH using sculpted blue light (shaded blue) results in inhibitory responses (shaded red) and excitatory visual responses (green) in tectal PVL neurons. **(B)** A raster plot of these responses (n = 46 inhibited neurons across six larvae) shows the z-scored ΔF/F of these inhibited neurons (top), and an average trace of these neurons through the experiment is shown (bottom). **(C)** Similar proportions of tectal cells were excited by a short pulse of blue light in ChR2^{+} larvae and ChR2^{-} controls, indicating that these are direct visual responses (green). Significantly more tectal neurons were inhibited in ChR2^{+} larvae vs. ChR2^{-} controls (red) by a prolonged illumination of the RH, indicating a causative effect of hypothalamic inputs. Dots represent individual larvae and mean ± SEM is indicated, mean value is reported above each scatter plot. *$p < 0.05$. n = 6 experimental, n = 6 controls.

pulse of blue light. Such stimulation excited a similar number of tectal neurons both in our experimental larvae and in controls not expressing ChR2, suggesting that the responses in these experiments are simply tectal visual responses to the flash of light from the SLM (**Figures 4A,C**). As a means of probing for inhibitory effects, we extended our light pulse to 5 s in order to produce prolonged inhibition of postsynaptic tectal neurons. If RH inputs are inhibitory, this should result in a decrease in GCaMP signal in the postsynaptic cells (Tian et al., 2009; Akerboom et al., 2012), followed either by a return to baseline, or "rebound firing" in response to the disinhibition of the postsynaptic neurons at the end of hypothalamic stimulation (Bennett, 1966; Aizenman and Linden, 1999; Jay et al., 2015). Based on these expectations, a small but significant proportion of tectal neurons appeared to be inhibited by RH input (**Figures 4B,C**). These PVL neurons, both as individuals and as a population, showed decreased GCaMP fluorescence following the hypothalamic excitation, and in most cases, rebound firing. Habituation of this rebound firing occurred during the course of our three-trial experiment (**Figure 4B**).

DISCUSSION

Nonretinal Projections to the Optic Tectum of Larval Zebrafish

The tecta of various teleost species, including zebrafish, are known to receive input from the retina, and from a host of regions throughout the brain. Here, we demonstrate that neurons within the RH project to the tectum in larval zebrafish. These findings are similar to those described in numerous fish species including the hagfish and lamprey, where numerous hypothalamic clusters have been observed projecting in an ipsilateral fashion to the optic tectum (Amemiya, 1983; Meek and Nieuwenhuys, 1998; de Arriba and Pombal, 2007). In inspecting these projections in more detail, we also show that they specifically target the tectal neuropil's deeper retinorecipient laminae, as well as a non-retinorecipient lamina between the SGC and SAC/SPV. This arrangement has several implications for the overall structure of the tectal neuropil. It has previously been shown that the broad laminae delineated by RGC axons each comprise several sublaminae with distinct contributions to visual processing (Xiao and Baier, 2007; Bollmann and Engert, 2009; Xiao et al., 2011; Robles et al., 2013, 2014). The RH projections that we have found in retinorecipient laminae, especially the SFGS, occupy a sharp subset of the lamina, suggesting that they may be restricted to specific sublaminae. This suggests a tight coupling between retinal and nonretinal inputs to these laminae, and potentially specific contributions from the RH to particular types of visual processing. RH afferents also target one lamina, between the SGC and SAC/SPV, that is not innervated by RGCs. Two conclusions can be drawn from this observation. First, it shows that this non-retinorecipient lamina is not exclusively involved with secondary visual processing, since it is also incorporating distinct nonretinal inputs. Second, since RH inputs innervate a sharp subset of the space between the SGC and the SAC/SPV, it appears that these non-retinorecipient laminae, like their retinorecipient counterparts, may contain functionally distinct sublaminae.

Functional Properties of the Tectum's Hypothalamic Inputs

Following the anatomical descriptions of these RH projections to the tectum, it was important to determine their functional contributions to tectal circuitry. This involved both short pulses of optogenetic stimulation to the RH (designed to elicit excitatory responses in tectal PVL neurons) and long pulses of RH stimulation (designed to identify inhibited PVL neurons). Short pulses of excitation in the RH led to tectal activity, but this was not significantly higher in ChR expressing animals than in ChR^{-} controls. This result is consistent with an absence of excitatory RH input to the tectum, or with a low level of excitatory input that fell below the sensitivity of our experiment. Long pulses of optogenetic stimulation to the RH drove inhibitory responses in the tectal PVL. The fact that there are apparently no tectal cells excited by RH stimulation suggests that the inhibited PVL neurons are directly post-synaptic to the projection neurons. Inhibition does not appear to result, for example, from the activation of tectal inhibitory neurons.

These experiments do not allow us to discriminate between the effects of direct monosynaptic connections and those resulting from more complex pathways. Therefore, it is possible that RH activity drives responses in an intermediate structure, which in turn inhibits PVL neurons. One candidate for such an intermediate structure would be the precursor to the preglomerular complex, the migrated posterior tubercular area (M2 region), which innervates the tectum (Mueller and Wullimann, 2005; Mueller, 2012). In the *Gal4*^{s1113t} line, this structure appears to receive neurites from RH neurons expressing Gal4 (**Figure 1I**), supporting this possibility. Given the direct anatomical projection from the RH to the tectal neuropil in this line, however, the most parsimonious explanation is that the RH projection neurons are feeding directly into the tectal circuit.

Implications for Tectal Processing

The combined results of our anatomical and functional analyses have implications for the roles that nonretinal inputs may play in tectal processing. Given the diverse roles for the hypothalamus including arousal (Prober et al., 2006; Chiu and Prober, 2013), the detection of prey (Filosa et al., 2016) and feeding (Yokobori et al., 2011, 2012; Nishiguchi et al., 2012) it seems likely that these inhibitory signals may provide some sort of modulatory effect, conceivably influencing approach/escape decisions or other behavioral calculations being carried out by tectal circuits (Barker and Baier, 2015; Bianco and Engert, 2015). Muto et al. (2017) have recently shown that visual prey stimuli trigger hypothalamic activity in larval zebrafish, and that this information is relayed through the pretectum prior to arriving in the hypothalamus. Furthermore, expression of toxins in the hypothalamus reduced prey capture behavior. This

raises a possible role for the hypothalamus in gating predatory behavior.

The anatomy of these projections appears to be similar with those described by Kaslin et al. (2004), who show that Orexin expression in the tectal neuropil is confined to the SAC in adult zebrafish. This finding suggests that orexin-expressing neurons within the hypothalamus of zebrafish may project to similar laminae of the optic tectum as the RH projections shown in this study. If our described projections are those described by Kaslin et al. (2004), it suggests that they could potentially be involved in controlling sleep and wakefulness (Kaslin et al., 2004). That the responses in the tectum are sparse and inhibitory further supports the idea that the hypothalamus' role is to influence or contextualize the sensory signals, rather than to be a major driver of them. Of course, the identity, morphology, and connectivity of the tectal cells inhibited by the RH will be of interest as this circuit is further explored, as would the activity of hypothalamic projection neurons in the contexts of predation, sleep and other behaviors.

More broadly, these results add to the direct evidence for a larval zebrafish tectum that receives more numerous and diverse inputs than had previously been recognized, more in line with what has been described in adult fish and tetrapods. The anatomical and circuit mapping experiments in this study compliment and extend recent work showing that the tectum and the Raphe, a structure known to target of hypothalamus in both larval and adult zebrafish (Lillesaar et al., 2009; Herculano and Maximino, 2014), work together to drive behaviors based on the feeding state of larvae (Filosa et al., 2016), and thus provides grounds to understand how the visual and metabolic systems work together to drive behaviors. Additionally, the results from the optogenetic studies presented here complement previous work describing the neurotransmitter profiles of neurons within the RH, showing in this context that they have inhibitory effects on postsynaptic partners (Kaslin et al., 2004). Combined, the facts that the tectum receives direct afferents from several brain regions (Yokogawa et al., 2012; Heap et al., 2013; Filosa et al., 2016), and responds to multiple sensory modalities (Thompson et al., 2016), paint a picture of a structure that is more completely homologous to its mammalian counterpart, the superior colliculus, than has previously been appreciated. They also suggest that the tectum may be less of a self-contained visual processing center, and more of an integrative locus for diverse information. While RGCs remain, both in anatomical and functional terms, the strongest single input to the tectum in larval zebrafish, it is increasingly clear that tectal function is broader and more nuanced than its traditional role as a visual processing center would suggest.

AUTHOR CONTRIBUTIONS

LAH designed experiments, collected and analyzed data and wrote the manuscript. GCV performed bioinformatic analyses of ontogenetics data. AWT created the UAS:syn-GFP line. IF-B and HR-D designed the sculpted light for optogenetics. IF-B performed these the experiments. EKS designed the experiment, interpreted the data and wrote the manuscript.

ACKNOWLEDGMENTS

We thank Rebecca Dunning for creating the PME-linker-MCS plasmid. We are grateful to Karl Deisseroth for providing the Channelrhodopsin-2(ET/TC) plasmid and Misha Ahrens for providing the *HuC:H2B-GCaMP6s* transgenic line. We thank Owen Randlett, Alexander Schier, and Florian Engert for providing the Z-Brain atlas prior to publication, as well as for assisting in Z-Brain analysis. We thank Jan Kaslin and members of the Scott laboratory for comments on the manuscript. Support was provided by the Australian Research Council Postgraduate Awards to LAH and AWT; an National Health and Medical Research Council (NHMRC) Project Grant (APP1066887), ARC Future Fellowship (FT110100887), a Simons Foundation Explorer Award (336331) and two ARC Discovery Project Grants (DP140102036 and DP110103612) to EKS; an ARC Discovery Project (DP140100753) to HR-D; a UQ Postgraduate Scholarship to IF-B; and an European Molecular Biology Organization (EMBO) Long-term Fellowship (ALTF 727-2014) to GCV. Imaging was performed at the Queensland Brain Institute's Advanced Microscopy Facility, generously supported by the Australian Government through the ARC LIEF grant LE130100078.

REFERENCES

Aizenman, C. D., and Linden, D. J. (1999). Regulation of the rebound depolarization and spontaneous firing patterns of deep nuclear neurons in slices of rat cerebellum. *J. Neurophysiol.* 82, 1697–1709.

Akerboom, J., Chen, T.-W., Wardill, T. J., Tian, L., Marvin, J. S., Mutlu, S., et al. (2012). Optimization of a GCaMP calcium indicator for neural activity imaging. *J. Neurosci.* 32, 13819–13840. doi: 10.1523/JNEUROSCI.2601-12.2012

Amemiya, F. (1983). Afferent connections to the tectum mesencephali in the hagfish, Eptatretus burgeri: an HRP study. *J. Hirnforsch.* 24, 225–236.

Barker, A. J., and Baier, H. (2015). Sensorimotor decision making in the zebrafish tectum. *Curr. Biol.* 25, 2804–2814. doi: 10.1016/j.cub.2015.09.055

Bennett, M. R. (1966). Rebound excitation of the smooth muscle cells of the guinea-pig taenia coli after stimulation of intramural inhibitory nerves. *J. Physiol.* 185, 124–131. doi: 10.1113/jphysiol.1966.sp007975

Berndt, A., Schoenenberger, P., Mattis, J., Tye, K. M., Deisseroth, K., Hegemann, P., et al. (2011). High-efficiency channelrhodopsins for fast neuronal stimulation at low light levels. *Proc. Natl. Acad. Sci. U S A* 108, 7595–7600. doi: 10.1073/pnas.1017210108

Best, J., Adatto, I., Cockington, J., James, A., and Lawrence, C. (2010). A novel method for rearing first-feeding larval zebrafish: polyculture with type L saltwater rotifers (*Brachionus plicatilis*). *Zebrafish* 7, 289–295. doi: 10.1089/zeb.2010.0667

Bianco, I. H., and Engert, F. (2015). Visuomotor transformations underlying hunting behavior in zebrafish. *Curr. Biol.* 25, 831–846. doi: 10.1016/j.cub.2015.01.042

Bolborea, M., and Dale, N. (2013). Hypothalamic tanycytes: potential roles in the control of feeding and energy balance. *Trends Neurosci.* 36, 91–100. doi: 10.1016/j.tins.2012.12.008

Bollmann, J. H., and Engert, F. (2009). Subcellular topography of visually driven dendritic activity in the vertebrate visual system. *Neuron* 61, 895–905. doi: 10.1016/j.neuron.2009.01.018

Chabot, N., Mellott, J. G., Hall, A. J., Tichenoff, E. L., and Lomber, S. G. (2013). Cerebral origins of the auditory projection to the superior colliculus of the cat. *Hear. Res.* 300, 33–45. doi: 10.1016/j.heares.2013.02.008

Chen, T. W., Wardill, T. J., Sun, Y., Pulver, S. R., Renninger, S. L., Baohan, A., et al. (2013). Ultrasensitive fluorescent proteins for imaging neuronal activity. *Nature* 499, 295–300. doi: 10.1038/nature12354

Chiu, C. N., and Prober, D. A. (2013). Regulation of zebrafish sleep and arousal states: current and prospective approaches. *Front. Neural Circuits* 7:58. doi: 10.3389/fncir.2013.00058

Corbo, C. P., Othman, N. A., Gutkin, M. C., Alonso, A. C., and Fulop, Z. L. (2012). Use of different morphological techniques to analyze the cellular composition of the adult zebrafish optic tectum. *Microsc. Res. Tech.* 75, 325–333. doi: 10.1002/jemt.21061

Crish, S. D., Comer, C. M., Marasco, P. D., and Catania, K. C. (2003). Somatosensation in the superior colliculus of the star-nosed mole. *J. Comp. Neurol.* 464, 415–425. doi: 10.1002/cne.10791

de Arriba, M. D. C., and Pombal, M. A. (2007). Afferent connections of the optic tectum in lampreys: an experimental study. *Brain Behav. Evol.* 69, 37–68. doi: 10.1159/000095272

Del Bene, F., Wyart, C., Robles, E., Tran, A., Looger, L., Scott, E. K., et al. (2010). Filtering of visual information in the tectum by an identified neural circuit. *Science* 330, 669–673. doi: 10.1126/science.1192949

Dräger, U. C., and Hubel, D. H. (1976). Topography of visual and somatosensory projections to mouse superior colliculus. *J. Neurophysiol.* 39, 91–101. doi: 10.1152/jn.1976.39.1.91

Druga, R., and Syka, J. (1984). Projections from auditory structures to the superior colliculus in the rat. *Neurosci. Lett.* 45, 247–252. doi: 10.1016/0304-3940(84)90234-9

Dunn, T. W., Gebhardt, C., Naumann, E. A., Riegler, C., Ahrens, M. B., Engert, F., et al. (2016). Neural circuits underlying visually evoked escapes in larval zebrafish. *Neuron* 89, 613–628. doi: 10.1016/j.neuron.2015.12.021

Easter, S. S. Jr., and Nicola, G. N. (1996). The development of vision in the zebrafish *(Danio rerio)*. *Dev. Biol.* 180, 646–663. doi: 10.1006/dbio.1996.0335

Fame, R. M., Brajon, C., and Ghysen, A. (2006). Second-order projections from the posterior lateral line in the early zebrafish brain. *Neural Dev.* 29, 1–4. doi: 10.1186/1749-8104-1-4

Favre-Bulle, I. A., Preece, D., Nieminen, T. A., Heap, L. A., Scott, E. K., and Rubinsztein-Dunlop, H. (2015). Scattering of sculpted light in intact brain tissue, with implications for optogenetics. *Sci. Rep.* 5:11501. doi: 10.1038/srep11501

Fernandes, A. M., Fero, K., Arrenberg, A. B., Bergeron, S. A., Driever, W., and Burgess, H. A. (2012). Deep brain photoreceptors control light-seeking behavior in zebrafish larvae. *Curr. Biol.* 22, 2042–2047. doi: 10.1016/j.cub.2012.08.016

Fiebig, E., Ebbesson, S., and Meyer, D. (1983). Afferent connections of the optic tectum in the piranha (*Serrasalmus nattereri*). *Cell Tissue Res.* 231, 55–72. doi: 10.1007/bf00215774

Filosa, A., Barker, A. J., Dal Maschio, M., and Baier, H. (2016). Feeding state modulates behavioral choice and processing of prey stimuli in the zebrafish tectum. *Neuron* 90, 596–608. doi: 10.1016/j.neuron.2016.03.014

Folgueira, M., Sueiro, C., Rodríguez-Moldez, I., Yáñez, J., and Anadón, R. (2007). Organization of the torus Longitudinalis in the rainbow trout (*Oncorhynchus mykiss*): an immunohistochemical study of the GABAergic system and a Dil tract-tracing study. *J. Comp. Neurol.* 503, 348–370. doi: 10.1002/cne.21363

Gabriel, J. P., Trivedi, C. A., Maurer, C. M., Ryu, S., and Bollmann, J. H. (2012). Layer-specific targeting of direction-selective neurons in the zebrafish optic tectum. *Neuron* 76, 1147–1160. doi: 10.1016/j.neuron.2012.12.003

Gahtan, E., Tanger, P., and Baier, H. (2005). Visual prey capture in larval zebrafish is controlled by identified reticulospinal neurons downstream of the tectum. *J. Neurosci.* 25, 9294–9303. doi: 10.1523/jneurosci.2678-05.2005

Gandhi, N. J., and Katnani, H. A. (2011). Motor functions of the superior colliculus. *Annu. Rev. Neurosci.* 34, 205–231. doi: 10.1146/annurev-neuro-061010-113728

Gerchberg, R. W., and Saxton, W. O. (1972). A practical algorithm for the determination of phase from image and diffraction plane pictures. *Optik* 35, 237–246.

Heap, L. A., Goh, C., Kassahn, K., and Scott, E. K. (2013). Cerebellar output in zebrafish: an analysis of spatial patterns and topography in eurydendroid cell projections. *Front. Neural Circuits* 7:53. doi: 10.3389/fncir.2013.00053

Herculano, A. M., and Maximino, C. (2014). Serotonergic modulation of zebrafish behavior: towards a paradox. *Prog. Neuropsychopharmacol. Biol. Psychiatry* 55, 50–66. doi: 10.1016/j.pnpbp.2014.03.008

Herget, U., Wolf, A., Wullimann, M. F., and Ryu, S. (2014). Molecular neuroanatomy and chemoarchitecture of the neurosecretory preoptic-hypothalamic area in zebrafish larvae. *J. Comp. Neurol.* 522, 1542–1564. doi: 10.1002/cne.23480

Hines, J. H., Ravanelli, A. M., Schwindt, R., Scott, E. K., and Appel, B. (2015). Neuronal activity biases axon selection for myelination *in vivo*. *Nat. Neurosci.* 18, 683–689. doi: 10.1038/nn.3992

Jay, M., De Faveri, F., and McDearmid, J. R. (2015). Firing dynamics and modulatory actions of supraspinal dopaminergic neurons during zebrafish locomotor behavior. *Curr. Biol.* 25, 435–444. doi: 10.1016/j.cub.2014.12.033

Jay, M. F., and Sparks, D. L. (1987). Sensorimotor integration in the primate superior colliculus. I. Motor convergence. *J. Neurophysiol.* 57, 22–34.

Kaslin, J., Nystedt, J. M., Ostergård, M., Peitsaro, N., and Panula, P. (2004). The orexin/hypocretin system in zebrafish is connected to the aminergic and cholinergic systems. *J. Neurosci.* 24, 2678–2689. doi: 10.1523/jneurosci.4908-03.2004

King, A. J., Schnupp, J. W., Carlile, S., Smith, A. L., and Thompson, I. D. (1996). The development of topographically-aligned maps of visual and auditory space in the superior colliculus. *Prog. Brain Res.* 112, 335–350. doi: 10.1016/s0079-6123(08)63340-3

Kita, E. M., Scott, E. K., and Goodhill, G. J. (2015). Topographic wiring of the retinotectal connection in zebrafish. *Dev. Neurobiol.* 75, 542–556. doi: 10.1002/dneu.22256

Knudsen, E. I. (1982). Auditory and visual maps of space in the optic tectum of the owl. *J. Neurosci.* 2, 1177–1194.

Kokoeva, M. V., Yin, H., and Flier, J. S. (2005). Neurogenesis in the hypothalamus of adult mice: potential role in energy balance. *Science* 310, 679–683. doi: 10.1126/science.1115360

Krauzlis, R. J., Lovejoy, L. P., and Zénon, A. (2013). Superior colliculus and visual spatial attention. *Annu. Rev. Neurosci.* 36, 165–182. doi: 10.1146/annurev-neuro-062012-170249

Kwan, K. M., Fujimoto, E., Grabher, C., Mangum, B. D., Hardy, M. E., Campbell, D. S., et al. (2007). The Tol2kit: a multisite gateway-based construction kit for Tol2 transposon transgenesis constructs. *Dev. Dyn.* 236, 3088–3099. doi: 10.1002/dvdy.21343

Lane, R. H., Allman, J. M., Kaas, J. H., and Miezin, F. M. (1973). The visuotopic organization of the superior colliculus of the owl monkey (*Aotus trivirgatus*) and the bush baby (*Galago senegalensis*). *Brain Res.* 60, 335–349. doi: 10.1016/0006-8993(73)90794-4

Lázár, G. (1973). The development of the optic tectum in *Xenopus laevis*: a Golgi study. *J. Anat.* 116, 347–355.

Legland, D., Arganda-Carreras, I., and Andrey, P. (2016). MorphoLibJ: integrated library and plugins for mathematical morphology with ImageJ. *Bioinformatics* 22, 3532–3534. doi: 10.1093/bioinformatics/btw413

Lillesaar, C., Stigloher, C., Tannhäuser, B., Wullimann, M. F., and Bally-Cuif, L. (2009). Axonal projections originating from raphe serotonergic neurons in the developing and adult zebrafish, *Danio rerio*, using transgenics to visualize raphe-specific *pet1* expression. *J. Comp. Neurol.* 512, 158–182. doi: 10.1002/cne.21887

Lister, J. A., Robertson, C. P., Lepage, T., Johnson, S. L., and Raible, D. W. (1999). nacre encodes a zebrafish microphthalmia-related protein that regulates neural-crest-derived pigment cell fate. *Development* 126, 3757–3767.

Lutz, C., Otis, T. S., DeSars, V., Charpak, S., DiGregorio, D. A., and Emiliani, V. (2008). Holographic photolysis of caged neurotransmitters. *Nat. Methods* 5, 821–827. doi: 10.1038/nmeth.1241

May, P. J. (2006). The mammalian superior colliculus: laminar structure and connections. *Prog. Brain Res.* 151, 321–378. doi: 10.1016/s0079-6123(05)51011-2

McPherson, A. D., Barrios, J. P., Luks-Morgan, S. J., Manfredi, J. P., Bonkowsky, J. L., Douglass, A. D., et al. (2016). Motor behavior mediated by continuously generated dopaminergic neurons in the zebrafish hypothalamus recovers after cell ablation. *Curr. Biol.* 26, 263–269. doi: 10.1016/j.cub.2015.11.064

Meek, J. (1983). Functional anatomy of the tectum mesencephali of the goldfish. An explorative analysis of the functional implications of the laminar structural organization of the tectum. *Brain Res. Rev.* 6, 247–297. doi: 10.1016/0165-0173(83)90008-5

Meek, J., and Nieuwenhuys, R. (1998). "Holosteans and teleosts," in *The Central Nervous System of Vertebrates*, (Vol. 2) eds R. Nieuwenhuys, H. J. ten Donkelaar and C. Nicholson (Berlin: Springer), 759–937.

Meek, J., and Schellart, N. A. (1978). A golgi study of the goldfish optic tectum. *J. Comp. Neurol.* 182, 89–121. doi: 10.1002/cne.901820107

Meyer, F., and Beucher, S. (1990). Morphological segmentation. *J. Vis. Commun. Image Represent.* 1, 21–46. doi: 10.1016/1047-3203(90)90014-M

Mueller, T. (2012). What is the thalamus in zebrafish? *Front. Neurosci.* 6:64. doi: 10.3389/fnins.2012.00064

Mueller, T., and Wullimann, M. (2005). *Atlas of Early Zebrafish Brain Development: A Tool for Molecular Neurogenetics.* Amsterdam: Elsevier.

Muto, A., Lal, P., Ailani, D., Abe, G., Itoh, M., and Kawakami, K. (2017). Activation of the hypothalamic feeding centre upon visual prey detection. *Nat. Commun.* 8:15029. doi: 10.1038/ncomms15029

Nevin, L. M., Robles, E., Baier, H., and Scott, E. K. (2010). Focusing on optic tectum circuitry through the lens of genetics. *BMC Biol.* 8:126. doi: 10.1186/1741-7007-8-126

Niell, C., and Smith, S. (2005). Functional imaging reveals rapid development of visual response properties in the zebrafish tectum. *Neuron* 45, 941–951. doi: 10.1016/j.neuron.2005.01.047

Nishiguchi, R., Azuma, M., Yokobori, E., Uchiyama, M., and Matsuda, K. (2012). Gonadotropin-releasing hormone 2 suppresses food intake in the zebrafish, *Danio rerio*. *Front. Endocrinol.* 3:122. doi: 10.3389/fendo.2012.00122

Northcutt, R. G. (1982). Localization of neurons afferent to the optic tectum in longnose gars. *J. Comp. Neurol.* 204, 325–335. doi: 10.1002/cne.902040404

Orger, M. B. (2016). The cellular organization of zebrafish visuomotor circuits. *Curr. Biol.* 26, R377–R385. doi: 10.1016/j.cub.2016.03.054

Perry, S. F., Ekker, M., Farrell, A. P., and Brauner, C. J. (2010). *Fish Physiology: Zebrafish.* Amerstand: Academic Press Elsevier.

Pityk, N. I. (1979). Hypothalamic influences on unit activity in the cat superior colliculus. *Neurophysiology* 11, 419–426. doi: 10.1007/bf01062837

Preibisch, S., Saalfeld, S., and Tomancak, P. (2009). Globally optimal stitching of tiled 3D microscopic image acquisitions. *Bioinformatics* 25, 1463–1465. doi: 10.1093/bioinformatics/btp184

Preuss, S. J., Trivedi, C. A., vom Berg-Maurer, C. M., Ryu, S., and Bollmann, J. H. (2014). Classification of object size in retinotectal microcircuits. *Curr. Biol.* 24, 2376–2385. doi: 10.1016/j.cub.2014.09.012

Prober, D. A., Rihel, J., Onah, A. A., Sung, R. J., and Schier, A. F. (2006). Hypocretin/orexin overexpression induces an insomnia-like phenotype in zebrafish. *J. Neurosci.* 26, 13400–13410. doi: 10.1523/JNEUROSCI.4332-06.2006

Randlett, O., Wee, C. L., Naumann, E. A., Nnaemeka, O., Schoppik, D., Fitzgerald, J. E., et al. (2015). Whole-brain activity mapping onto a zebrafish brain atlas. *Nat. Methods* 12, 1039–1046. doi: 10.1038/nmeth.3581

Rieck, R. W., Huerta, M. F., Harting, J. K., and Weber, J. T. (1986). Hypothalamic and ventral thalamic projections to the superior colliculus in the cat. *J. Comp. Neurol.* 243, 249–265. doi: 10.1002/cne.902430208

Robinson, D. L., and McClurkin, J. W. (1989). The visual superior colliculus and pulvinar. *Rev. Oculomot. Res.* 3, 337–360.

Robles, E., Filosa, A., and Baier, H. (2013). Precise lamination of retinal axons generates multiple parallel input pathways in the tectum. *J. Neurosci.* 33, 5027–5039. doi: 10.1523/JNEUROSCI.4990-12.2013

Robles, E., Laurell, E., and Baier, H. (2014). The retinal projectome reveals brain-area-specific visual representations generated by ganglion cell diversity. *Curr. Biol.* 24, 2085–2096. doi: 10.1016/j.cub.2014.07.080

Robles, E., Smith, S. J., and Baier, H. (2011). Characterization of genetically targeted neuron types in the zebrafish optic tectum. *Front. Neural Circuits* 5:1. doi: 10.3389/fncir.2011.00001

Sas, E., and Maler, L. (1986). The optic tectum of gymnotiform teleosts Eigenmannia virescens and Apteronotus leptorhynchus: a Golgi study. *Neuroscience* 18, 215–246. doi: 10.1016/0306-4522(86)90190-9

Scott, E. K., and Baier, H. (2009). The cellular architecture of the larval zebrafish tectum, as revealed by Gal4 enhancer trap lines. *Front. Neural Circuits* 3:13. doi: 10.3389/neuro.04.013.2009

Scott, E. K., Mason, L., Arrenberg, A. B., Ziv, L., Gosse, N. J., Xiao, T., et al. (2007). Targeting neural circuitry in zebrafish using GAL4 enhancer trapping. *Nat. Methods* 4, 323–326. doi: 10.1038/nmeth1033

Semmelhack, J. L., Donovan, J. C., Thiele, T. R., Kuehn, E., Laurell, E., and Baier, H. (2014). A dedicated visual pathway for prey detection in larval zebrafish. *Elife* 3:e04878. doi: 10.7554/eLife.04878

Smith, S. M., and Vale, W. W. (2006). The role of the hypothalamic-pituitary-adrenal axis in neuroendocrine responses to stress. *Dialogues Clin. Neurosci.* 8, 383–395.

Sparks, D. L. (1988). Neural cartography: sensory and motor maps in the superior colliculus. *Brain Behav. Evol.* 31, 49–56. doi: 10.1159/000116575

Sparks, D. L., and Hartwich-Young, R. (1989). The deep layers of the superior colliculus. *Rev. Oculomot. Res.* 3, 213–255.

Streidter, G., and Northcutt, R. (1989). Two distinct visual pathways through the superficial pretectum in a percomorph teleost. *J. Comp. Neurol.* 283, 342–354. doi: 10.1002/cne.902830304

Struermer, C. (1988). Retinotopic organization of the developing retinotectal projection in the zebrafish embryo. *J. Neurosci.* 8, 4513–4530.

Tay, T. L., Ronneberger, O., Ryu, S., Nitschke, R., and Driever, W. (2011). Comprehensive catecholaminergic projectome analysis reveals single-neuron integration of zebrafish ascending and descending dopaminergic systems. *Nat. Commun.* 2:171. doi: 10.1038/ncomms1171

Temizer, I., Donovan, J. C., Baier, H., and Semmelhack, J. L. (2015). A visual pathway for looming-evoked escape in larval zebrafish. *Curr. Biol.* 25, 1823–1834. doi: 10.1016/j.cub.2015.06.002

Thompson, A. W., Vanwalleghem, G. C., Heap, L. A., and Scott, E. K. (2016). Functional profiles of visual, auditory and water flow responsive neurons in the zebrafish tectum. *Curr. Biol.* 26, 743–754. doi: 10.1016/j.cub.2016.01.041

Tian, L., Hires, S. A., Mao, T., Huber, D., Chiappe, M. E., Chalasani, S. H., et al. (2009). Imaging neural activity in worms, flies and mice with improved GCaMP calcium indicators. *Nat. Methods* 6, 875–881. doi: 10.1038/nmeth.1398

Udin, S. B. (2012). Binocular maps in Xenopus tectum: visual experience and the development of isthmotectal topography. *Dev. Neurobiol.* 72, 564–574. doi: 10.1002/dneu.20933

Ulrich-Lai, Y. M., and Herman, J. P. (2009). Neural regulation of endocrine and autonomic stress responses. *Nat. Rev. Neurosci.* 10, 397–409. doi: 10.1038/nrn2647

Vanegas, H., Laufer, M., and Amat, J. (1974). The optic tectum of a perciform teleost. I. General configuration and cytoarchitecture. *J. Comp. Neurol.* 154, 43–60. doi: 10.1002/cne.901540104

Vanwalleghem, G., Heap, L. A., and Scott, E. (2017). A profile of auditory-responsive neurons in the larval zebrafish brain. *J. Comp. Neurol.* 525, 3031–3043. doi: 10.1002/cne.24258

Vladimirov, N., Mu, Y., Kawashima, T., Bennett, D. V., Yang, C. T., Looger, L. L., et al. (2014). Light-sheet functional imaging in fictively behaving zebrafish. *Nat. Methods* 11, 883–884. doi: 10.1038/nmeth.3040

Westerfield, M. (2000). *The Zebrafish Book. A Guide for the Laboratory Use of Zebrafish (Danio rerio).* 4th Edn. Eugene, OR: University of Oregon Press.

Whyte, G., and Courtial, J. (2005). Experimental demonstration of holographic three-dimensional light shaping using a Gerchberg-Saxton algorithm. *New J. Phys.* 7:117. doi: 10.1088/1367-2630/7/1/117

Withington-Wray, D. J., Binns, K. E., Dhanjal, S. S., Brickley, S. G., and Keating, M. J. (1990). The maturation of the superior collicular map of auditory space in the guinea pig is disrupted by developmental auditory deprivation. *Eur. J. Neurosci.* 2, 693–703. doi: 10.1111/j.1460-9568.1990.tb00459.x

Xiao, T., and Baier, H. (2007). Lamina-specific axonal projections in the zebrafish tectum require the type IV collagen Dragnet. *Nat. Neurosci.* 10, 1529–1537. doi: 10.1038/nn2002

Xiao, T., Staub, W., Robles, E., Gosse, N. J., Cole, G. J., and Baier, H. (2011). Assembly of lamina-specific neuronal connections by slit bound to type IV collagen. *Cell* 146, 164–176. doi: 10.1016/j.cell.2011.06.016

Xue, H.-G., Yamamoto, N., Yoshimoto, M., Yang, C.-Y., and Ito, H. (2001). Fiber connections of the nucleus isthmi in the carp (*Cyprinus carpio*) and tilapia (*Oreochromis niloticus*). *Brain Behav. Evol.* 58, 185–204. doi: 10.1159/000057563

Yokobori, E., Azuma, M., Nishiguchi, R., Kang, K. S., Kamijo, M., Uchiyama, M., et al. (2012). Neuropeptide Y stimulates food intake in the Zebrafish, *Danio rerio*. *J. Neuroendocrinol.* 24, 766–773. doi: 10.1111/j.1365-2826.2012.02281.x

Yokobori, E., Kojima, K., Azuma, M., Kang, K. S., Maejima, S., Uchiyama, M., et al. (2011). Stimulatory effect of intracerebroventricular administration of orexin A on food intake in the zebrafish, *Danio rerio*. *Peptides* 32, 1357–1362. doi: 10.1016/j.peptides.2011.05.010

Yokogawa, T., Hannan, M. C., and Burgess, H. A. (2012). The dorsal raphe modulates sensory responsiveness during arousal in zebrafish. *J. Neurosci.* 32, 15205–15215. doi: 10.1523/JNEUROSCI.1019-12.2012

Conflict of Interest Statement: The authors declare that the research was conducted in the absence of any commercial or financial relationships that could be construed as a potential conflict of interest.

Advantages of publishing in Frontiers

OPEN ACCESS
Articles are free to read for greatest visibility and readership

FAST PUBLICATION
Around 90 days from submission to decision

HIGH QUALITY PEER-REVIEW
Rigorous, collaborative, and constructive peer-review

TRANSPARENT PEER-REVIEW
Editors and reviewers acknowledged by name on published articles

Frontiers
Avenue du Tribunal-Fédéral 34
1005 Lausanne | Switzerland

Visit us: www.frontiersin.org
Contact us: info@frontiersin.org | +41 21 510 17 00

REPRODUCIBILITY OF RESEARCH
Support open data and methods to enhance research reproducibility

DIGITAL PUBLISHING
Articles designed for optimal readership across devices

FOLLOW US
@frontiersin

IMPACT METRICS
Advanced article metrics track visibility across digital media

EXTENSIVE PROMOTION
Marketing and promotion of impactful research

LOOP RESEARCH NETWORK
Our network increases your article's readership